UC Berkeley

UC Berkeley Electronic Theses and Dissertations

Title

Mechanical, Biological and Electrochemical Investigations of Advanced Micro/Nano Materials for Tissue Engineering and Energy Storage

Permalink

https://escholarship.org/uc/item/65b5q43k

Author

Pu, Juan

Publication Date

2016

Peer reviewed|Thesis/dissertation

Mechanical, Biological and Electrochemical Investigations of Advanced Micro/Nano Materials for Tissue Engineering and Energy Storage

By

Juan Pu

A dissertation submitted in partial satisfaction of the

requirements for the degree of

Doctor of Philosophy

in

Engineering - Mechanical Engineering

in the

Graduate Division

of the

University of California, Berkeley

Committee in charge:

Professor Kyriakos Komvopoulos, Chair
Professor Lisa Pruitt
Professor Song Li

Fall 2016

Mechanical, Biological and Electrochemical Investigations of Advanced Micro/Nano Materials for Tissue Engineering and Energy Storage

Abstract

Mechanical, Biological and Electrochemical Investigations of Advanced Micro/Nano Materials for Tissue Engineering and Energy Storage

by

Juan Pu

Doctor of Philosophy in Engineering - Mechanical Engineering

University of California, Berkeley

Professor Kyriakos Komvopoulos, Chair

Various micro/nano materials have been extensively studied for applications in tissue engineering and energy storage. Tissue engineering seeks to repair or replace damaged tissue by integrating approaches from cellular/molecular biology and material chemistry/engineering. A major challenge is the consistent design of three-dimensional (3D) scaffolds that mimic the structure and biological functions of extracellular matrix (ECM), guide cell migration, provide mechanical support, and regulate cell activity. Electrospun micro/nanofibers have been investigated as promising tissue engineering scaffolds because they resemble native ECM and possess tunable surface morphologies. Supercapacitors, one of the energy storage devices, bridge the performance gap between rechargeable batteries and conventional capacitors. Active electrode materials of supercapacitors must possess high specific surface area, high conductivity, and good electrochemical properties. Carbon-based micro/nano-particles, such as graphene, activated carbon (AC), and carbon nanotubes, are commonly used as active electrode materials for storing charge in supercapacitors by the electrical double layer mechanism due to their high specific surface area and excellent conductivity.

In this thesis, the mechanical properties of electrospun bilayer microfibrous membranes were investigated for potential applications in tissue engineering. Bilayer microfibrous membranes of poly(l-lactic acid) (PLLA) were fabricated by electrospinning using a parallel-disk mandrel configuration, which resulted in the sequential deposition of a layer with aligned fibers (AFL) across the two parallel disks and a layer with random fibers (RFL), both deposited by a single process step. The membrane structure and fiber alignment were characterized by scanning electron microscopy and two-dimensional fast Fourier transform. Because of the intricacies of the generated electric field, the bilayer membranes exhibited higher porosity than the membranes fabricated with a single drum collector. However, despite their higher porosity, the bilayer membranes exhibited generally higher elastic modulus, yield strength, and toughness than single-layer membranes consisting of random fibers. Bilayer deformation at relatively high strain rates comprised multiple abrupt microfracture events comprising discontinuous fiber breakage. Bilayer membrane elongation yielded excessive necking of the RFL and remarkable fiber stretching (on the order of 400%) of the AFL. In both layers, however, the fibers exhibited multiple localized necking, attributed to the nonuniform distribution of crystalline phases

in the fibrillar structure. The high membrane porosity and good mechanical properties of the electrospun bilayer membranes and good biocompatibility and biodegradability of PLLA demonstrated in this work make these bilayer membranes good scaffold candidates for various tissue engineering applications.

Furthermore, the bilayer PLLA scaffolds showed gradual variation in through-thickness porosity and fiber alignment and an average porosity much higher than that of conventionally electrospun scaffolds (controls) with randomly distributed fibers. The biocompatibility and biological performance of the bilayer fibrous scaffolds was evaluated by *in vivo* experiments involving subcutaneous scaffold implantation in Sprague-Dawley rats, followed by histology and immunohistochemistry studies. The results illustrate the potential of bilayer scaffolds to overcome major limitations of conventionally electrospun scaffolds associated with intrinsically small pores, low porosity and, consequently, poor cell infiltration. The significantly higher porosity and larger pore size of the RFL enhanced cell motility through the scaffold thickness, whereas the relatively dense structure of the AFL provided adequate mechanical strength. The bilayer scaffolds showed more than two times higher cell infiltration than controls during implantation *in vivo*. Moreover, the unique structure of bilayer scaffolds promoted collagen fiber deposition, cell proliferation, and ingrowth of smooth muscle cells and endothelial cells *in vivo*. The results of this work reveal the high potential of the fabricated bilayer fibrous scaffolds for tissue engineering and regeneration.

Novel all-solid-state microsupercapacitors (MSCs) with 3D electrodes consisting of active materials (i.e., graphene or AC particles) and a polymer electrolyte (PE) designed for high-energy-density storage applications were fabricated and tested. The incorporation of a PE in the electrode material enhanced the accessibility of the surface of active materials by electrolyte ions and decreased the ion diffusion path during electrochemical charging/discharging. For a scan rate of 5 mV s^{-1}, the MSCs with graphene/PE and AC/PE composite electrodes demonstrated a very high areal capacitance of 95 and 134 mF cm^{-2}, respectively, comparable with that of 3D MSCs having a liquid electrolyte. In addition, the graphene/PE MSCs showed ~70% increase in specific capacitance after 10,000 charge/discharge cycles, attributed to an electro-activation process resulting from ion intercalation between the graphene nanosheets. The AC/PE MSCs also demonstrated excellent stability. The obtained results illustrate the suitability of the present 3D MSCs for various high-density solid-state energy storage applications.

Single-walled carbon nanotube (SWCNT) networks were deposited on an ultrathin polyimide substrate using the spray-deposition technique and patterned into interdigital electrodes to construct ultrahigh-power, extremely flexible, and foldable MSCs capable of operating at an ultrahigh scan rate (up to 1000 V s^{-1}) and delivering a stack capacitance of 18 F cm^{-3} and an energy density of 1.6 mWh cm^{-3}, which is comparable with that of lithium thin-film batteries. An ultrahigh power density of 1125 W cm^{-3} and extremely small time constant of 1 ms were obtained with SWCNT MSCs, comparable with aluminum electrolytic capacitors. The present MSCs showed superior electrochemical stability, with 96% capacity retention after 100,000 cycles. Furthermore, these microdevices could be reversibly and elastically bent, folded, and rolled without undergoing significant performance degradation. The developed SWCNT MSCs demonstrate high potential for

integration in flexible and wearable electronic systems for high-rate energy storage or ac line filtering.

A honeycomb polydimethylsiloxane substrate was introduced for stretchable MSC arrays based on SWNCT interdigital electrodes, which enables facile integration in flexible or wearable electronics. The honeycomb structure accommodates large deformation without generating large strains in the MSCs and interconnects. The results show that such stretchable MSC arrays with SWCNT electrodes demonstrate excellent rate capability and power performance as well as electrochemical stability up to 150% (zero prestrain) or 275% (–50% prestrain) stretching and under excessive bending or twisting. The present stretchable MSC arrays with honeycomb structures show high potential for integration with other electronics, such as energy harvesters, power management circuits, wireless charging circuits, and various sensors, encompassing a wide range of wearable, bio-implantable electronic systems.

Table of Contents

Acknowledgements

First of all, I would like to express my sincere gratitude to my advisor, Professor Kyriakos Komvopoulos, for the opportunity to study at Berkeley and the continuous support of my Ph.D. research. He has been a great mentor to me. I learned from him not only fundamental knowledge, but also the strict attitude to scientific research. He has given me the freedom to pursue various projects and provided insightful discussions and suggestions about the research. I am very grateful to Prof. Komvopoulos for his scientific advice and knowledge, his encouragement and guidance. He also gave me strong support for me to conduct part of my Ph.D. research in Tsinghua University. I truly appreciate his kindness. I would also like to express my gratitude to Prof. Komvopoulos's group members: Qian Chen, Hua Xiang, Zhichao Song, Mehrzad Tartibi, Huaming Xu, Jozef Matlak, Feifei Shi, Jun Xie, Renxiao Xu, Shengxi Wang, Jipeng Qi, et al. They have provided me valuable suggestions and help on my research.

I would also like to thank my committee members, Prof. Lisa Pruitt and Prof. Song Li for serving as my committee members and providing valuable comments and suggestions to my dissertation. I learned from Prof. Lisa Pruitt how to apply polymer engineering to biomedical devices. Prof. Song Li has provided my opportunity to conduct electrospinning and biological experiments in his group. He also gave me insightful suggestions on how to analyze the biological experiments and how to find the applications of the biological projects. I appreciate his kindness and help.

I would like to acknowledge Prof. Xiaohong Wang for providing me great opportunity to conduct part of my research work (energy storage devices) in her group at Tsinghua University. She gave me valuable guidance and support on energy storage devices-related research, I truly appreciate that. I would also like to thank the students in Prof. Wang's group, Siwei Li, Si Chen, Yingxian Lu, Xia Liu, Xuanlin Kuang, Sixing Xu, Zhonglin Wu, Mei Wang, Chen Zhou, Xiaozhao Li, Fei Teng, et al., who provided me help on my research and made me feel not alone while in Beijing.

A special thanks to my family. Words cannot express how grateful I am to my husband, my mom, my daughter, my mom and dad in law. Without them, I would never get here.

Lastly, I want to thank everyone I met at Berkeley.

Juan

Berkeley, CA

December 2016

List of Figures

row) and AFL (second row) surfaces corresponding to characteristic points of the σ-ε curve shown in (a). Red arrows indicate the direction of the applied tensile stress. All magnification bars are equal to 10 μm. (d) and (e) High-magnification SEM images of as-processed and deformed (point B in (a)) membrane, respectively. For all data, $t_a = 30\,\mu m$, $\dot{\varepsilon} = 0.017\,s^{-1}$, and the stress is applied in the direction of the aligned fibers.

Fig. 4.1 A bilayer scaffold consisting of an aligned-fiber layer (AFL) and a random-fiber layer (RFL) is produced between the aluminum disks. RFL formation commences as soon as AFL reaches a critical thickness, which significantly changes the electric field distribution due to the high dielectric constant of the deposited polymer fibers.

Fig. 4.2 Representative confocal microscopy images of an electrospun bilayer scaffold for a distance from the AFL surface z = 0–50 µm (z = 0 corresponds to the AFL surface). To enhance the observation with the confocal microscope, the fibers were doped with FITC fluorescent dye. All images have the same magnification.

Fig. 4.3 Representative cross-sectional images of (a, c) control and (b, d) bilayer scaffolds subcutaneously implanted in Sprague-Dawley rats for 5 and 14 days showing cell infiltration in vivo. Cell nuclei (blue) were stained with DAPI. Dashed and solid lines indicate the boundaries between surrounding tissue and scaffold surfaces with random and aligned fibers, respectively. Aligned fibers are at the right scaffold surface in (b) and (d). All images have the same magnification.

Fig. 4.4 (a) Cell infiltration in vivo quantified by the cell density of control and bilayer scaffolds subcutaneously implanted in Sprague-Dawley rats for 5 and 14 days. Statistically significant differences ($p<0.05$) between bilayer and control scaffold data (obtained by a two-tailed unpaired t-test) are indicated by an asterisk (*). Representative fluorescent cross-sectional images of DAPI-stained (b) control and (c) bilayer scaffolds show cell infiltration in different regions. Dashed and solid lines indicate the boundaries between surrounding tissue and scaffold surfaces with random and aligned fibers, respectively. Dashed-dot lines are used to divide the scaffolds in four regions of equal thickness denoted by 0–25%, 25–50%, 50–75%, and 75–100%. For both control and bilayer scaffolds, the 0% line represents the scaffold interface with rat muscle and fat tissues, whereas the 100% line represents the scaffold interface with superficial fascia during implantation in vivo. Aligned fibers are along the 100% line in (c). (d) Cell infiltration in vivo obtained from different regions of control and bilayer scaffolds subcutaneously implanted in Sprague-Dawley rats for 5 and 14 days. Six cryosections (six images per cryosection) were used to quantify each data point. The cross-sectional scaffold area used to quantify cell infiltration is in the range of 0.10–0.15 mm^2.

Fig. 4.5 Trichrome-stained control and bilayer scaffolds subcutaneously implanted in Sprague-Dawley rats for (a)–(d) 5 days and (e)–(h) 14 days (collagen (blue); muscle (red); cell nuclei (dark purple)). The cross-sectional images shown in (b), (d), (f), and (h) are enlarged views of regions enclosed by rectangular frames in

List of Tables

Chapter 1 – Introduction

This chapter provides a general overview of micro/nanostructured materials, with special emphasis on the two applications – micro/nanofibrous scaffolds for tissue engineering and micro/nanoscale electrode materials for energy storage devices.

1.1 Micro/nanofibrous scaffolds for tissue engineering

As defined by Langer and Vacanti in 1993, tissue engineering is "an interdisciplinary field that applies the principles of engineering and life sciences toward the development of biological substitutes that restore, maintain, or improve tissue function."[1] One aspect of tissue engineering is the design of polymeric scaffolds with specific mechanical and biological properties similar to those of native extracellular matrix (ECM) to modulate key cellular behavior, such as infiltration, migration, proliferation, and differentiation. *In vivo*, the ECM is in contact with a vast majority of cells and consists of a network of nanometer-sized proteins and glycosaminoglycans.[2] The intricate complexities of this spatial and temporal environment dynamically influence phenotypic and other cellular behavior by providing indirect and direct signaling cues.[3] Thus, the more closely the *in vivo* environment (i.e., chemical composition, morphology, surface functional groups and topographic cues) is recreated, the more likely is the success of tissue engineered scaffolds.[4-6]

Tissue engineered scaffolds function as temporary ECMs until repair or regeneration occurs. The desired properties of scaffolds include: (1) *biocompatibility* – the scaffold must be integrated with the host tissue without eliciting a major immune response;[7,8] (2) *porosity* – the scaffold must be sufficiently porous and have a high surface-volume ratio to promote cell attachment and in-growth, as well as exchange of nutrients in both *in vitro* and *in vivo* environments,[7,9] and angiogenesis upon implantation in a defect site (for vascularized tissues); (3) *ECM-like architecture and functionalities* – a scaffold must mimic the architecture and functions of native ECM[7,10] because it acts as temporary support for the cells to adhere and proliferate; and (4) *biodegradability* – the scaffolds must be biodegradable so that a revision surgery is not needed to remove the implant.[10] The rate of degradation should coincide or at least be controllable to mimic the rate of neo-tissue formation.[8]

Micro/nanofibrous scaffolds, with high porosity and surface-to-volume ratio, are promising engineering materials for tissue formation. Their fibrillar structure is of great importance for cell attachment, proliferation, and differentiation in tissue formation and may lead to engineered tissues more closely resembling native tissues. Different approaches have been developed for the formation of micro/nanofibrous scaffolds, including self-assembly, phase separation, and electrospinning.

Self-assembly systems provide attractive platforms for engineering materials with controlled micro/nanostructures. A significant research effort has been devoted on using peptides or proteins to create self-assembly scaffolds for potential applications in tissue engineering and biomedical fields. For example, Zhao et al. [11] self-assembled two

peptides, RADAFI and RADAFII, into scaffold networks with twisted and flat β-sheet nanofibers under the same conditions, respectively. Liu et al. [12] developed a mild self-assembly process to prepare porous and nanofibrous silk-based scaffolds from aqueous solution for tissue engineering. The self-assembly approach presents two main advantages: (1) the kinetics and overall mechanical properties can be controlled precisely by the peptide design and (2) various chemical functionalities are available via side chains, in combination with the capability to array these functionalities, providing possibilities to endow engineering materials with the desired structure and chemical properties.

The phase separation process forms a porous structure with a three-dimensional (3D) continuous fibrous network, which is similar to natural collagen. The fibrous network contains fibers ranging from 50 to 500 nm and may have porosity in excess of 98% within blocks of the material. Nanofibrous scaffolds produced by phase separation provide control and scaffold diversity – everything from the fiber diameter to the interconnected pore structure can be controlled to tailor the scaffold to specific application requirements. With such fine control, batch-to-batch consistency may be easily achieved. Liu [13] developed a processing technique to create 3D nanofibrous gelatin scaffolds that mimic both the physical architecture and chemical composition of natural collagen. He et al. [14] fabricated a biodegradable poly(l-lactic acid) (PLLA) 3D scaffold with macro/micropores and nanofibrous structure by phase separation from a ternary PLLA/dioxane/water system.

Electrospinning is a well-established process that can produce ultrafine fibers by electrically charging a suspended droplet of polymer melt or solution. Electrospun fibers typically have dimensions in the nano- to micro-scale range, although fiber diameters in the sub-micrometer range are mainly observed. These fibrous scaffolds are characterized by high porosity, variable pore size distribution, high surface-to-volume ratio, and most importantly, morphology closely mimicking that of the native ECM in various tissues. Moreover, the topography and mechanical properties of electrospun fibrous scaffolds can be tuned to reproduce specific functions of the ECM and match the mechanical properties of surrounding tissue *in vivo*. Electrospinning can be used to fabricate constructs consisting of various biodegradable natural or synthetic polymers, including collagen, fibrinogen, poly(glycolic acid), poly(D,L-lactide-*co*-glycolide) (PLGA), poly(L-lactic acid) (PLLA), and poly(ε-caprolactone) (PCL).

1.2 Micro/nanoscale electrode materials for energy storage

Energy storage devices usually include fuel cells, batteries, and supercapacitors. Supercapacitors, also called electrochemical capacitors (ECs), bridge the performance gap between rechargeable batteries and conventional capacitors. ECs are used in applications requiring fast charge/discharge rates, long operation life (i.e., thousands to millions of cycles), and adequate energy densities, such as vehicle regenerative braking, camera LED flash, and battery loading buffer. An EC consists of two electrodes, electrolyte, and separator, which electrically isolates the two electrodes (Fig. 1a). The most important component is the electrode material. Based on their charge storage mechanisms, ECs can be divided into two categories – electric double-layer capacitors (EDLCs) and pseudocapacitors.

EDLCs store static charges at the interface of high-surface-area electrodes and ion-containing electrolytes (Fig. 1b), and their electrode material consists of various carbon and carbon-based materials. In EDLCs, a charge is not transferred across the electrode/electrolyte interface and no net ion exchange occurs between the electrode and the electrolyte. In this way, energy is stored in the double-layer interface. The capacitance of an EDLC is given by

$$C = \frac{A\varepsilon}{4\pi d} \tag{1.1}$$

where A is the active surface area of the porous electrode, ε is the electrolyte dielectric constant, and d is the effective thickness of the electric double layer.
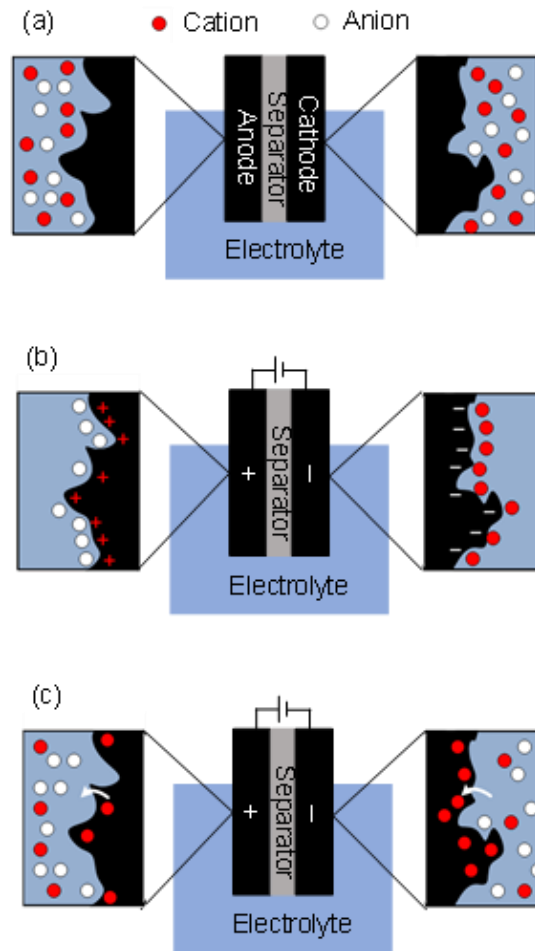
Fig. 1.1 (a) Typical structure of a supercapacitor and operation principle of (b) electric double-layer capacitor and (c) pseudocapacitor.

Pseudocapacitors use fast and reversible surface or near-surface redox reactions to storage charge (Fig. 1c). Charging and discharging of pseudocapacitors involve the passage of charge across the double layer, resulting in the passage of faradaic current through the

3

supercapacitor cell. Active materials for pseudocapacitors include transition metal oxides and conductive polymers. Since the electrochemical processes occur both at the surface and within the near-surface bulk of the solid electrode, a pseudocapacitor exhibits much larger capacitance and energy density than an EDLC. However, a pseudocapacitor usually suffers from relatively lower power density than an EDLC, because faradaic processes are normally slower than non-faradaic processes. Moreover, because redox reactions occur at the electrode, a pseudocapacitor often lacks stability during cycling.

According to Eq. (1.1), the capacity of a supercapacitor strongly depends on the total surface area of the electrodes. To obtain high capacity and fast charge/discharge, micro/nanoscale materials are commonly used as electrode materials because they exhibit high specific surface area and high porosity. Recently, notable research has been focused on the design and fabrication of highly conductive electrodes with optimized micro/nanostructures (such as onion-like carbon [15], carbide-derived carbon [16,17], carbon nanotube[18,19], graphene[20-22], graphene/carbon nanotube carpet[23]) for high specific surface area and easy electron/ion transport in order to improve the energy and power densities of MCSs, respectively. Generally, the more porous the electroactive material, the faster the electrolyte ions transport within the electrode. However, the increase in active material porosity usually results in the decrease of volumetric energy density. Therefore, it is still challenging to further enhance the power density (>1000 W cm^{-3}) at ultrafast rates (e.g., <1 ms), while maintaining relatively high energy density (> 10 mWh cm^{-3}).

Active electrode materials for supercapacitors must possess high specific surface area, high conductivity, and good electrochemical properties. Graphene, activated carbon (AC) and single-walled carbon nanotubes (SWCNTs) are promising electrode materials for storing charge in supercapacitors by the EDL mechanism. Graphene exhibits high specific surface area (up to 2630 m^2/g) and excellent conductivity. AC shows a specific surface area of $\sim$2000 m^2/g and is widely used in commercial energy storage products. SWCNT networks provide significantly higher conductivity due to the lower contact resistance of few particle-particle contacts compared with other carbonaceous materials used as electrode materials of high-power MSCs. Additionally, carbon nanotube (CNT) networks demonstrate superior robustness under bending, abrasion, and stretching conditions, and their functionalities are not affected by mechanical stresses. Various methods have been successfully developed to fabricate CNT networks for energy storage applications, including vacuum filtration to form thick, free-standing membranes (known as "buckypaper")[24,25], mixing with binder material[26,27], electrophoretic deposition[19], and spray-deposition methods[28].

1.3 Objectives

The principal objective of this dissertation is to investigate advanced micro/nano materials, such as electrospun PLLA micro/nanofibers and micro/nanoscale carbon materials, and their applications in tissue engineering and energy storage devices, respectively. The mechanical properties, *in vivo* cell infiltration and vascularization of electrospun bilayer microfibrous PLLA membranes were studied. In addition, MSCs based on micro/nanoscale

carbon particles, including AC, graphene, and single-walled carbon nanotube (SWCNT), were designed, fabricated, and tested.

1.4 Thesis organization

This dissertation is organized as following:

Chapter 1 introduces the background and motivation of this dissertation. It also provides an overview of mciro/nanomaterials and their applications in tissue engineering and energy storage devices.

Chapter 2 provides details of the two micro/nano materials deposition techniques, namely electrospinning and spray deposition, used to fabricate microfibrous PLLA membranes and SWCNT electrodes, respectively. The three material characterization techniques (scanning electron microscopy (SEM), mechanical tests and electrochemical tests) are also introduced in this chapter.

Chapter 3 introduces the fabrication of bilayer microfibrous PLLA membranes by electrospinning using a parallel-disk mandrel configuration, which results in the sequential deposition of a layer with aligned fibers across the two parallel disks and a layer with random fibers; both layers are deposited in a single process step. The focus of this chapter is on the mechanical properties of the fabricated bilayer PLLA membrane, in particular, elastic modulus, yield strength, ultimate tensile strength, and toughness. The effect of strain rate on the mechanical properties and deformation process of the bilayer scaffolds are also examined in this chapter.

Chapter 4 provides an assessment of the biocompatibility and biological performance of bilayer microfibrous PLLA scaffolds in the light of *in vivo* experiments involving subcutaneous scaffold implantation in Sprague-Dawley rats, followed by histology and immunohistochemistry.

Chapter 5 introduces novel all-solid-state 3D MSCs using AC particles/polymer electrolyte (PE) or graphene/PE composites as active materials. The electrode structure, areal capacitance, rate capability, power and energy densities, and electrochemical stability of the MSCs are investigated in this chapter.

Chapter 6 presents an ultrahigh-power, extremely flexible and foldable MSC with in-plane interdigital electrodes consisting of spray deposited SWCNT networks on an ultrathin polyimide substrate. The excellent rate capability, ultrahigh power density, and extremely small time constant of this MSC are characterized and compared with those of aluminum electrolytic capacitors. The unique flexibility and insignificant performance degradation during bending, folding, and rolling of the MSC are also presented in this chapter.

Chapter 7 introduces a novel stretchable MSC array based on spray deposited SWCNT electrodes and a honeycomb polydimethylsiloxane (PDMS) substrate. The mechanical stretchability and electrochemical performance of MSC arrays subjected to excessive bending or twisting are also illustrated in this chapter.

Chapter 8 summarizes the main findings and innovative contributions of this dissertation.

1.5 References

[1] Langer, R. and Vacanti, J.P., 1993. Tissue engineering. Science, 260(5110), pp.920-926.

[2] Xu, C., Inai, R., Kotaki, M. and Ramakrishna, S., 2004. Electrospun nanofiber fabrication as synthetic extracellular matrix and its potential for vascular tissue engineering. Tissue Engineering, 10(7-8), pp.1160-1168.

[3] Behonick, D.J. and Werb, Z., 2003. A bit of give and take: the relationship between the extracellular matrix and the developing chondrocyte. Mechanisms of development, 120(11), pp.1327-1336.

[4] Li, W.J., Laurencin, C.T., Caterson, E.J., Tuan, R.S. and Ko, F.K., 2002. Electrospun nanofibrous structure: a novel scaffold for tissue engineering. Journal of Biomedical Materials Research, 60(4), pp.613-621.

[5] Mo, X.M., Xu, C.Y., Kotaki, M. and Ramakrishna, S., 2004. Electrospun P(LLA-CL) nanofiber: a biomimetic extracellular matrix for smooth muscle cell and endothelial cell proliferation. Biomaterials, 25(10), pp.1883-1890.

[6] Smith, L.A. and Ma, P.X., 2004. Nano-fibrous scaffolds for tissue engineering. Colloids and surfaces B: biointerfaces, 39(3), pp.125-131.

[7] Liu, X. and Ma, P.X., 2004. Polymeric scaffolds for bone tissue engineering. Annals of Biomedical Engineering, 32(3), pp.477-486.

[8] Hutmacher, D.W., 2000. Scaffolds in tissue engineering bone and cartilage. Biomaterials, 21(24), pp.2529-2543.

[9] Sharma, B. and Elisseeff, J.H., 2004. Engineering structurally organized cartilage and bone tissues. Annals of Biomedical Engineering, 32(1), pp.148-159.

[10] Rosso, F., Marino, G., Giordano, A., Barbarisi, M., Parmeggiani, D. and Barbarisi, A., 2005. Smart materials as scaffolds for tissue engineering. Journal of Cellular Physiology, 203(3), pp.465-470.

[11] Zhao, Y., Tanaka, M., Kinoshita, T., Higuchi, M. and Tan, T., 2010. Nanofibrous scaffold from self-assembly of β-sheet peptides containing phenylalanine for controlled release. Journal of Controlled Release, 142(3), pp.354-360.

[12] Lu, Q., Wang, X., Lu, S., Li, M., Kaplan, D.L. and Zhu, H., 2011. Nanofibrous architecture of silk fibroin scaffolds prepared with a mild self-assembly process. Biomaterials, 32(4), pp.1059-1067.

[13] Liu, X. and Ma, P.X., 2009. Phase separation, pore structure, and properties of nanofibrous gelatin scaffolds. Biomaterials, 30(25), pp.4094-4103.

[14] He, L., Zhang, Y., Zeng, X., Quan, D., Liao, S., Zeng, Y., Lu, J. and Ramakrishna, S., 2009. Fabrication and characterization of poly (l-lactic acid) 3D nanofibrous scaffolds with controlled architecture by liquid–liquid phase separation from a ternary polymer–solvent system. Polymer, 50(16), pp.4128-4138.

[15] Pech, D., Brunet, M., Durou, H., Huang, P., Mochalin, V., Gogotsi, Y., Taberna, P.L. and Simon, P., 2010. Ultrahigh-power micrometre-sized supercapacitors based on onion-like carbon. Nature Nanotechnology, 5(9), pp.651-654.

[16] Korenblit, Y., Rose, M., Kockrick, E., Borchardt, L., Kvit, A., Kaskel, S. and Yushin, G., 2010. High-rate electrochemical capacitors based on ordered mesoporous silicon carbide-derived carbon. ACS Nano, 4(3), pp.1337-1344.

[17] Tsai, W.Y., Gao, P.C., Daffos, B., Taberna, P.L., Pérez, C.R., Gogotsi, Y., Favier, F. and Simon, P., 2013. Ordered mesoporous silicon carbide-derived carbon for high-power supercapacitors. Electrochemistry Communications, 34, pp.109-112.

[18] Futaba, D.N., Hata, K., Yamada, T., Hiraoka, T., Hayamizu, Y., Kakudate, Y., Tanaike, O., Hatori, H., Yumura, M. and Iijima, S., 2006. Shape-engineerable and highly densely packed single-walled carbon nanotubes and their application as super-capacitor electrodes. Nature Materials, 5(12), pp.987-994.

[19] Du, C. and Pan, N., 2006. Supercapacitors using carbon nanotubes films by electrophoretic deposition. Journal of Power Sources, 160(2), pp.1487-1494.

[20] Wu, Z.S., Parvez, K., Feng, X. and Müllen, K., 2013. Graphene-based in-plane micro-supercapacitors with high power and energy densities. Nature Communications, 4.

[21] Qi, D., Liu, Z., Liu, Y., Leow, W.R., Zhu, B., Yang, H., Yu, J., Wang, W., Wang, H., Yin, S. and Chen, X., 2015. Suspended wavy graphene microribbons for highly stretchable microsupercapacitors. Advanced Materials, 27(37), pp.5559-5566.

[22] Niu, Z., Zhang, L., Liu, L., Zhu, B., Dong, H. and Chen, X., 2013. All-Solid-State Flexible Ultrathin Micro-Supercapacitors Based on Graphene. Advanced Materials, 25(29), pp.4035-4042.

[23] Lin, J., Zhang, C., Yan, Z., Zhu, Y., Peng, Z., Hauge, R.H., Natelson, D. and Tour, J.M., 2012. 3-dimensional graphene carbon nanotube carpet-based microsupercapacitors with high electrochemical performance. Nano Letters,13(1), pp.72-78.

[24] Kim, J.H., Nam, K.W., Ma, S.B. and Kim, K.B., 2006. Fabrication and electrochemical properties of carbon nanotube film electrodes. Carbon, 44(10), pp.1963-1968.

[25] Ma, C.W., Huang, P.C. and Yang, Y.J., 2015, January. A paper-like micro-supercapacitor with patterned buckypaper electrodes using a novel vacuum filtration technique. In 28th IEEE International Conference on Micro Electro Mechanical Systems (MEMS), pp. 1067-1070.

[26] Zhang, H., Cao, G., Yang, Y. and Gu, Z., 2008. Comparison between electrochemical properties of aligned carbon nanotube array and entangled carbon nanotube electrodes. Journal of the Electrochemical Society, 155(2), pp.K19-K22.

[27] Liu, C.G., Fang, H.T., Li, F., Liu, M. and Cheng, H.M., 2006. Single-walled carbon nanotubes modified by electrochemical treatment for application in electrochemical capacitors. Journal of Power Sources, 160(1), pp.758-761.

[28] Kaempgen, M., Chan, C.K., Ma, J., Cui, Y. and Gruner, G., 2009. Printable thin film supercapacitors using single-walled carbon nanotubes. Nano Letters, 9(5), pp.1872-1876.

Chapter 2 – Experimental methods

This chapter provides an introduction to the micro/nano material deposition techniques, (i.e., electrospinning and spray deposition) and material characterization methods (i.e., scanning electron microscopy (SEM) and mechanical and electrochemical tests) used in this dissertation. The electrospinning technique was used to fabricate microfibrous poly(l-lactic acid) (PLLA) membranes for tissue engineering, whereas the spray deposition technique was used to fabricate single-walled carbon nanotube (SWCNT) thin-film electrodes for energy storage microdevices.

2.1 Micro/nano material deposition techniques

2.1.1 Electrospinning technique

The electrospinning process, originally developed to produce ultrafine polymer fibers [1-9], has recently re-emerged as a novel tool for generating micro/nanoscale fibrous biopolymer scaffolds for tissue engineering. In this process, a polymer solution is ejected from the capillary outlet of a syringe needle by a strong electrostatic force and is deposited as a non-woven fabric mat on a grounded collector (counter electrode) (Fig. 2.1). As this jet travels through the air, the solvent evaporates, leaving behind ultrafine polymer fibers. A high voltage (5-50 kV) is applied between the syringe needle and the collector. The typical distance between the syringe needle and collector is 5-50 cm.
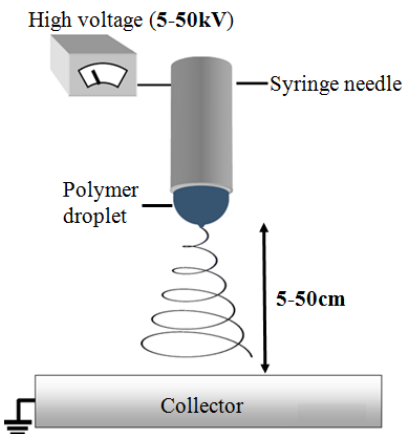
Fig. 2.1 Schematic illustration of the electrospinning process.

One of the important functions of microfibrous polymer scaffolds in tissue engineering is to support the desired cell functions and maintain phenotype-specific activities. For functional tissue regeneration, the scaffold interspace is critical for cell growth and associated activities. The porosity, pore size, and pore interconnectivity are key factors in cell infiltration in nonwoven scaffolds. Pore sizes of several hundred micrometers are often necessary for optimal cell migration [10]. In general, a porosity of ~90% or higher is desirable for cell infiltration, provided the mechanical strength of the scaffold satisfies the requirements of the specific application.
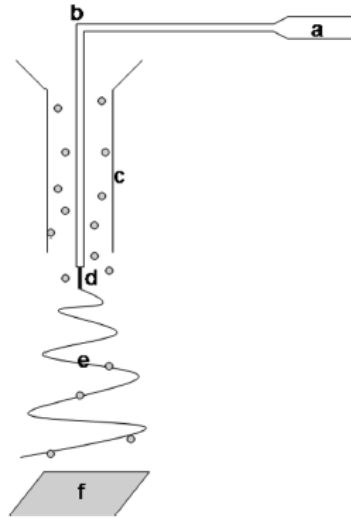
Fig. 2.2 Schematic illustration of the electrospinning setup showing the introduction of salt particles during electrospinning process to enhance the porosity of the membranes. a. syring pump, b. extension tube, c. sheath surrounding the needle into which the salt particles are added, d. needle, e. electrospun fiber interacting with falling salt particles, and f. grounded collector. (Reproduced from reference [15]).
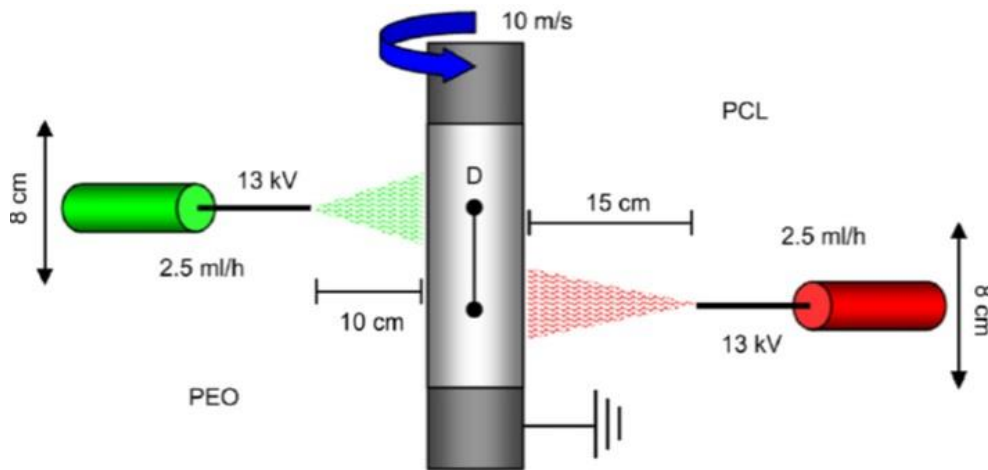
Fig. 2.3 Schematic illustration of the co-electrospinning setup used to fabricate PCL/PEO composite fibrous membranes. (Reproduced from reference [16]).

A common approach for producing electrospun mats with large pores is by the selective removal of sacrificial materials. For example, scaffolds of high porosity and pore sizes in the range of 900–5000 μm^2 were fabricated by a cryogenic electrospinning process that uses ice crystals as templates [14], whereas scaffolds comprising large fiber-free regions were produced by combining electrospinning and salt leaching (Fig. 2.2) [15]. High-porosity scaffolds have also been synthesized by co-electrospinning poly(ε-caprolactone) (PCL) functional material and water-soluble polyethylene oxide (PEO) and then removing the PEO fibers by water rinsing [16] (Fig. 2.3). In this work, a novel technique was

developed and used to fabricate bilayer microfibrous membranes with porosity of 87.5%, which is nearly 10% higher than conventionally electrospun random microfibrous membranes, in order to enhance cell infiltration and vascularization *in vivo*.

2.1.2 Spray deposition

Purified SWCNTs (P3-SWNT, Carbon Solutions) with 1–3 at% carboxylic acid surface functional groups were used as electrode materials. The SWCNTs were dispersed in deionized (DI) water with a tip sonicator for 1–2 h to form a 0.5–1 mg/mL stable suspension. The suspension was then sprayed onto the Cr/Au layer and placed on a plate heated to 40–60°C to form ~280-nm-thick SWCNT films. The sprayed SWCNT films were used as MSC electrodes without further treatment.

2.2 Material characterization techniques

2.2.1 SEM

A scanning electron microscope (SEM) uses a focused electron beam to scan a sample surface and create an image. The electrons in the beam interact with the sample, producing various signals that can be used to obtain information about the surface topography and composition. The micro/nanostructure of materials can be examined with SEM. For the electrospun bilayer microfibrous PLLA membranes, the cross sections of the membranes were examined to investigate the fiber organization in the membrane. Before SEM imaging, membranes were cut into appropriate sizes with ultrasharp Pt-coated blades and coated with a thin (~10 Å) Au-Pd layer to improve surface conductance. The SEM technique was also used to examine the electrode structure of energy storage microdevices, including graphene or activated carbon (AC)/polymer electrolyte composite electrodes and spray-deposited SWCNT electrodes.

2.2.2 Mechanical tests

The mechanical properties of the electrospun fibrous scaffolds are of critical importance in tissue engineering because the *in vivo* environment is not stress free. Tensile tests were performed with an Instron machine to investigate the mechanical properties, including elastic modulus, yield strength, ultimate tensile strength, and toughness, of electrospun bilayer microfibrous PLLA scaffolds. The effect of strain rate on the mechanical properties of the bilayer PLLA scaffolds was also studied with the Instron machine.

For the stretchable MSCs array with honeycomb polydimethylsiloxane (PDMS) substrate and SWCNT electrodes, the stress-strain response of the device is of great importance for the potential application in wearable electronic systems. The stress-strain response of these devices was also obtained with the Instron machine and compared with those of a flat PDMS substrate.

2.2.3 Electrochemical tests

The electrochemical properties of the developed MSCs were characterized with an electrochemical workstation that uses a two-electrode system. The electrochemical

characterizations include cyclic voltammetry (CV) tests, galvanostatic charge-discharge (GCD) tests, life cycle tests, and electrochemical impedance spectroscopy (EIS).

In the CV tests, the MSCs were subjected to a cyclic linear potential change with time at a scan rate $dV/dt = s$, generating a response current $\pm I = C\,(\pm s)$, where C is the capacitance of the MSCs. This procedure provides a convenient and sensitive method for characterizing both the double-layer and pseudocapacitance behavior of capacitors. Under conditions where the response is reversible to positive and negative moving sweeps, the resulting voltammogram for one direction of the potential sweep is the mirror image of that generated by the opposite direction sweep, provided there is no diffusion control. Thus, it is a useful criterion of reversibility in capacitive or pseudocapacitative charge and discharge processes and is a fundamental characteristic of pure capacitive behavior.

For a given scan rate s, the capacitance of the material or the supercapacitor can be obtained from CV measurements using the following equation

$$C = \frac{Q}{\Delta V} = \frac{1}{\Delta V} \int I\, dt \qquad\qquad (2.1)$$

where Q is the total charge during the charge or discharge process, ΔV is the potential range, and I is the current during the CV test that varies with time. To determine the specific capacitance, the areal or volumetric capacitance was normalized by the footprint area or the volume of the electrodes.

In the GCD test, a train of charging and discharging currents was applied and the resulting voltage was recorded. The charge/discharge curves were almost linear and symmetric. The MSC cells were subjected to GCD tests of varying current density. The specific capacitance was calculated from the linear part of the GCD curves using the relation

$$C = \frac{I \times t}{\Delta V} \qquad\qquad (2.2)$$

where I is the discharge current in A, t the discharge time in s, and ΔV is the scan potential window in V.

Life cycle testing was performed by cyclic voltammetry. The capacitance was recorded in each charge/discharge cycle and plotted as a function of number of cycles to investigate the electrochemical stability of the MSCs.

EIS provide the electronic/ionic conductivity of electrode materials during charging/discharging. Either voltage control (potentiostatic) or current control (galvanostatic) mode can be used. Impedance responses of the MSCs recorded by the EIS instrument were shown as Nyquist plots, illustrating the relationship between the imaginary impedance and real impedance. Normally, the capacitance of MSCs shows frequency dependence, particularly in the case of porous electrodes. At high frequencies, the capacitance is only due to the electrode because the electrolyte ions do not have enough

time to diffuse into the nanoporous material; in this case the capacitance is low. At low frequencies, the whole surface may be charged, resulting in high capacitance.

2.3 References

[1] Liu, S.J., Kau, Y.C., Chou, C.Y., Chen, J.K., Wu, R.C. and Yeh, W.L., 2010. Electrospun PLGA/collagen nanofibrous membrane as early-stage wound dressing. Journal of Membrane Science, 355(1), pp.53-59.

[2] Zeng, J., Xu, X., Chen, X., Liang, Q., Bian, X., Yang, L. and Jing, X., 2003. Biodegradable electrospun fibers for drug delivery. Journal of Controlled Release, 92(3), pp.227-231.

[3] Zong, X., Ran, S., Fang, D., Hsiao, B.S. and Chu, B., 2003. Control of structure, morphology and property in electrospun poly (glycolide-co-lactide) non-woven membranes via post-draw treatments. Polymer, 44(17), pp.4959-4967.

[4] Qin, X.H. and Wang, S.Y., 2006. Filtration properties of electrospinning nanofibers. Journal of Applied Polymer Science, 102(2), pp.1285-1290.

[5] Matthews, J.A., Wnek, G.E., Simpson, D.G. and Bowlin, G.L., 2002. Electrospinning of collagen nanofibers. Biomacromolecules, 3(2), pp.232-238.

[6] Wnek, G.E., Carr, M.E., Simpson, D.G. and Bowlin, G.L., 2003. Electrospinning of nanofiber fibrinogen structures. Nano Letters, 3(2), pp.213-216.

[7] Li, W.J., Laurencin, C.T., Caterson, E.J., Tuan, R.S. and Ko, F.K., 2002. Electrospun nanofibrous structure: a novel scaffold for tissue engineering.Journal of biomedical materials research, 60(4), pp.613-621.

[8] Zong, X., Kim, K., Fang, D., Ran, S., Hsiao, B.S. and Chu, B., 2002. Structure and process relationship of electrospun bioabsorbable nanofiber membranes. Polymer, 43(16), pp.4403-4412.

[9] Lee, K.H., Kim, H.Y., Khil, M.S., Ra, Y.M. and Lee, D.R., 2003. Characterization of nano-structured poly (ε-caprolactone) nonwoven mats via electrospinning. Polymer, 44(4), pp.1287-1294.

[10] Ratner, B.D., Hoffman, A.S., Schoen, F.J. and Lemons, J.E., 2004. Biomaterials science: an introduction to materials in medicine. Academic press.

[11] Leong, M.F., Rasheed, M.Z., Lim, T.C. and Chian, K.S., 2009. In vitro cell infiltration and in vivo cell infiltration and vascularization in a fibrous, highly porous poly (D, L-lactide) scaffold fabricated by cryogenic electrospinning technique. Journal of Biomedical Materials Research Part A, 91(1), pp.231-240.

[12] Nam, J., Huang, Y., Agarwal, S. and Lannutti, J., 2007. Improved cellular infiltration in electrospun fiber via engineered porosity. Tissue engineering,13(9), pp.2249-2257.

[13] Baker, B.M., Gee, A.O., Metter, R.B., Nathan, A.S., Marklein, R.A., Burdick, J.A. and Mauck, R.L., 2008. The potential to improve cell infiltration in composite fiber-aligned electrospun scaffolds by the selective removal of sacrificial fibers. Biomaterials, 29(15), pp.2348-2358.

Chapter 3 – Mechanical properties of electrospun bilayer microfibrous membranes

This chapter focuses on the mechanical properties of electrospun bilayer microfibrous membranes for potential applications in tissue engineering. Bilayer microfibrous membranes of poly(l-lactic acid) (PLLA) were fabricated by electrospinning using a parallel-disk mandrel configuration, resulting in the sequential deposition of a layer with aligned fibers across the two parallel disks and a layer with random fibers both in a single process step. Bilayer membranes demonstrated generally higher elastic modulus, yield strength, and toughness than single-layer membranes consisting of random fibers.

3.1 Introduction

Electrospinning is an effective technique for fabricating fibrous membrane-like structures consisting of various polymers. In addition to its versatility, low cost, and simplicity, electrospinning enables the fabrication of fibrous structures with aligned fibers of a narrow diameter distribution. Potential applications of fibrous polymeric membranes include wound dressing [1], drug delivery [2], scaffolds for tissue engineering [3], filters [4], and nanocomposite materials [5]. The structure of electrospun fibrous membranes resembles that of extracellular matrix (ECM) in various native tissues and organs and also exhibits a high specific surface area, which is conducive to the attachment of cells and bioactive molecules. Moreover, electrospinning is effective in tuning the membrane morphology and can be used to fabricate constructs of a wide range of polymer materials.

The recovery of the functionality of damaged tissue *in vivo* and reconstruction of tissue architecture *in vitro* while allowing for exquisite tissue-specific functions are critical in tissue engineering. Consequently, biodegradable three-dimensional fibrous membranes are promising scaffolds for tissue engineering. Micro/nanofibrous constructs have been synthesized from various biodegradable natural or synthetic polymers, including collagen [6], fibrinogen [7], poly(glycolic acid) [8], poly(D,L-lactide-*co*-glycolide) (PLGA) [9], poly(L-lactic acid) (PLLA) [10], and poly(ε-caprolactone) (PCL) [11]. PLLA is commonly used in implants and sutures [12] because in addition to its biodegradability, it possesses sufficient strength to endure mechanical stresses *in vivo*.

Native ECM exhibits a specific arrangement depending on the type of tissue and mechanical stimulus. For example, collagen fibers demonstrate circumferential orientation in the meniscus, skeletal muscles show a highly organized structure of long parallel bundles consisting of multinucleated myotubes, and blood vessels possess a hierarchical structure showing a preferential fiber alignment in the direction of the repeatedly applied force. However, the *in vivo* architecture is a key determinant in tissue engineering where well-defined scaffold architectures with controlled pore size, porosity, and topographies conducive to cell attachment and growth are of critical importance. Hierarchical structures with integrated layers of aligned and random fibers fabricated by electrospinning are beneficial for certain tissue engineering applications, such as nerve [13] and spinal cord

regeneration [14] and cardiovascular remodeling [15]. However, electrospun materials demonstrate relatively low porosity for biological applications. While several methods have been developed to enhance the porosity of electrospun scaffolds, e.g., salt leaching [16], laser ablation [17], and sacrificial fibers [18], the increase of porosity usually compromises the mechanical strength of the scaffold. Therefore, electrospinning methods that produce fibrous scaffolds with ECM-like structures, high porosity, and good mechanical strength are of high importance in tissue engineering.

Although earlier studies have provided insight into the mechanical properties of scaffolds with either random or aligned fibers, very little is known about the mechanical behavior and deformation mechanisms of bilayer fibrous scaffolds. The objective of this study was twofold: (1) development of a single-step electrospinning process for fabricating fully integrated bilayer membranes consisting of layers with aligned and random fibers and (2) examination of the mechanical behavior of the bilayer membranes subjected to a wide range of elongation and strain rate. While the role of the layer with aligned fibers is to provide spatial cues that resemble native tissue and can guide cell attachment and growth, the role of the layer with loosely packed and randomly distributed fibers is to promote cell infiltration and tissue growth. Despite the higher porosity of bilayer membranes compared to single-layer membranes with random fibers, bilayer membranes demonstrate significantly improved mechanical properties due to the distinctly different deformation characteristics of the two layers, resulting in multiple necking and fracture of the highly stretched fibers.

3.2 Materials and methods

3.2.1 Sample fabrication

In contrast to the conventional collector used in previous studies [14,19], electrospinning of bilayer membranes consisting of layers with aligned and random fibers was accomplished with a parallel-plate conductive collector. A 19% w/v PLLA solution of 1.09 dL/g inherent viscosity (Lactel Absorbable Polymers, Pelham, AL) was prepared in hexafluoroisopropanol (HFIP) by sonication at room temperature for 1 h. The polymer solution was electrospun using a custom-made electrospinning setup (Fig. 3.1(a)). The PLLA solution was delivered by a syringe pump at a constant rate to the tip of a stainless steel needle of 0.43 mm inner diameter suspended over a rotating mandrel (collector). The mandrel comprised two parallel aluminum disks of 55 mm diameter and 3 mm thickness connected with a 15-mm-long aluminum rod of 3 mm diamterer. To restrict fiber deposition only between the the two disks, the rod was coated with ~15-mm-thick polydimethylsiloxane (PDMS).

The electrospinning process shown in Fig. 3.1(b) and (c) demonstrated the formation of bilayer membrane between two parallel disks. A dc power supply (Gamma ES30, Gamma High Voltage Research, Ormond Beach, FL) was used to apply a potential difference of 12 kV between the needle and the grounded mandrel, which was rotated by an ac motor at a rotational speed of 15 rpm. The solution feeding rate was 1.0 mL/h and the distance between the needle and mandrel axis was fixed at 12 cm. Under electrostatic field, the pendant droplet of the polymer solution at the needle was deformed into a conical shape.

When the electrostatic forces overcame the surface tension, a charged polymer jet was ejected from the droplet and moved towards the grounded collector. As driven by the electrostatic interactions, the charged fibers were stretched to span across the gap between two aluminum disks and thus to form alignment in the direction perpendicular to the disk edges as shown in Fig. 3.1(b). However, the fibers deposited on the aluminum disks were randomly orientated. After deposition of aligned fibers suspended between two disks at a critical layer thickness, the subsequent fiber deposition became random (as shown in Fig. 3.1(c)) because the previously deposited fibers acted as an insulation layer, affecting the electric field distribution. Thus, the membrane obtained between two disks has a bilayer structure with one layer of aligned fibers and another layer of randomly orientated fibers.

Membranes of purely aligned PLLA fibers were obtained by interrupting the electrospinning process before the onset of random fiber deposition. To fabricate membranes with fully random fibers, similar to the random layer of the bilayer PLLA membranes, polyethylene oxide (PEO) fibers were first deposited to form the aligned layer of the bilayer membrane, followed by the deposition of a layer with random PLLA fibers. Single-layer membranes with fully random PLLA fibers were then obtained by peeling off the PLLA layer from the PEO layer with aligned fibers. The PEO solution was prepared by dissolving 2.6 g of PEO powder (molecular weight = 100,000 g/mol, Sigma-Aldrich, St. Louis, MO) in 1 mL of deionized water and 11 mL of ethanol and stirring at 60 $^{\circ}$C overnight. The electrospinning parameters for PEO fiber deposition were identical to those of PLLA fiber deposition.
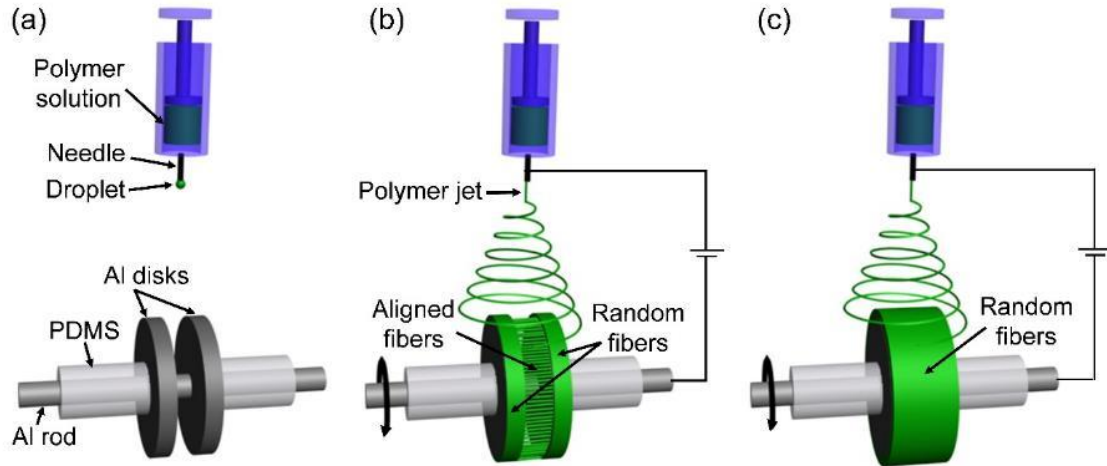
Fig. 3.1 Schematic illustrations of (a) electrospinning apparatus and (b-c) formation of bilayer membrane. (a) An aluminum mandrel consisting of a rod and two parallel disks is used as a collector of the polymer fibers ejected from a needle. The rod is coated with PDMS to restrict fiber deposition only between the parallel disks. (b) The deposition of aligned fibers between two parallel disks. During electrospinning, the rotating mandrel is grounded, while the stationary needle is subjected to a high dc voltage. (c) The subsequent deposition of random fibers between the two disks, when the layer thickness of previously deposited aligned fibers reaches a critical value.

The bilayer membrane thickness was varied in the range of 50–200 µm. The thickness of the single-layer membranes with aligned fibers was fixed at 30 µm, whereas that of single-layer membranes with randomly oriented fibers fabricated with the parallel-disk system and the solid drum collector was fixed at 100 and 250 µm, respectively. Membrane thickness measurements were obtained with a thickness gauge (Mitutoyo Absolute No. 547-500, Mitutoyo America, Aurora, IL). After electrospinning, the membranes were air-dried under a hood overnight to remove any HFIP residue.

Single-layer fibrous membranes were also fabricated by electrospinning with a conventional set up that uses a solid drum as the collector (Fig. 3.2). The electrospinning parameters were the same as those used to fabricate the bilayer membranes (i.e., 19% w/v PLLA solution, 1.0 mL/h flow rate, 12 kV voltage, 15 rpm rotational speed, and 12 cm needle-to-mandrel axis distance). The mandrel consisted of an aluminum drum with 55 mm diameter and 21 mm thickness and an aluminum rod of 3 mm diameter. Fiber deposition was restricted to the drum surface by coating the aluminum rod with ~15-mm-thick PDMS.
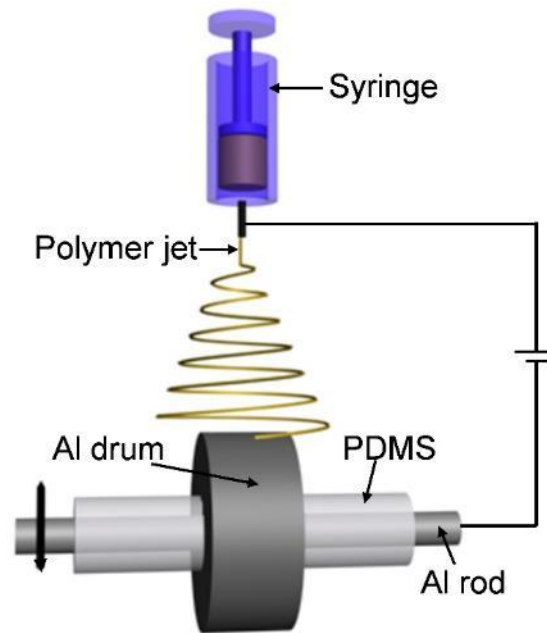
Fig. 3.2 Schematic illustration of the electrospinning setup for fabricating random membranes. The mandrel consists of an aluminum solid drum and an aluminum rod coated with PDMS to restrict polymer deposition only on the drum. During electrospinning, the mandrel is rotated around its axis at a speed of 15 rpm, the drum is grounded, and the stationary syringe needle is subjected to a high dc voltage.

3.3.2 Electrical field distribution simulation

The electric field distribution for the electrospinning systems with a solid-drum or parallel-disk collector was analyzed with the COMSOL finite element code. Fig. 3.3(a) shows the 3D geometric model of the parallel-disk electrospinning system with air as the surrounding medium (a similar model was used for the single-drum case), whereas Fig. 3.3(b) shows a

close view of the electrospinning components, i.e., double-disk aluminum collector, syringe needle, and needle holder.
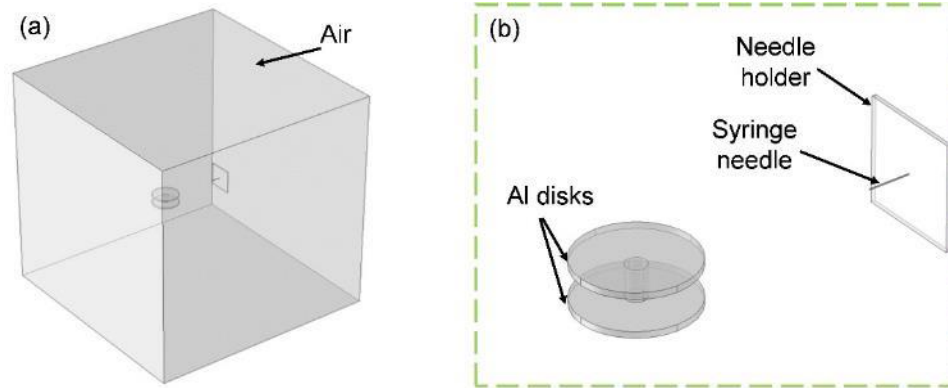
Fig. 3.3 (a) 3D model of electrospinning system with a parallel-disk collector surrounded by air used in the electric field simulations and (b) close view of system components (syringe needle, needle holder, and collector consisting of two parallel aluminum disks).

Table 3.1 Dimensions used in the electric field simulations

Parallel-disk collector system	Single-drum collector system
Air cage: $500 \times 500 \times 500$ mm^3	Air cage: $500 \times 500 \times 500$ mm^3
Aluminum disk: $d = 55$ mm, $t = 3$ mm	Aluminum drum: $d = 55$ mm, $t = 21$ mm
Syringe needle: $d = 0.625$ mm, $l = 20$ mm	Syringe needle: $d = 0.625$ mm, $l = 20$ mm
Needle holder: $50 \times 50 \times 2$ mm^3	Needle holder: $50 \times 50 \times 2$ mm^3
Needle-to-mandrel axis distance: 120 mm	Needle-to-mandrel axis distance: 120 mm
Spacing between disks: 15 mm	

Table 3.2 Material properties and boundary conditions used in the electric field simulations

Materials	Properties	Boundary conditions
Air	Relative permittivity = 1 Electrical conductivity = 0 S/m	Outer surfaces: insulated ($\boldsymbol{n} \cdot \boldsymbol{D} = 0$)
Aluminum (collectors)	Electrical conductivity = 3.77×10^7 S/m Density = 2700 kg/m^3	Grounded
Steel (syringe needle, needle holder)	Electrical conductivity = 4×10^6 S/m Density = 7850 kg/m^3	Potential = 12 kV

The component dimensions (diameter d, length l, and thickness t), material properties, and boundary conditions used in the simulations are given in Tables 3.1 and 3.2. The material for the collector was aluminum, while for the syringe needle and needle holder it was steel. A potential of 12 kV was applied to the syringe needle and needle holder and the collector was grounded. The outer surface of the air cage was assumed to be insulated, i.e., $\boldsymbol{n} \cdot \boldsymbol{D} = 0$, where $\boldsymbol{n}$ and $\boldsymbol{D}$ represent the outer normal vector of the surfaces and the electric displacement vector, respectively.

3.2.3 Scanning electron microscopy

Microscopic images of electrospun fibrous membranes were captured at different magnifications using a scanning electron microscope (SEM, TM-1000, Hitachi, Tokyo, Japan). Before SEM imaging, membranes were cut into appropriate sizes and coated with a thin (~10 Å) Au-Pd layer to improve surface conductance. For cross-section imaging, membranes were cut with ultrasharp Pt-coated blades.

3.2.4 Characterization of fiber alignment

To examine the through-thickness variation of fiber alignment in the bilayer membranes, the electrospinning process was interupted several times to perform SEM imaging. A modified fast Fourier transform (FFT) technique [20] was used to quantify the fiber alignment in the SEM images. Briefly, SEM images (2000X magnification) of membrane surfaces were converted to gray scale, cropped to 1024×1024 pixels, and masked with a circular pattern with a gradation of gray scale pixels (darkest at the periphery and lightest at the inner ring) using special software (Adobe Photoshop, Adobe, San Jose, CA). The images were then imported into ImageJ software (NIH, http://rsb.info.nih.gov/ij/) and transformed using two-dimensional FFT, which converted spatial information of an image to a mathematically defined frequency domain. Transformed images were rotated by 90º to match the alignment of the original images. Pixel intensities along each radian of the transformed images were summed up using the oval-profile ImageJ plugin (courtesy of Bill O'Connell, http://rsbweb.nih.gov/ij/plugins/oval-profile.html). Since the original images were largely symmetric, pixel intensity data from 0º to 180º were used for further analysis. To account for differences in the sample thickness and contrast/brightness of the original images, the pixel intensity at each radian was subtracted from the lowest value and the result was normalized by the sum from 0º to 180º. Normalized data represent percentages of fibers aligned in a given direction.

3.2.5 Mechanical testing

Tensile testing of electrospun PLLA samples was carried out with an Instron 5544 tester (Instron, Norwood, MA). Specimens for mechanical testing were prepared by cutting electrospun PLLA membranes into 15 mm × 5 mm strips. For bilayer and single-layer membranes with fully aligned fibers, the longer edges of the strips were cut and the external stress was applied in the direction of fiber alignment. Before tensile testing, three thickness measurements were obtained with a thickness gauge along the length of each strip, which were then averaged to calculate the sample thickness. Likewise, three measurements of the strip width were obtained with a digital caliper and averaged to estimate the strip width. After placing the tensile specimen between the grips, the gauge length was estimated as the

average of three measurements. Specimens were stretched up to a specific elongation or to failure at a constant strain rate of 0.0017, 0.017, or 0.17 s^{-1}, while the applied force and elongation were recorded with a special software (Bluehill, Instron, Norwood, MA). For mechanical tests, the thickness of single-layer membranes with aligned fibers was 30 µm and with randomly orientated fibers was 100 µm, and three different thickness (50, 100, and 200 µm) of bilayer membranes was used. To image the stretched membranes with the SEM, elongated specimens were glued onto a hollow aluminum disk so that both the front and the back specimen sides to be observable with the SEM. All tensile experiments were performed in displacement-control mode.

Engineering stress σ versus engineering strain ε responses were obtained by normalizing the measured force and elongation by the original cross section area (thickness $\times$ width) and gauge length, respectively. The elastic modulus E was determined as the slope of the linear region of the stress-strain curve, while the yield strength σ_Y was defined as the intersection of the stress-strain curve and a line parallel to the elastic part of the curve crossing the strain axis at a 0.002 offset strain. The ultimate tensile strength σ_u was obtained as the maximum stress in the engineering stress-strain response. The strain energy density at fracture (toughness) u_f was calculated as the area below the engineering stress-strain curve of the fractured specimen.

3.3 Results and Discussion

3.3.1 Electrical field distribution simulation

Fig. 3.4 shows a comparison of the 2D electric field distributions of the parallel-disk (Figs. 3.4(a)–(c)) and single-drum (Figs. 3.4(d)–(f)) electrospinning systems. Figs. 3.4(b,e) and 3.4(c,f) show magnified plots of the electric field around the syringe needle and the collector, respectively. In both systems, the highest intensity of the electric field is encountered at the tip of the syringe needle, with the intensity of the parallel-disk system being less than that of the single-drum system by 20%. The electric field at the parallel-disk collector surface is concentrated at the disk edges and shows a significant decrease in the region between the two disks, while the electric field distribution is relatively more uniform at the surface of the single-drum collector.

Fig. 3.5(a) shows the variation of the electric field intensity from the center of the collector ($x = 0$, $y = 0$) to the tip of the syringe needle ($x = 0$, $y = 92.5$ mm). The electric field intensity initially decreases, then slightly increases within a distance of 80 mm from the collector, and, finally, sharply increases in the vicinity of the tip of the syringe needle. Close to the collector, the electric field intensity increases slightly more in the case of the single-drum system than the parallel-disk system.
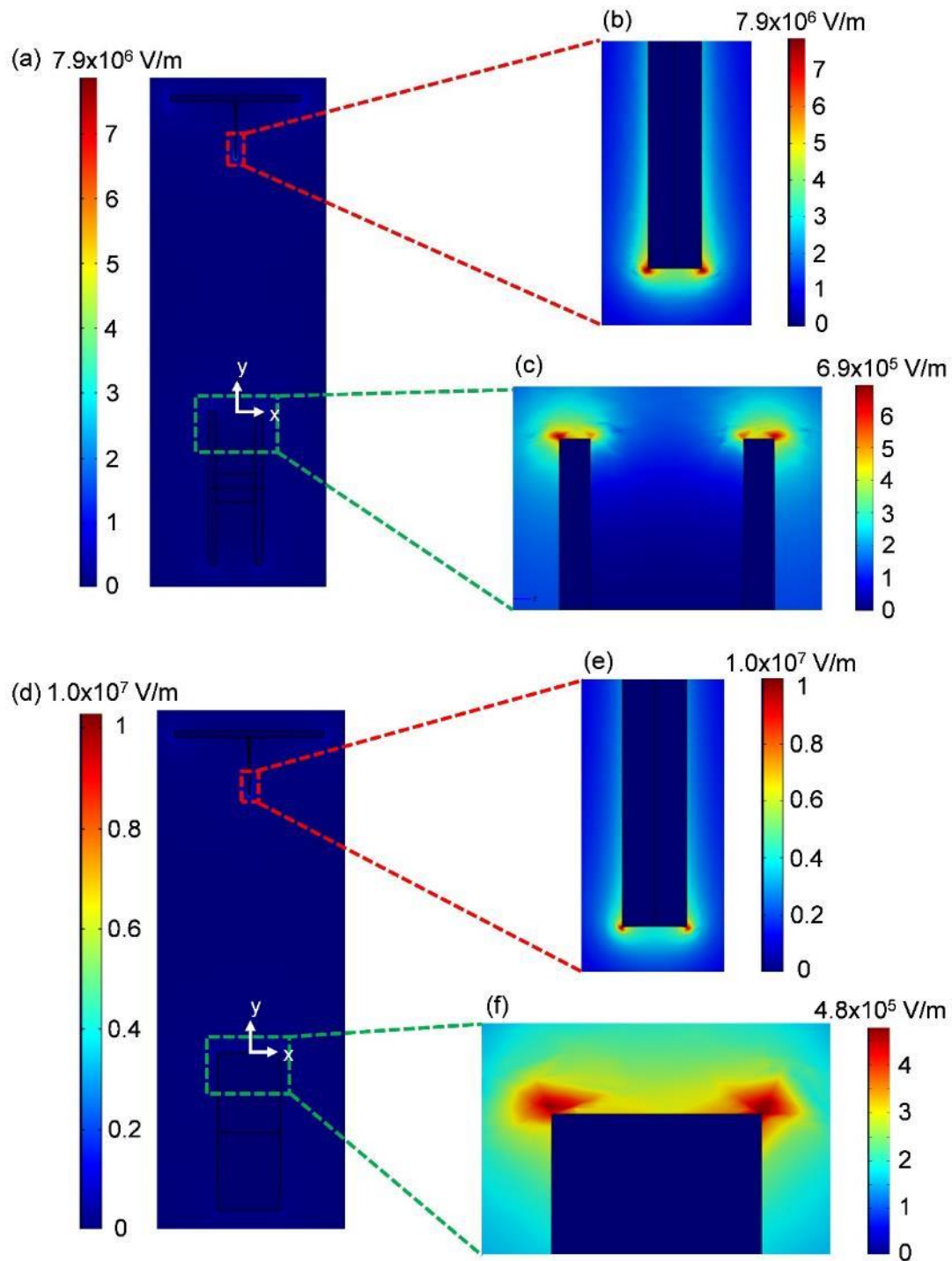
Fig. 3.4 2D contour plots of the electric field distribution in (a)–(c) parallel-disk and (d)–(f) single-drum electrospinning systems, (b), (c) and (e), (f) represent the enlarged view (but plotted in different scales) of the corresponding regions enclosed by the dash box in (a) and (d).

Fig. 3.5(b) shows the variation of the electric field intensity from the collector center ($x = 0$, $y = 0$) to a point 5 mm away from the collector edge ($x = 15.5$ mm, $y = 0$). The two peaks in the curve of the parallel-disk system correspond to the two edges of the right disk (see Fig. 3.4(c)) and the single peak in the curve of the single-drum system corresponds to the right edge of the drum (see Fig. 3.4(f)). In both simulation cases, the electric field is concentrated at the disk or drum edges; however, the parallel-disk collector exhibits significantly more differences in electric field intensity between the disk edges and the collector center, which may contribute to the fiber bridging (alignment) between the two disks and relatively less fiber packing during electrospinning.
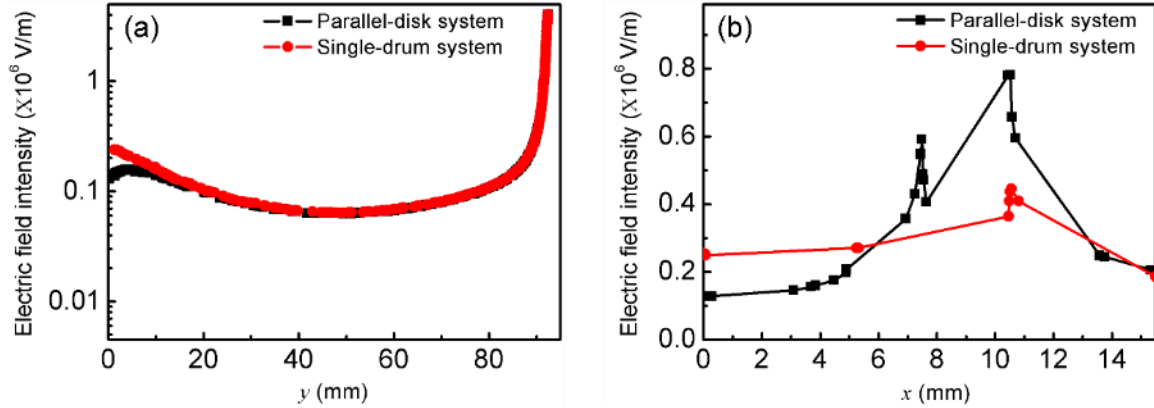
Fig. 3.5 Variation of electric field intensity from the collector center (x = 0, y = 0) to (a) the tip of the syringe needle (x = 0, y = 92.5 mm) and (b) a point 5 mm away from the disk or drum edges (x = 15.5 mm, y = 0). (The x and y coordinates are shown in Fig. 3.4.)

3.3.2 Structure of fiber distribution

Fig. 3.6(a) shows cross-sectional images of a bilayer PLLA membrane with a total thickness of 200 µm, while Figs. 3.6(b)–2(d) show high-magnification images of select through-thickness regions, enclosed by rectangular frames in Fig. 3.6(a). The formation of a layer with fully aligned fibers across the two aluminum disks was followed by that of a layer with random fibers (Fig. 3.6(a)–3.6(b)). The boundary between the two layers is indicated by a dashed line in Fig. 3.6(b). The cross-sectional images shown in Figs. 3.6(b)–3.6(d) reveal a gradual decrease in fiber packing (density) from the aligned-fiber layer (AFL) toward the random-fiber layer (RFL). This change in fiber density is attributed to the weakening of the electric field intensity with the increase of the RFL thickness. The average membrane porosity, which is the ratio of the volume of voids in the membrane to the total volume of the membrane, was measured with a previously reported method [21].
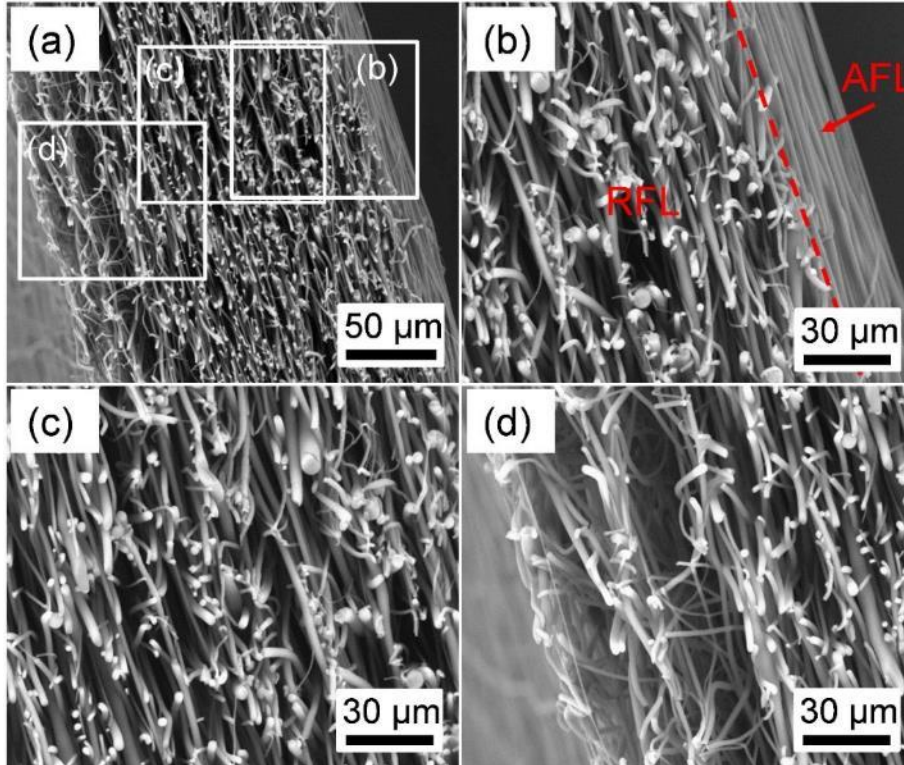
Fig. 3.6 (a) Cross-sectional SEM image of electrospun fibrous PLLA bilayer membrane of total thickness equal to 200 m. (b)–(d) High-magnification SEM images of through-thickness regions, enclosed by rectangular frames in (a), showing a decrease in fiber density from the layer with aligned fibers (AFL) toward the layer with randomly oriented fibers (RFL).

Fig. 3.7 compares a ~250-µm-thick single-layer membrane of randomly distributed PLLA fibers with a ~200-µm-thick bilayer membrane. It appears that the single-layer membrane exhibits more uniform through-thickness density and fibers more densely packed than the bilayer membrane. The average membrane porosity of the bilayer membrane (Fig. 3.7(b)) was found equal to 87.5%, which is nearly 10% higher than the 77.9% porosity of the single-layer membrane with randomly oriented fibers collected on a solid drum (Fig. 3.7(a)). The increase of membrane porosity is beneficial for scaffolds where cell infiltration is of critical importance. The increased membrane porosity of the bilayer membrane fabricated with the parallel-disk collector may be attributed to the high intensity of the electric field at the disk edges and the significant decrease of the electric field intensity between the aluminum disks.
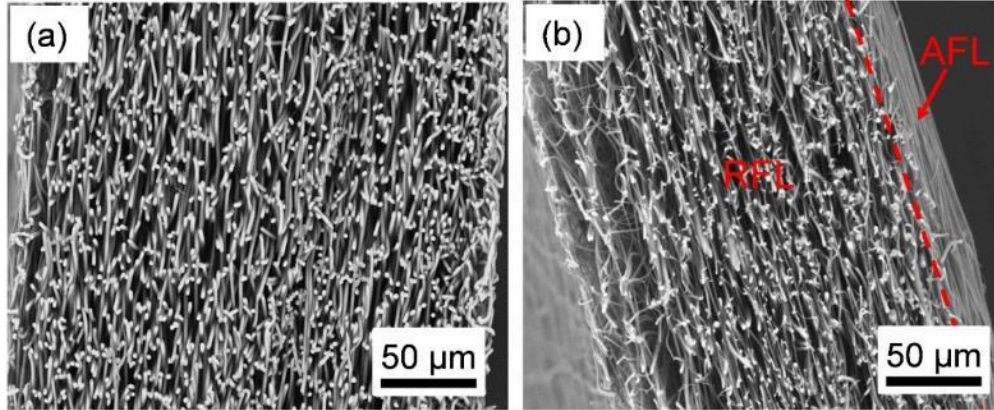
Fig. 3.7 Cross-sectional SEM images of electrospun PLLA membranes: (a) ~250-µm-thick single-layer membrane with randomly oriented fibers and (b) ~200-µm-thick bilayer PLLA membrane consisting of an aligned-fiber layer (AFL) and a random-fiber layer (RFL).

Surface images and corresponding fiber alignment plots are shown in Figs. 3.8(a)–3.8(d) and 3.8(e)–3.8(h), respectively, for a distance measured from the AFL surface in the range of 0–100 µm. The fiber diameter of the bilayer membranes is calculated as 1.4 ± 0.3 µm based on 6000X-magnification surface SEM images (10 images for each surface with a distance from AFL of 0, 30, 50 and 100 µm). The results shown in Fig. 3.8 were obtained by interrupting the electrospinning process at a given time and observing the membrane surface with a SEM. The relatively sharp and narrow peak at ~90° for zero distance (Fig. 3.8(e)) indicates that the majority of the fibers at the AFL surface are aligned between the parallel drums. However, for a distance of 30 µm (Fig. 3.8(f)), the presence of additional peaks and a broadening of the fiber-alignment distribution, suggesting less fiber alignment in the 90° direction. Further deviation of the fiber orientation from the 90° direction is observed for a distance of 50 µm (Fig. 3.8(g)), and random fiber orientation for a distance of 100 µm (Fig. 3.8(h)). The change in fiber orientation from predominantly 90° to random with the increase of the distance from the AFL surface (i.e., RFL thickness) is due to the effect of the membrane thickness on the electric field intensity.

In the light of Figs. 3.6 and 3.8, it may be inferred that under the present electrospinning conditions (controlled by the mandrel geometry and the electrical properties of the electrospun material) the maximum AFL thickness is ~30 µm, while the RFL thickness depends only on the electrospinning time. Thus, the results discussed below in terms of the bilayer thickness t $(= t_a + t_r)$ are for fixed AFL thickness ($t_a = 30$ µm) and RFL thickness t_r in the range of 20–170 µm.
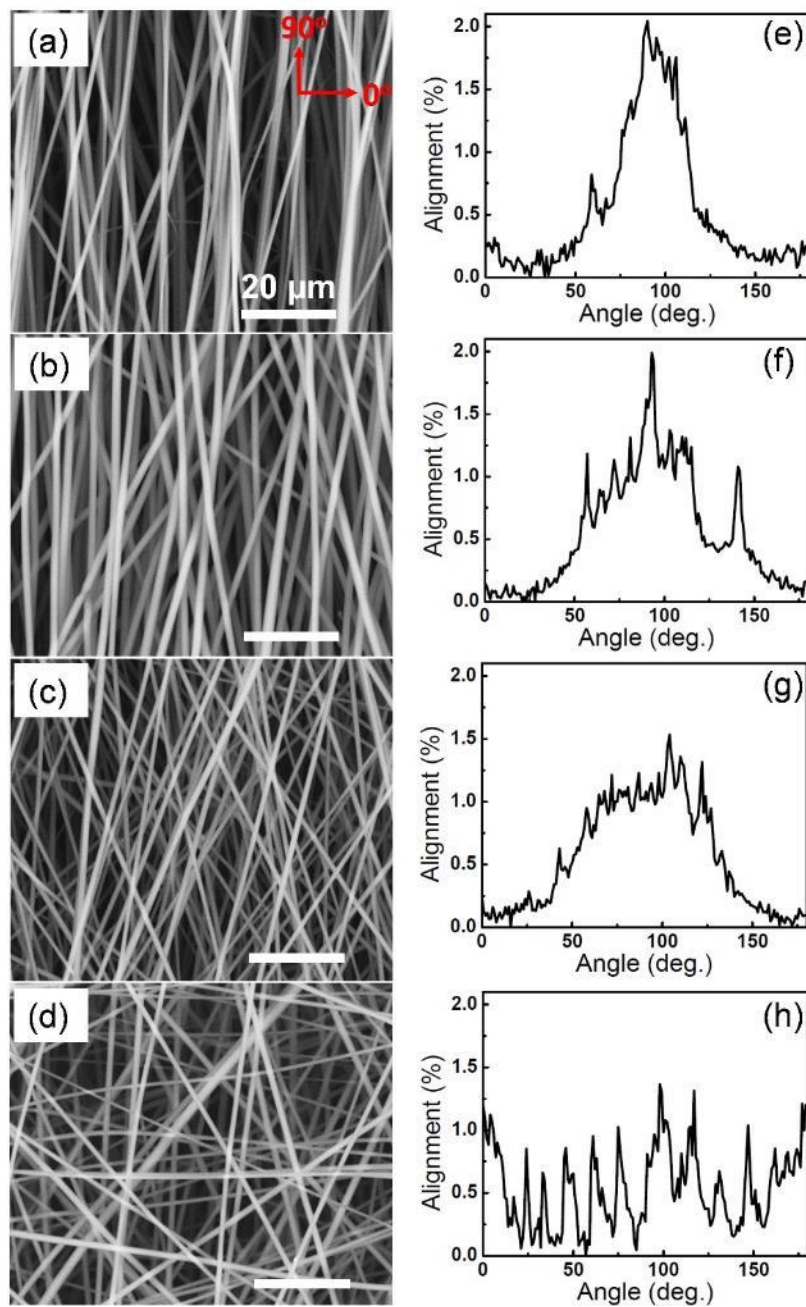
Fig. 3.8 Representative top-view SEM images (left column) and corresponding distributions of fiber alignment (right column) of electrospun fibrous PLLA membranes for a distance from the AFL surface of (a,e) 0, (b,f) 30, (c,g) 50, and (d,h) 100 μm. All magnification bars in (a)–(d) are equal to 20 μm.

3.3.3 Stress-strain response

Fig. 3.9 shows representative stress-strain responses of different fibrous membranes for fixed strain rate ($\dot{\varepsilon} = 0.017$ s^{-1}). A comparison of Figs. 3.9(a) and 3.9(b) shows that the AFL membrane demonstrates superior mechanical properties (i.e., E, σ_Y, and σ_u) than

the RFL membrane, and that the mechanical behavior of the bilayer membrane is bounded by those of the AFL and RFL membranes, in agreement with the strength increase of an electrospun PCL membrane with the increase of the fiber alignment observed in a previous study [22]. However, the bilayer membrane shows a gradual stress decrease during fracture and significantly higher strain at fracture. Moreover, the RFL membrane exhibits more strain hardening than the AFL and bilayer membranes (Fig. 3.9(a)), which may be attributed to the higher degree of fiber reorientation along the stress direction, similar to that of molecular chains in stretched bulk polymers [23].

To examine the effect of the bilayer membrane thickness on the resulting mechanical properties, tensile tests were performed with three groups of bilayer membranes of thickness t = 50, 100, and 200 µm (i.e., t_a = 30 µm and t_r = 20, 70, and 170 µm). Figs. 3.9(c) and 3.9(d) show representative stress-strain responses from these tests. It is evident that both the elastic modulus and the yield strength decrease with the increase of the membrane thickness. The 50-µm-thick bilayer membrane (Fig. 3.9(c)) exhibits a similar stress-strain distribution with the 30-µm-thick AFL membrane (Fig. 3.9(a)), which does not show a long tail during fracture as the thicker membranes. This may be attributed to the presence of a significant fraction of aligned fibers in the 20-µm-thick RFL, because the transition from aligned to random fibers occurs gradually through the membrane thickness (Fig. 3.8).
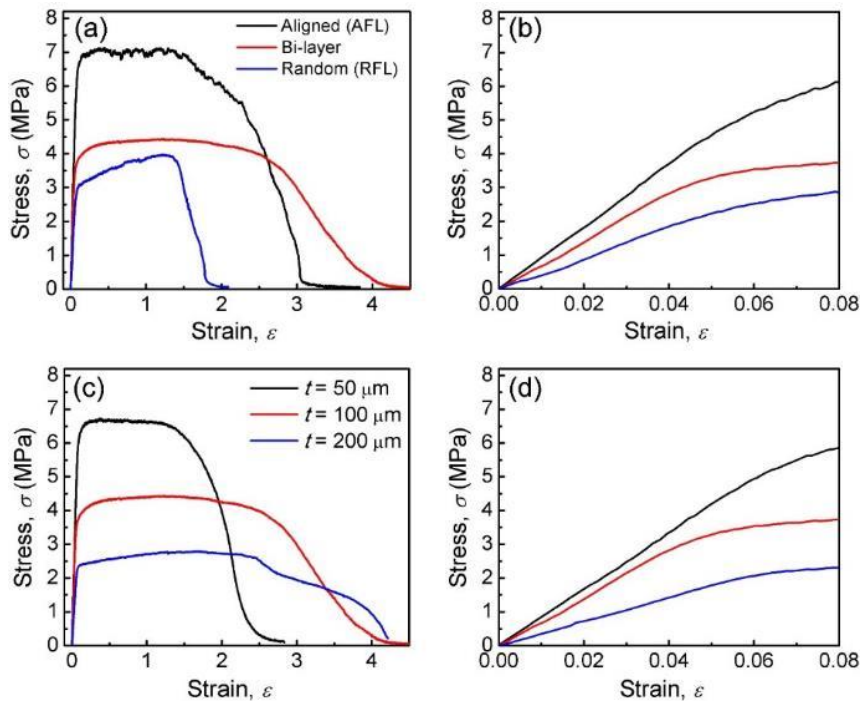
Fig. 3.9 Stress-strain response of electrospun fibrous PLLA membranes for strain rate $\dot{\varepsilon} = 0.017$ s^{-1}: (a) single layer with aligned fibers (t = 30 µm), bilayer (t = 100 µm), and single layer with randomly oriented fibers (t = 100 µm), (b) magnified low-strain regions of the stress-strain responses shown in (a), (c) bilayers of different thickness (t = 50, 100, and 200 µm), and (d) magnified low-strain regions of the stress-strain responses shown in (c). For all data, t_a = 30 µm and the stress is applied in the direction of the aligned fibers.

3.3.4 Mechanical properties

Fig. 3.10 shows the dependence of the mechanical properties of fibrous PLLA membranes on the AFL-to-total thickness ratio t_a/t. Although single-layer membranes consisting of random fibers ($t_a/t = 0$) show slightly better mechanical properties (i.e., E, σ_Y, and σ_u) than the bilayer membranes with $t_a/t = 0.15$, the general trend is for the mechanical properties to improve with the increase of t_a/t. The increase of E with t_a/t can be explained by a simple model of the bilayer membrane elastic modulus (see section 3.3.6). The deviation of the data for $t_a/t = 0$ from the general trend may be related to the lower membrane porosity (81.5%) of these membranes than that (87.5%) of bilayer membranes with $t_a/t = 0.15$. This is attributed to the higher conductivity of the PEO fibrous layer used to fabricate the AFL of the membranes consisting of fully random PLLA fibers. The enhancement of the mechanical properties with the increase of t_a/t indicates a profound AFL effect on the mechanical behavior of bilayer membranes. Despite the higher membrane porosity, bilayer membranes exhibited higher toughness than single-layer membranes consisting of randomly oriented fibers.
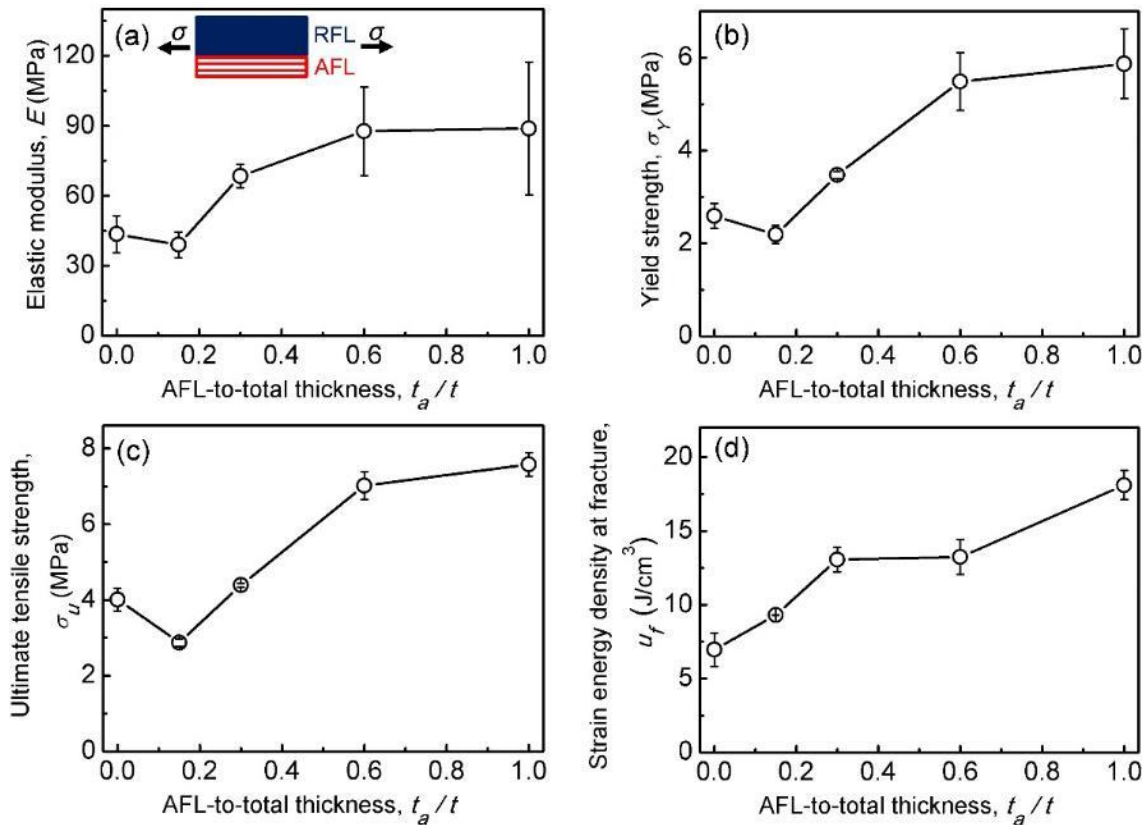
Fig. 3.10 (a) Elastic modulus E, (b) tensile yield strength σ_Y, (c) ultimate tensile strength σ_u, and (d) strain energy density at fracture u_f of electrospun fibrous PLLA membranes versus AFL-to-total thickness ratio t_a/t for strain rate $\dot{\varepsilon} = 0.017$ s^{-1}. Except for $t_a/t = 0$, for all other data $t_a = 30$ μm and $t_r = 0$–170 μm (i.e., $t = 30$–200 μm). Data points represent mean values of five measurements obtained with identical samples and error bars indicate one standard deviation above and below the corresponding mean value.

3.3.5 Effect of strain rate on mechanical behavior

Fig. 3.11 shows the effect of strain rate $\dot{\varepsilon}$ on the stress-strain response of bilayer membranes of thickness $t = 100$ and 200 μm. Several important observations about the mechanical properties of bilayer membranes can be derived from these results: (1) both σ_Y and strain hardening increase with $\dot{\varepsilon}$, (2) u_f first increases and then decreases with the increase of $\dot{\varepsilon}$, (3) the σ-ε responses at small $\dot{\varepsilon}$ (0.0017% and 0.017%) demonstrate a gradual stress decrease during fracture, and (4) a transition from a smooth σ-ε response to a step-like σ-ε response occurs with the increase of $\dot{\varepsilon}$ and t, suggesting a discontinuous deformation process comprising several abrupt unloading events. One-step brittle fracture has been reported for homogeneous bulk polymers subjected to high loading (strain) rates due to the limited time for polymer chain unfolding, slipping, and stretching [24]. The fibers in the bilayer membranes may be thought to play a similar role to polymer chains in bulk polymers but in the presence of significantly weaker interaction forces, whereas the multiple sharp stress drops may be attributed to microfracture of the fibers aligned in the stress direction, which was more localized in the thicker membrane (i.e., thicker RFL).
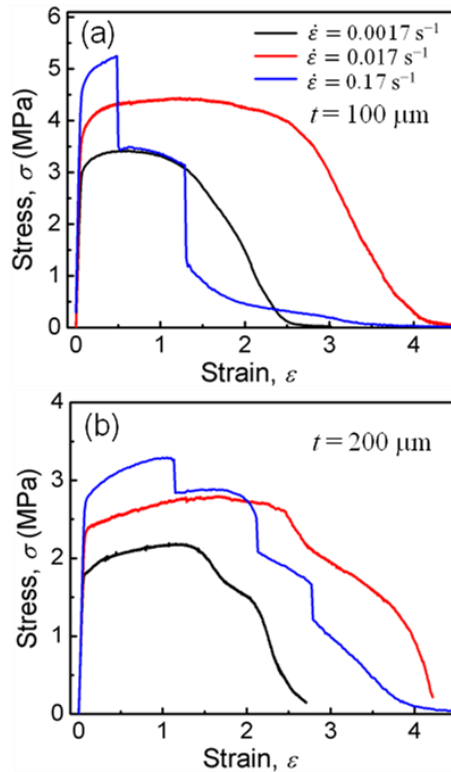
Fig. 3.11 Stress-strain response of electrospun fibrous PLLA membranes of thickness t equal to (a) 100 μm and (b) 200 μm for strain rate $\dot{\varepsilon} = 0.0017$, 0.017, and 0.17 s^{-1}. For all data, $t_a = 30$ μm and the stress is applied in the direction of the aligned fibers.

The strain rate effect on the stress-strain response can be further interpreted on the basis of the results shown in Fig. 3.12. Significantly higher E and σ_u were obtained with thinner bilayer membranes regardless of the variation of $\dot{\varepsilon}$. In addition, the general trend is for E

and σ_u to increase with $\dot{\varepsilon}$ for both $t = 100$ and 200 μm, which may be attributed to less disentanglement and more crystallization due to fiber stretching with higher strain rate [25].
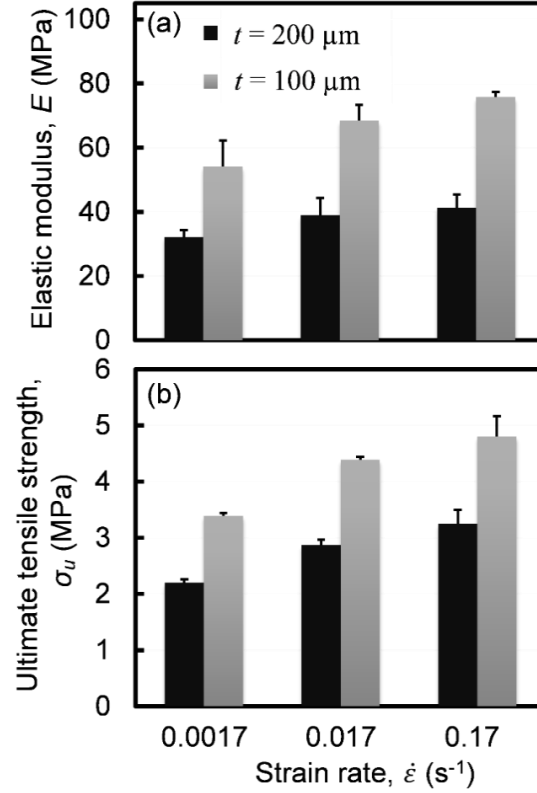
Fig. 3.12 (a) Elastic modulus E and (b) ultimate tensile strength σ_u of electrospun fibrous PLLA membranes of thickness $t = 100$ and 200 μm versus strain rate $\dot{\varepsilon}$. For all data, $t_a = 30$ μm and the stress is applied in the direction of the aligned fibers.

3.3.6 Elastic model of bilayer membrane

The elastic behavior of bilayer membranes can be analyzed by a simple model derived from classical mechanics of composite materials, assuming PLLA and air as the fiber and matrix materials. AFL can be modeled as an orthotropic material consisting of fibers aligned in the stress direction and RFL as a homogeneous isotropic material with spatially uniform fiber distribution. For an ideal layer with all fibers aligned in one direction, the elastic modulus perpendicular to the direction of the aligned fibers E_{a2} is approximately equal to zero, whereas the elastic modulus in the fiber direction E_{a1} is given by

$$E_{a1} = E_f v_f = E_f (1 - p_a) \tag{3.1}$$

where E_f is the fiber elastic modulus, v_f is the fiber volume fraction of AFL, and p_a is the average porosity of AFL.

The elastic modulus of the RFL layer E_r can be obtained as

$$E_r = 2\pi \int_0^{\pi/2} E(\theta) d\theta$$

$$= 2\pi \int_0^{\pi/2} \left[\frac{1}{\bar{E}_{a1}} \cos^4\theta + \left(\frac{1}{\bar{G}_{12}} - \frac{2\bar{v}_{12}}{\bar{E}_{a1}} \right) \cos^2\theta \sin^2\theta \right.$$

$$\left. + \frac{1}{\bar{E}_{a2}} \sin^4\theta \right]^{-1} d\theta \approx \frac{3}{8}\bar{E}_{a1} + \frac{5}{8}\bar{E}_{a2}$$

$$= \frac{3}{8}\bar{E}_{a1} \tag{3.2}$$

where $E(\theta)$ is the elastic modulus in a direction making an angle θ with the direction of fiber alignment in the equivalent AFL layer (i.e., a layer with the same porosity as RFL but with fibers aligned in one direction), and $\bar{G}_{12}$ and $\bar{v}_{12}$ are the shear modulus and Poisson's ratio of the equivalent AFL layer, respectively.

From Eqs. (3.1) and (3.2), it follows that

$$E_r \approx \frac{3}{8} E_f (1 - p_r) \tag{3.3}$$

where p_r is the average porosity of the RFL layer.

Using the parallel model of composite materials (i.e., AFL parallel with RFL, AFL elongation equal to that of RFL, total force equals to the sum of the AFL and RFL forces, and bilayer membrane elastic modulus $E_1 = E_{a1}v_a + E_r v_r$, where $v_r = 1 - v_a$), the elastic modulus of the bilayer membrane E_1 in the direction of the aligned fibers in AFL can be obtained as

$$E_1 = E_{a1}v_a + E_r(1 - v_a) = \frac{3}{8} E_f (1 - p_r) + E_f \left(\frac{5}{8} - p_a + \frac{3}{8} p_r \right) \frac{t_a}{t} \tag{3.4}$$

where v_a, t_a, and t are the AFL volume fraction in the bilayer membrane, the AFL thickness, and the total membrane thickness, respectively. Equation (3.4) indicates that E increases with the increase of t_a/t and/or the decrease of p_a and p_r.

3.3.7 Deformation and fracture mechanisms

Unlike homogeneous membranes exhibiting uniform through-thickness necking during tensile loading [26], bilayer membranes demonstrated significantly different deformation behavior. Fig. 3.13(a) shows a representative stress-strain curve of a 200-µm-thick bilayer membrane for $\dot{\varepsilon} = 0.017$ s^{-1}, including sample images (with RFL at the front and AFL at the back) at characteristic points, which are schematically reproduced in Fig. 3.13(b) to distinguish the AFL and RFL deformation behaviors. Similar results and observations were obtained with 100-µm-thick bilayer membranes. After yielding ($\sigma_Y \approx 2.6$ MPa), the bilayer exhibited strain hardening accompanied by the partial separation of AFL from RFL, with RFL exhibiting significant necking and AFL uniform stretching without necking (points B and C). Stretching beyond point C yielded a gradual stress decrease, resulting in a long tail that significantly differs from the abrupt stress decrease upon the fracture of homogenous

materials [27–29]. The relatively gradual stress decrease is attributed to AFL fiber fracturing and further RFL necking (point D), locally affecting the stress distribution between AFL and RFL. Fiber breakage at AFL edges and microfracture of the highly necked RFL occurred with further elongation, leading to the fracture of the specimen, with a few fibers at the AFL center (point E) still attached to the two specimen parts.

Fig. 3.13(c) shows fiber morphologies on AFL and RFL surfaces, corresponding to points A–E (Fig. 3.13(a)), providing insight into the effect of macroscopic deformation on the alignment and deformation at the fiber level. The initial AFL and RFL fiber morphologies were greatly affected by deformation. Fiber alignment along the stress direction in RFL and localized fiber necking in both RFL and AFL occurred after yielding and during strain hardening (points B and C). Necked fiber segments elongated with further stretching (point D), with the RFL surface morphology (fiber alignment) becoming almost identical to that of AFL at very large strains (point E). High-magnification images of fibers in as-fabricated and deformed AFL (point B in Fig. 3.13(a)), shown in Figs. 3.13(d) and 3.13(e), respectively, illustrate significant alignment and multiple necking of the fibers. Zussman et al. [30] have also reported multiple necking of electrospun PEO fibers during stretching. Liu et al. [5] observed a similar phenomenon with electrospun composite fibers under tension and attributed it to the nonuniform distribution of molecular chain entanglements within individual fibers. Tan et al. [31] reported that the fibrillar structure of electrospun PLLA fibers consists of alternating crystalline and amorphous regions. Since fiber necking in the present study was much more significant than that reported by Liu et al. [5], multiple fiber necking may be attributed to the inhomogeneous crystalline phase density of fibrils, with fiber segments possessing relatively lower cystallinity undergoing pronounced thinning (necking) in the stress direction. Relatively higher density of multiple necking was observed in AFL than RFL, apparently due to a significant fraction of the strain energy density expended in fiber rearrangement and alignment along the stress direction in RFL. The fiber surface morphology and crystalline structures in fibrils can be examined by atomic force microscopy [31–33] and wide-angle X-ray diffraction [34,35]. This will be the main objective of a future study dealing with the effect of crystalline morphology on the deformation behavior of bilayer membranes fabricated by the present electrospinning method.
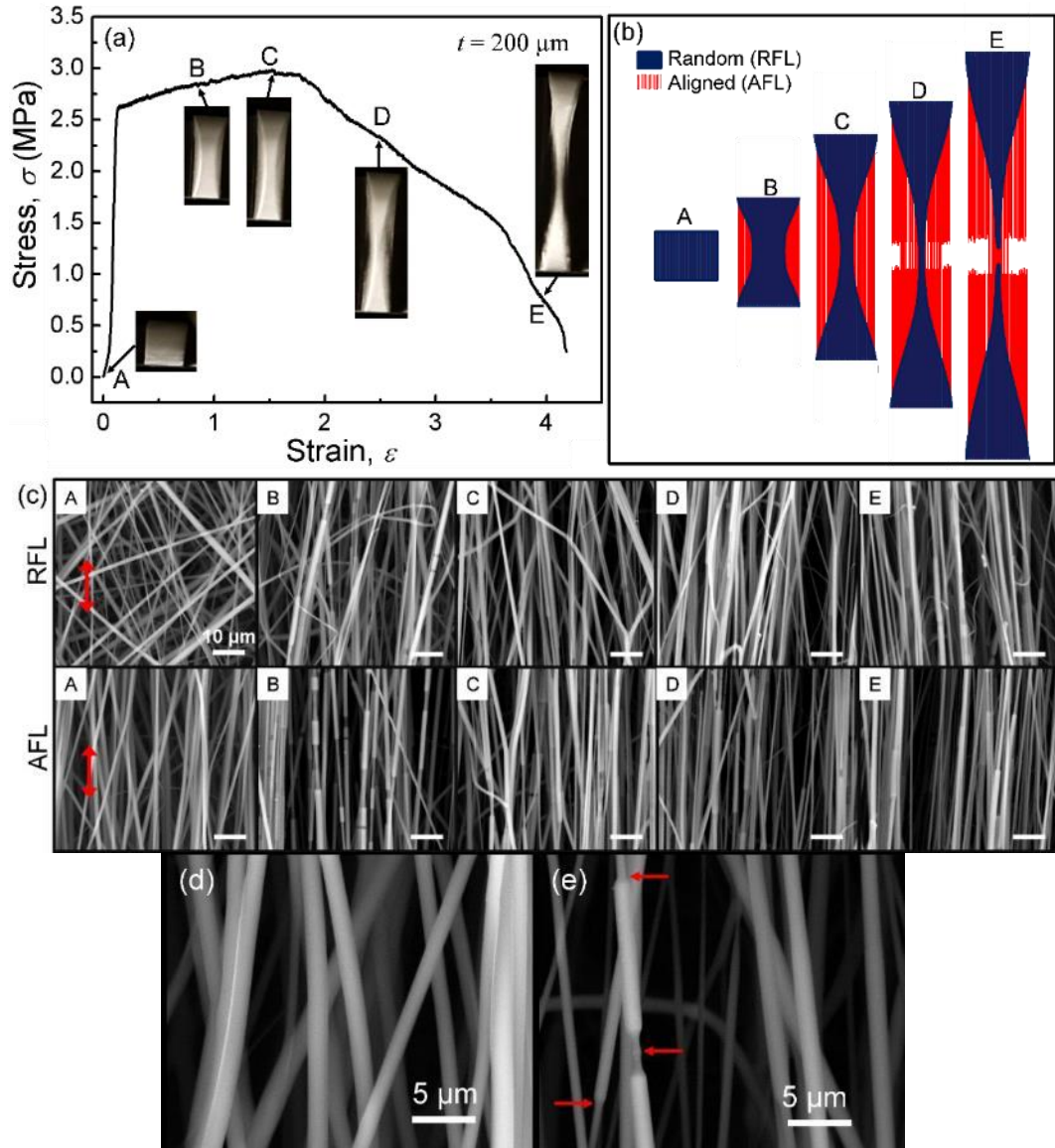
Fig. 3.13 (a) Typical stress-strain response of electrospun fibrous PLLA membrane of thickness t = 200 μm. Insets are optical images obtained at characteristic points of the σ-ε response. Front and back sample sides show deformed RFL and AFL, respectively. (b) Schematics of deformed AFL and RFL corresponding to characteristic points of the σ-ε curve shown in (a). (c) SEM images of RFL (first row) and AFL (second row) surfaces corresponding to characteristic points of the σ-ε curve shown in (a). Red arrows indicate the direction of the applied tensile stress. All magnification bars are equal to 10 μm. (d) and (e) High-magnification SEM images of as-processed and deformed (point B in (a)) membrane, respectively. For all data, t_a = 30 μm, $\dot{\varepsilon}$ = 0.017 s^{-1}, and the stress is applied in the direction of the aligned fibers.

3.4 Conclusions

The mechanical properties of electrospun bilayer membranes consisting of a layer with aligned fibers (AFL) and a layer with randomly oriented fibers (RFL) were investigated in the light of mechanical testing and microscopy results. Bilayer membranes were found to be more porous than single-layer membranes with randomly oriented fibers fabricated with a solid drum. Cross-sectional SEM images showed loose fiber packing and larger pores in RFL, which is beneficial for cell infiltration in tissue engineering. Despite the higher membrane porosity, bilayer membranes exhibited better mechanical properties than single-layer membranes with randomly oriented fibers. The enhancement of bilayer membrane properties increased with the AFL-to-total thickness ratio and strain rate. Strain hardening of bilayer membranes comprised fiber alignment in the stress direction and localized necking. Contrary to traditional fracture characterized by an abrupt stress decrease, bilayer membranes demonstrated a long tail of gradually decreasing stress comprising multiple instantaneous stress relaxation (microfracture events) events, especially at high strain rates. The overall gradual stress decrease observed at very large elongations (on the order of 400%) resulted in higher toughness and is a consequence of the excessive necking of RFL and localized fiber necking in both RFL and AFL. The high membrane porosity and good mechanical properties of the present bilayer membranes in conjunction with the good biocompatibility and biodegradability of PLLA scaffolds reported in previous studies are illustrative of the potential of these membranes for tissue engineering applications.

3.5 References

[1] Chen, J.P., Chang, G.Y. and Chen, J.K., 2008. Electrospun collagen/chitosan nanofibrous membrane as wound dressing. Colloids and Surfaces A: Physicochemical and Engineering Aspects, 313, pp.183-188.

[2] Zeng, J., Xu, X., Chen, X., Liang, Q., Bian, X., Yang, L. and Jing, X., 2003. Biodegradable electrospun fibers for drug delivery. Journal of Controlled Release, 92(3), pp.227-231.

[3] Zong, X., Ran, S., Fang, D., Hsiao, B.S. and Chu, B., 2003. Control of structure, morphology and property in electrospun poly (glycolide-co-lactide) non-woven membranes via post-draw treatments. Polymer, 44(17), pp.4959-4967.

[4] Qin, X.H. and Wang, S.Y., 2006. Filtration properties of electrospinning nanofibers. Journal of Applied Polymer Science, 102(2), pp.1285-1290.

[5] Liu, L.Q., Tasis, D., Prato, M. and Wagner, H.D., 2007. Tensile mechanics of electrospun multiwalled nanotube/poly (methyl methacrylate) nanofibers.Advanced Materials, 19(9), pp.1228-1233.

[6] Matthews, J.A., Wnek, G.E., Simpson, D.G. and Bowlin, G.L., 2002. Electrospinning of collagen nanofibers. Biomacromolecules, 3(2), pp.232-238.

[7] Wnek, G.E., Carr, M.E., Simpson, D.G. and Bowlin, G.L., 2003. Electrospinning of nanofiber fibrinogen structures. Nano Letters, 3(2), pp.213-216.

[8] Boland, E.D., Telemeco, T.A., Simpson, D.G., Wnek, G.E. and Bowlin, G.L., 2004. Utilizing acid pretreatment and electrospinning to improve biocompatibility of poly (glycolic acid) for tissue engineering. Journal of Biomedical Materials Research Part B: Applied Biomaterials, 71(1), pp.144-152.

[9] Li, W.J., Laurencin, C.T., Caterson, E.J., Tuan, R.S. and Ko, F.K., 2002. Electrospun nanofibrous structure: a novel scaffold for tissue engineering.Journal of biomedical materials research, 60(4), pp.613-621.

[10] Zong, X., Kim, K., Fang, D., Ran, S., Hsiao, B.S. and Chu, B., 2002. Structure and process relationship of electrospun bioabsorbable nanofiber membranes. Polymer, 43(16), pp.4403-4412.

[11] Lee, K.H., Kim, H.Y., Khil, M.S., Ra, Y.M. and Lee, D.R., 2003. Characterization of nano-structured poly (ε-caprolactone) nonwoven mats via electrospinning. Polymer, 44(4), pp.1287-1294.

[12] Ikada, Y. and Tsuji, H., 2000. Biodegradable polyesters for medical and ecological applications. Macromolecular rapid communications, 21(3), pp.117-132.

[13] Zhu, Y., Wang, A., Patel, S., Kurpinski, K., Diao, E., Bao, X., Kwong, G., Young, W.L. and Li, S., 2011. Engineering bilayer nanofibrous conduits for peripheral nerve regeneration. Tissue Engineering Part C: Methods, 17(7), pp.705-715.

[14] Zhu, Y., Wang, A., Shen, W., Patel, S., Zhang, R., Young, W.L. and Li, S., 2010. Nanofibrous patches for spinal cord regeneration. Advanced functional materials, 20(9), pp.1433-1440.

[15] Shalumon, K.T., Sreerekha, P.R., Sathish, D., Tamura, H., Nair, S.V., Chennazhi, K.P. and Jayakumar, R., 2011. Hierarchically designed electrospun tubular scaffolds for cardiovascular applications. Journal of biomedical nanotechnology, 7(5), pp.609-620.

[16] Lee, Y.H., Lee, J.H., An, I.G., Kim, C., Lee, D.S., Lee, Y.K. and Nam, J.D., 2005. Electrospun dual-porosity structure and biodegradation morphology of Montmorillonite reinforced PLLA nanocomposite scaffolds. Biomaterials,26(16), pp.3165-3172.

[17] Lee, B.L.P., Jeon, H., Wang, A., Yan, Z., Yu, J., Grigoropoulos, C. and Li, S., 2012. Femtosecond laser ablation enhances cell infiltration into three-dimensional electrospun scaffolds. Acta biomaterialia, 8(7), pp.2648-2658.

[18] Baker, B.M., Gee, A.O., Metter, R.B., Nathan, A.S., Marklein, R.A., Burdick, J.A. and Mauck, R.L., 2008. The potential to improve cell infiltration in composite fiber-aligned electrospun scaffolds by the selective removal of sacrificial fibers. Biomaterials, 29(15), pp.2348-2358.

[19] Li, D., Wang, Y. and Xia, Y., 2003. Electrospinning of polymeric and ceramic nanofibers as uniaxially aligned arrays. Nano letters, 3(8), pp.1167-1171.

[20] Ayres, C.E., Jha, B.S., Meredith, H., Bowman, J.R., Bowlin, G.L., Henderson, S.C. and Simpson, D.G., 2008. Measuring fiber alignment in electrospun scaffolds: a user's guide to the 2D fast Fourier transform approach. Journal of Biomaterials Science, Polymer Edition, 19(5), pp.603-621.

[21] Zhu, X., Cui, W., Li, X. and Jin, Y., 2008. Electrospun fibrous mats with high porosity as potential scaffolds for skin tissue engineering.Biomacromolecules, 9(7), pp.1795-1801.

[22] Thomas, V., Jose, M.V., Chowdhury, S., Sullivan, J.F., Dean, D.R. and Vohra, Y.K., 2006. Mechano-morphological studies of aligned nanofibrous scaffolds of polycaprolactone fabricated by electrospinning. Journal of Biomaterials Science, Polymer Edition, 17(9), pp.969-984.

[23] Kabir, R., Albuerne, J., Simon, P.F., Filiz, V., Abetz, C., Böttcher, H., Perlich, J. and Abetz, V., 2013. Deformation and orientation behavior of polystyrene-b-

polybutadiene-b-poly (methyl methacrylate) triblock terpolymers: Influence of polybutadiene microstructures and the molar masses. Polymer, 54(2), pp.673-684.

[24] Bhardwaj, R. and Mohanty, A.K., 2007. Modification of brittle polylactide by novel hyperbranched polymer-based nanostructures. Biomacromolecules,8(8), pp.2476-2484.

[25] Zhang, X., Schneider, K., Liu, G., Chen, J., Brüning, K., Wang, D. and Stamm, M., 2011. Structure variation of tensile-deformed amorphous poly (L-lactic acid): Effects of deformation rate and strain. Polymer, 52(18), pp.4141-4149.

[26] K. Komvopoulos, Mechanical Testing of Engineering Materials. Cognella, San Diego, CA. pp. 43-50, 2010.

[27] Yuan, X., Mak, A.F. and Yao, K., 2003. Surface degradation of poly (L-lactic acid) fibres in a concentrated alkaline solution. Polymer degradation and stability, 79(1), pp.45-52.

[28] He, W., Ma, Z., Yong, T., Teo, W.E. and Ramakrishna, S., 2005. Fabrication of collagen-coated biodegradable polymer nanofiber mesh and its potential for endothelial cells growth. Biomaterials, 26(36), pp.7606-7615.

[29] Yuan, X., Mak, A.F. and Yao, K., 2002. Comparative observation of accelerated degradation of poly (L-lactic acid) fibres in phosphate buffered saline and a dilute alkaline solution. Polymer degradation and stability, 75(1), pp.45-53.

[30] Zussman, E., Rittel, D. and Yarin, A.L., 2003. Failure modes of electrospun nanofibers. Applied physics letters, 82(22), pp.3958-3960.

[31] Tan, E.P. and Lim, C.T., 2006. Effects of annealing on the structural and mechanical properties of electrospun polymeric nanofibres. Nanotechnology,17(10), p.2649.

[32] Lim, C.T., Tan, E.P.S. and Ng, S.Y., 2008. Effects of crystalline morphology on the tensile properties of electrospun polymer nanofibers. Applied Physics Letters, 92(14), p.141908.

[33] Jaeger, R., Schönherr, H. and Vancso, G.J., 1996. Chain packing in electro-spun poly (ethylene oxide) visualized by atomic force microscopy.Macromolecules, 29(23), pp.7634-7636.

[34] Zong, X., Ran, S., Fang, D., Hsiao, B.S. and Chu, B., 2003. Control of structure, morphology and property in electrospun poly (glycolide-co-lactide) non-woven membranes via post-draw treatments. Polymer, 44(17), pp.4959-4967.

[35] Kakade, M.V., Givens, S., Gardner, K., Lee, K.H., Chase, D.B. and Rabolt, J.F., 2007. Electric field induced orientation of polymer chains in macroscopically aligned electrospun polymer nanofibers. Journal of the American Chemical Society, 129(10), pp.2777-2782.

Chapter 4 – *In vivo* cell infiltration and vascularization of electrospun bilayer microfibrous scaffolds

The biocompatibility and biological performance of the PLLA bilayer fibrous scaffolds was evaluated by *in vivo* experiments involving subcutaneous scaffold implantation in Sprague-Dawley rats, followed by histology and immunohistochemistry studies in this chapter. The results illustrate the potential of the bilayer scaffolds to overcome major limitations of conventionally electrospun scaffolds associated with intrinsically small pores, low porosity and, consequently, poor cell infiltration.

4.1 Introduction

Tissue engineering seeks to repair or replace damaged tissue by integrating approaches from cellular/molecular biology and material chemistry/engineering. A major challenge is the consistent design of three-dimensional (3D) scaffolds that mimic the structure and biological functions of extracellular matrix (ECM), guide cell migration, provide mechanical support, and regulate cell activity. Because of the high specific surface area (similar to the ECM structure) and tunable surface morphology, electrospun fibrous scaffolds demonstrate high potential for engineering various types of tissue, such as skin [1,2], cardiac muscle [3], nerves [4], and vascular vessels [5,6]. Fibrous scaffolds possess a skeletal 3D structure comprising fibers with diameters ranging from tens of nanometers to a few micrometers. Various biodegradable polymers, such as poly(glycolic acid) [7], poly(D,L-lactide-*co*-glycolide) [8], poly(L-lactic acid) (PLLA) [9], and poly(ε-caprolactone) (PCL) [10], can be processed by electrospinning. Changes in the structure of biodegradable fibrous scaffolds due to the gradual degradation of the fibers promote proliferation of infiltrating cells, resulting in ECM formation and, ultimately, tissue regeneration.

One of the important functions of fibrous polymer scaffolds in tissue engineering is to support the desired cell functions and maintain phenotype-specific activities. For functional tissue regeneration, the scaffold interspace is critical for cell growth and associated activities. Porosity, pore size, and pore interconnectivity are key factors in cell infiltration in nonwoven scaffolds. Although electrospun materials generally exhibit interconnected pore networks, they are characterized by a relatively low porosity (70–80%) and small pore size, typically less than 5 µm [11]. These inherent characteristics of conventionally electrospun scaffolds inhibit cell migration (infiltration) through the scaffold thickness, limiting cell-scaffold interactions at the surface and inhibiting vascular vessel ingrowth. These limitations hinder the use of 3D scaffolds because the cells in the constructs depend on diffusion from the vasculature for nutrient and waste transfer. While the pore size depends on the cell type, it should be larger than the cell size (i.e., ~10 µm) [12]. Nevertheless, pore sizes of several hundred micrometers are often necessary for optimal cell migration [13]. In general, a porosity of ~90% or higher is desirable for cell infiltration, provided the mechanical strength of the scaffold satisfies the requirements of the specific application.

Among various electrospinning methods for fabricating scaffolds with high porosity and large-diameter pores, a common approach for producing electrospun mats with large pores is by the selective removal of sacrificial materials. For example, scaffolds of high porosity and pore sizes in the range of 900–5000 μm^2 were fabricated by a cryogenic electrospinning process that uses ice crystals as templates [14], whereas scaffolds comprising large fiber-free regions were produced by combining electrospinning and salt leaching [15]. High-porosity scaffolds have also been synthesized by co-electrospinning PCL functional material and water-soluble polyethylene oxide (PEO) and, finally, removing the PEO fibers by water rinsing [16]. Although the scaffolds of these studies show increased cell infiltration compared to those processed by conventional electrospinning, they are also characterized by mechanical instabilities, including distortion [16], shrinkage [17], and delamination or pore collapse [18], because the increase of the pore size and porosity is detrimental to the mechanical properties. The fiber density and porosity in transverse planes of electrospun membranes have also been varied by using stainless steel wire meshes as collectors [19] or laser ablation as a post-processing method [20]. However, the scaffolds fabricated by these methods demonstrate abrupt changes in fiber density in transverse planes, making them susceptible to mechanical failure due to the existence of stress raisers. Thus, fabrication of scaffolds with large pores, high porosity, and adequate mechanical strength is a challenging task of high importance in tissue engineering and regeneration.

The objective of this study is to introduce a new fabrication paradigm of highly porous scaffolds based on an electrospinning technique that uses two slowly rotating parallel disks as the collector. Fibrous PLLA scaffolds fabricated by this technique exhibit a bilayer structure consisting of a ~30-µm-thick aligned-fiber layer (AFL) and a ~190-µm-thick random-fiber layer (RFL). Scanning electron microscopy, histology, confocal microscopy, and immunohistochemistry results of scaffolds implanted *in vivo* show the following unique characteristics: (1) a gradual change in porosity and fiber alignment through the scaffold thickness without the formation of stress raisers, (2) a bilayer scaffold structure consisting of a densely packed layer (AFL) for mechanical support and a highly porous layer (RFL) for cell infiltration and tissue growth, (3) higher porosity in conjunction with superior mechanical properties [21] compared to scaffolds fabricated by conventional electrospinning (controls), and (4) more than two times higher cell infiltration and significantly higher collagen deposition, cell proliferation, and vascularization after implantation *in vivo* than controls.

4.2 Experimental procedures

4.2.1 Sample preparation

Bilayer fibrous scaffolds consisting of PLLA were fabricated by electrospinning, as described in section 3.2.1 (the electrospinning process is shown in Fig. 3.1). Electrostatic interactions between the two-disk collector and the impinging polymer jet resulted in fiber bridging across the gap of the parallel disks. While fiber deposition on the aluminum disks was random, electrostatic repulsion of the positively charged neighboring fibers caused fiber alignment in the space between the disks and perpendicular to the disk planes (Fig. 1(b)). A gradual transition from aligned to random fiber deposition occurred when the layer

with aligned fibers reached a critical thickness due to altering of the electric field distribution by the deposited fibers. Thus, the fibrous scaffolds formed between the two parallel disks exhibited a bilayer structure consisting of an aligned-fiber layer (AFL) and a random-fiber layer (RFL), as illustrated in Fig. 4.1.
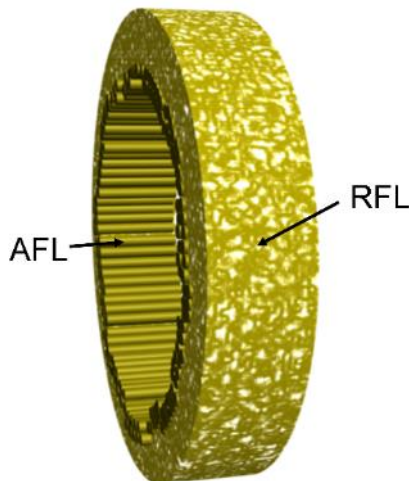
Fig. 4.1 A bilayer scaffold consisting of an aligned-fiber layer (AFL) and a random-fiber layer (RFL) is produced between the aluminum disks. RFL formation commences as soon as AFL reaches a critical thickness, which significantly changes the electric field distribution due to the high dielectric constant of the deposited polymer fibers.

For scaffold characterization and implantation *in vivo*, the bilayer scaffolds were cut into small rectangular pieces. Scaffolds consisting of only random fibers (controls) were fabricated with a single-drum collector (diameter = 55 mm, thickness = 21 mm). For comparison, the same electrospinning parameters were used to fabricate both bilayer and control scaffolds. The thickness of the bilayer and control scaffolds used in the *in vivo* experiments was about 220 and 250 µm, respectively. Film thickness measurements were obtained with a thickness gauge (Mitutoyo Absolute No. 547-500, Mitutoyo America, Aurora, IL). The AFL and RFL thickness (determined from ten cross-sectional SEM images obtained from different regions) was found equal to 30 and 190 µm, respectively. After electrospinning, the scaffolds were air-dried overnight under a hood to remove any HFIP residue.

4.2.2 Characterizations of electrospun microfibrous scaffolds

To examine changes in fiber alignment through the scaffold thickness, the PLLA solution was doped with 0.05 wt% fluorescein isothiocyanate (FITC) (Sigma-Aldrich, St. Louis, MO). Imaging of the FITC-doped scaffolds was performed at 5-µm distance intervals in the thickness direction using a Zeiss LSM510 confocal microscope, while maintaining the same exposure in all images. Because as-fabricated PLLA scaffolds are semicrystalline (54% crystallinity) [22], their low transparency hinders the detection of the fluorescent signal through the scaffold. This difficulty was overcome by applying a drop of immersion oil (Carl Zeiss Immersol, Fisher Scientific, Hampton, NH) which made the scaffold

transparent. It was observed that scaffold wetting by immersion oil increased the detection depth of the fluorescent signal (generated by 488-nm excitation light) from about 5 to 80 µm. Finally, the scaffold surface was covered by a glass slip in preparation for imaging.

4.2.3 *In vivo* implantation

To investigate cell infiltration through the electrospun scaffolds, three samples of each group were subcutaneously implanted in the cavity of Sprague-Dawley rats (Charles River Laboratories, Wilmington, MA) for 5 or 14 days. Control and bilayer scaffolds were cut into $0.5 \times 0.5 \text{ cm}^2$ pieces and sterilized by ethylene oxide gas for ~12 h at room temperature. Before scaffold implantation, the rats were anesthetized with isofluorane and the incision sites were disinfected with 70% ethanol. After making three incisions on each side of the lower abdominal wall, the controls were placed on the left side, while the bilayer scaffolds were placed on the right side with the surface with aligned fibers facing the superficial fascia and the surface with random fibers facing the rat muscle and fat tissue. The two diagonal corners of each specimen were fixed to the underlying tissue by suturing. Finally, the incisions were closed using mattress sutures (Interrupted 5-0 Monocryl, Ethicon, Somerville, NJ). Three rats were used for each implantation time (i.e., 5 and 14 days).

All animals were monitored on a daily basis by a veterinarian. No adverse incidents were observed in any of the animals during implantation *in vivo*. After scaffold implantation for 5 or 14 days, the rats were returned to the operating room where they were given general anesthesia and an overdose of euthanasia solution. The scaffolds together with their immediate surrounding tissue were then explanted and immediately embedded in optimal cutting temperature (OCT) compound (TissueTek, Elkhart, IN) on dry ice.

4.2.4 Histology and immunohistochemistry

Cross sections (~10 µm thick) were cut from the OCT-embedded samples using a –20°C cryosectioner. All sections were obtained through the scaffold thickness (*z*-direction). Bilayer scaffolds were cut along the direction of fiber alignment. Masson's trichrome (Ameican MasterTech, Lodi, CA) staining was used to assess the morphology and collagen deposition in histologic cross sections of the scaffolds. In trichrome stained cross sections, the cell cytoplasm, collagen fibers, and cell nuclei appear in red, blue, and dark purple colors, respectively. Immunohistochemistry was performed to detect pan macrophages, secretion of collagen type II, smooth muscle cells, and endothelial cells.

For immunostainning, the sections were air-dried under a hood to ensure good adhesion to the glass slides. Before staining, the scaffolds were fixed with 4% PFA for 5 min, permeabilized with 0.5% Triton X-100 for 15 min, and blocked with 5% FBS for 30 min. Then, they were immunostained for pan macrophages with mouse anti-rat CD68 (Serotec, Raleigh, NC), for cell proliferation with rabbit anti-rat Ki67 (Abcam, Cambridge, MA), for smooth muscle cells with mouse anti-rat α-actin (Epitomics, Burlingame, CA), for endothelial cells with rabbit anti-rat CD31 (BD Pharmingen, San Diego, CA), and for collagen II secretion with rabbit anti-rat collagen type II (all used in 1:200 dilution). The secondary antibody used was AlexaFluor 546 donkey anti-mouse IgG (Invitrogen, Carlsbad, CA) for CD68 and α-actin and AlexaFluor 546 donkey anti-rabbit IgG

(Invitrogen, Carlsbad, CA) for Ki67, CD31, and collagen II. All samples were subsequently counterstained for cell nuclei with DAPI. Control and bilayer scaffold samples extracted from the same animal were stained in parallel and representative images of immunostainning were obtained for each implantation time (5 or 14 days). All stained samples were observed under the Zeiss microscope. The same light intensity, contrast, and exposure time were used in all microscopy images of immunostainning. At least six cryosections of each scaffold were examined to ensure consistency between sections.

4.2.5 Cell infiltration

A typical software (ImageJ, NIH, http://rsb.info.nih.gov/ij/) was used to study cell infiltration. DAPI images of scaffold cryosections were captured using the 20× objective of the Zeiss microscope. Images were sequentially converted to greyscale, thresholded, and converted to binary. The threshold level was selected to maximize the removal of noise without hampering the detection of nuclei and was fixed in all images by keeping the same brightness and exposure time. Any portions of the images above the threshold level were set white and those below the threshold were set black. Then, the scaffold peripheries were manually defined. The area of each cluster of black pixels in the scaffold, representing either a single cell nucleus or a cluster of cell nuclei, was calculated by executing the "analyze particle" command of ImageJ. Finally, the number of infiltrating cells was estimated by dividing the total area of cell nuclei in the scaffold by the average area of a single cell nucleus calculated from 100 cell nuclei randomly selected from the same scaffold. To account for variations in the scaffold cross-sectional area, the cell density was obtained by normalizing the total number of cells in the scaffold by the scaffold cross-sectional area. Six cryosections (six images per cryosection) of each scaffold were used to quantify cell infiltration.

To further examine cell infiltration in different scaffold regions, DAPI images of scaffold cryosections were divided into four regions of equal thickness. To define the boundaries of the four regions, 20 evenly spaced cross sections along the scaffold-width direction were defined in the DAPI images of the scaffold cryosections. In each cross section, the scaffold thickness was divided into four regions of equal thickness denoted by 0–25%, 25–50%, 50–75%, and 75–100%. Finally, 20 points were obtained for each percentage (25%, 50%, and 75%) of scaffold thickness. The curves connecting the 20 points corresponding to 25%, 50%, or 75% of the scaffold thickness represent the interfaces among the four regions. The number of infiltrating cells in each region was determined with the method described above and normalized to the total number of cells in each scaffold to obtain the percentage of infiltrating cells in each region. Six cryosections (six images per cryosection) of each scaffold were used to quantify cell infiltration in different scaffold regions.

4.2.6. Statistical analysis

Results are presented in the form of mean and standard deviation (error bars) data, assuming the data follow a normal distribution. All data were compared using one-way ANOVA tests. Two-tailed Student's t-test was used to assess significant differences between groups of bilayer and control scaffolds. A p-value less than 0.05 was used to determine statistically significant differences.

4.3 Results

4.3.1 Characterization of bilayer scaffolds

The bilayer structure consisting of a ~30-µm-thick AFL and a ~190 µm thick RFL, as shown in Fig. 3.7(b). The progressive decrease of the fiber packing density from the AFL toward the RFL is attributed to the gradual weakening of the electric field with the increase of the scaffold thickness. The RFL shows much larger inter-fibrillar voids than the AFL. Compared to the bilayer scaffolds, the controls (Fig. 3.7(a)) possess more uniform through-thickness fiber packing. The overall porosity (defined as the ratio of the void volume to the apparent scaffold volume) of the controls and bilayer scaffolds was estimated to be 77.9% and 87.5%, respectively. As shown below, the much higher porosity of the bilayer scaffolds was instrumental for cell infiltration through the scaffold thickness during in vivo implantation.
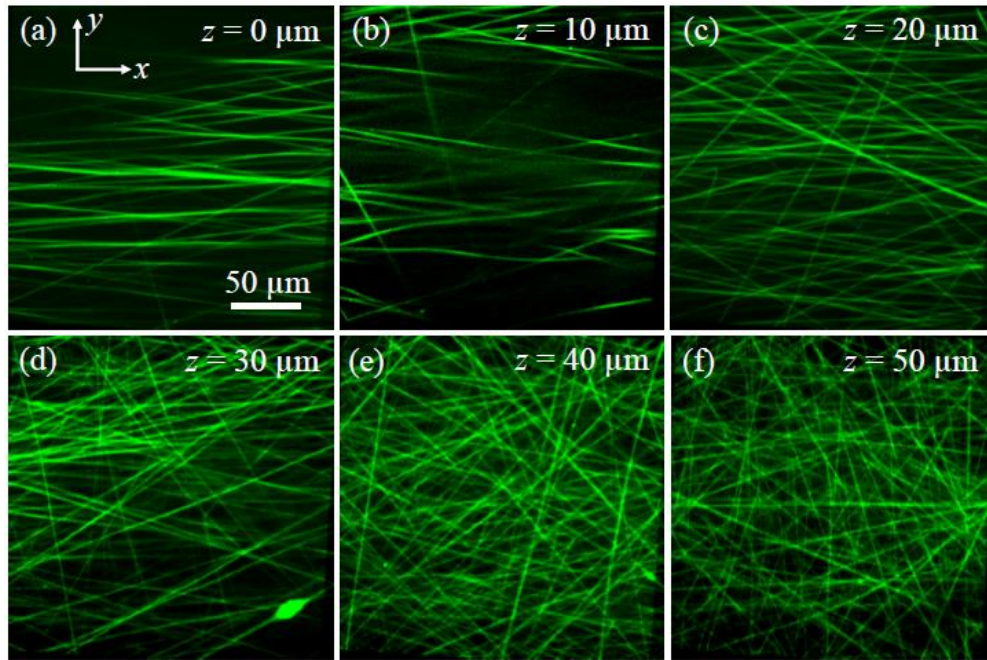
Fig. 4.2 Representative confocal microscopy images of an electrospun bilayer scaffold for a distance from the AFL surface z = 0–50 µm (z = 0 corresponds to the AFL surface). To enhance the observation with the confocal microscope, the fibers were doped with FITC fluorescent dye. All images have the same magnification.

To examine the fiber orientation through the thickness of the bilayer scaffolds, confocal imaging was performed using FITC-doped bilayer scaffolds. Fig. 4.2 shows fluorescent images of PLLA fibers on different planes at a distance from the AFL surface $z = 0$–50 µm. The confocal images shown in Fig. 4.2 do not reveal the real packing density of the fibers because the scaffold surface exhibits height fluctuations of several tens of micrometers. The AFL surface ($z = 0$) shows nearly perfect fiber alignment, with most fibers predominantly oriented in the x-direction (Fig. 4.2(a)), i.e., perpendicular to the parallel disks of the collector. A comparison of the images shown in Figs. 4.2(a)–4.2(f)

indicates that the fiber orientation increasingly deviates from the x-direction with increasing distance from the AFL surface. This trend is attributed to the effect of the scaffold thickness on the electric field distribution during electrospinning. The random fiber distribution observed at distances $z = 40$ and 50 µm from the AFL surface indicates that, under the present electrospinning conditions, the AFL thickness is ~30 µm; thus, the region beyond this distance corresponds to the RFL. The AFL thickness depends on the collector geometry (e.g., distance between the two parallel disks) and the electrical properties of the electrospun material, whereas the RFL thickness is affected only by the electrospinning time.

4.3.2. In vivo cell infiltration

To investigate cell infiltration through the scaffolds, control and bilayer scaffolds of 220 and 250 µm thickness, respectively, were subcutaneously implanted in Sprague-Dawley rats for 5 and 14 days. Fig. 4.3 shows representative cross-sectional images of control and bilayer scaffolds retrieved after 5 and 14 days of implantation in vivo. DAPI-stained cell nuclei are shown in blue color. Dashed and solid lines in Fig. 4.3 (as well as in subsequent figures) represent the boundaries between surrounding tissue and bilayer scaffold surfaces with random and aligned fibers, respectively, whereas both boundaries of control scaffolds (single-layer scaffolds with randomly distributed fibers) are indicated by dashed lines. The scaffold boundaries were determined from the phase images. Although both scaffold types show an increase in cell infiltration with implantation time, the controls show relatively less cell infiltration, which is mainly confined at the tissue-scaffold boundary. Cell infiltration in the bilayer scaffolds is much more pronounced, with cell colonization mostly appearing in the 50–80-µm-thick region of low fiber density of the RFL after implantation for 5 days. This result suggests that cell infiltration in the bilayer scaffolds occurred from the RFL surface because of the larger pores and higher porosity of RFL than AFL. The significantly more homogeneous cell distribution in the bulk of the bilayer scaffolds implanted for 14 days may be attributed to the gradual migration and proliferation of cells infiltrating from the RFL surface.

Further insight into cell infiltration can be obtained from Fig. 4.4(a), which shows the cell density of control and bilayer scaffolds after 5 and 14 days of implantation in vivo. Only cells within the scaffold boundaries were considered in the calculations. The cell density of bilayer scaffolds implanted for 5 and 14 days is about 3 and 2 times higher than that of controls, respectively ($p<0.05$). These results indicate that the higher porosity of the bilayer scaffolds is conducive to cell infiltration in vivo. To further quantify the distribution of infiltrating cells, the scaffold cross sections were divided into four regions of equal thickness (0–25%, 25–50%, 50–75%, and 75–100% regions in Figs. 4.4(b) and 4.4(c), where percentages refer to the total scaffold thickness). The dashed and solid lines indicate the boundaries between surrounding tissue and scaffold surfaces with random and aligned fibers, respectively, while the dashed-dot lines represent the interfaces among the four regions. For both control and bilayer scaffolds, the 0% line corresponds to the scaffold interface with rat muscle and fat tissue, whereas the 100% line corresponds to the scaffold interface with superficial fascia. The number of infiltrating cells in each region (obtained by the method described in section 2.5) was normalized to the total number of cells in each scaffold to determine the percentage of infiltrating cells in each region. Fig. 4.4(d) shows

results from this analysis for control and bilayer scaffolds implanted for 5 and 14 days. For 5-day implantation, cell fraction in the 0–25% and 25–50% regions of bilayer scaffolds is significantly higher than that of controls, whereas the opposite is observed for the 50–75% and 75–100% regions. Considering the scaffolds were attached to the underneath muscle and fat tissue during implantation, the slightly higher cell infiltration in the 0–25% region than the 75–100% region of the controls implanted for 5 days may be attributed to more intimate contact with muscle and fat tissue than with superficial fascia. The much higher (by a factor of ~3) cell infiltration in the 0–25% region than the 75–100% region of bilayer scaffolds implanted for 5 days is attributed to the presence of larger interconnected pores in the region adjacent to the RFL surface (Fig. 3.7(b)). For 14-day implantation, only a small fraction of cells exists in the center region of controls (~14% and ~12% of total cell population was found in the 25–50% and 50–75% regions of the controls, respectively), whereas significantly more cells migrated to the center region of the bilayer scaffolds. Additionally, all four regions of bilayer scaffolds show similar cell densities, an indication of homogeneous cell colonization. Thus, from an in vivo tissue regeneration perspective, bilayer scaffolds are superior to single-layer controls with random fiber distribution because homogeneous cell colonization in the scaffolds is a perquisite for homogeneous tissue reconstruction.

Fig. 4.3 Representative cross-sectional images of (a, c) control and (b, d) bilayer scaffolds subcutaneously implanted in Sprague-Dawley rats for 5 and 14 days showing cell infiltration in vivo. Cell nuclei (blue) were stained with DAPI. Dashed and solid lines indicate the boundaries between surrounding tissue and scaffold surfaces with random and aligned fibers, respectively. Aligned fibers are at the right scaffold surface in (b) and (d). All images have the same magnification.

Fig. 4.4 (a) Cell infiltration in vivo quantified by the cell density of control and bilayer scaffolds subcutaneously implanted in Sprague-Dawley rats for 5 and 14 days. Statistically significant differences ($p<0.05$) between bilayer and control scaffold data (obtained by a two-tailed unpaired t-test) are indicated by an asterisk (*). Representative fluorescent cross-sectional images of DAPI-stained (b) control and (c) bilayer scaffolds show cell infiltration in different regions. Dashed and solid lines indicate the boundaries between surrounding tissue and scaffold surfaces with random and aligned fibers, respectively. Dashed-dot lines are used to divide the scaffolds in four regions of equal thickness denoted by 0–25%, 25–50%, 50–75%, and 75–100%. For both control and bilayer scaffolds, the 0% line represents the scaffold interface with rat muscle and fat tissues, whereas the 100% line represents the scaffold interface with superficial fascia during implantation in vivo. Aligned fibers are along the 100% line in (c). (d) Cell infiltration in vivo obtained from different regions of control and bilayer scaffolds subcutaneously implanted in Sprague-Dawley rats for 5 and 14 days. Six cryosections (six images per cryosection) were used to quantify each data point. The cross-sectional scaffold area used to quantify cell infiltration is in the range of 0.10–0.15 mm².

4.3.3. Histology of scaffolds implanted in vivo

Collagen was not detected in the bulk of controls implanted for 5 days (Figs. 4.5(a) and 4.5(b)) and 14 days (Figs. 4.5(e) and 4.5(f)); however, collagen deposition was observed in the bulk of the bilayer scaffolds implanted for 5 days (Figs. 4.5(c) and 4.5(d)) and 14 days (Figs. 4.5(g) and 4.5(h)), suggesting that infiltrating fibroblasts remained viable and functional contributing to the remodeling of bilayer scaffolds. For both implantation times, the interfaces of bilayer scaffold sides with random fibers and surrounding tissue (left boundaries in Figs. 4.5(c), 4.5(d), 4.5(g), and 4.5(h)) are not distinguishable, indicating

good integration of native tissue with the side of the bilayer scaffolds having randomly distributed fibers; however, the boundaries between control scaffolds and surrounding tissue are visible even after implantation for 14 days (Figs. 4.5(a), 4.5(b), 4.5(e), and 4.5(f)). In addition, more collagen fibers exist in the surrounding tissue near the surface of the controls than the surface of the bilayer scaffolds (especially after implantation for 14 days), which may be illustrative of a tendency for fibrous capsule formation around the controls.
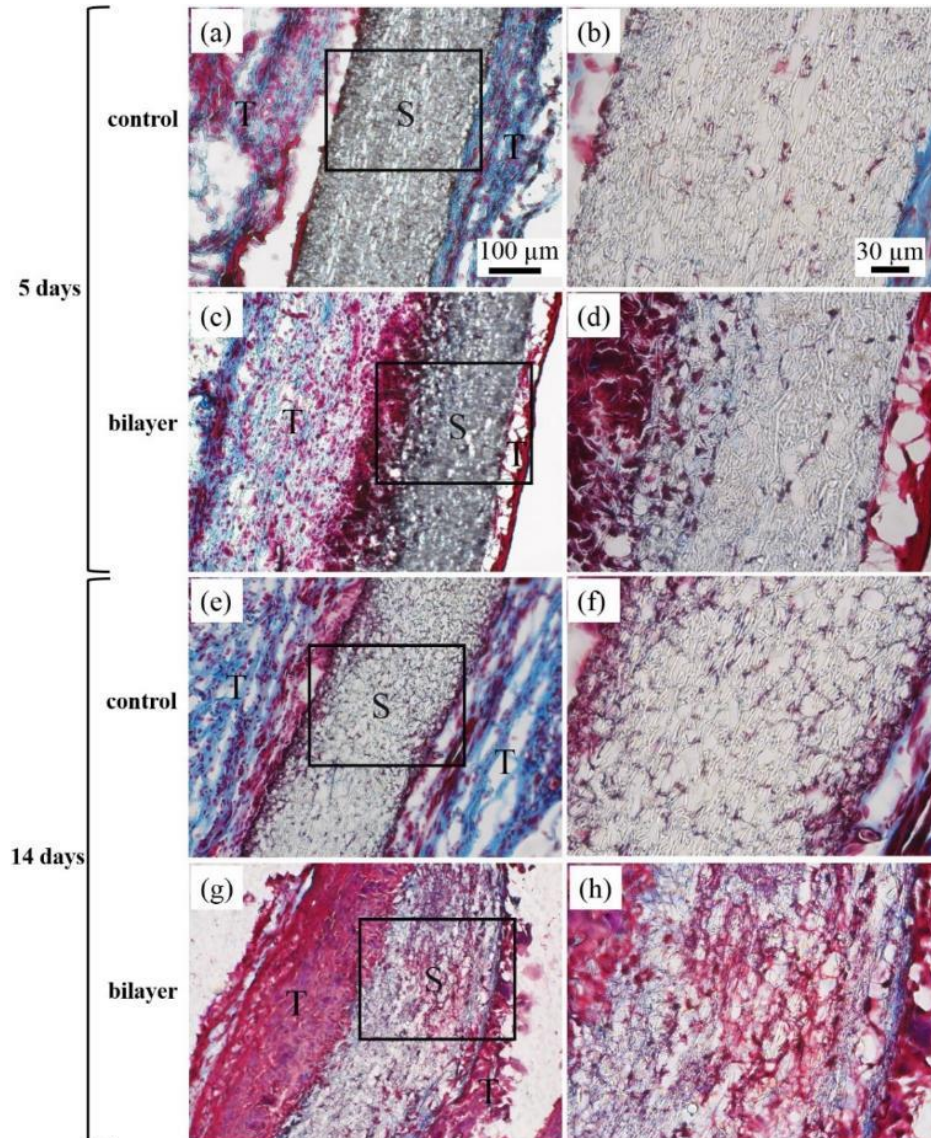
Fig. 4.5 Trichrome-stained control and bilayer scaffolds subcutaneously implanted in Sprague-Dawley rats for (a)–(d) 5 days and (e)–(h) 14 days (collagen (blue); muscle (red); cell nuclei (dark purple)). The cross-sectional images shown in (b), (d), (f), and (h) are enlarged views of regions enclosed by rectangular frames in (a), (c), (e), and (g), respectively. S and T indicate scaffold and surrounding native tissue, respectively. Aligned fibers are at the right scaffold surface in (c), (d), (g), and (h). All images of each column have the same magnification.

4.3.4. Immunohistochemistry of scaffolds implanted in vivo

To further characterize the in vivo biological performance of the bilayer scaffolds, cross sections of scaffolds subcutaneously implanted in Sprague-Dawley rats were immunostained with CD68 for pan macrophages, Ki67 for cell proliferation, α-actin for smooth muscle cells, and CD31 for endothelial cells. CD68 positive macrophages were observed in the surrounding host tissue and within the scaffolds implanted for 5 and 14 days (Fig. 4.6, left column). For 5-day implantation, the bilayer scaffolds demonstrated significantly higher cell infiltration including macrophages (Fig. 4.6(c)) than controls (Fig. 4.6(a)), although there was no difference in the percentage of CD68 positive cells (normalized to the total cell population in the scaffolds). However, after implantation for 14 days, a significant increase in macrophage accumulation was observed at the surface and in the bulk of the controls (Fig. 4.6(c)) but significantly less in the bilayer scaffolds (Fig. 4.6(g)), suggesting that the porous structure of the bilayer scaffolds suppressed macrophage recruitment and inflammatory response in the long term. In addition, although a few Ki67 positive cells were detected in the controls implanted for 5 days (Fig. 4.6(b)), significantly more Ki67 positive cells were found in the bilayer scaffolds implanted for 5 days and the host tissue surrounding the RFL (Fig. 4.6(d)), suggesting an increase of cell proliferation in the bilayer scaffolds during the early stage of in vivo biological response. It may be inferred that the large pores at the RFL surface promoted cell proliferation in the host tissue surrounding the RFL, as shown in Fig. 4.6(d). Although longer implantation (14 days) increased the fraction of Ki67 positive cells in the controls near the surface, more Ki67 positive cells were observed in the bulk of the bilayer scaffolds compared to the controls (Figs. 4.6(f) and 4.6(h)).

Staining the samples for markers of smooth muscle cells and endothelial cells (α-actin and CD31, respectively) was performed to further identify the types of infiltrating cells and to evaluate the extent of angiogenesis and vessel ingrowth in the implanted scaffolds. Very few α-actin positive cells were found in the controls implanted for 5 and 14 days, with α-actin positive cells primarily distributed at the scaffold surface and within the surrounding host tissue (Figs. 4.7(a) and 4.7(e)). However, significant ingrowth of smooth muscle cells (or their precursors) occurred in the bilayer scaffolds implanted for 5 days (Fig. 4.7(c) and 14 days (Fig. 4.7(g)). Moreover, CD31 staining indicated endothelial cell infiltration in the bilayer scaffolds during the early stage (5 days) of tissue response in vivo (Fig. 4.7(d)). Endothelial cell infiltration in the bilayer scaffolds became even more prominent after longer (14 days) implantation (Fig. 4.7(h)). In contrast, significantly less endothelial cells were detected in the controls during the early stage of in vivo implantation (Fig. 4.7(b)) and only a few endothelial cells after longer implantation, mainly in regions near the scaffold interface with surrounding tissue (Fig. 4.7(f)). These results suggest that bilayer scaffolds enhanced endothelial cell infiltration and angiogenesis.

Type II collagen expression was evaluated by immunohistochemical staining using antibodies against type II collagen. Fig. 4.8 shows more collagen type II secretion in the bilayer scaffolds than the controls implanted for 5 and 14 days. Collagen type II expression was mainly concentrated in the surrounding host tissue and peripheries of the controls (Figs. 4.8(a) and S1(b)), whereas clusters of positive collagen type II were observed in the bulk of the bilayer scaffolds implanted for 14 days (Fig. 4.8(d)); although in the early

implantation stage (5 days), a higher distribution of positive collagen type II was observed in regions close to the RFL surface due to the high local density of infiltrating cells (Fig. 4.8(c)).
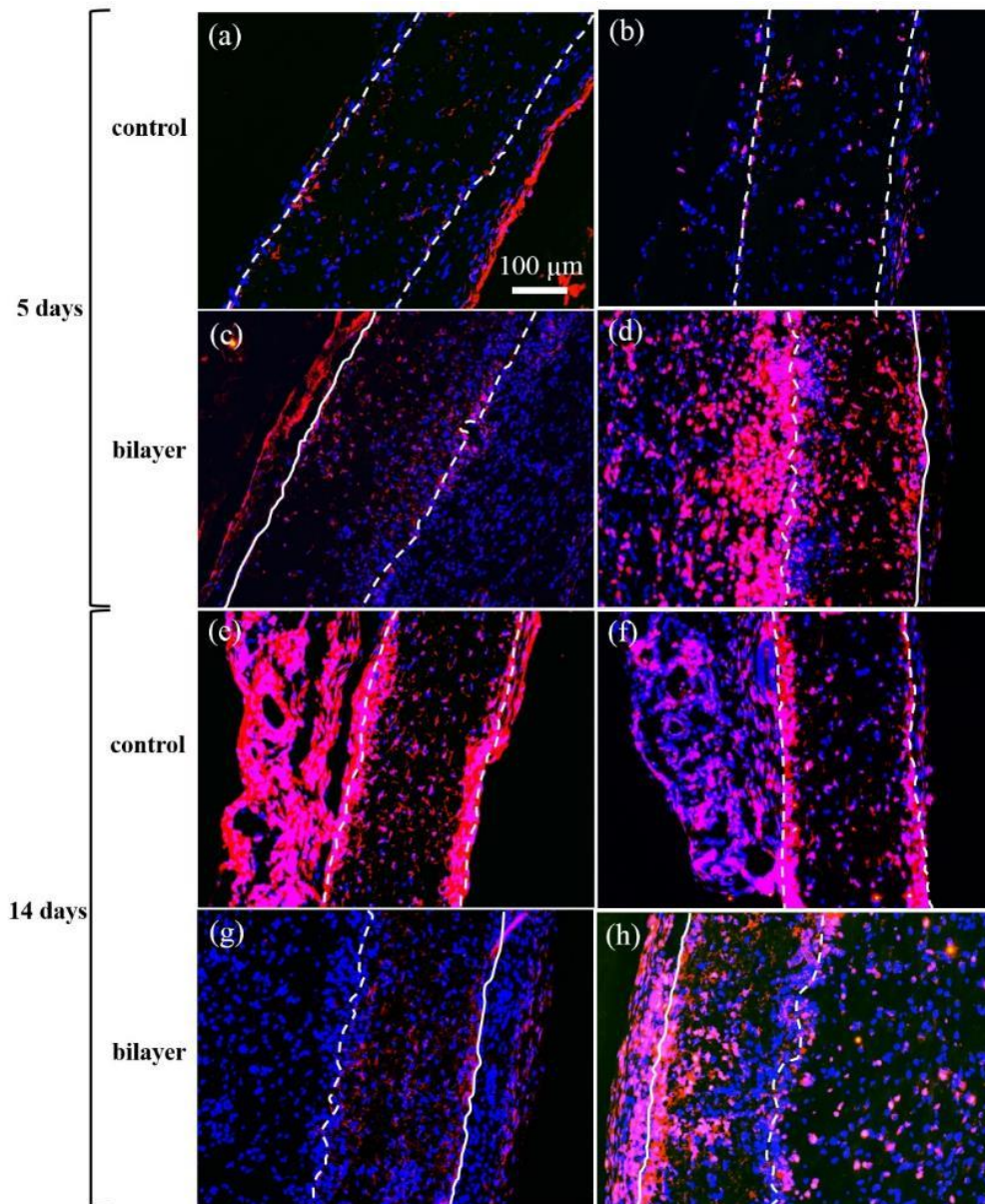
Fig. 4.6 Representative cross-sectional images of control and bilayer scaffolds subcutaneously implanted in Sprague-Dawley rats for (a)–(d) 5 days and (e)–(h) 14 days. Left column: DAPI (nuclei, blue), CD68 (pan macrophages, red). Right column: DAPI (nuclei, blue), Ki67 (cell proliferation, red). Dashed and solid lines indicate the boundaries between surrounding tissue and scaffold surfaces with random and aligned fibers, respectively. Aligned fibers are on the left surface in (c) and (h) and the right surface in (d) and (g). All images have the same magnification.
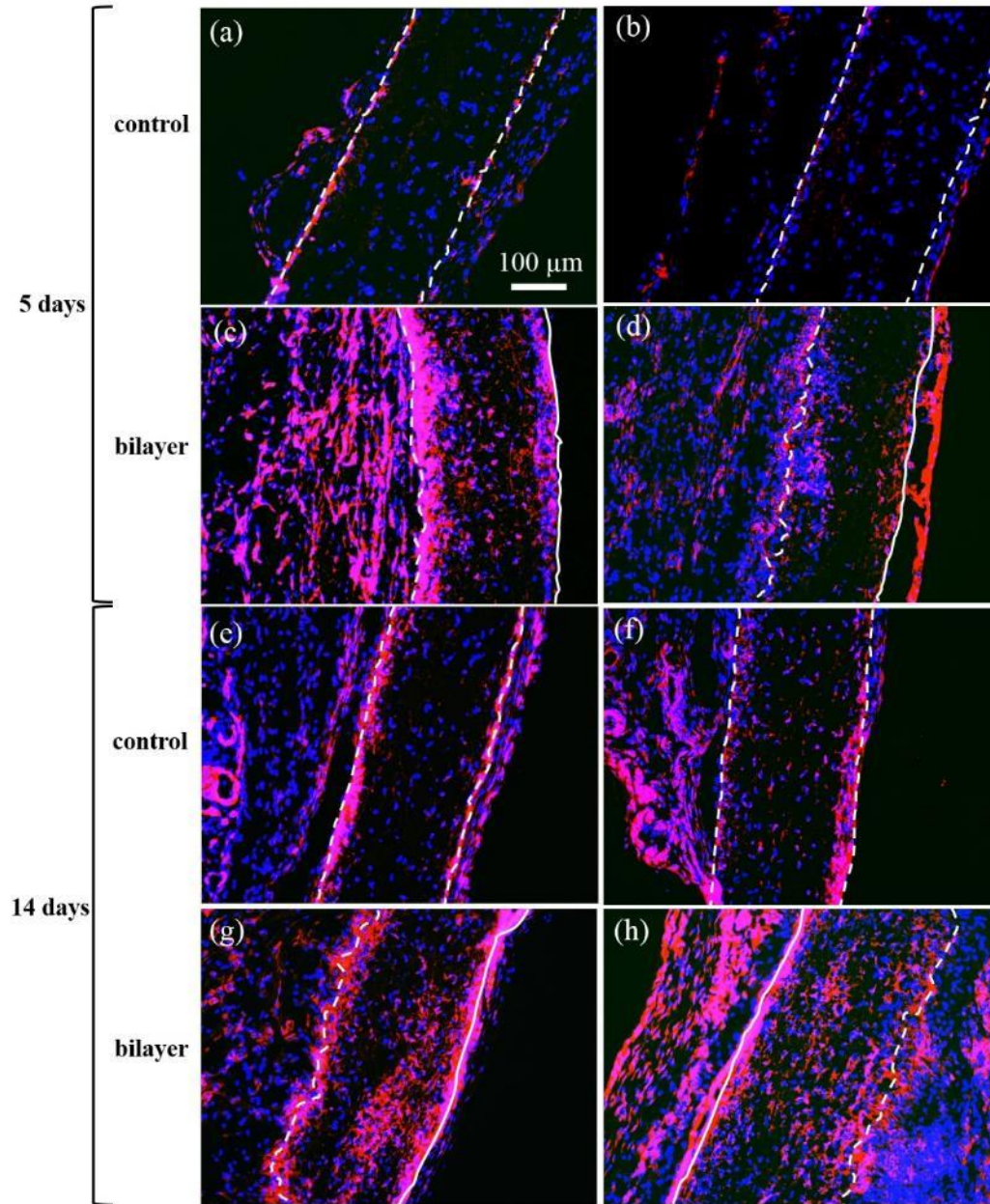
Fig. 4.7 Representative cross-sectional images of control and bilayer scaffolds subcutaneously implanted in Sprague-Dawley rats for (a)–(d) 5 days and (e)–(h) 14 days. Left column: DAPI (nuclei, blue), a-actin (smooth muscle cells, red). Right column: DAPI (nuclei, blue), CD31 (endothelial cells, red)). Dashed and solid lines indicate the boundaries between surrounding tissue and scaffold surfaces with random and aligned fibers, respectively. Aligned fibers are at the right scaffold surface in (c), (d), and (g) and the left scaffold surface in (h). All images have the same magnification.
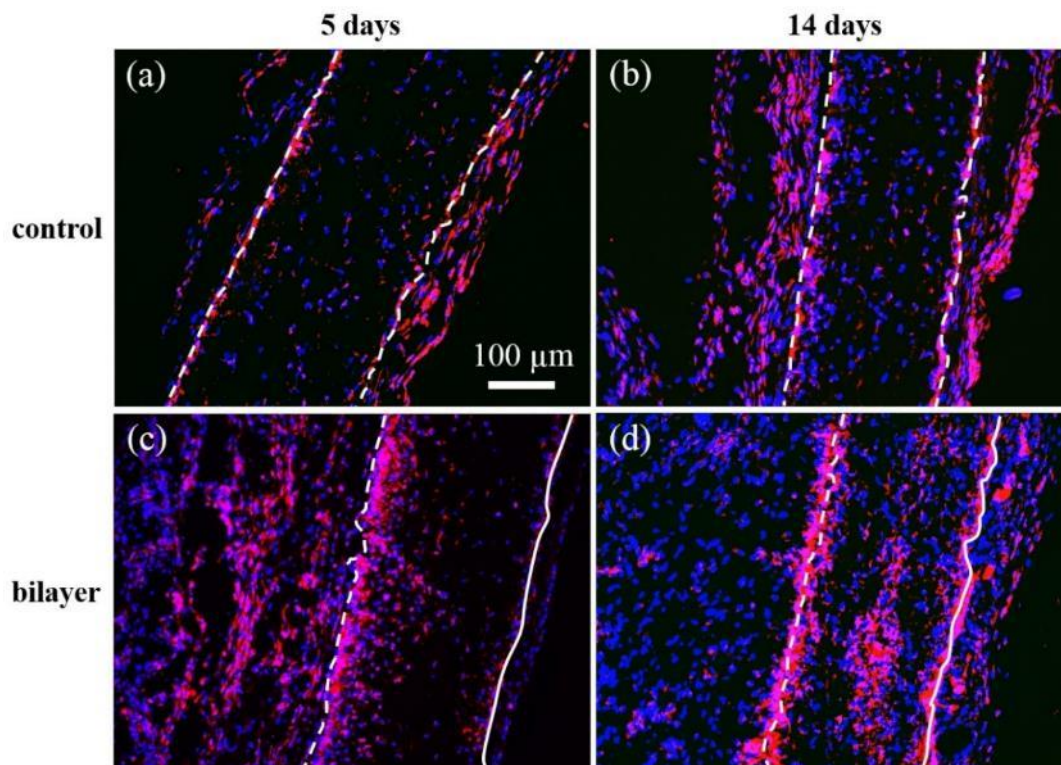
Fig. 4.8 Representative cross-sectional images of control and bilayer scaffolds subcutaneously implanted in Sprague-Dawley rats for (a, c) 5 days and (b, d) 14 days (DAPI (nuclei, blue); collagen type II (red)). Dashed and solid lines indicate the boundaries between surrounding tissue and scaffold surfaces with random and aligned fibers, respectively. Aligned fibers are on the right surface in (c) and (d). All images have the same magnification.

4.4 Discussion

The electrospinning technique used in this study produces bilayer scaffolds consisting of a highly porous layer with randomly orientated fibers (RFL) and a relatively dense layer with aligned fibers (AFL). The RFL provides an easy path for cells to migrate through the scaffold during implantation in vivo, whereas the AFL serves as the major structural component that provides the necessary mechanical strength to the scaffold. There is no abrupt change in fiber alignment and porosity between the AFL and RFL. Instead, there is a gradual decrease in fiber alignment and an increase in porosity from the AFL toward the RFL. This structure endows the bilayer scaffolds good mechanical properties [21] and excellent in vivo cell infiltration, which are both critical factors in tissue engineering.

Fiber alignment in the AFL is due to the particular collector geometry. The electric field intensity is significantly higher at the disk edges than between the disks [21], resulting in fiber deposition over the disk edges and fiber bridging between the disks. The fibers bridging the two disks align in the same direction (i.e., perpendicular to the disk planes) due to the electrostatic repulsion between neighboring fibers (all fibers at the surface are positively charged). Li et al. [23] examined the electrostatic field and Coulomb interaction

between two parallel collectors separated by a non-conductive gap and showed that the resulting electrostatic field results in fiber alignment and stretching. During the initial stage of the present electrospinning experiments, fiber alignment occurred between the parallel disks perpendicular to the disk planes and randomly over the disk edges, which is consistent with the results of other studies [19,23–25]. Random fiber distribution in the RFL is attributed to the insulating nature of the deposited fibers, which changed the electric field distribution between the two parallel conductive disks beyond a critical thickness (~30 μm). The effect of the two parallel disks on the electric field distribution decreased with increasing scaffold thickness, producing a more uniform electric field around the disks. This resulted in random fiber deposition similar to that obtained with a single conductive disk or plate.

Pore size, porosity, and pore interconnectivity are important scaffold features for cell infiltration. The pore size and porosity of electrospun materials are closely related to the fiber diameter and fiber density [26]. Lowery et al. [27] reported a linear relation between pore size and fiber width and average pore-to-fiber diameter ratio equal to ~5. Eichhorn and Sampson [26] showed that a local increase in fiber density causes a decrease in average pore radius and local porosity. The bilayer scaffolds of the present study exhibit an overall highly porous structure, especially the RFL (Fig. 3.7). In the context of theories advanced in previous studies [26,27], the increase of the pore size and porosity of RFL is mainly due to the decrease of the fiber packing density, because the average fiber diameter was the same with that of controls. The average porosity of bilayer scaffolds is higher than that of controls by ~12.3%. According to a previous study [21], the increase in average porosity is due to the significant decrease of the electric field intensity between the two parallel disks relative to the disk edges. Another important feature of the bilayer scaffolds is the formation of a 3D network of interconnected pores (Fig. 3.7(b) and Fig. 4.2), which is vital for in vivo cell infiltration and vascularization.

Scaffold strength is another important factor in tissue engineering because the human body is not a stress-free environment. An increase in scaffold porosity is always accompanied by degradation of the mechanical properties. As mentioned previously (section 1), several methods have been used to increase the porosity of electrospun scaffolds, but with adverse effects on the scaffold stiffness and strength. For example, the tensile strength of scaffolds fabricated using a rotating metal-frame cylinder as the collector decreased by ~50% compared to that of scaffolds fabricated with a metal-plate collector with the increase of porosity from 68% to 79% [2], whereas the elastic modulus of porous scaffolds fabricated by removing the sacrificial fibers was found to be ~60% that of electrospun scaffolds without sacrificial fibers [16]. In addition, scaffolds with varying porosity in transverse planes fabricated by laser ablation [20] or using a stainless steel wire mesh as the collector [19] did not show improved mechanical properties compared to scaffolds of uniform porosity, presumably because the abrupt changes in fiber packing density introduced stress raisers in the former scaffolds. Because the fiber density and porosity change gradually through the thickness of the bilayer scaffolds, they are free of stress raisers induced by abrupt structure changes. Despite the relatively high porosity of bilayer scaffolds, they possess higher elastic modulus, yield strength, and toughness than single-layer scaffolds

consisting of random fibers [21]. Moreover, the bilayer scaffolds did not show any breakage, distortion, or delamination even after 14 days of implantation in vivo.

It is well known that the scaffold structure influences cell viability, ingrowth, and distribution as well as ECM formation by specific cell types [28,29]. To investigate whether the bilayer structure and high porosity are beneficial for in vivo cell infiltration and tissue growth in the scaffolds, the biological performance of the bilayer scaffolds was compared to that of controls using a rat subcutaneous cell infiltration model. The experimental evidence indicated a significant enhancement of cell infiltration in the bilayer scaffolds. The main path for cells to migrate into the bilayer scaffolds was from the highly porous RFL surface. A homogeneous cell distribution was achieved in the bilayer scaffolds after 14 days of implantation in vivo. Cell infiltration in the bilayer scaffolds was higher than that of controls by a factor larger than 2. The homogeneous cell distribution in the bilayer scaffolds implanted for 14 days may increase the maturation rate of the construct and, in turn, enhance functional tissue replacement [17]. Deposition, remodeling, and organization of the ECM by fibroblasts are essential functions for tissue growth. Histologic trichrome staining performed to identify the presence of collagen in the scaffolds showed more collagen deposition in the bilayer scaffolds than the controls. In addition, more collagen fibers deposited in the surrounding tissue near the surface of the controls than the side of the bilayer scaffolds with random fibers, implying potential formation of a thicker fibrous capsule around the controls. However, longer implantation (several months) studies are necessary to fully elucidate fibrous capsule formation around the controls and bilayer scaffolds.

The immunomodulatory response was assessed by staining for pan macrophages in the scaffolds. Although significant differences between the percentages of macrophages in the bilayer and control scaffolds were not observed after implantation for 5 days, much more macrophages were detected in the controls than the bilayer scaffolds implanted for 14 days, in good agreement with recent studies [30,31] showing minimal foreign body reaction for porous materials implanted in vivo compared to their non-porous counterparts. Pan macrophages include two phenotypes: M1 (pro-inflammatory, activated macrophages associated with signs of inflammation [32–34]) and M2 (anti-inflammatory, "alternatively" activated macrophages promoting immunoregulation, tissue repair, and constructive tissue remodeling [35]). Further identification of macrophage phenotypes is needed to determine the dominant activity of infiltrating macrophages. However, the bilayer scaffolds showed higher cell proliferation than the controls during in vivo implantation, which is consistent with previous findings [17].

Scaffold vascularization was examined by immnunostaining explanted scaffolds with α-actin and CD31, which is a mandatory prerequisite for functional tissue. After scaffold implantation, all infiltrating cells depend on the adequate supply of oxygen and nutrients for survival. Because transport of oxygen and nutrients during implantation exclusively occurs by diffusion, it is crucial for any implanted scaffold to rapidly develop sufficient vasculature in vivo [28,36]. It has been reported that the scaffold porosity significantly affects neovascularization in scaffolds implanted in vivo [17,36]. The present in vivo experiments show that the gradual change in porosity through the thickness of the bilayer

scaffold and the increased average pore size amplified neovascularization in these scaffolds, revealing the high potential of bilayer scaffolds for tissue regeneration.

Under the electrospinning conditions of this study, the maximum thickness of the fabricated bilayer scaffolds was limited to ~220 µm because the weakened electric field prevented further fiber deposition. This may limit the application of the bilayer scaffolds in certain physiological scenarios. One possible way to address this issue is to gradually increase the voltage applied to the needle during electrospinning in order to compensate for the decrease of the electric field intensity with increasing scaffold thickness. Alternatively, the fiber conductivity may be increased by adding conductive components (e.g., carbon nanotubes) in the electrospinning solution to facilitate the deposition of thicker bilayer scaffolds.

Another important advantage of the bilayer scaffolds is that their mechanical properties can be tuned by varying the AFL-to-RFL thickness ratio. This can be accomplished by designing a series of parallel-disk collectors with different geometries and dimensions (e.g., in situ adjustable gap between the two parallel disks). These traits make the present bilayer scaffolds good candidates for tissue engineering applications where mechanical failure is critical to scaffold biofunctionality and matching of the implant mechanical properties with those of the surrounding tissue is imperative. Moreover, the unique structure of the bilayer scaffolds endows them multiple functions. For example, in the case of deep wound repair, the densely packed structure of AFL could potentially inhibit the intrusion of bacteria, whereas fiber alignment can promote cell migration at the scaffold surface [37], which should be beneficial for wound healing. In addition, the high porosity of RFL enhances cell infiltration, which is of critical importance in 3D tissue engineering. Further studies will include long-term implantation in vivo (several months) and combinations of various scaffold structures and chemical cues, such as various growth factors.

4.5 Conclusions

Bilayer scaffolds consisting of PLLA and demonstrating a gradual increase in through-thickness porosity (from the AFL toward the RFL) were fabricated by a novel electrospinning method. The potential of these bilayer scaffolds for tissue regeneration was assessed in the light of in vivo experiments involving subcutaneous scaffold implantation in Sprague-Dawley rats and microscopy, histology, and immunohistochemistry studies. The bilayer scaffolds exhibited much higher average porosity than those fabricated by conventional electrospinning and good mechanical strength because of their unique structure. In vivo implantation studies using a rat model showed that the bilayer scaffolds enhanced cell infiltration, cell distribution, collagen formation, cell proliferation, and vascularization. The results of this study suggest that limitations due to the inadequate porosity and mechanical strength of scaffolds fabricated by conventional electrospinning can be overcome by the present method, thereby enabling further advances in the application of electrospun fibrous scaffolds in tissue engineering.

4.6 References

[1] Venugopal, J. and Ramakrishna, S., 2005. Biocompatible nanofiber matrices for the engineering of a dermal substitute for skin regeneration. Tissue engineering, 11(5-6), pp.847-854.

[2] Zhu, X., Cui, W., Li, X. and Jin, Y., 2008. Electrospun fibrous mats with high porosity as potential scaffolds for skin tissue engineering.Biomacromolecules, 9(7), pp.1795-1801.

[3] Fleischer, S., Shapira, A., Regev, O., Nseir, N., Zussman, E. and Dvir, T., 2014. Albumin fiber scaffolds for engineering functional cardiac tissues.Biotechnology and bioengineering, 111(6), pp.1246-1257.

[4] Yang, F., Murugan, R., Wang, S. and Ramakrishna, S., 2005. Electrospinning of nano/micro scale poly (L-lactic acid) aligned fibers and their potential in neural tissue engineering. Biomaterials, 26(15), pp.2603-2610.

[5] Xu, C.Y., Inai, R., Kotaki, M. and Ramakrishna, S., 2004. Aligned biodegradable nanofibrous structure: a potential scaffold for blood vessel engineering. Biomaterials, 25(5), pp.877-886.

[6] Rayatpisheh, S., Heath, D.E., Shakouri, A., Rujitanaroj, P.O., Chew, S.Y. and Chan-Park, M.B., 2014. Combining cell sheet technology and electrospun scaffolding for engineered tubular, aligned, and contractile blood vessels. Biomaterials, 35(9), pp.2713-2719.

[7] Boland, E.D., Telemeco, T.A., Simpson, D.G., Wnek, G.E. and Bowlin, G.L., 2004. Utilizing acid pretreatment and electrospinning to improve biocompatibility of poly (glycolic acid) for tissue engineering. Journal of Biomedical Materials Research Part B: Applied Biomaterials, 71(1), pp.144-152.

[8] Li, W.J., Laurencin, C.T., Caterson, E.J., Tuan, R.S. and Ko, F.K., 2002. Electrospun nanofibrous structure: a novel scaffold for tissue engineering.Journal of biomedical materials research, 60(4), pp.613-621.

[9] Zong, X., Kim, K., Fang, D., Ran, S., Hsiao, B.S. and Chu, B., 2002. Structure and process relationship of electrospun bioabsorbable nanofiber membranes. Polymer, 43(16), pp.4403-4412.

[10] Lee, K.H., Kim, H.Y., Khil, M.S., Ra, Y.M. and Lee, D.R., 2003. Characterization of nano-structured poly (ε-caprolactone) nonwoven mats via electrospinning. Polymer, 44(4), pp.1287-1294.

[11] Lannutti, J., Reneker, D., Ma, T., Tomasko, D. and Farson, D., 2007. Electrospinning for tissue engineering scaffolds. Materials Science and Engineering: C, 27(3), pp.504-509.

[12] Hu, C., Tercero, C., Ikeda, S., Nakajima, M., Tajima, H., Shen, Y., Fukuda, T. and Arai, F., 2013. Biodegradable porous sheet-like scaffolds for soft-tissue engineering using a combined particulate leaching of salt particles and magnetic sugar particles. Journal of bioscience and bioengineering, 116(1), pp.126-131.

[13] Ratner, B.D., Hoffman, A.S., Schoen, F.J. and Lemons, J.E., 2004.Biomaterials science: an introduction to materials in medicine. Academic press.

[14] Leong, M.F., Rasheed, M.Z., Lim, T.C. and Chian, K.S., 2009. In vitro cell infiltration and in vivo cell infiltration and vascularization in a fibrous, highly porous poly (D, L-

lactide) scaffold fabricated by cryogenic electrospinning technique. Journal of Biomedical Materials Research Part A, 91(1), pp.231-240.

[15] Nam, J., Huang, Y., Agarwal, S. and Lannutti, J., 2007. Improved cellular infiltration in electrospun fiber via engineered porosity. Tissue engineering,13(9), pp.2249-2257.

[16] Baker, B.M., Gee, A.O., Metter, R.B., Nathan, A.S., Marklein, R.A., Burdick, J.A. and Mauck, R.L., 2008. The potential to improve cell infiltration in composite fiber-aligned electrospun scaffolds by the selective removal of sacrificial fibers. Biomaterials, 29(15), pp.2348-2358.

[17] Horst, M., Milleret, V., Nötzli, S., Madduri, S., Sulser, T., Gobet, R. and Eberli, D., 2014. Increased porosity of electrospun hybrid scaffolds improved bladder tissue regeneration. Journal of Biomedical Materials Research Part A, 102(7), pp.2116-2124.

[18] Ekaputra, A.K., Prestwich, G.D., Cool, S.M. and Hutmacher, D.W., 2008. Combining electrospun scaffolds with electrosprayed hydrogels leads to three-dimensional cellularization of hybrid constructs. Biomacromolecules,9(8), pp.2097-2103.

[19] Vaquette, C. and Cooper-White, J.J., 2011. Increasing electrospun scaffold pore size with tailored collectors for improved cell penetration. Acta Biomaterialia, 7(6), pp.2544-2557.

[20] Lee, B.L.P., Jeon, H., Wang, A., Yan, Z., Yu, J., Grigoropoulos, C. and Li, S., 2012. Femtosecond laser ablation enhances cell infiltration into three-dimensional electrospun scaffolds. Acta biomaterialia, 8(7), pp.2648-2658.

[21] Pu, J. and Komvopoulos, K., 2014. Mechanical properties of electrospun bilayer fibrous membranes as potential scaffolds for tissue engineering. Acta biomaterialia, 10(6), pp.2718-2726.

[22] Tan, E.P. and Lim, C.T., 2006. Effects of annealing on the structural and mechanical properties of electrospun polymeric nanofibres. Nanotechnology,17(10), p.2649.

[23] Li, D., Wang, Y. and Xia, Y., 2003. Electrospinning of polymeric and ceramic nanofibers as uniaxially aligned arrays. Nano letters, 3(8), pp.1167-1171.

[24] Zhu, Y., Wang, A., Patel, S., Kurpinski, K., Diao, E., Bao, X., Kwong, G., Young, W.L. and Li, S., 2011. Engineering bilayer nanofibrous conduits for peripheral nerve regeneration. Tissue Engineering Part C: Methods, 17(7), pp.705-715.

[25] Zhu, Y., Wang, A., Shen, W., Patel, S., Zhang, R., Young, W.L. and Li, S., 2010. Nanofibrous patches for spinal cord regeneration. Advanced functional materials, 20(9), pp.1433-1440.

[26] Eichhorn, S.J. and Sampson, W.W., 2005. Statistical geometry of pores and statistics of porous nanofibrous assemblies. Journal of the royal society Interface, 2(4), pp.309-318.

[27] Lowery, J.L., Datta, N. and Rutledge, G.C., 2010. Effect of fiber diameter, pore size and seeding method on growth of human dermal fibroblasts in electrospun poly (ε-caprolactone) fibrous mats. Biomaterials, 31(3), pp.491-504.

[28] Fedorovich, N.E., Kuipers, E., Gawlitta, D., Dhert, W.J. and Alblas, J., 2011. Scaffold porosity and oxygenation of printed hydrogel constructs affect functionality of embedded osteogenic progenitors. Tissue Engineering Part A, 17(19-20), pp.2473-2486.

[29] Zeltinger, J., Sherwood, J.K., Graham, D.A., Müeller, R. and Griffith, L.G., 2001. Effect of pore size and void fraction on cellular adhesion, proliferation, and matrix deposition. Tissue engineering, 7(5), pp.557-572.

[30] Underwood, R.A., Usui, M.L., Zhao, G., Hauch, K.D., Takeno, M.M., Ratner, B.D., Marshall, A.J., Shi, X., Olerud, J.E. and Fleckman, P., 2011. Quantifying the effect of pore size and surface treatment on epidermal incorporation into percutaneously implanted sphere-templated porous biomaterials in mice. Journal of Biomedical Materials Research Part A,98(4), pp.499-508.

[31] Madden, L.R., Mortisen, D.J., Sussman, E.M., Dupras, S.K., Fugate, J.A., Cuy, J.L., Hauch, K.D., Laflamme, M.A., Murry, C.E. and Ratner, B.D., 2010. Proangiogenic scaffolds as functional templates for cardiac tissue engineering. Proceedings of the National Academy of Sciences, 107(34), pp.15211-15216.

[32] Mantovani, A., Sica, A., Sozzani, S., Allavena, P., Vecchi, A. and Locati, M., 2004. The chemokine system in diverse forms of macrophage activation and polarization. Trends in immunology, 25(12), pp.677-686.

[33] Badylak, S.F., Valentin, J.E., Ravindra, A.K., McCabe, G.P. and Stewart-Akers, A.M., 2008. Macrophage phenotype as a determinant of biologic scaffold remodeling. Tissue Engineering Part A, 14(11), pp.1835-1842.

[34] Brown, B.N., Londono, R., Tottey, S., Zhang, L., Kukla, K.A., Wolf, M.T., Daly, K.A., Reing, J.E. and Badylak, S.F., 2012. Macrophage phenotype as a predictor of constructive remodeling following the implantation of biologically derived surgical mesh materials. Acta biomaterialia, 8(3), pp.978-987.

[35] Fishman, J.M., Lowdell, M.W., Urbani, L., Ansari, T., Burns, A.J., Turmaine, M., North, J., Sibbons, P., Seifalian, A.M., Wood, K.J. and Birchall, M.A., 2013. Immunomodulatory effect of a decellularized skeletal muscle scaffold in a discordant xenotransplantation model. Proceedings of the National Academy of Sciences, 110(35), pp.14360-14365.

[36] Feng, B., Jinkang, Z., Zhen, W., Jianxi, L., Jiang, C., Jian, L., Guolin, M. and Xin, D., 2011. The effect of pore size on tissue ingrowth and neovascularization in porous bioceramics of controlled architecture in vivo.Biomedical Materials, 6(1), p.015007.

[37] Patel, S., Kurpinski, K., Quigley, R., Gao, H., Hsiao, B.S., Poo, M.M. and Li, S., 2007. Bioactive nanofibers: synergistic effects of nanotopography and chemical signaling on cell guidance. Nano letters, 7(7), pp.2122-2128.

Chapter 5 – Graphene or activated carbon/polymer electrolyte composite for high-energy-density, all-solid-state microsupercapacitors

All-solid-state microsupercapacitors (MSCs) with three-dimensional (3D) electrodes consisting of active materials (i.e., graphene or activated carbon (AC) particles) and polymer electrolyte (PE) designed for high-energy-density storage applications were fabricated and tested in this chapter. For a scan rate of 5 mV s^{-1}, the MSCs with graphene/PE and AC/PE composite electrodes demonstrate a very high areal capacitance of 95 and 134 mF cm^{-2}, respectively. In addition, the graphene/PE MSCs show a ~70% increase in specific capacitance after 10,000 charge/discharge cycles. The results of this study illustrate the potential of the present 3D MSCs for various high-density solid-state energy storage applications.

5.1 Introduction

Energy storage units are of significant importance to energy conversion devices, such as piezoelectric nanogenerators, solar and thermoelectric cells, and other electronic circuits used in self-powered micro/nanodevice systems. Microsupercapacitors (MSCs) have attracted significant attention for on-chip energy storage applications because they demonstrate high charge/discharge rate [1,2], long operation life [3], and relatively high energy density [4]. Depending on charge storage mechanisms, MSCs can be classified as electric double-layer capacitors (EDLCs) and pseudocapacitors. EDLCs store static charges at electrode/electrolyte interfaces, whereas pseudocapacitors rely on rapid and reversible surface or near-surface redox reactions for charge storage. Compared to pseudocapacitors, EDLCs usually demonstrate lower energy density, but better rate capability, higher power density, and longer life.

An effective means of increasing the capacity of MSCs over a limited footprint area is to use three-dimensional (3D) electrode structures. Significant research has been devoted to developing 3D microelectrodes for high-energy-density storage applications. For example, Sun and Chen [5] designed MSCs with 3D polypyrrole electrodes and NaCl solution electrolyte, which demonstrated an areal capacitance of 27 mF cm^{-2}. Jiang et al. [6] tested ~150-μm-thick MSCs with carbon nanotube (CNT) forests decorated with Ni nanoparticles in 0.1 M KOH liquid electrolyte and reported an areal capacitance of 18.8 mF cm^{-2}. Shen et al. [7,8] fabricated 3D MSCs by injecting polyvinylidene fluoride (PVDF) with AC particles into the deep trenches of a Si wafer and measured an areal capacitance of 90.7 mF cm^{-2} in 1 M NaNO$_3$ liquid electrolyte. These studies indicate that a 3D electrode structure is beneficial for improving the energy storage capability of MSCs.

Although a high capacitance has been reported in previous studies of MSCs, the use of a liquid electrolyte in an electrochemical device has several potential drawbacks, in particular electrolyte leakage and electrical shortage of the electrodes. Compared to liquid-electrolyte MSCs, solid-state MSCs have many advantages, such as higher safety, environmental friendliness, excellent portability, and higher stability [9]. Therefore, solid-

state MSCs are promising microdevices for various flexible and wearable electronic applications, including implantable electronic devices, portable health monitoring systems, and smart watches. In view of the high potential of portable and wearable electronics, reliable solid-state energy storage microdevices are of critical importance to further developing these electronic devices.

Despite the aforementioned advantages, solid-state MSCs exhibit low areal energy density. The difficulty of solid electrolyte to diffuse into the bulk of thick electrodes limits the use of 3D electrodes in all-solid-state MSCs, thus reducing the energy storage capability. Most of current solid-state MSCs use two-dimensional electrodes of thickness <1 µm and yield an areal capacitance of <1 mF cm^{-2} [10–13]. A higher areal capacitance can be achieved with pseudocapacitive electrode materials and relatively thick (a few micrometers) electrodes. For example, Wang et al. [14] fabricated solid-state MSCs consisting of MnO_2/onion-like composite electrodes and polyvinyl alcohol-phosphoric acid (PVA-H_3PO_4) electrolyte and reported an areal capacitance of 7.04 mF cm^{-2}. Meng et al. [15] investigated the electrochemical performance of solid-state MSCs with polyaniline nanowire electrodes and observed higher areal capacitance with thicker electrodes (e.g., 45.2 mF cm^{-2} for ~10-µm-thick electrodes). For solid-state PVA-H_3PO_4 electrolyte, Kaempgen et al. [16] discovered that due to limited solid electrolyte diffusion into the bulk of thick electrodes, the maximum effective thickness of electrodes made of single-walled CNTs is ~20 µm. Pushparaj et al. [17] developed an electrode-spacer-electrolyte integrated nanocomposite unit of a few tens of micrometers in thickness by infiltrating viscous cellulose-room temperature ionic liquid (RTIL) solution into electrodes of aligned CNTs; however, despite the high potential as a structural material of 3D electrodes of solid-state supercapacitors, the very low density of the CNT array used to enhance the infiltration of the cellulose-RTIL solution limits the energy density of these devices. An overview of recent progress in solid-state MSCs can be found in a review article by Xiong et al. [18].

The main objective of the present investigation is to introduce high-energy-density, all-solid-state MSCs with 3D active material-electrolyte composite electrodes. To obtain MSCs with increased electronic/ionic conductivity and charge storage capability, electrodes of effective thickness ≤300 µm were fabricated by incorporating carbon-based particles, such as graphene or activated carbon (AC), in PVA-H_3PO_4 gel electrolyte. To the authors' best knowledge, this is the thickest electrode ever used for solid-state MSCs. Because of the thick electrodes, an areal capacitance of 95 and 134 mF cm^{-2} was achieved with 300-µm-thick graphene/PE and 250-µm-thick AC/PE composite electrodes, respectively. There are three principal advantages for incorporating PE with active materials into the electrode bulk: (1) the diffusion of PE in the bulk of thick electrodes leads to the formation of a 3D ionic conductive network; (2) the accessibility of the electrode surface by electrolyte ions is enhanced by coating the active materials with PE, resulting in higher specific capacitance; and (3) the resulting intimate contact of active materials with electrolyte reduces the ion diffusion path in the electrodes, resulting in fast charge/discharge. Therefore, the fabrication method developed in this study has a high potential for increasing the energy density of solid-state MSCs for portable and wearable electronic devices.

5.2 Design and methods

5.2.1 Electrode materials

For electrolyte ions to access the entire through-thickness area of 3D electrodes, the electrode material must possess sufficiently large pores to allow the highly viscous gel electrolyte to infiltrate through the bulk of the thick electrodes. Composites consisting of carbon particles (electrochemically active) and polymer (binder) exhibit large inter-particle voids (tens of nanometers to a few micrometers, depending on particle size), which is advantageous for PE gel diffusion into the electrode bulk of 3D solid-state MSCs. PVDF [7,19] and polytetrafluoro-ethylene [19,20] are common polymers for binding carbon particles. While these binder materials enhance the electrode mechanical stability, they partially block the ions from accessing the porous structure of carbon particles, increase the ion migration resistance, and decrease the electrode electrical conductivity, hence decreasing the capacitance and degrading the power performance of the device. To obtain high-performance 3D solid-state MSCs, the PE in the electrode material not only must bind the carbon particles but also provide cations and anions in the proximity of the electrode surface, yielding high energy density storage and fast charge/discharge. Moreover, direct intermixing of the carbon particles with PE, assisted by stirring and sonication, is beneficial to the diffusion of PE into the particle nanoporous structure.

Active electrode materials should possess high specific surface area, high conductivity, and good electrochemical properties. Graphene is commonly used as an active electrode material for storing charge in supercapacitors by the electrical double layer (EDL) mechanism [3,10,11,21,22] because it exhibits high specific surface area (up to 2630 m^2/g [23]) and excellent conductivity. The graphene powder used in this study (The Sixth Element, Changzhou, China) has a specific surface area of >1500 m^2/g and an average particle size of ≤10 μm. The surface of the graphene particles was not modified. Each graphene particle contains ~10 layers of graphene nanosheets with a total thickness of ~5 nm. AC was also used as an active electrode material because it is widely used in commercial energy storage products. The specific surface area and bulk density of the AC powder used in this work is 2000 m^2/g and 0.7 g/cm^3, respectively (Shanghai Carbosino Material, Shanghai, China).

Carbon/PE composites were prepared by adding carbon (either graphene or AC) powder to an aqueous solution of PVA-H_3PO_4, mixing by sonication for 1 h, and, finally, magnetically stirring for an additional 1 h. The PVA:H_3PO_4 ratio in the PE was fixed at 1:1 wt/vol. To fabricate electrodes of adequate mechanical stability and form an effective 3D ionic conductive path, a sufficient amount of PE must be incorporated in the electrodes. However, the addition of a polymer compromises the electrical conductivity of electrodes, increases the equivalent series resistance (ESR), and degrades the power performance. Thus, the amount of PVA in the composites was carefully tuned to maximize the electrical and ionic conductance without degrading the electrode structural stability. Carbon black (CB) was used as a conductive agent to increase the conductivity of the AC composite electrodes. The weight ratio of carbon particles to PVA in the composite electrodes was set at 5:1 (i.e., graphene:PVA = 5:1 and AC:CB:PVA = 4:1:1). This optimum composition was determined after finding that less PVA leads to fast degradation of the capacitance

during repeated charge/discharge, presumably due to the reduced contact intimacy of carbon particles, whereas more PVA produces poor rate capability. For comparison, a graphene composite having PVDF as the binder material was prepared by a similar approach. Dimethyl sulfoxide was used as the solvent of PVDF. In the graphene/PVDF composite, the graphene:PVDF weight ratio was fixed at 5:1. Hereafter, the three composites consisting of graphene (Gr) and PE, carbon (AC and CB) and PE, and graphene and PVDF will be referred to as Gr/PE, AC/PE, and Gr/PVDF, respectively, for brevity.

5.2.2 Structure and fabrication of 3D MSCs

In-plane interdigital electrode architecture with carbon-based composite electrodes and high aspect ratio separator consisting of SU-8 was used in this study. SU-8 is widely used to fabricate microstructures because of its excellent mechanical strength and capability for direct lithography. Using a high aspect ratio SU-8 structure to support the electrodes enables the fabrication of thick interdigital microelectrodes with a small gap, which enhances the capacitance of MSCs over a limited footprint area and reduces the ion transport path between the electrodes. The PE (PVA-H_3PO_4) polymer gel coating of the electrodes plays the role of an electrolyte reservoir. The left and right schematics of Fig. 5.1 show the carbon particle/PE composite electrode before and after coating with the PE gel, respectively. To enhance the diffusion of PE into the electrode bulk and form a 3D PE network, which would increase the ionic conductance in the electrodes, PE containing cations and anions was incorporated in the electrode material before forming the 3D microelectrodes.
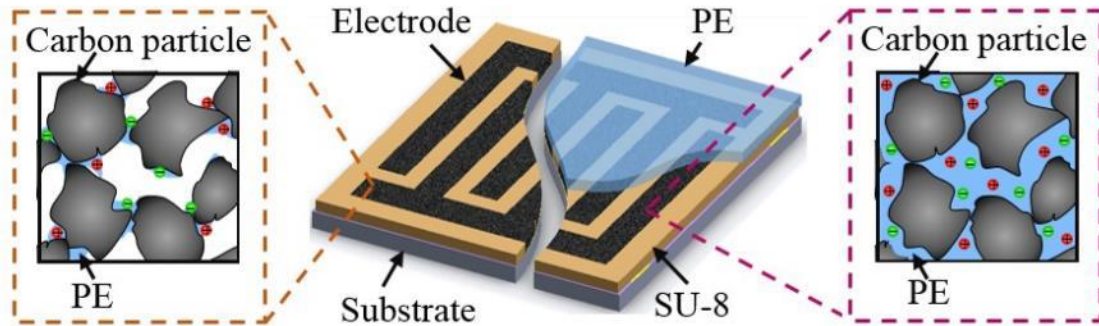
Fig. 5.1 Schematic of a 3D all-solid-state MSC with interdigital electrodes consisting of carbon particle/PE composite. The left and right schematics illustrate the MSC structure before and after coating the electrodes with PE to form electrolyte reservoirs, respectively. The incorporation of ion-containing PE in the electrode material before the formation of the electrode (left schematic) promotes the diffusion of PE in the electrode bulk after PE gel coating (right schematic), resulting in the formation of a 3D PE network.

The all-solid-state 3D MSCs were fabricated by a process schematically shown in Fig. 5.2 First, an insulation 100-nm-thick silicon nitride (Si_3N_4) layer was deposited on a Si(100) wafer by low-pressure-chemical-vapor deposition, followed by the evaporation of a bilayer film consisting of a 10-nm-thick Cr underlayer and a 100-nm-thick Au top layer, which was then patterned to the desired interdigital structure to serve as current collector (Fig.

5.2(a)). The gap between the interdigital fingers and the finger width are 60 and 300 µm, respectively. To form a serpentine-like wall between the interdigital fingers, 100- or 300-µm-thick SU-8 was spin-coated onto the wafer and lithographically patterned (Fig. 5.2(b)). To construct 3D electrodes, the carbon-based composite material was injected into the SU-8 trenches and allowed to dry at room temperature (Fig. 5.2(c)). Because solvent evaporation induced material shrinkage, multiple injections were used to fill up the SU-8 trenches with as much material as possible. The electrode footprint area (i.e., the area of the interdigital fingers plus the area of the SU-8 separator) is ~20 mm^2. To preserve the structural integrity of the electrodes, the patterned SU-8 serpentine-like wall was not removed from the substrate. Finally, an all-solid-state 3D MSC was obtained by coating the electrodes with PE (PVA-H$_3$PO$_4$) to provide an ion reservoir and to form an ion conduction path between the electrodes (Fig. 5.2(d)). The PVA-H$_3$PO$_4$ electrolyte was prepared by mixing 10 mL of deionized (DI) water with 10 mL of phosphoric acid by magnetic stirring for 30 min and dissolving 10 g of PVA in 90 mL of DI water at 90°C, also assisted by magnetic stirring for 1 h. Finally, the two solutions were intermixed by magnetic stirring for 1 h. The PVA:H$_3$PO$_4$ ratio in the PE was fixed at 1:1 vol/wt, which is the same as that in the composite electrode materials.
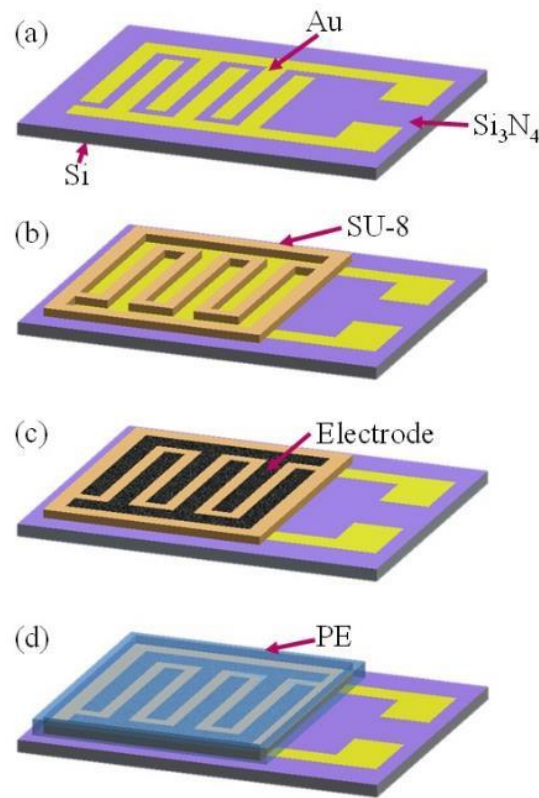
Fig. 5.2 Fabrication process of 3D all-solid-state MSCs: (a) deposition of a Si$_3$N$_4$ insulation layer on the Si substrate and micropatterning of the Au layer used as a current collector, (b) micropatterning of the SU-8 separators, (c) filling of the SU-8 trenches with electrode material, and (d) electrode coating with polymer electrolyte (PE).

5.2.3 Characterization and electrochemical testing

The microstructure of electrode materials and structure of 3D interdigital electrodes were examined with a scanning electron microscope (SEM) (S-5500, Hitachi, Tokyo, Japan). To perform cross-sectional SEM imaging of the electrodes, the MSCs were sectioned perpendicular to the finger length. The elemental composition at different electrode regions was examined by *in situ* energy dispersive spectroscopy (EDS).

Electrochemical tests were performed in two-electrode electrochemical cells. One of the interdigital electrodes was used as the working electrode and the other one as the counter electrode, while solid-state PVA-H_3PO_4 was used as the electrolyte. Cyclic voltammetry (CV) experiments were performed in the voltage range of –0.8 to 0.8 V for a scan rate between 5 and 1000 mV s^{-1}. In the galvanostatic charge/discharge (GCD) tests, the devices were first charged to 1 V and then discharged to 0 V at a constant current density of 0.5 mA cm^{-2}. Electrochemical impedance spectra (EIS) were obtained by applying a 10 mV ac signal in the frequency range of 0.01–500,000 Hz. The CV and GCD tests were performed with a CHI 860D electrochemical workstation (Beijing Chinese Science Days Technology, Beijing, China), whereas the EIS tests were carried out with a Solartron 1260 Impedance/Gain-Phase Analyzer (AMETEK Advanced Measurement Technology, Farnborough, Hampshire, UK). All of the electrochemical tests were performed at room temperature.

5.3 Results and discussion

Fig. 5.3(a) shows a digital photograph of a typical MSC obtained before coating with PVA-H_3PO_4 electrolyte. Fig. 5.3(b) shows a high-magnification photograph of the region enclosed by red dash lines in Fig. 5.3(a), which illustrates the effective electrode area consisting of a Gr/PE interdigital electrode and SU-8 separator. Fig. 5.3(c) shows a tilted SEM image of the effective area revealing the 3D electrode structure, whereas Fig. 5.3(d) shows a top-view SEM image of the electrode and SU-8 separator. The Gr/PE electrodes possess a rough surface topography containing some small cracks generated as a result of solvent evaporation during drying.

Figs. 5.4(a) and (g) show that the thickness of graphene-based composite electrodes (i.e., Gr/PE and Gr/PVDF) is close to the thickness of the SU-8 separator. However, Fig. 5.4(d) shows that the thickness of the AC/PE electrodes is less than that of the SU-8 separator, apparently due to the more pronounced shrinkage of the AC composite during drying. The average thickness of the Gr/PE, Gr/PVDF, and AC/PE electrodes formed inside the 300-µm-deep SU-8 trenches is 300, 300, and 250 µm, respectively. To examine the PE distribution through the electrode thickness, the elemental compositions of three different regions (denoted by A, B, and C in Figs. 5.4(a), (d), and (g)) of electrode cross sections were analyzed by EDS. The detection of P in all electrode regions (Figs. 5.4(b), (e), and (h)) indicates that the large inter-particle pores enhanced the diffusion of PE in the electrode bulk. The slightly larger amount of P in the Gr/PE electrodes (Fig. 5.4(b)) than AC/PE electrodes (Fig. 5.4(e)) may be attributed to the lower volume density of the Gr/PE electrodes compared to the AC/PE electrodes [23], which increased the diffusion of the PE gel in the graphene electrodes. The small amount of F in the Gr/PVDF electrode is due to

the PVDF binder (Fig. 5.4(h)). The slightly more F at the electrode bottom (region C) than the top (region A) reveals the presence of more polymer binder at the bottom of the Gr/PVDF electrode. The pristine AC particles possess relatively smooth surfaces (inset of Fig. 5.4(f)), whereas the AC/PE composite shows a polymer-like rough surface (Fig. 5.4(f)), indicating good coating of the AC particles by PE. When compared to pristine graphene particles (inset of Fig. 5.4(c)), the morphologies of Gr/PE and Gr/PVDF composites (Figs. 5.4(c) and (i), respectively) demonstrate insignificant differences, presumably due to the relatively low affinity of graphene particles for PVA and PVDF.
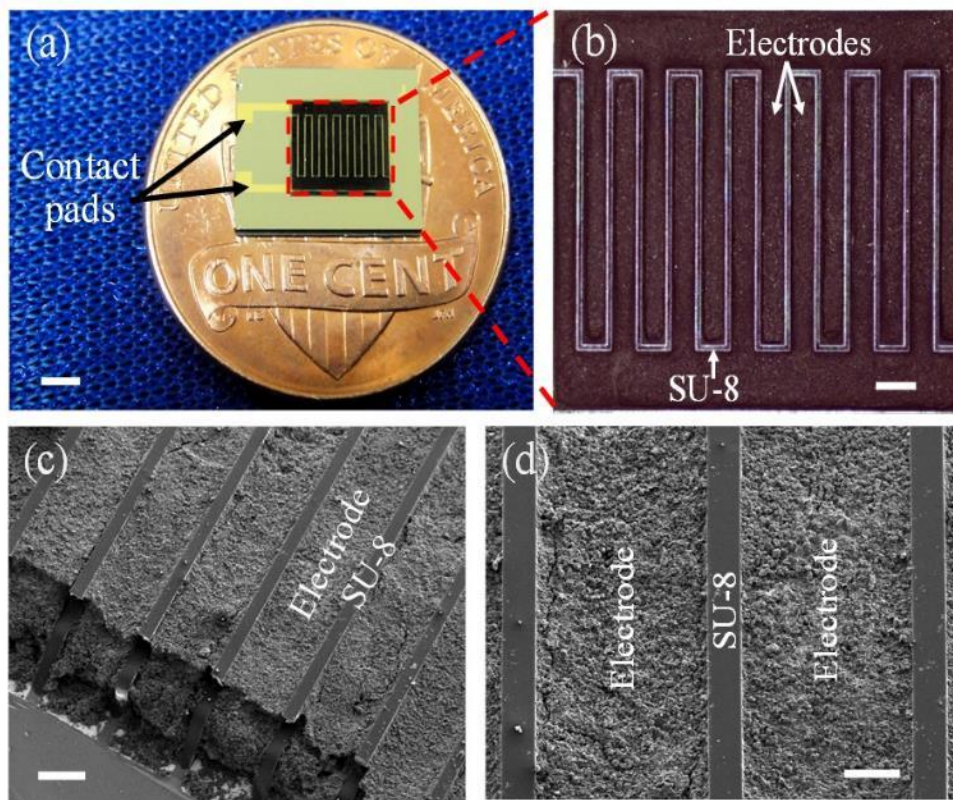
Fig. 5.3 (a) Digital image of a 3D all-solid-state MSC on a US coin, (b) high-magnification digital image showing the effective area consisting of interdigital Gr/PE electrodes and SU-8 separator, and (c) tilted-view and (d) top-view SEM images of Gr/PE electrodes and SU-8 separator. (The scale bar in (a)–(d) is equal to 2 mm, 500 μm, 200 μm, and 100 μm, respectively.)

Figs. 5.5(a)–(e) show representative CV curves of MSCs with different electrode thickness and composition for a scan rate in the range of 5–50 mV s^{-1}. Rectangular voltammograms, high electrochemical current, and symmetric anodic and cathodic paths characterize an ideal capacitor. The Gr/PE MSCs (Figs. 5.5(a) and (c)) demonstrate relatively more rectangular-like CV responses, high charge/discharge rate, and symmetric anodic/cathodic response. In contrast, the CV curves of Gr/PVDF MSCs (Figs. 5.5(b) and (d)) and the AC/PE MSCs (Fig. 5.5(e)) show a non-rectangular shape at a scan rate of 50 mV s^{-1}, implying slower ion diffusion during electrochemical charge/discharge and higher internal

resistance. In addition, the Gr/PVDF MSCs exhibit much lower electrochemical current compared to Gr/PE and AC/PE MSCs, implying a much lower capacitance.
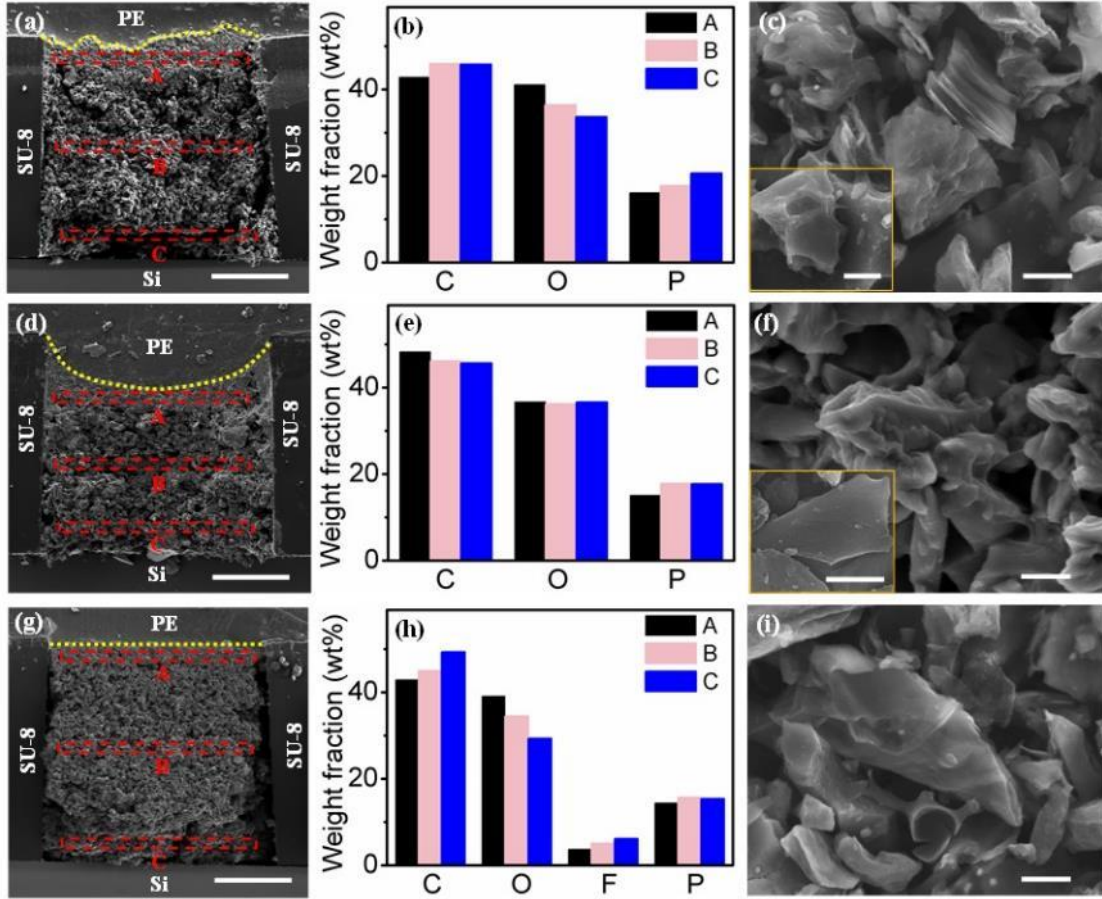
Fig. 5.4 Cross-sectional images of single 3D electrodes consisting of (a) Gr/PE, (d) AC/PE, and (g) Gr/PVDF (the interfaces between the electrodes and the PE coating are indicated by yellow dot lines); (b), (e), and (h) elemental compositions of A, B, and C regions enclosed by red dash lines in (a), (d), and (g), respectively; (c), (f), and (i) high-magnification SEM images of Gr/PE, AC/PE, and Gr/PVDF composites, respectively. The inset SEM images in (c) and (f) show pristine graphene and AC particles, respectively. The scale bar in (a), (d), and (g) is equal to 100 μm, while in (c), (f), and (i) and the inset of (c) and (f) the scale bar is equal to 1 μm.

To further examine the scan rate effect on the areal capacitance of the 3D MSCs, the variation of the areal capacitance C_A with the scan rate was determined from the CV curves and the relation

$$C_A = \frac{1}{A\Delta V} \int I(t)\, dt \tag{5.1}$$

where ΔV is the potential range (= 1.6 V), A is the total electrode and SU-8 footprint area ($\approx$ 20 mm^2), and $I(t)$ is the current measured during CV testing. As shown in Fig.

5.5(f), the MSCs with PE binder demonstrate much higher areal capacitance than the MSCs with PVDF binder at all scan rates. For example, for a scan rate of 5 mV s^{-1}, the 100- and 300-µm-thick Gr/PE MSCs show an areal capacitance of 59 and 95 mF cm^{-2}, respectively, i.e., about 2 and 4 times higher than that of 100- and 300-µm-thick Gr/PVDF MSCs, respectively. The higher areal capacitance of MSCs with thicker Gr/PE electrodes obtained at a low scan rate (5 mV s^{-1}) suggests that the charge/discharge process occurred through the entire thickness of the composite electrode; however, this was not encountered at a high scan rate ($\geq$50 mV s^{-1}) where electronic conduction and ion migration rate are the dominant factors. Compared to Gr/PE and AC/PE MSCs, the Gr/PVDF MSCs (even those with thicker electrodes) exhibit significantly lower capacitance at all scan rates. Although a high specific area can be obtained by increasing the electrode thickness, this also increases both the electronic resistance and the ion diffusion resistance, thus slowing down the charge transfer process. In the case of Gr/PVDF MSCs, the extremely slow charge transfer may not provide sufficient time for ions to access the surface area of electrodes thicker than 100 µm even at a low scan rate (5 mV s^{-1}), which explains the slightly lower capacitance of 300-µm-thick Gr/PVDF MSCs compared to 100-µm-thick Gr/PVDF MSCs. Among all tested MSCs, the 250-µm-thick AC/PE MSC demonstrates the highest areal capacitance (134 mF cm^{-2}) at the lowest scan rate (5 mV s^{-1}). This can be attributed to the higher volume density of the AC composite electrode [23] and more effective coating of the AC particles by PE (Fig. 5.4(f)).

The monotonic decrease of the MSC areal capacitance with increasing scan rate (Fig. 5.5(f)) is related to progressively less efficient ion infiltration through the electrode microstructure with increasing scan rate [24]. The 100-µm-thick Gr/PE electrodes show the best rate capability with 49% capacitance retention for scan rate increasing from 5 to 200 mV s^{-1}. This is due to the higher conductivity of graphene and faster ion transport in thinner electrodes. Despite the highest capacitance at a low scan rate, the 250-µm-thick AC/PE MSCs exhibit a faster decrease in areal capacitance with increasing scan rate (~10% capacitance retention at 200 mV s^{-1} scan rate) than both thin and thick Gr/PE MSCs due to the lower electronic conductivity of AC particles. The Gr/PVDF MSCs show even poorer rate capability, with their capacitance decreasing to <10% of that obtained at a low scan rate (5 mV s^{-1}) when the scan rate increases to 200 mV s^{-1}. The poor rate capability of the Gr/PVDF MSCs may be attributed to the smaller pores and longer ion diffusion paths obtained with the PVDF binder. The results shown in Figs. 5.5(a)–(f) confirm that incorporating PE in the electrode material significantly enhances the capacitance and rate capability of all-solid-state 3D MSCs.

The electrochemical performance of the present 3D MSCs can be further examined in the context of GCD results. Fig. 5.5(g) shows representative GCD curves of various MSCs for a current density equal to 0.5 mA cm^{-2}. A longer discharge time is indicative of a higher areal capacitance. The 250-µm-thick AC/PE MSC shows the longest discharge time, corresponding to the highest areal capacitance, i.e., consistent with the CV results for low scan rate (5 mV s^{-1}). The IR drop, defined as the sharp voltage decrease at the onset of the GCD discharge (indicated by black arrows in Fig. 5.5(g)), provides a measure of the overall resistance and correlates with the rate capability and power performance of the microdevice. Fig. 5.5(h) shows that Gr/PVDF MSCs demonstrate a much larger IR drop than Gr/PE and

AC/PE MSCs. The smallest IR drop (0.05 V) corresponds to 100-µm-thick Gr/PE MSCs. The data shown in Fig. 5.5(h) indicate that thicker electrodes yield larger IR drops. Considering the capacitance and rate capability performance of 3D MSCs, the GCD results are in good agreement with the CV results.
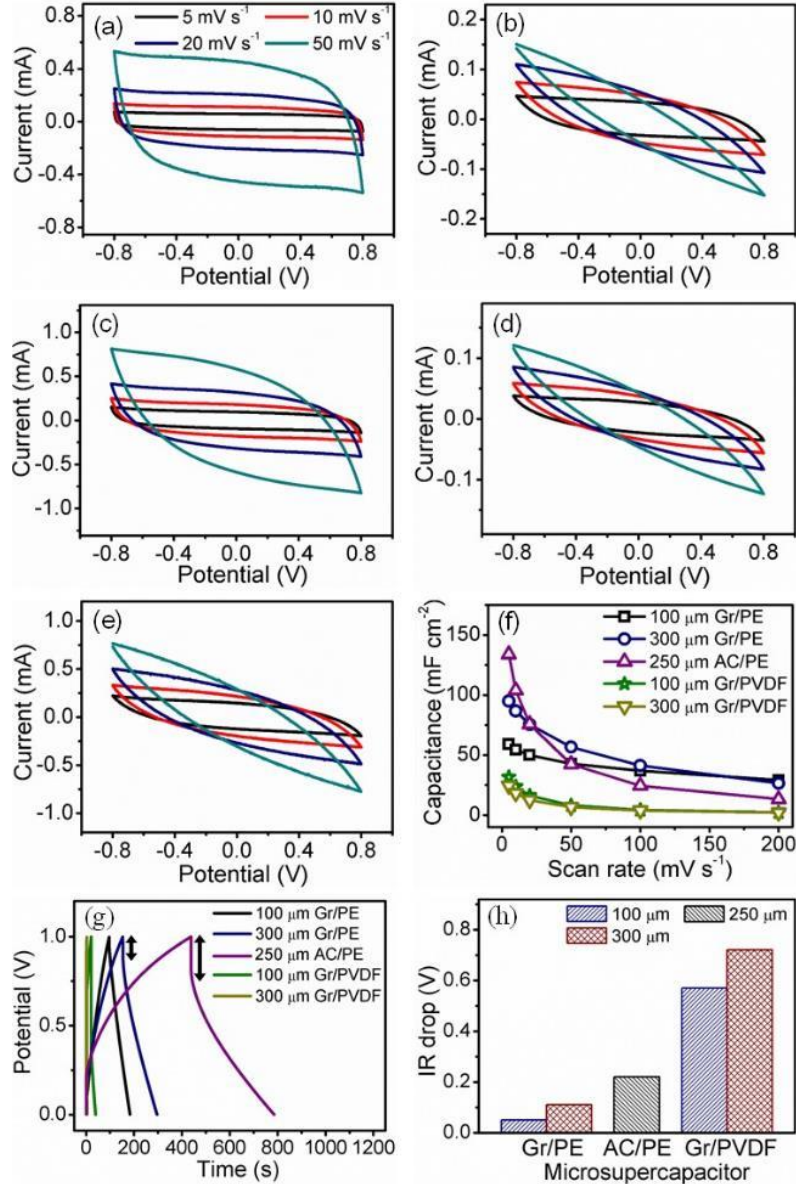
Fig. 5.5 Representative CV responses of (a) 100-µm-thick Gr/PE, (b) 100-µm-thick Gr/PVDF, (c) 300-µm-thick Gr/PE, (d) 300-µm-thick Gr/PVDF, and (e) 250-µm-thick AC/PE MSCs for a scan rate in the range of 5–50 mV s⁻¹, (f) areal capacitance of different MSCs obtained from the CV experiments, (g) representative GCD responses of 100- and 300-µm-thick Gr/PE, 250-µm-thick AC/PE, and 100- and 300-µm-thick Gr/PVDF MSCs for a current density of 0.5 mA cm⁻², and (h) IR drop of different MSCs determined from the GCD experiments.

In the process of preparing all-solid-state MSCs by coating the 3D interdigital microelectrodes with PE gel (PVA-H_3PO_4), the highly viscous PE diffused into the pores generated by the carbon particles to form a 3D ionic conductive network. The evaporation of excess water resulted in the gradual solidification of the PVA-H_3PO_4 gel. Carbon particles bounded by PVDF may produce sealed cavities (Fig. 5.6(a)), which inhibit PE diffusion and EDL formation (Fig. 5.6(c)). The PVDF surrounding the carbon particles limits the accessibility of electrolyte ions to the electrode surface by partially blocking the pores at the surface of carbon particles (Fig. 5.6(b)). In the case of carbon/PE MSCs, the incorporation of PE in the electrode material produces a 3D ionic conductive network and promotes EDL formation on particle surfaces (Figs. 5.6(d)–(f)). The PE gel applied after forming the 3D microelectrodes infiltrates through the sealed cavities, accessing the carbon surfaces in the cavities, because the binder material (solidified PVA-H_3PO_4 electrolyte) is effectively wetted and slowly re-dissolved by the PE gel. As a result, a greater fraction of carbon particle surface area in the carbon/PE electrodes is accessible for ion adsorption/desorption during electrochemical charge/discharge as opposed to carbon/PVDF electrodes, resulting in higher capacitance and energy density. Moreover, the PVDF binder may cause detouring of the ion transfer path, thus increasing the inner resistance of MSCs and retarding ion mobility in the micropores. In contrast, a shorter ion diffusion path is obtained with carbon/PE electrodes, which results in faster charge/discharge and improved power performance.
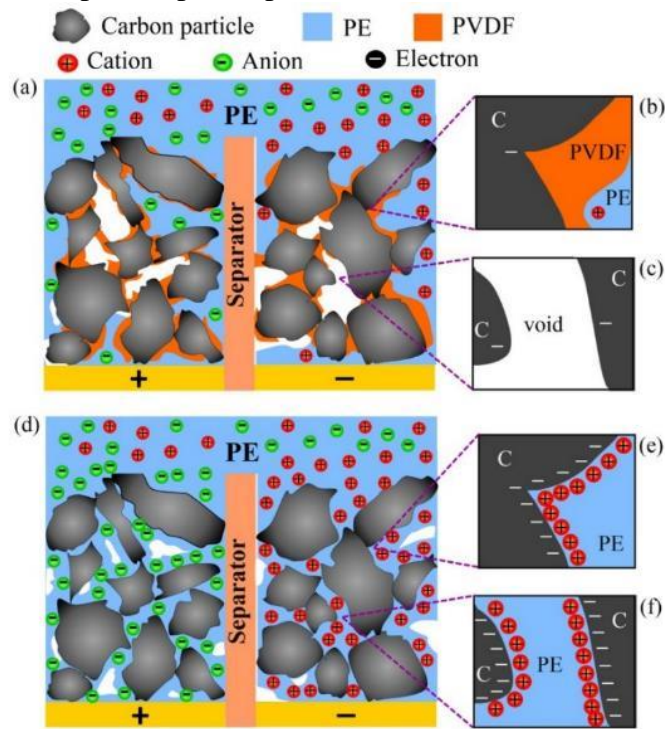
Fig. 5.6 Illustrative comparison of 3D all-solid-state MSCs with (a)–(c) carbon/PVDF electrodes and (d)–(f) carbon/PE (PE = PVA-H_3PO_4) electrodes showing that the incorporation of PE in the electrode material is conducive to EDL formation around the AC particles.

The MSC performance can be further evaluated in the context of Ragone plots, shown in Fig. 5.7(a) for a scan rate in the range of 5–1000 mV s^{-1}. The areal energy density E_A and power density P_A were obtained from the CV responses using the relations

$$E_A = \frac{1}{2}\, C_A \Delta V'^2 / 3{,}600 \tag{5.2}$$

$$P_A = \frac{1}{2}\frac{C_A \Delta V'^2}{t} \tag{5.3}$$

where $\Delta V'$ is the positive (or negative) potential scan window (= 0.8 V), which because of the symmetric scan potential, is equal to one-half of the whole potential window, and t (in seconds) is the discharge time. Remarkably, for a scan rate of 5 mV s^{-1}, the maximum areal energy density of the 250-µm-thick AC/PE MSC is 12×10^{-3} mWh cm^{-2}, which is more than 5 times higher than that of the 300-µm-thick Gr/PVDF MSC, whereas the maximum areal energy density of 100- and 300-µm-thick Gr/PE MSCs is 5.2×10^{-3} and 8.4×10^{-3} mWh cm^{-2}, respectively, and that of 100- and 300-µm-thick Gr/PVDF MSCs is 2.8×10^{-3} and 2.2×10^{-3} mWh cm^{-2}, respectively. For a scan rate of 1000 mV s^{-1}, the maximum areal power density of 100- and 300-µm-thick Gr/PVDF MSCs is 4.5 and 2.9 mW cm^{-2}, respectively, which is about 18 and 13 times higher than that of Gr/PVDF MSCs.

Table 5.1 shows a comparison of the performance of the Gr/PE and AC/PE all-solid-state MSCs developed in this study with different MSCs reported in the literature. All the MSCs listed in Table 1 possess in-plane electrode structures. The Gr/PE and AC/PE MSCs of this study demonstrate much higher areal capacitance and energy density than previous solid-state MSCs [3,11,14,15] and comparable areal capacitance and energy density with liquid-state MSCs [5–7,23]. The lower power density of the Gr/PE and AC/PE MSCs compared with previous solid-state and liquid-state MSCs (except MnO$_2$/onion-like carbon solid-state MSCs [14]) may be attributed to the longer ion diffusion path because of the SU-8 separator. The power density of the present MSCs may be increased by creating self-supporting composite electrodes and removing the SU-8 separator after the fabrication of the electrodes.

To investigate the lifetime of the 3D MSCs, cyclic CV tests were performed in the potential range of 0–0.8 V for a scan rate of 50 mV s^{-1}. As shown in Fig. 5.7(b), the capacitance of the 100-µm-thick Gr/PE MSC increased by ~70% after 10,000 charge/discharge cycles, possibly due to an electro-activation process in the graphene electrodes. It is believed that intercalation of electrolyte ions between the graphene nanosheets increased the spacing between sheets and, in turn, the graphene surface area accessed by electrolyte ions. A similar phenomenon has been reported by Cheng et al. [25], who detected a 60% increase in the specific capacitance of pristine graphene electrodes after long-term cycling. Different from the continuous increase of the specific capacitance during extended cycling observed previously [25], a ~20% drop in the capacitance of the 100-µm-thick Gr/PE MSC was observed after ~4,000 cycles, presumably because the intercalation of electrolyte ions was detrimental to the contact intimacy of the graphene microparticles. The former two competing mechanisms occur at the nano- and micro-scale, respectively, and are

considered to be responsible for the fluctuation of the specific capacitance of the Gr/PE MSC, which shows an overall increasing trend. The 250-μm-thick AC/PE MSC demonstrates a good cycling performance characterized by ~80% capacitance retention after 10,000 charge/discharge cycles (Fig. 5.7(b)). The lower and less fluctuating capacitance of this MSC is attributed to the absence of the electro-activation process encountered with Gr/PE electrodes. The origin of this important process is the increase of the spacing between multiple nanosheets in each graphene particle, resulting in the exposure of more electrode surface area to the electrolyte. However, this process cannot occur in AC/PE electrodes because both the structure and size of surface pores on the AC particles were fixed.

Table 5.1 Performance of MSCs developed in this work and in previous studies.

Electrode material	Electrode thickness (μm)	Electrolyte	Areal capacitance (mF cm^{-2})	Energy density (mWh cm^{-2})	Power density (mW cm^{-2})	Reference
Gr/PE[a]	100	PVA-H$_3$PO$_4$	59	0.0052	4.5	this work
	300	PVA-H$_3$PO$_4$	95	0.0084	2.9	this work
AC/PE[a]	250	PVA-H$_3$PO$_4$	134	0.012	1.3	this work
Reduced GO[a]	7.6	PVA-H$_2$SO$_4$	2.32	0.00032[c]	45.6[c]	[3]
Reduced GO[a]	0.006–0.1	PVA-H$_3$PO$_4$	0.081	0.000025[c]	4.95[c]	[11]
MnO$_2$/onion-like carbon[a]	~10	PVA-H$_3$PO$_4$	7.04	0.00062	0.09	[14]
Polyaniline nanowire[a]	10.1	PVA-H$_2$SO$_4$	45.2	0.00074[c]	8.0[c]	[15]
Polypyrrole[b]	~2.5	NaCl	27	—	—	[5]
Ni-decorated CNT forest[b]	~150	0.1 M KOH	18.8	—	—	[6]
AC[b]	50–70	1M NaNO$_3$	90.7	~0.013[d]	51.5	[7]
AC[b]	200	ionic liquid BMIM-BF$_4$	311	~0.05[e]	~10.0[e]	[23]

[a]Solid-state MSC.
[b]Liquid-state MSC.
[c]Estimated from Ragone plots and the electrode thickness found in the literature.
[d]Estimated from the areal capacitance and potential range found in the literature.
[e]Estimated from Ragone plots found in the literature.

Figs. 5.8(a) and (b) show Nyquist plots of the 3D all-solid-state MSCs examined in this study. For an EDLC, the low-frequency range of the Nyquist plot comprises a straight line.

The larger the slope of this line, the closer the behavior to that of an ideal capacitor. The semicircular response of the MSC in the high-frequency range is attributed to ion migration across the bulk electrolyte/electrode interface [26–28]. The Nyquist plot of the 100-µm-thick Gr/PE MSC shows a straight line with a slope of ~90° in the low-frequency range, but not a semicircle in the high-frequency range (Fig. 5.8(a)), which is indicative of a good capacitive performance and fast ion transport in the electrodes. However, other MSCs demonstrate notable semicircles in the high-frequency range (Figs. 5.8(a) and (b)), indicating relatively slow ion transport in the electrodes of these MSCs. The low-frequency responses of MSCs with thicker electrodes (i.e., 250 or 300 µm) are lines with slopes <90°, an indication of relatively poor capacitive performance.
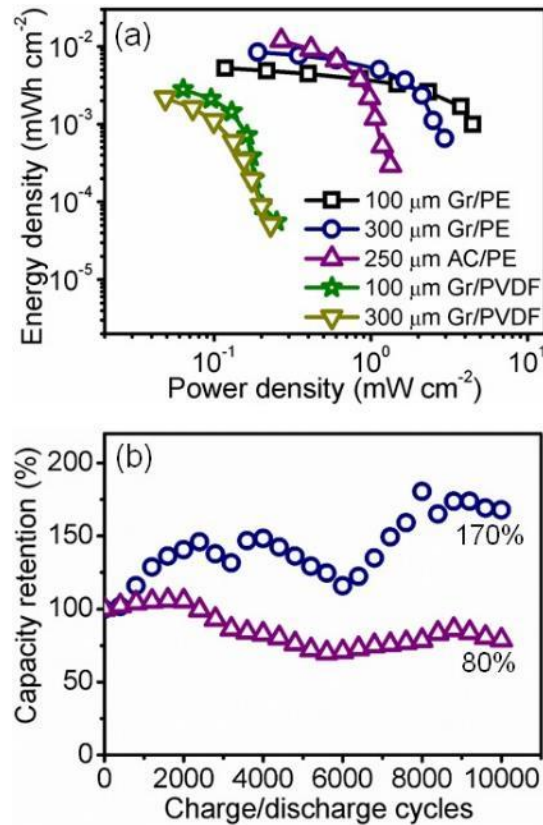
Fig. 5.7 (a) Ragone plots of 100- and 300-µm-thick Gr/PE, 250-µm-thick AC/PE, and 100- and 300-µm-thick Gr/PVDF MSCs for scan rate in the range of 5–1000 mV s^{-1} and (b) capacity retention cycling of 300-µm-thick Gr/PE and 250-µm-thick AC/PE MSCs versus charge/discharge cycles for a scan rate of 50 mV s^{-1}.

The impedance data were further analyzed by fitting with ZView software (AMETEK Solartron Analytical, Farnborough, Hampshire, UK) and using an equivalent circuit of the electrolyte and electrode bulk resistance R_s, the charge transfer resistance at the electrolyte-electrode interface R_{ct}, the Warburg impedance W, and the constant phase element *CPE* (Fig. 5.8(c)). The results of the ESR (obtained as the sum of R_s and R_{ct} [29]), shown in Fig. 5.8(c), indicate that Gr/PVDF MSCs exhibit much higher ESR than AC/PE and Gr/PE MSCs, with the latter microdevices showing the lowest ESR (~140 and ~330 Ω for 100-

and 300-µm-thick Gr/PE electrodes, respectively), consistent with the corresponding rate capability and IR drop results. The higher ESR of the AC/PE MSC compared to Gr/PE MSCs is mainly attributed to the poorer intrinsic electrical conductivity and smaller and more complex pore structure of the AC particles [23]. The extremely high ESR (>4,000 Ω) of Gr/PVDF MSCs may be associated with the smaller pores [30] and the decrease of the ion mobility due to coating the graphene particles with PVDF.
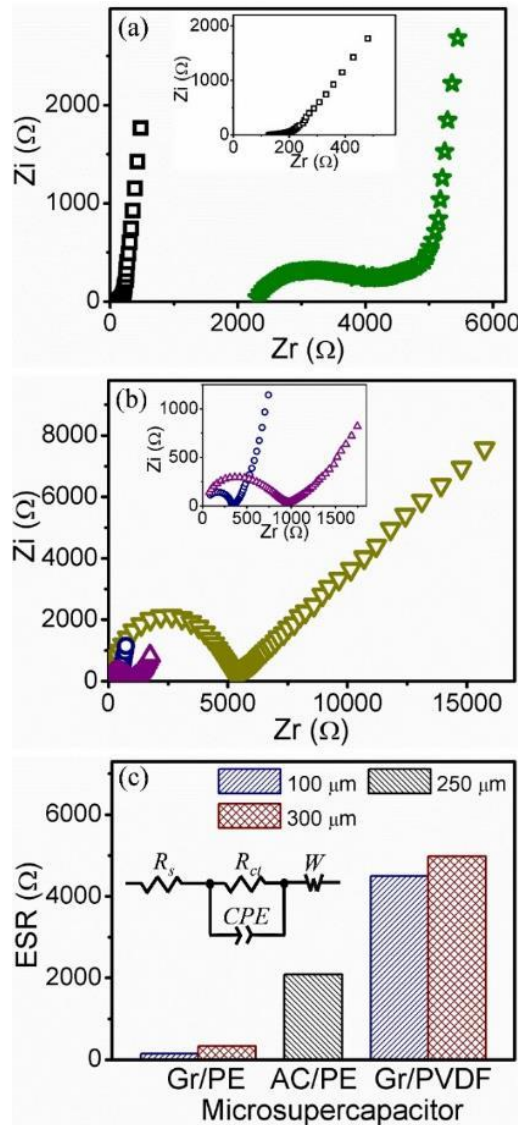
Fig. 5.8 Nyquist plots of (a) 100-µm-thick Gr/PE (–☐–) and Gr/PVDF (–✭–) MSCs, (b) 300-µm-thick Gr/PE (–○–), 250-µm-thick AC/PE (–△–), and 300-µm-thick Gr/PVDF (–▽–) MSCs, and (c) ESR of different MSCs obtained by fitting the impedance spectra. The insets in (a) and (b) show magnified Nyquist plots of a 100-µm-thick Gr/PE MSC and 300-µm-thick Gr/PE and 250-µm-thick AC/PE MSCs, respectively, whereas the inset in (c) shows the circuit model used to fit the impedance spectra.

The results of this study demonstrate that carbon particle/PE composites are promising electrode materials for all-solid-state MSCs, allowing a variety of applications to benefit from high-energy-density storage over a limited footprint area. Because of the highly porous electrode structure, the PE gel effectively diffused into the bulk of the thick electrodes to form a 3D ionic conductive network, hence enabling the use of a 3D microelectrode structure in solid-state MSCs. Most importantly, the PE incorporated in the electrode material played the dual role of binder and ion containing medium, which improved the accessibility of the electrode surface by electrolyte ions and shortened the ion diffusion path during electrochemical charge/discharge, thus enhancing both the energy density and power density of the microdevice. To further increase the energy density of the present MSCs, the graphene/PE electrodes can be electro-activated by extensive charge/discharge cycling.

5.4 Conclusions

All-solid-state 3D MSCs exhibiting superior electrochemical performance were fabricated by incorporating PE in the electrode material before forming the electrodes. The MSCs with PE in the electrode material demonstrated significantly better electrochemical performance (i.e., higher capacitance and better rate capability) than MSCs with PVDF in the electrode material, confirming the effectiveness of active material/PE electrodes to increase the surface area of active materials accessible by electrolyte ions and to shorten the ion diffusion path. The AC/PE MSCs showed higher areal capacitance, but poorer rate capability than Gr/PE MSCs. A threefold increase in electrode thickness of Gr/PE MSCs resulted in ~60% higher areal capacitance and energy density but ~36% lower areal power density. Electrolyte ion diffusion between the graphene nanosheets in the Gr/PE electrodes triggered an electro-activation process, which increased the specific capacitance by ~70% after 10,000 charge/discharge cycles. The AC/PE MSCs also showed good cyclic performance, exhibiting 80% capacitance retention after 10,000 charge/discharge cycles. The findings of this study demonstrate the high potential of 3D all-solid-state MSCs with PE incorporated in the electrode material for a wide range of power microsystem applications.

5.5 References

[1] Pech, D., Brunet, M., Durou, H., Huang, P., Mochalin, V., Gogotsi, Y., Taberna, P.L. and Simon, P., 2010. Ultrahigh-power micrometre-sized supercapacitors based on onion-like carbon. Nature nanotechnology, 5(9), pp.651-654.
[2] Chmiola, J., Largeot, C., Taberna, P.L., Simon, P. and Gogotsi, Y., 2010. Monolithic carbide-derived carbon films for micro-supercapacitors. Science,328(5977), pp.480-483.
[3] El-Kady, M.F. and Kaner, R.B., 2013. Scalable fabrication of high-power graphene micro-supercapacitors for flexible and on-chip energy storage.Nature communications, 4, p.1475.
[4] Zhang, Z., Xiao, F., Qian, L., Xiao, J., Wang, S. and Liu, Y., 2014. Facile Synthesis of 3D MnO2–Graphene and Carbon Nanotube–Graphene Composite Networks for High-Performance, Flexible, All-Solid-State Asymmetric Supercapacitors. Advanced Energy Materials, 4(10).

[5] Sun, W. and Chen, X., 2009. Preparation and characterization of polypyrrole films for three-dimensional micro supercapacitor. Journal of Power Sources,193(2), pp.924-929.

[6] Jiang, Y., Wang, P., Zang, X., Yang, Y., Kozinda, A. and Lin, L., 2013. Uniformly embedded metal oxide nanoparticles in vertically aligned carbon nanotube forests as pseudocapacitor electrodes for enhanced energy storage. Nano letters, 13(8), pp.3524-3530.

[7] Shen, C., Wang, X., Zhang, W. and Kang, F., 2011. A high-performance three-dimensional micro supercapacitor based on self-supporting composite materials. Journal of Power Sources, 196(23), pp.10465-10471.

[8] Shen, C., Wang, X., Li, S., Zhang, W. and Kang, F., 2013. A high-energy-density micro supercapacitor of asymmetric MnO 2–carbon configuration by using micro-fabrication technologies. Journal of Power Sources, 234, pp.302-309.

[9] Vincent, C.A., 1987. Polymer electrolytes. Progress in solid state chemistry,17(3), pp.145-261.

[10] Beidaghi, M., and Wang, C., 2012. Micro-Supercapacitors Based on Interdigital Electrodes of Reduced Graphene Oxide and Carbon Nanotube Composites with Ultrahigh Power Handling Performance. Adv. Funct. Mater., 22, pp. 4501.

[11] Wu, Z.S., Parvez, K., Feng, X. and Müllen, K., 2013. Graphene-based in-plane micro-supercapacitors with high power and energy densities. Nature communications, 4.

[12] Hong, S.Y., Yoon, J., Jin, S.W., Lim, Y., Lee, S.J., Zi, G. and Ha, J.S., 2014. High-Density, Stretchable, All-Solid-State Microsupercapacitor Arrays (vol 8, pg 8844, 2014). ACS NANO, 8(12), pp.12895-12895.

[13] Kim, D., Shin, G., Kang, Y.J., Kim, W. and Ha, J.S., 2013. Fabrication of a stretchable solid-state micro-supercapacitor array. ACS nano, 7(9), pp.7975-7982.

[14] Wang, Y., Shi, Y., Zhao, C.X., Wong, J.I., Sun, X.W. and Yang, H.Y., 2014. Printed all-solid flexible microsupercapacitors: towards the general route for high energy storage devices. Nanotechnology, 25(9), p.094010.

[15] Meng, C., Maeng, J., John, S.W. and Irazoqui, P.P., 2014. Ultrasmall Integrated 3D Micro-Supercapacitors Solve Energy Storage for Miniature Devices. Advanced Energy Materials, 4(7).

[16] Kaempgen, M., Chan, C.K., Ma, J., Cui, Y. and Gruner, G., 2009. Printable thin film supercapacitors using single-walled carbon nanotubes. Nano letters,9(5), pp.1872-1876.

[17] Pushparaj, V.L., Shaijumon, M.M., Kumar, A., Murugesan, S., Ci, L., Vajtai, R., Linhardt, R.J., Nalamasu, O. and Ajayan, P.M., 2007. Flexible energy storage devices based on nanocomposite paper. Proceedings of the National Academy of Sciences, 104(34), pp.13574-13577.

[18] Xiong, G., Meng, C., Reifenberger, R.G., Irazoqui, P.P. and Fisher, T.S., 2014. A review of graphene-based electrochemical microsupercapacitors.Electroanalysis, 26(1), pp.30-51.

[19] Abbas, Q., Pajak, D., Frąckowiak, E. and Béguin, F., 2014. Effect of binder on the performance of carbon/carbon symmetric capacitors in salt aqueous electrolyte. Electrochimica Acta, 140, pp.132-138.

[20] Gambou-Bosca, A. and Bélanger, D., 2014. Effect of the formulation of the electrode on the pore texture and electrochemical performance of the manganese dioxide-based

electrode for application in a hybrid electrochemical capacitor. Journal of Materials Chemistry A, 2(18), pp.6463-6473.

[21]Wang, Y., Shi, Z., Huang, Y., Ma, Y., Wang, C., Chen, M. and Chen, Y., 2009. Supercapacitor devices based on graphene materials. The Journal of Physical Chemistry C, 113(30), pp.13103-13107.

[22]Liu, C., Yu, Z., Neff, D., Zhamu, A. and Jang, B.Z., 2010. Graphene-based supercapacitor with an ultrahigh energy density. Nano letters, 10(12), pp.4863-4868.

[23]Li, S., Wang, X., Xing, H. and Shen, C., 2013. Micro supercapacitors based on a 3D structure with symmetric graphene or activated carbon electrodes.Journal of Micromechanics and Microengineering, 23(11), p.114013.

[24]Niu, Z., Du, J., Cao, X., Sun, Y., Zhou, W., Hng, H.H., Ma, J., Chen, X. and Xie, S., 2012. Electrophoretic Build-Up of Alternately Multilayered Films and Micropatterns Based on Graphene Sheets and Nanoparticles and their Applications in Flexible Supercapacitors. Small, 8(20), pp.3201-3208.

[25]Cheng, Q., Tang, J., Ma, J., Zhang, H., Shinya, N. and Qin, L.C., 2011. Graphene and carbon nanotube composite electrodes for supercapacitors with ultra-high energy density. Physical Chemistry Chemical Physics,13(39), pp.17615-17624.

[26]Andrieu X 2000 Energy Storage Systems for Electronics (Osaka T and Datta M (eds.), Amsterdam, The Netherlands: Gordon and Breach Science Publishers) 529

[27]Pell, W.G., Conway, B.E. and Marincic, N., 2000. Analysis of non-uniform charge/discharge and rate effects in porous carbon capacitors containing sub-optimal electrolyte concentrations. Journal of electroanalytical chemistry, 491(1), pp.9-21.

[28] Li, H.Q., Luo, J.Y., Zhou, X.F., Yu, C.Z. and Xia, Y.Y., 2007. An ordered mesoporous carbon with short pore length and its electrochemical performances in supercapacitor applications. Journal of the Electrochemical Society, 154(8), pp.A731-A736.

[29]Garcia, B.B., Feaver, A.M., Zhang, Q., Champion, R.D., Cao, G., Fister, T.T., Nagle, K.P. and Seidler, G.T., 2008. Effect of pore morphology on the electrochemical properties of electric double layer carbon cryogel supercapacitors. Journal of Applied Physics, 104(1), p.014305.

[30]Chen, W.C., Wen, T.C. and Teng, H., 2003. Polyaniline-deposited porous carbon electrode for supercapacitor. Electrochimica Acta, 48(6), pp.641-649.

Chapter 6 – Ultrahigh-power, flexible and foldable micro supercapacitors based on SWCNT networks

In this chapter, we demonstrate an ultrahigh-power, extremely flexible and foldable micro supercapacitor (MSC) with in-plane interdigital electrodes consisting of single-walled carbon nanotube (SWCNT) networks on ultrathin polyimide substrate. The fabricated all-solid-state MSCs can operate at very high scan rates (up to 1000 V s^{-1}) and have a stack capacitance of 18 F cm^{-3} and an energy density of 1.6 mWh cm^{-3}, which is comparable to that of lithium thin-film batteries. The ultrahigh power density (1125 W cm^{-3}) and extremely small time constant (1 ms) of the present MSCs are comparable to those of aluminum electrolytic capacitors. Furthermore, the microdevices demonstrate a superior electrochemical stability with 96% capacity retention even after 100,000 charge/discharge cycles. More importantly, the MSCs can be reversibly bent, folded, and rolled purely elastically without degradation in performance. The present MSCs demonstrate a high potential for integration in flexible and wearable electronic systems for high-rate energy storage and ac line filtering.

6.1 Introduction

Electric double-layer capacitors (EDLCs), also known as supercapacitors or ultracapacitors, rely on the rapid and reversible adsorption/desorption of ions at electrolyte/electrode interfaces for charge storage. This charge storage mechanism offers EDLCs several desirable properties, including long-cycle life (>10,000 cycles) and high power density. Typically, EDLCs deliver a power density about an order of magnitude higher than that of lithium-ion batteries and an energy density two orders of magnitude higher than that of electrolytic capacitors. Therefore, EDLCs represent the type of devices that can potentially replace traditional electrolytic capacitors to reduce the size of electronic circuits. However, the poor frequency response of commercial EDLCs presents a major obstacle for this application.

The rapid growth of miniaturized electronics has increased the demand for microscale energy storage units, such as microsupercapacitors (MSCs). MSCs with two-dimensional (2D) in-plane electrode structures allow facile integration to on-chip electronics. Because the ionic diffusion pathways in 2D in-plane electrodes are much shorter than those in conventional supercapacitors possessing sandwiched electrodes, the rate capability and power performance of the devices can be greatly improved [1–3]. These properties are particularly important if the MSCs need to be coupled with microbatteries, microfuel cells, and energy harvesters to provide maximum power, or if they have to replace electrolytic capacitors in applications like filtering voltage ripples in line-powered electronics (ac line filtering) [4,5]. Recently, a significant effort has been focused on the design and fabrication of highly conductive electrodes with optimized micro/nanostructures, such as onion-like carbon[6], carbide-derived carbon[7,8], carbon nanotube [6], carbide-derived carbon[7,8], carbon nanotube[9,10], graphene[11–13], graphene/carbon nanotube carpet[14], which enhance electron/ion transport and improve the power performance of MSCs. In general, the more porous the electroactive material the faster the electrolyte ion transport through

the electrode. However, increasing the porosity of active materials usually results in the decrease of the volumetric energy density. Therefore, the further improvement of the power density (>1000 W cm^{-3}) at ultrafast rate of <1 ms, while maintaining relatively high energy density (> 10 mWh cm^{-3}), is still challenging.

Single-walled carbon nanotube (SWCNT) networks provide significantly higher conductivity because the presence of few interparticle contacts yield a lower contact resistance than other carbonaceous materials[15] used as electrode materials of high-power MSCs. Additionally, carbon nanotube (CNT) networks show superior robustness under bending, abrasion, and stretching, while their functionality is not affected by mechanical stresses[16–20]. Also, networks in general offer a high fault tolerance because many different current pathways still exist even with a few disconnected or missing links in the network. Various methods have been successfully developed to fabricate CNT networks for energy storage applications, including vacuum filtration to form thick, free-standing membranes[21,22], mixing with binder material[23,24], and electrophoretic deposition[10]. However, these methods are either difficult or too expensive to scale up for widespread commercialization and are incompatible with conventional microfabrication methods of fabricating high-power, in-plane electrode structures.

Here, we report a facile and scalable method for fabricating in-plane interdigital electrodes consisting of SWCNT networks by combining a simple spray-deposition technique with a single-step lift-off process. The produced SWCNT network is ultrathin, extremely flexible, and fully accessible by electrolyte ions during charging and discharging. The high flexibility and surface mountability of the present SWCNT MSCs are largely due to the ultrathin (~1.3 µm thick) polyimide (PI) substrate. Because of the high electrical conductivity of the spray-coated SWCNT networks and the small gap (40 µm) between the in-plane interdigital electrodes, the resulting all-solid-state MSCs can operate at a high scan rate of 1000 V s^{-1}, demonstrating a stack capacitance of 18 F cm^{-3}, a maximum energy density of 1.6 mWh cm^{-3} (comparable to that of lithium thin-film batteries), and a maximum power density of 1125 W cm^{-3}. To the best of our knowledge, the power density achieved with these SWCNT MSCs is the highest among those currently reported for energy storage microdevices. Our microdevices also exhibit superior electrochemical stability (96% capacity after 100,000 charge/discharge cycles) and exceptional flexibility with insignificant performance degradation even after excessive bending, folding, or rolling.

6.2 Methods

6.2.1 Spray deposition of SWCNT electrodes

Purified SWCNTs (P3-SWNT, Carbon Solutions) with 1–3 at% carboxylic acid surface functional groups were used as electrode materials. The SWCNTs were dispersed in deionized (DI) water with a tip sonicator for 1–2 h to form a 0.5–1 mg/mL stable suspension. The suspension was then sprayed onto the wafer and placed onto a plate heated to 40–60 ºC to form ~140-nm-thick SWCNT films. The sprayed SWCNT films were used as MSC electrodes without further treatment.

6.2.2 Preparation of the gel electrolyte

The polymer electrolyte (PE) was prepared by mixing 10 mL of DI water with 10 mL of phosphoric acid (H_3PO_4) using magnetic stirring for 30 min and dissolving 10 g of polyvinyl alcohol (PVA) in 90 mL of DI water at 90 °C. The mixing was again assisted by magnetic stirring for 1 h. Then, the two solutions were intermixed by magnetic stirring for 1 h. The PVA:H_3PO_4 ratio in the PE was fixed at 1:1 wt/vol.

6.2.3 Fabrication of the flexible SWCNT MSCs

MSCs with SWCNT electrodes were first fabricated on a Si substrate using standard microfabrication techniques and, subsequently, peeled off to obtain free-standing flexible MSCs. The first step of the fabrication process was to spin-coat a PI layer onto a Si wafer (Fig. 6.1(a)). The PI solution (ZKPI-306II, POME Sci-tech, Beijing, China) was mixed with a PI thinner (POME Sci-tech, Beijing, China) to a weight ratio of 5:1 to form a diluted PI solution and left overnight to allow the bubbles in the diluted PI solution to escape. Then, the diluted PI solution was spin-coated onto a Si wafer in two steps (step 1: 800 rpm for 18 s; step 2: 6000 rpm for 60 s), soft baked in an oven at 80 °C for ~3 h for the solvent to evaporate, and cured in the oven at 250 °C for ~2 h. The thickness of deposited PI film was found to be equal to ~1.3 µm. A bilayer consisting of a ~10-nm-thick Cr underlayer and a ~130-nm-thick Au top layer was evaporated onto the wafer and patterned using a lift-off process to form the interdigital current collectors and contact pads of the MSCs (Fig. 6.1(b)). The lift-off process was performed in acetone by applying a very gentle sonication. The SWCNTs were then spray-deposited onto the interdigital electrode area and patterned to interdigital electrodes by a lift-off process (Fig. 6.1(c)). The interdigital pattern of the SWCNT layer was the same as that of the underlying Cr/Au bilayer. For the lift-off process of the Cr/Au bilayer or the SWCNT layer, two layers of a photoresist film were spin-coated onto the substrates. The first photoresist layer (AR-P 5480, 100:50 dilution, Microchemicals) was spin-coated at 700 rpm for 9 s and 2000 rpm for 40 s and then soft baked at 170 °C for 5 min. The second photoresist layer (AZ 601, Microchemicals) was spin-coated at 700 rpm for 9 s and 3000 rpm for 40 s and then soft baked at 100 °C for 2 min. Finally, the two layers of photoresist were exposed to UV light and developed.

The fabricated devices were carefully peeled-off from the Si substrate (Fig. 6.1(d)) using the methods schematically shown in Fig. 6.2. After that, the PVA-H_3PO_4 gel electrolyte was coated onto the interdigital electrodes and left at room temperature overnight for the excess water to evaporate (Fig. 6.1(e)). A 10–20-µm-thick layer of PDMS was used to encapsulate the microdevices (Fig. 6.1(f)). The PDMS resin and curing agent (10:1 weight ratio) were mixed for 5 min, degassed in a vacuum for ~30 min, carefully placed on the device surface, and finally cured at room temperature for ~24 h.

6.2.4 Characterization techniques

The microstructure of the sprayed SWCNTs was examined with an SEM (S-5500, Hitachi, Tokyo, Japan). For cross-sectional SEM imaging, the microdevices were sectioned perpendicular to the finger length direction and coated with a ~1-nm-thick Au-Pd layer to improve the surface conductance. To prepare samples for TEM imaging, the SWCNT powder was dispersed in DI water with a tip sonicator for ~2 h to form a 0.05 mg/mL stable

suspension. Lastly, a drop of the prepared suspension was applied on a standard Cu grid for imaging with the TEM (JEOL JEM2011, Peabody, MA, USA).
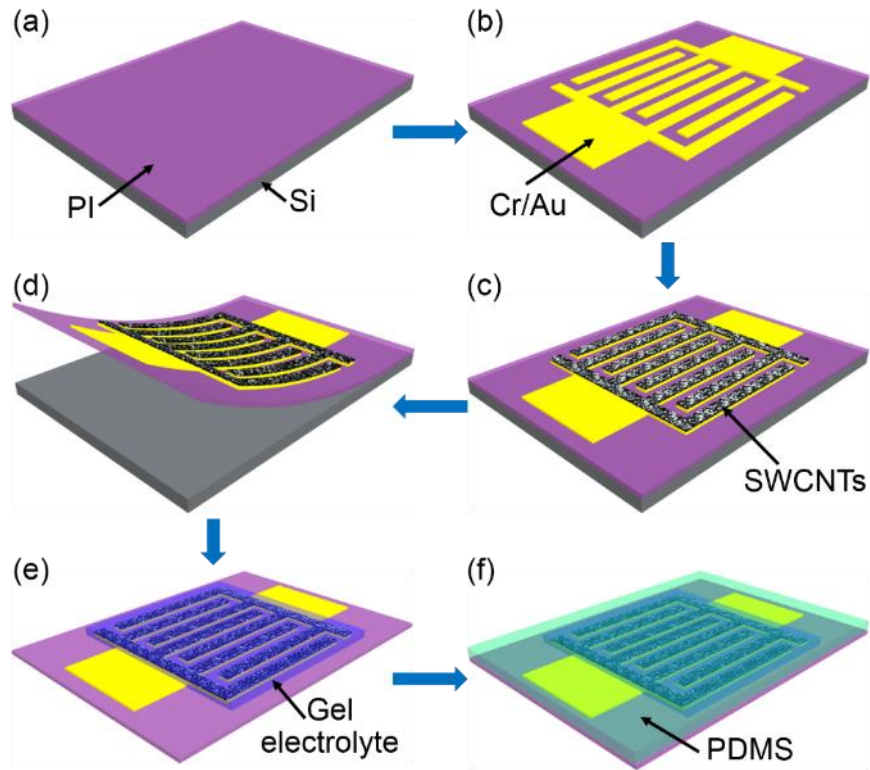
Fig. 6.1. Fabrication process of flexible SWCNT MSCs on an ultrathin PI substrate: (a) spin coating of a PI layer on a Si wafer, (b) evaporation and micropatterning of a Cr/Au bilayer, (c) spray deposition and micropatterning of interdigital SWCNT electrodes, (d) peel-off of the device from the Si wafer, (e) coating of the interdigital SWCNT electrodes with a gel electrolyte, and (f) encapsulation of the device with PDMS.
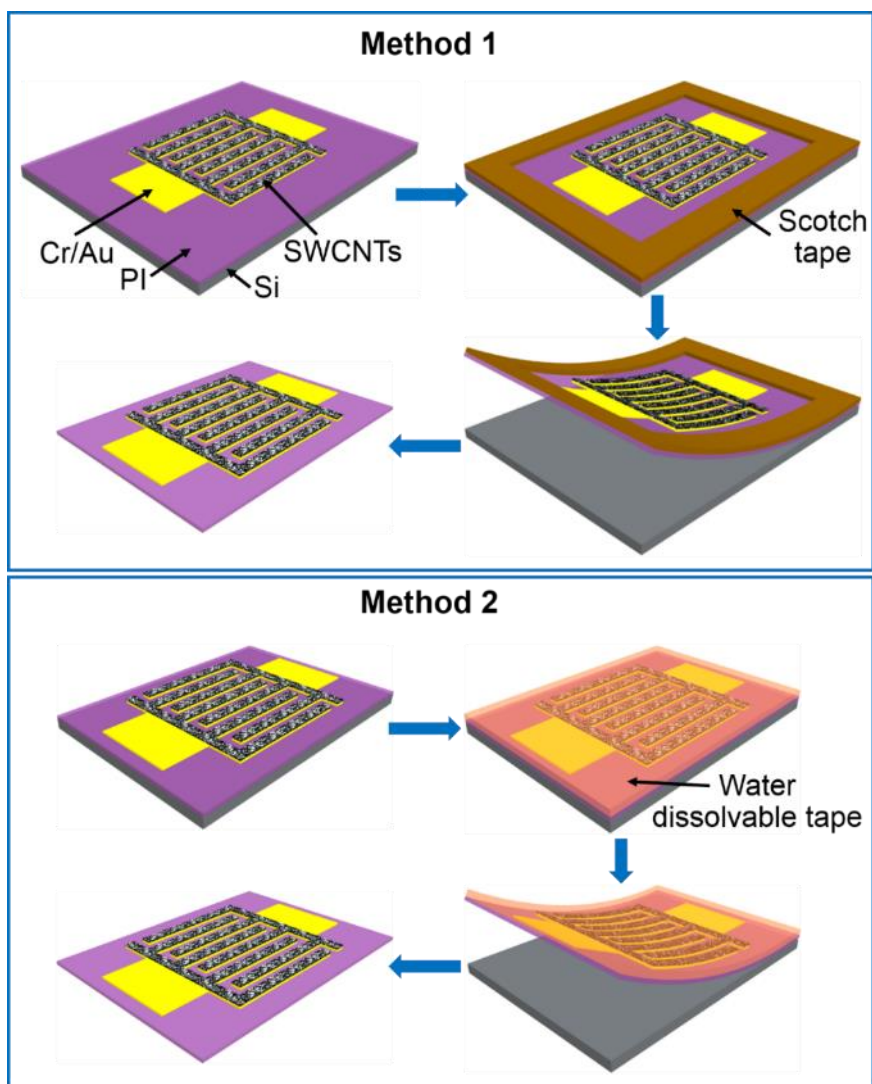
Fig. 6.2. Peel-off processes of the PI layer with the device from the Si substrate. Method 1: A scotch tape was applied onto the PI surface around the device area and removed after peeling off from the Si substrate. Method 2: A 3M water dissolvable tape was applied onto the device surface and then dissolved in DI water after peeling off from the Si substrate.

6.2.5 Electrochemical testing

The electrochemical performance of the SWCNT MSCs was evaluated with a two-electrode system and PVA-H_3PO_4 gel electrolyte. CV and GCD experiments were performed with a CHI 860D electrochemical workstation. In the CV tests, the scan rate and the voltage were varied in the range of 0.5–1000 V s^{-1} and 0–0.8 V, respectively. In the GCD experiments, the microdevices were charged and discharged using a charging/discharging current of 10 nA cm^{-2} and a voltage in the range of 0–0.8 V.

The stack capacitance C_s was determined from the CV response for scan rates in the range of 0.5–1000 V s^{-1} using the relation

$$C_s = \frac{1}{\mathcal{V}\,\Delta V}\int I(t)\,\mathrm{d}t \tag{6.1}$$

where ΔV is the potential range (= 0.8 V), $\mathcal{V}$ is the total electrode volume, which includes the volume of both the electrodes and the space between them, $I(t)$ is the current measured during CV testing, and t is the time.

To determine the capacitance of the SWCNT layer, the capacitance of the Au current collector was subtracted from the total capacitance of the Au+SWCNT layers. In this paper, the MSC capacitance refers to that contributed only by the SWCNT electrodes.

The volumetric energy density E_V and power density P_V were calculated from the CV responses for a scan rate in the range of 0.5–1000 V s^{-1} using the relations

$$E_V = \frac{1}{2}\,C_s\Delta V^2/3{,}600 \tag{6.2}$$

$$P_V = \frac{1}{2}\frac{C_s\Delta V^2}{t_d} \tag{6.3}$$

where t_d (in seconds) is the discharge time; the energy and power densities refer to those contributed by the SWCNT electrodes.

EIS tests were performed by applying a 10 mV ac signal in the frequency range of 1–10^6 Hz using a Solartron 1260 impedance/gain-phase analyzer (AMETEK Advanced Measurement Technology, Farnborough, Hampshire, UK). The real and imaginary parts of the impedance Z' and Z'', respectively, were recorded in the whole frequency range and plotted as a Nyquist plot. The real and imaginary parts of the capacitance C' and C'', respectively, were obtained by

$$C' = \frac{1}{2}\frac{-Z''}{\pi f|Z|^2} \tag{6.4}$$

$$C'' = \frac{1}{2}\frac{Z'}{\pi f|Z|^2} \tag{6.5}$$

To investigate the electrochemical stability of the devices, cyclic CV tests were performed in the potential range of 0–0.8 V at a scan rate of 50 V s^{-1}. A total of 100,000 charge/discharge cycles were applied to the MSCs. To evaluate the electrochemical stability of the microdevices during bending, folding, and rolling, CV curves were recorded in the potential range of 0–0.8 V at a scan rate of 10 V s^{-1}.

6.25 FEA simulations

A three-dimensional finite element analysis (FEA) was used to study the microdevice deformation under various loading conditions, including wrapping around rods of varying radius, folding, and rolling. The FEA was performed with the multi-physics code

ABAQUS. In each FEA model, the elastomers (i.e., PDMS) and multilayer circuit (i.e., Au/PI) were modeled with eight-node hexahedral brick solid elements (C3D8R) and quadrilateral shell elements (S4R), respectively. The CNTs and Cr coatings were not modeled because of their negligible effect to the microdevice mechanics. Because of the good adhesion of the device materials, a perfect interfacial bonding was assumed in all the FEA simulations. Refined meshes were used to ensure accurate strain mapping. The Mooney-Rivlin model was used to simulate the behavior of the PDMS with 1.1 MPa effective elastic modulus[11] and 0.49 Poisson' ratio. The PI layer was modeled as a linear elastic material with 2.5 GPa elastic modulus and 0.34 Poisson's ratio. The Au layer was modeled as an elastic-perfectly plastic material with 78 GPa elastic modulus, 0.44 Poisson's ratio, and 234 MPa yield strength.

6.2.6 An analytical model predicting the dependence of ε_b on the bending radius

Fig. 6.3 shows a simplified cross-sectional geometry of the MSC. The bottom layer (layer 1) consists of PI ($E_{PI} = 2.5$ GPa, $v_{PI} = 0.34$, $w_{PI} = w = 5720$ μm, $t_1 = t_{PI} = 1.3$ μm). There are $n = 14$ interdigital fingers made of Au ($E_{Au} = 78$ GPa, $v_{Au} = 0.44$) with a rectangular cross-section ($w_{Au} = 300$ μm, $t_2 = t_{Au} = 130$ nm) deposited on top of the PI. The encapsulation layer consisting of PDMS ($E_{PDMS} = 1.1$ MPa, $v_{PDMS} = 0.49$, $t_3 = t_{PDMS} = 10$ μm) spontaneously fills the gaps between the fingers. The effective modulus of the first (PI), second (Au), and third (PDMS) layer is

$$E_1 = E_{PI} \qquad (6.6)$$

$$E_2 = \frac{nW_{Au}}{W} \cdot E_{Au} + \frac{W - nW_{Au}}{W} \cdot E_{PDMS} \qquad (6.7)$$

$$E_3 = E_{PDMS} \qquad (6.8)$$

The distance y_0 between the neutral axis and the bottom PI surface of the MSC is given by

$$y_0 = \frac{\sum_{i=1}^{3}\left[E_i t_i\left(-\frac{t_i}{2} + \sum_{j=1}^{i} t_j\right)\right]}{\sum_{i=1}^{3} E_i t_i} \qquad (6.9)$$

Substitution of the dimensions and material properties in Eq. (6.9) yields $y_0 = 1.155$ μm. The neutral axis is denoted by the dash-dot line in Fig. 6.3. The maximum bending strain ε_b in the metal is given by

$$\varepsilon_b = (t_1 + t_2 - y_0)/R \qquad (6.10)$$

where R is the bending radius.

When the MSC is wrapped around rods of radius R_0, $R = R_0 + y_0$. When the MSC is rolled, the shape of the deformed MSC can be modeled by an Archimedes spiral of the form

$$r(\theta) = R_0 + t\left(\frac{\theta}{2\pi}\right) \tag{6.11}$$

where $t = \sum_{i=1}^{3} t_i$ is the total thickness of the MSC and $r(\theta)$ is the radius at an angle θ.

The spiral length L can be calculated by integrating $r(\theta)$ from 0 to a given rotation angle Θ as

$$L = \int_0^{\Theta} r(\theta)d\theta = R_0\Theta + \frac{t}{4\pi}\Theta^2 \tag{6.12}$$

Because ε_b corresponds to the smallest bending radius in the MSC, the smallest bending radius for $L = 8400$ μm and 2.5 rounds ($\Theta = 5\pi$) is $R = R_0 = [L - (t/4\pi)\Theta^2]/\Theta \approx 520.5$ μm. Substitution of $R = 520.5$ μm into Eq. (6.10) gives $\varepsilon_b = 5.29 \times 10^{-4}$.
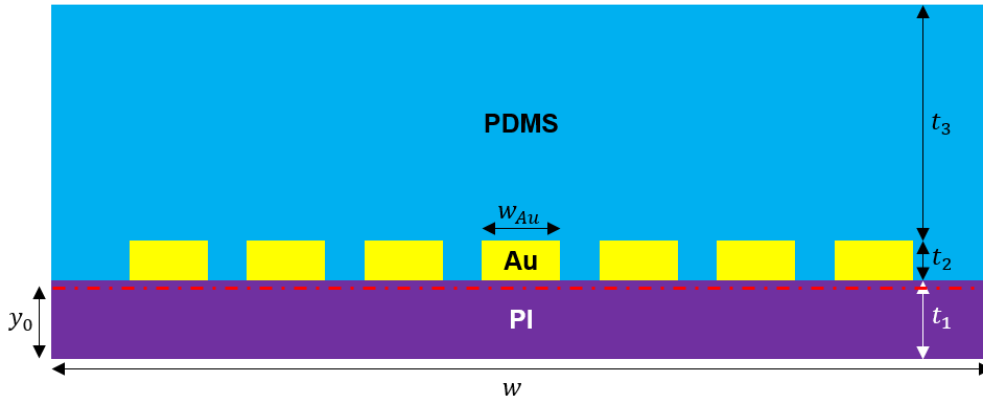
Fig. 6.3. Simplified cross sectional geometry of a SWCNT MSC.

6.3 Results and Discussion

The SWCNT MSCs were fabricated on ultrathin PI substrates in order to be extremely flexible and easily mountable on various surfaces, thus enabling enormous applications in flexible and wearable electronics. A schematic illustration of the flexible SWCNT MSC on an ultrathin PI substrate and its layered structure are shown in Figs. 6.4(a)and (b), respectively. Conventional lithography and mechanical peel-off techniques were combined to fabricate all-solid-state MSCs with in-plane interdigital SWCNT electrodes on free-standing ultrathin PI substrates. Briefly, a ~1.3-µm-thick PI layer was spin coated on a Si substrate and cross-linked at ~250 °C in oven to form a stable membrane (Fig. 6.1(a)). Subsequently, ~140-nm-thick Cr/Au current pathways were lithographically defined on the PI layer (Fig. 6.1(b)), and a ~140-nm-thick SWCNT layer was spray-deposited and lithographically patterned into the interdigital electrodes using a lift-off process (Fig. 6.1(c)). Spray deposition is a facile and effective method for depositing active materials exhibiting high surface area-to-volume ratio, which can function as the active electrodes of electrochemical capacitors. To obtain flexible and surface-mountable ultrathin MSCs, the PI membrane with the microdevice on top of it was carefully peeled off from the Si substrate (Fig. 6.1(d)) (the two peel-off processes used in this work are schematically shown in Fig. 6.2) and the electrodes were coated with polyvinyl alcohol-phosphoric acid

(PVA-H$_3$PO$_4$) gel electrolyte (Fig. 6.1(e)). Finally, for long-term stability in ambient environment, the fabricated microdevice was encapsulated by a 10- to 20-µm-thick PDMS layer (Fig. 6.1(f)). Further fabrication details are given in the section 6.2.3.
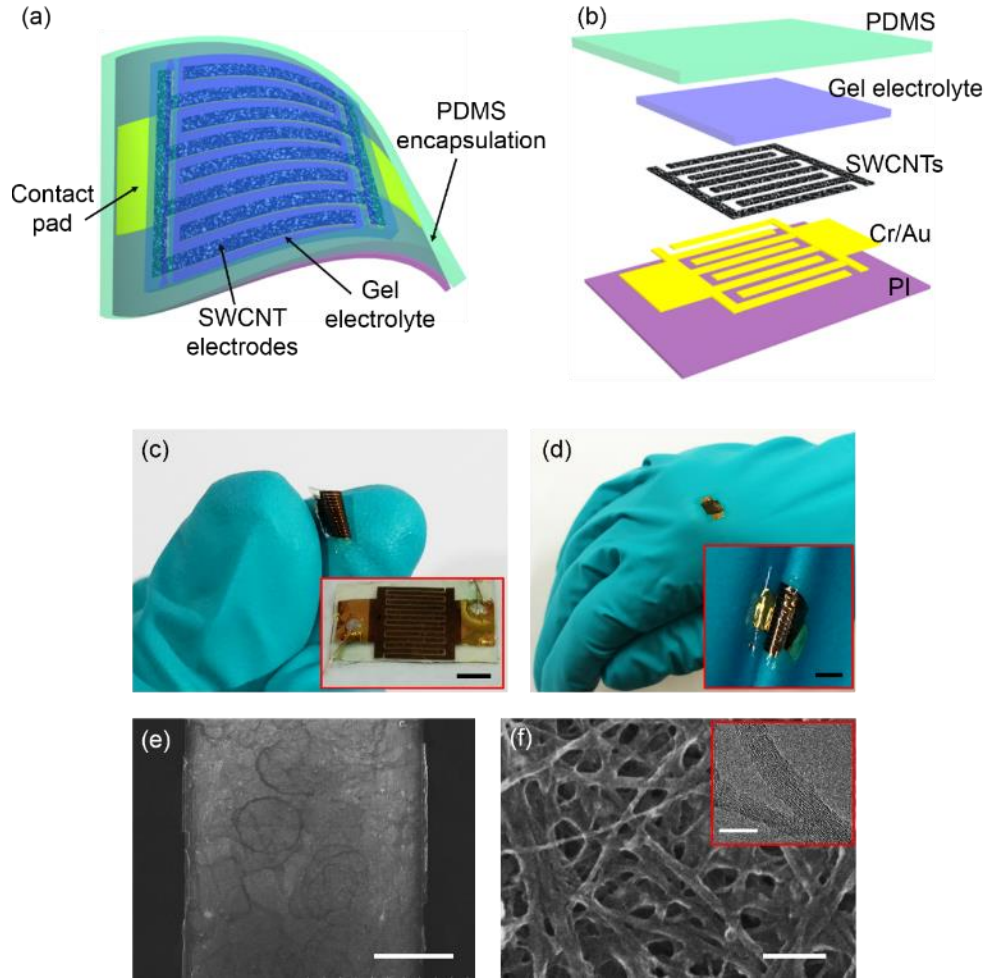
Fig. 6.4. Flexible, surface mountable MSCs and SWCNT electrode microstructure: (a) schematic of flexible SWCNT MSC on an ultrathin PI substrate; (b) exploded view of the MSC layered structure; (c) digital photograph of a SWCNT MSC bent between two fingers (the inset shows the undeformed SWCNT MSC; scale bar = 2 mm); (d) digital photograph of a SWCNT MSC mounted on a latex glove (the inset shows that the MSC has been conformably mounted onto the raggedy glove surface; scale bar = 2 mm); (e) top-view SEM image of the SWCNT electrode; and (f) high-magnification SEM image of the spray-deposited SWCNT network (the inset shows a TEM image of the SWCNTs). The scale bar in (e), (f), and the inset of (f) represents 100 µm, 100 nm, and 20 nm, respectively.

Figs. 6.4(c) and (d) show the fabricated microdevice bent between two fingers and mounted on a latex glove, respectively. The inset of Fig. 6.4(c) shows the undeformed microdevice, whereas the inset of Fig. 6.4(d) illustrates the conformal attachment of the microdevice onto the rugged glove surface. Optical microscope images obtained before peeling-off the

microdevice from the PI/Si substrate showed that the width of the interdigital fingers is 300 µm, while the gap between the fingers is 40 µm (Fig. 6.5). Figs. 6.4(e) and (f) show low- and high-magnification scanning electron microscope (SEM) images of SWCNT electrodes, respectively. The ring-like patterns on the SWCNT electrodes (Fig. 6.4(e)) occurred during the drying of the sprayed tiny droplets of SWCNT aqueous solution. The spray-deposition process produced a random network of entangled SWCNTs (Fig. 6.4(f)). The high current carrying capacity and mechanical strength of the SWCNT networks are critical factors for the robustness and flexibility of the microdevices. The transmission electron microscope (TEM) image shown in the inset of Fig. 6.4(f) reveals that the diameter of the SWCNTs is in the range of 10–30 nm. A comparison of the cross-sectional SEM images of Cr/Au+SWCNTs and Cr/Au layers on a PI layer (Figs. 6.6(a) and (b), respectively) indicates that the thickness of the SWCNT layer deposited onto the Cr/Au bilayer is equal to ~140 nm.
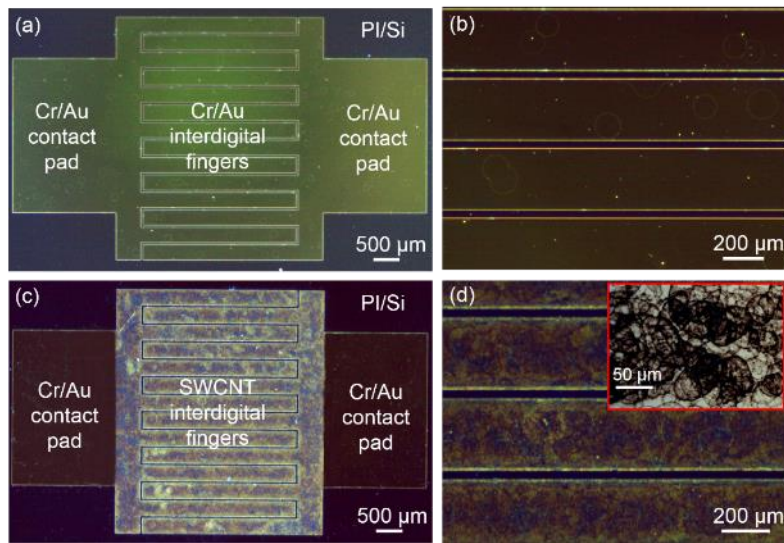
Fig. 6.5. Optical microscope images of (a) patterned Cr/Au on a PI-coated Si substrate, (b) interdigital Cr/Au fingers, (c) patterned SWCNTs on top of Cr/Au layers, and (d) SWCNT interdigital fingers. The inset of (d) shows a close-up view of the SWCNT electrode.
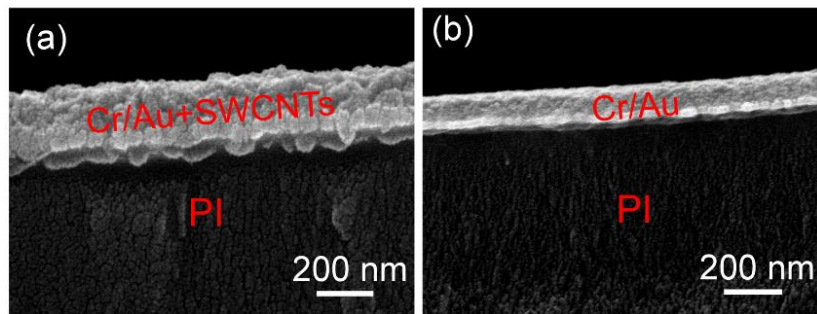
Fig. 6.6. Cross-sectional SEM images of (a) Cr/Au+SWCNTs and (b) Cr/Au layers on a PI layer.

Raman and Fourier transform infrared (FTIR) spectroscopy were used to examine the molecular structure and chemical structure of the SWCNTs, respectively. The very low D-to-G band ratio ($I_D/I_G = 0.078$) calculated from the Raman spectrum (Fig.6.7(a)) indicates that the SWCNTs are of high purity and contain a very small amount of defects[25,26]. The carboxylate –OH stretch peak centered at 3448 cm^{-1} of the FTIR spectrum (Fig.6.7(b)) confirms surface functionalization of the SWCNTs by carboxylic acid groups[27].
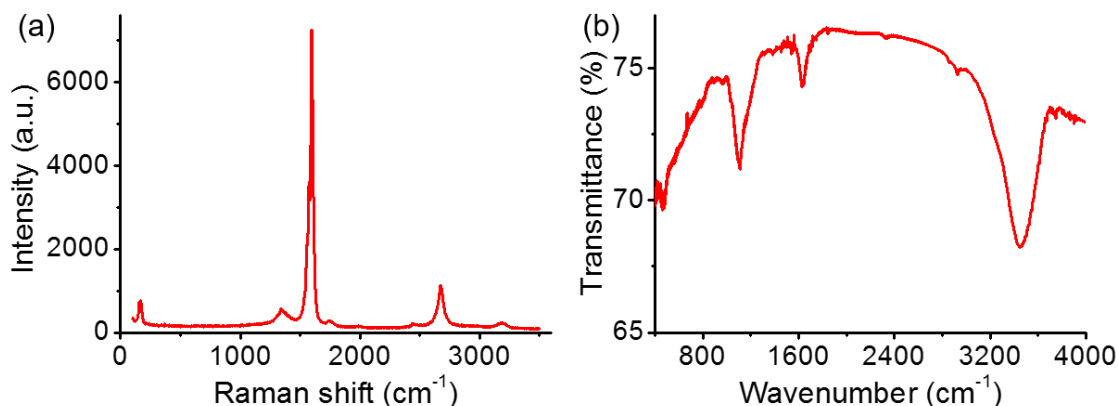
Fig. 6.7. (a) Raman and (b) FTIR spectra of SWCNTs. For the Raman spectrum shown in (a), I_D/I_G = 0.078. The peaks at 1112, 1635, and 3448 cm^{-1} in the FTIR spectrum shown in (b) correspond to –CH bending, CNT back bone, and carboxylate –OH stretching, respectively.

To evaluate the electrochemical performance of the SWCNT MSCs in terms of the capacitance and power capability, we acquired cyclic voltammograms (CV) in the scan rate range of 0.5–1000 V s^{-1}. For a scan rate between 1 and 200 V s^{-1}, we observed CV curves of 'rectangular' shape (Figs. 6.8(a–d)), suggesting the formation of an efficient EDLC and a fast electrode charging process. For extremely high scan rates (e.g., 1000 V s^{-1}), the shape of the CV curve became quasi-rectangular (Fig. 6.8(e)). We also observed a linear discharge current response up to a scan rate of 200 V s^{-1} (Fig. 6.8(f)), which is indicative of a high rate capability. The SWCNT MSCs of this study outperform most of the reported MSCs in terms of perfect electric double layer formation and high power capacity (rate capability)[28-32]. In general, the smaller the gap between interdigital electrodes, the higher the power capability of the microdevices because of the significant decrease of the mean ion diffusion path between the electrodes. The smallest gap between the interdigital electrodes is usually limited by the fabrication capability. Here, we were able to produce a very small gap (40 µm) between spray-deposited SWCNT electrodes with a high yield using bilayer lift-off photoresists (Fig. 6.9).
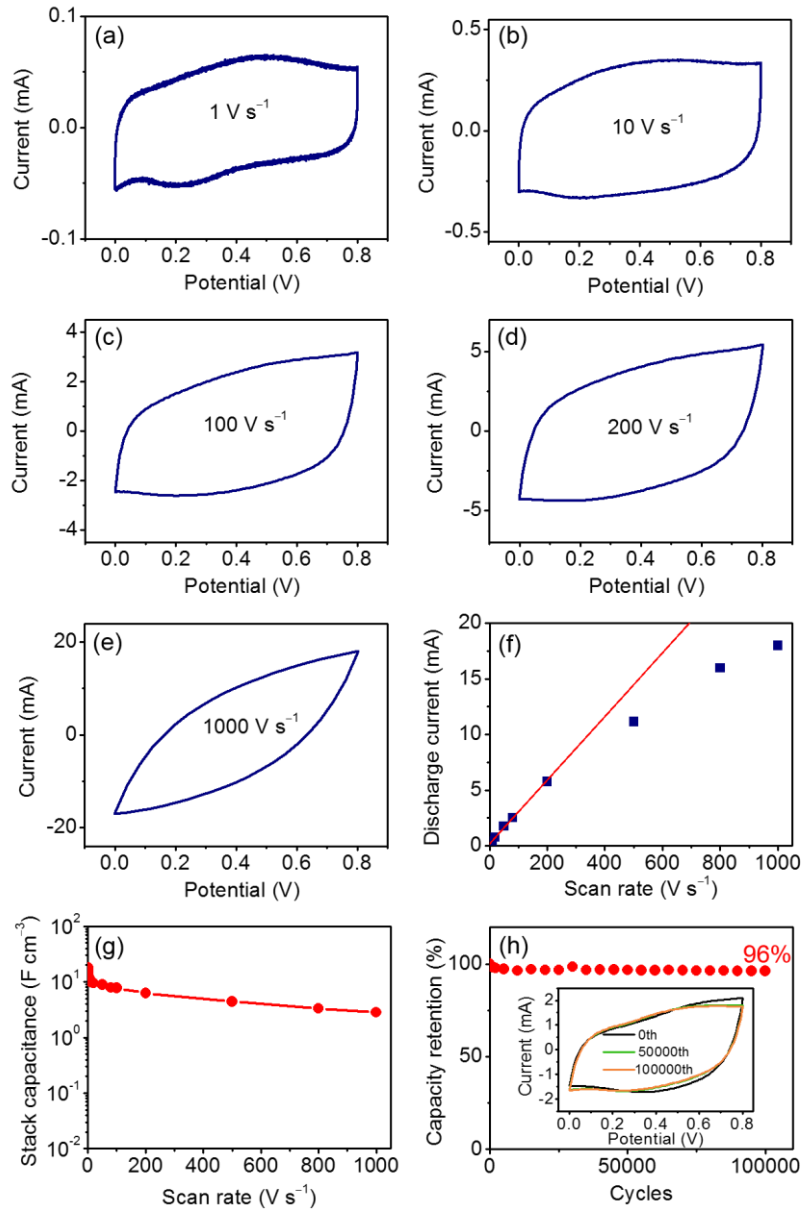
Fig. 6.8. Electrochemical performance of SWCNT MSCs: (a)–(e) representative CV curves of a SWCNT MSC for a scan rate of 1, 10, 100, 200, and 1000 V s-1, respectively, (f) discharge current vs scan rate, (g) stack capacitance C_V vs scan rate, and (h) capacity retention vs electrochemical charge/discharge cycles for a scan rate of 50 V s-1 (the inset shows CV curves obtained after 0, 50000, and 100000 cycles).

For a low scan rate of 0.5 V s^{-1}, the stack capacitance of the microdevice is equal to 18.1 F cm^{-3}, decreasing to 10 F cm^{-3} upon increasing the scan rate to 10 V s^{-1} (Fig. 6.8(g)), implying a 55% capacitance retention. A further increase of the scan rate to 100 V s^{-1} decreases the stack capacitance to 7.7 F cm^{-3}, which represents 43% and 77% of the stack capacitance at a scan rate of 0.5 and 10 V s^{-1}, respectively. The all-solid-state microdevice exhibits a very high stack capacitance of 2.8 F cm^{-3} even for a very high scan rate of 1000

V s^{-1}. The capacitance of bare Au electrodes is less than that of SWCNT electrodes by more than an order of magnitude (Fig. 6.10(e)). Thus, it may be interpreted that the capacitance of the microdevice is mainly due to ion intercalation in the microstructure of the SWCNT network. In this work, the capacitance of the MSCs is due to the capacitance of the SWCNT electrodes. The electrochemical properties of the SWCNT MSCs can be further elucidated by comparing their performance with those of other reported MSCs. The specific capacitance of our SWCNT MSCs is comparable to those of most reported EDLC MSCs (0.2–20 F/cm^{-3})[6,12,28-32]. Some other reported MSCs, such as reduced graphene oxide MSCs[13] and polyaniline nanowire MSCs[33], show higher specific capacitance but poorer rate capability and frequency response.
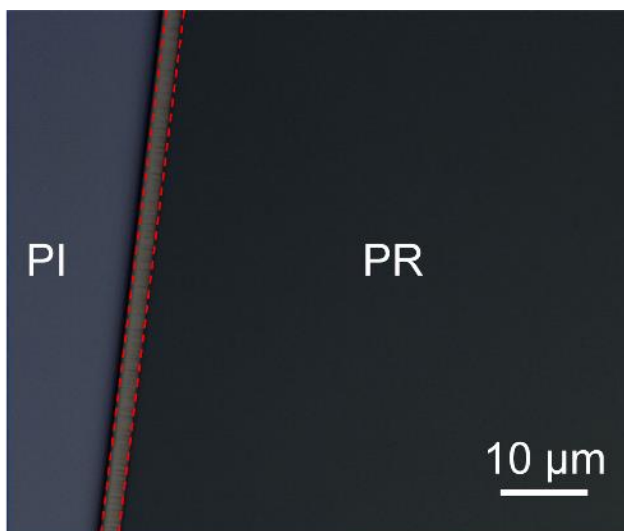
Fig. 6.9. Double edges (indicated by two red dashed lines) of the bilayer lift-off photoresist (PR) after UV exposure and development, indicating the formation of an undercut surface for assisting the lift-off process.

The galvanostatic charge/discharge (GCD) response of the SWCNT MSC for a current density of 10 nA cm^{-2} is fairly symmetric, approximately triangular, and does not demonstrate an obvious IR drop, i.e., a sudden voltage decrease at the onset of GCD discharging (Fig. 6.11). This is illustrative of the high Coulombic efficiency, fast charging across the electrodes, and low equivalent series resistance (ESR) of these devices, in agreement with the CV results presented above. We observed reproducible and stable capacitive behavior up to 100,000 electrochemical charge/discharge cycles for MSCs with SWCNT electrodes and PVA-H$_3$PO$_4$ solid-state electrolyte (Fig. 6.8(h)). The microdevices maintained 96% of their initial capacitance even after 100,000 cycles. This unprecedented electrochemical stability obtained with our all-solid-state SWCNT MSCs shows great potential for long-term, high-cycle applications, such as energy storage for energy harvesting systems.

Electrochemical impedance spectroscopy (EIS) further confirmed the superior power performance of the present microdevices. We observed a nearly vertical-line response in the low-frequency region of the Nyquist plot of SWCNT MSCs (Fig. 6.12(a)), reflecting a

nearly ideal capacitive performance. The absence of a semicircle-like response in the high-frequency region (see inset of Fig. 6.12(a)) also confirms the ultrahigh ionic conductivity at the electrode/electrolyte interface [34], which is consistent with the observed high rate capability and high power performance. The microdevice exhibits a pure capacitive behavior even at a high frequency of 3171 Hz (see inset of Fig. 6.12(a)), which is attributed to the highly accessible surface of the SWCNT network. The ESR (estimated from the *x*-intercept in the Nyquist plot) of the microdevice is ~7.5 Ω. This extremely low ESR is attributed to the highly conductive network deposited onto the Cr/Au current collector that produced a low internal and interfacial resistance, and the interconnected micropores of the SWCNT network, which are fully accessible for ion adsorption/desorption.

For a more informative analysis of the EIS results, we examined the dependence of the real and imaginary parts (C' and C'', respectively) of the stack capacitance on the frequency (Fig. 6.12(b)). The fast frequency response of the SWCNT MSCs is further confirmed by the very small relaxation time constant $\tau_0 =$ of 1 ms (Fig. 6.12(b)), which represents the minimum time for fully discharging the device with an efficiency greater than 50% [6,35] and can be determined from the peak frequency f_0 of C'' using the relation $\tau_0 = 1/f_0$. The relaxation time of SWCNT MSCs is significantly smaller than that of conventional EDLC MSCs ($\tau_0 \approx 10$ s) and most of previously reported high-rate MSCs ($\tau_0 =$ 3–30 ms)[6,30,32,36-38], and comparable to that of an aluminum electrolytic capacitor ($\tau_0 \approx 1$ ms). Electrochemically reduced graphene oxide MSCs[4] and graphene/carbon nanotube carpets MSCs[14] have similar τ_0 but lower specific capacitance compared with the SWCNT MSCs of this work. (For a more detailed comparison of different high-power MSCs the reader is referred to Table 6.1). The impedance phase angle versus frequency of SWCNT MSC and commercial activated carbon supercapacitors (AC-SC)[37] and aluminum electrolytic capacitors (AEC)[37] are compared in Fig. 6.12(c). The phase angle of the SWCNT MSCs reaches –45° at 1266 Hz compared with ~1000 Hz of AEC and ~0.15 Hz of AC-SC, which also indicates the extremely small relaxation time constant of the SWCNT MSCs.

The excellent performance of the SWCNT MSCs is also illustrated by the Ragone plots shown in Fig. 6.12(d). The energy and power density of different commercial energy storage devices designed for power microelectronic applications, i.e., 4 V/500 µAh Li thin-film battery[31], 3 V/300 µF AEC[31], 2.75 V/40 mF AC-SC[31], laser-scribed graphene (LSG) MSC[37], onion-like carbon (OLC) MSC[6], and activated mesophase pitch (aMP) MSC[36], are also shown for comparison. Remarkably, the SWCNT MSC shows a maximum energy density of 1.6 mWh cm^{-3}, which is more than three orders of magnitude higher than that of AEC, two times higher than that of LSG MSC and AC-SC, and comparable to those of Li thin-film battery and OLC MSC. The maximum power density of 1125 W cm^{-3} of the SWCNT MSC is significantly higher than that reported for high-power performance MSCs, namely ~4 times higher compared with OLC MSC and an order of magnitude higher compared with LSG and aMP MSCs and comparable with that of AEC (10^1–10^3 W cm^{-3})[31]. The present SWCNT MSC represents a new generation of microdevices with a power similar to that of AEC, but orders of magnitude higher energy density. A detailed comparison of our microdevice with previously reported high-power MSCs can be found in Table 6.1. To the best of our knowledge, no other microdevices,

including state-of-the-art batteries and supercapacitors, show such excellent performance with regard to ultrahigh power and energy density.
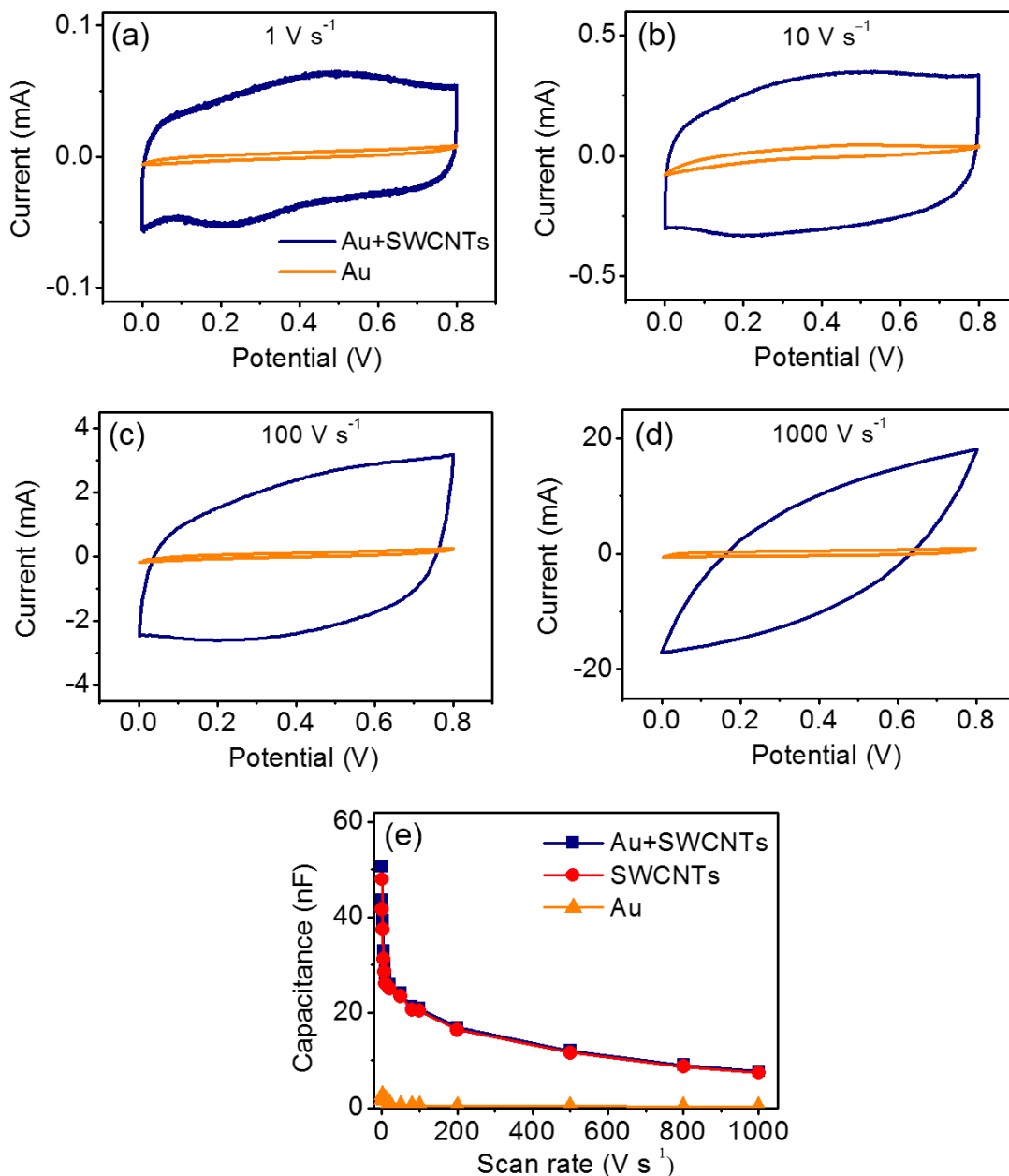
Fig. 6.10. Comparison of CV curves of Au and Au+SWCNTs electrodes for a scan rate of (a) 1, (b) 10, (c) 100, and (d) 1000 V s–1, and (e) capacitance of Au+SWCNTs, pure SWCNTs, and bare Au electrodes vs scan rate. The capacitance of the SWCNTs electrodes was obtained by subtracting the capacitance of Au electrodes from the total capacitance of the Au+SWCNTs electrodes.
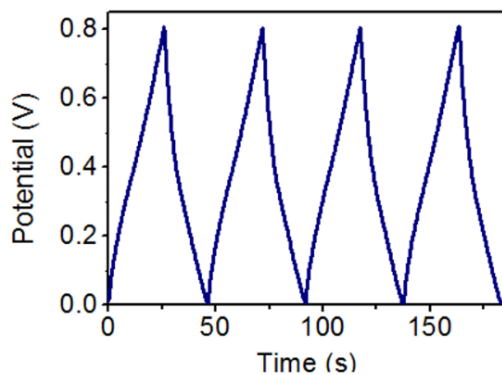
Fig. 6.11. GCD curve of the SWCNT MSCs at a current density of 10 nA cm^{-2}.
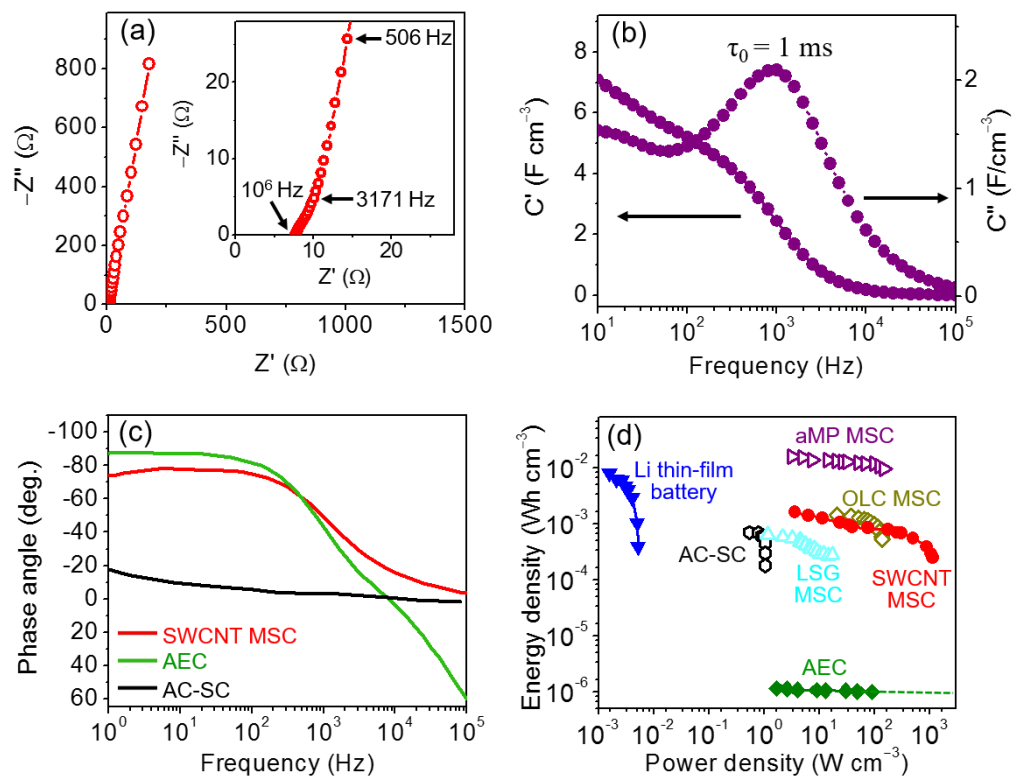
Fig. 6.12. Frequency response, energy density, and power density of SWCNT MSCs: (a) Nyquist plot (imaginary impedance Z″ vs real impedance Z′) with the magnified high-frequency region shown in the inset; (b) real and imaginary parts (C′ and C″, respectively) of stack capacitance vs frequency; (c) impedance phase angle vs frequency of SWCNT MSCs and commercial activated carbon supercapacitors (AC-SC)[37] and aluminum electrolytic capacitors (AEC)[37]; (d) Ragone plots (energy density vs power density) of SWCNT MSCs and commercial 4 V/500 μAh Li thin-film battery31, 2.75 V/44 mF AC-SC[31], 3 V/300 μF AEC[31], LSG MSC[37], OLC MSC[6], and aMP MSC[36].

Table 6.1. Performance comparison of MSCs developed in this work and previous studies.

Electrode material	Electrode thickness (μm)	Electrolyte	Volumetric capacitance ($F\ cm^{-3}$)	Energy density ($mWh\ cm^{-3}$)	Power density ($W\ cm^{-3}$)	Time constant τ_0 (ms)	Ref.
SWCNTs	0.14	PVA–H_3PO_4	18 (0.5 V s^{-1})	1.6	1125	1	this work
RGO-CNT (9:1)	6	3 M KCl	6.1 (0.01 V s^{-1})	~0.68	~77	4.8	[32]
OLC	7	1 M Et_4NBF_4/ anhydrous $C_4H_6O_3$	1.3 (1 V s^{-1})	~1.4[a]	~250[a]	26	[6]
SWCNT	~3.5	3.6 M H_2SO_4	1.04	1.73[b]	568[b]	7	[30]
aMP	5	PVA–H_3PO_4	12 (0.1 V s^{-1})	1.6	90	14	[36]
G/CNTCs	10-20	1 M Na_2SO_4	1.1 (0.2 V s^{-1})	0.16	30	1.8	[14]
LSG	7.6	PVA–H_3PO_4	2.0 (1 V s^{-1})	0.25	65	19	[37]
ERGO	20	25% KOH	0.24 (40 $\mu A\ cm^{-2}$)	---	---	0.17	[4]
Porous diamond foam	~2.6	3 M $NaClO_4$	2.3	1[b]	202[b]	3.16	[38]

RGO = reduced graphene oxide; OLC = onion-like carbon; aMP = activated mesophase pitch; G/CNTCs = Graphene/carbon nanotube carpets; LSG = laser-scribed graphene; ERGO = electrochemically reduced graphene oxide.

[a]Estimated from Ragone plots from the literature

[b]Estimated from energy and power densities of electrodes from the literature ($E_{cell} = \frac{1}{4} E_{electrodes}$, $P_{cell} = \frac{1}{4} P_{electrodes}$)

Fig. 6.13 illustrates the flexibility of SWCNT MSCs on an ultrathin PI substrate, demonstrated by the unique capability to undergo excessive bending, folding, and rolling without significant performance degradation. Fig. 6.13(a) shows digital photographs of a SWCNT MSC on a PI substrate bent around rods of radius of curvature equal to 1.5–4 mm. The CV performance of the microdevice versus the bending radius for 10 V s^{-1} scan rate (Fig. 6.13(d)) shows insignificant changes in electrical performance due to bending. In fact, the microdevice retained ~91% of its capacity when bent around a rod of 1.5 mm radius (Fig. 6.14). Fig. 6.13(b) shows a microdevice folded along its middle axis without the formation of a crease. Despite the significant deformation that reduced the device area by 50%, the CV response was not affected (Fig. 6.13(e)) and the folded microdevice demonstrated ~100% capacity retention, showing excellent mechanical stability. Moreover, rolling the SWCNT MSC on the PI substrate into a tube of ~1.2 mm diameter (Fig. 6.13(c)), which significantly reduced the device area, also had no effect on the electrical performance (Fig. 6.13(f)), with the roled microdevice retaining ~92% of the capacitance in its undeformed (flat) configuration. These findings indicate that folding and rolling are effective ways to increase the areal capacitance of these microdevices. Thus, the configuration of the SWCNT MSCs on ultrathin PI substrates can be easily altered by bending, folding, and rolling according to the device area and energy storage capacity required in specific applications.

A finite element analysis (FEA) was performed with the multi-physics code ABAQUS to model the deformation of SWCNT MSCs in the aforementioned scenarios. Fig. 6.13(g) shows the distribution of the maximum (first principal) strain ε_{max} at the top surface of the Au current collector for a microdevice bent around rods of different radii. For each bending radius, ε_{max} was obtained at the center, edge, and corner of the interdigital fingers (Fig. 6.13(g)). As shown in Fig. 6.13(h), ε_{max} at the center, edge, and corner of interdigital fingers (triangular, rectangular, and circular data points, respectively) is smaller than the yield strain (~0.003) by at least an order of magnitude. An analytical model (elaborated in the section 6.2.6) was developed to predict the dependence of maximum bending strain ε_b, the dominant contribution to ε_{max} ($\varepsilon_{max} \approx \varepsilon_b$), on the bending radius, reasonably agreeing with the results obtained by FEA in both values and tendencies. For rolled SWCNT MSCs, considered to be an extreme case of bending, the analytical model yields $\varepsilon_{max} = 5.29 \times 10^{-4}$, which is significantly below the yield strain. Therefore, the deformation due to bending and rolling is elastic and reversible. Since the formation of an irreversible fold crease with excessive strain localization can significantly affect the electronic performance, we folded the MSCs without creating a crease using sequential bending, aligning, and pressing steps (Fig. 6.15). In the last step, surface adhesion resulted in partial bonding of the two opposing PDMS surfaces of the MSC, leaving the free-standing part to deform into a shape resembling a tennis racket[39,40]. In both experiments and corresponding FEA models, the lengths of the free-standing parts are equal to ~725 µm.
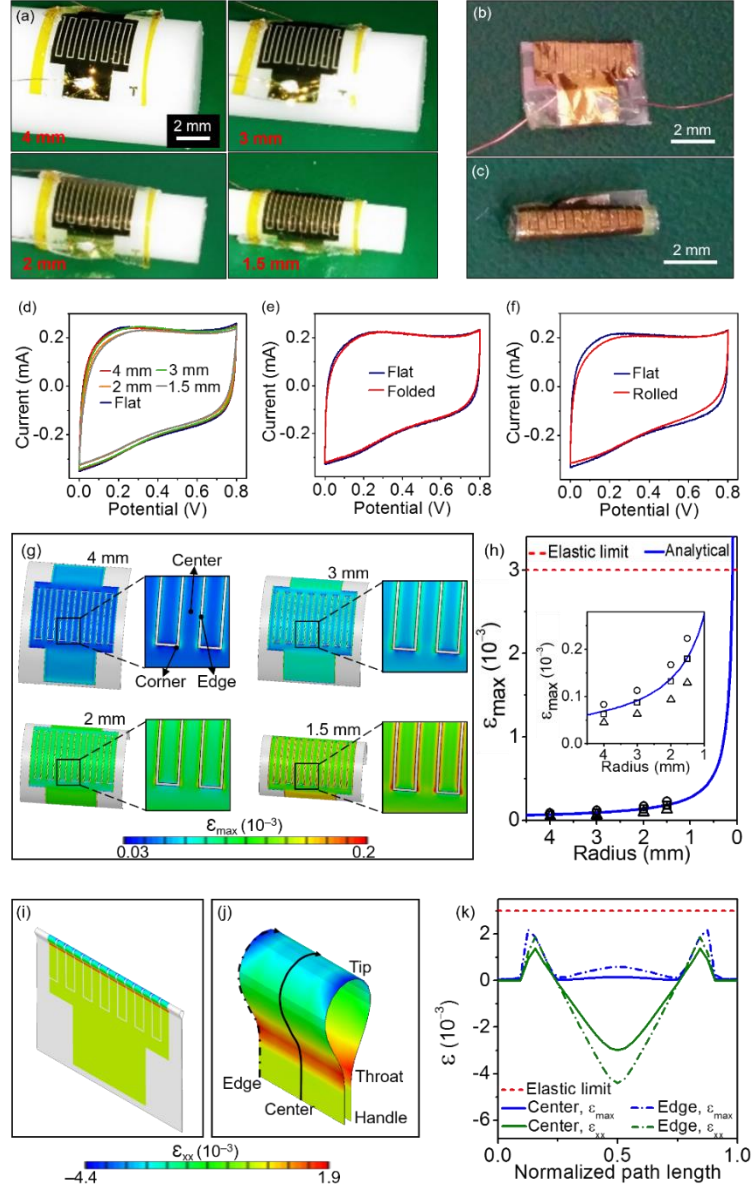
Fig. 6.13. Flexibility and mechanical stability of SWCNT MSCs: digital photographs of (a) bent (bending radius between 1.5 and 4 mm), (b) folded, and (c) rolled MSCs, CV curves of MSCs (d) bent around rods of radius between 1.5 and 4 mm, (e) folded, and (f) rolled to a dimeter of ~1.2 mm with undeformed (flat) MSCs, (g) maximum (first principal) strain ε_{max} distribution in the Au layer of MSCs bent around rods of radius in the range of 1.5–4 mm, (h) ε_{max} vs bending radius (the inset shows an enlarged view; triangular, rectangular, and circular data points represent ε_{max} at the center, edge, and corner of an interdigital finger, respectively), (i) distribution of ε_{xx} in the Au layer of a folded MSC, (j) magnified plot of ε_{xx} in the Au layer of an interdigital finger of a folded MSC (the x-direction is along the arrowed curves), (k) variation of ε_{max} and ε_{xx} along the paths shown in (j) (the arrowed solid and dash-dot curves represent one-half of the full paths along the center and edge of the electrode finger, respectively).

Figs. 6.13(i) and (j) show the distribution of strain in the x-direction ε_{xx} in the Au layer of the folded MSC and a folded interdigital finger, respectively. The x-direction is along the arrowed curves shown in Fig. 6.13(j) (also indicated in the undeformed device shown in Fig. 6.15(a)). The distribution of ε_{xx} near the folding site (Fig. 6.13(j)) shows the tip of the racket in compression, while both the throat and the handle are in tension. Along the arrowed edge and center paths (the curves in Fig. 6.13(j) show half of the path with a total length of 967 µm), the maximum tensile and compressive ε_{xx} strains at the finger edge are about 1.9×10^{-3} and -4.4×10^{-3}, respectively, whereas at the finger center they are about 1.4×10^{-3} and -3×10^{-3}, respectively (Fig. 6.13(k)). Away from the folding site, the strain in the Au layer is almost zero due to the absence of bending. The highest value of ε_{max} in the Au layer is ~2.2×10^{-3} (Fig. 6.13(k)), which is below the yield strain. In all of the above simulations, the strain in the Au interdigital fingers is below the yield strain, indicating that deformation is fully reversible (elastic). Interestingly, although the FEA predicts higher strains in the folded MSC fingers compared with bent and rolled fingers, the folded MSC exhibits higher capacity retention (Fig. 6.13(d-f)). These seemingly contradictory findings are likely due to the strain in the Au contact pads of bent and rolled MSCs. At contact pads, the leads were electrically connected with silver paste. Once cured, the silver paste (typically ~100-µm-thick) thickened the local region by ~5 times. Consequently, the local bending strain increased significantly at the silver paste, leading to the observed deteriorated retention in Fig. 6.13(d) and (f) (The FEM simulation in this paper did not take into account the increased strain at the silver paste). In comparison, the Au pads in the folded MSC are almost strain free (as shown in Fig. 6.13(i)). Therefore, the folded MSC shows uncompromised capacity retention. More robust electrical connections between the leads and the Au pads will further improve the overall flexibility of the microdevice. The ultrathin nature and intrinsic high flexibility of the PI substrate, coupled with the excellent mechanical stability of the SWCNT network endow exceptional flexibility and surface-mount capability of the SWCNT MSCs, which can be potentially integrated into various flexible and/or stretchable chips for applications in roll-up electronics (e.g., displays and TVs), electronic paper, smart sensors, and even wearable electronics.
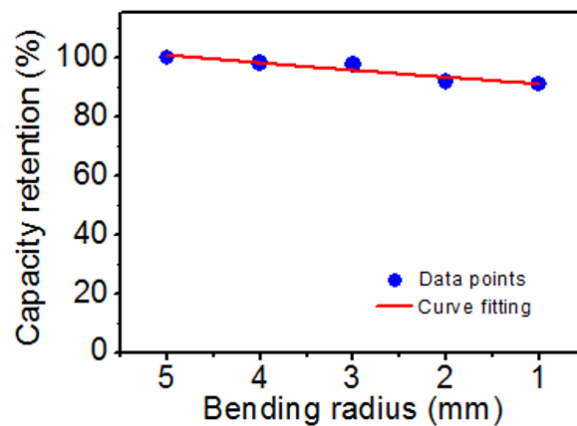
Fig. 6.14. Capacity retention of flexible SWCNT MSC vs bending radius.
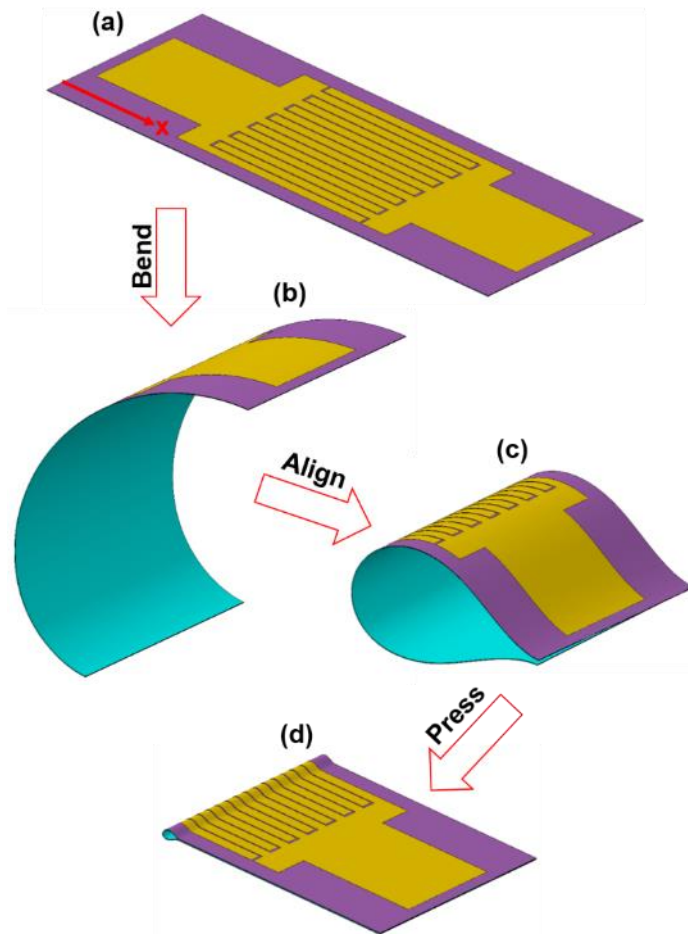
Fig. 6.15. Folding process of a SWCNT MSC.

6.4 Summary

SWCNT MSCs on free-standing ultrathin PI substrates were fabricated by combining conventional lithography and mechanical peeling-off techniques. The SWCNTs were spray coated onto the PI substrate to form a mechanically stable and highly conductive SWCNT network without using any organic binders, conductive additives or polymer separators, which are often needed in commercial supercapacitors, thus enhancing the device performance due to easy access of electrolyte ions to the active material. The unprecedented power density of 1125 W cm^{-3} obtained with the current SWCNT MSCs is attributed to the high conductivity and easily accessible surface area of the spray-deposited SWCNT network and the small gap between the interdigital fingers of the in-plane electrodes. The microdevices developed in this work combine the power density of electrolytic capacitors with the energy density of microbatteries, which may have a significant impact on high-power microelectronics. These findings also provide a solution to microscale energy storage in numerous areas in which electrolytic capacitors cannot provide sufficient energy density. Furthermore, the present microdevices demonstrate excellent electrochemical stability with ~96% of the original capacity retained even after 100,000 charge/discharge cycles. This characteristic feature is very important when

compared with microbatteries whose relatively short lifetime is a major limitation in most applications. The long life of our microdevices is especially important when combined with energy harvesters to produce on-chip self-powered systems. The exceptional flexibility of the present microdevices, demonstrated by bending, folding, and rolling experiments and numerical analysis, paves the way for potential applications of all-solid-state SWCNT MSCs as flexible energy storage devices in portable, stretchable, and wearable electronic devices.

6.5 References

[1] Shen, C., Wang, X., Zhang, W. and Kang, F., 2011. A high-performance three-dimensional micro supercapacitor based on self-supporting composite materials. Journal of Power Sources, 196(23), pp.10465-10471.

[2] Shen, C., Wang, X., Zhang, W. and Kang, F., 2011. A high-performance three-dimensional micro supercapacitor based on self-supporting composite materials. Journal of Power Sources, 196(23), pp.10465-10471.

[3] Pu, J., Wang, X., Zhang, T., Li, S., Liu, J. and Komvopoulos, K., 2015. High-energy-density, all-solid-state microsupercapacitors with three-dimensional interdigital electrodes of carbon/polymer electrolyte composite. Nanotechnology, 27(4), p.045701.

[4] Sheng, K., Sun, Y., Li, C., Yuan, W. and Shi, G., 2012. Ultrahigh-rate supercapacitors based on eletrochemically reduced graphene oxide for ac line-filtering. Scientific reports, 2, p.247.

[5] Miller, J.R., Outlaw, R.A. and Holloway, B.C., 2010. Graphene double-layer capacitor with ac line-filtering performance. Science, 329(5999), pp.1637-1639.

[6] Pech, D., Brunet, M., Durou, H., Huang, P., Mochalin, V., Gogotsi, Y., Taberna, P.L. and Simon, P., 2010. Ultrahigh-power micrometre-sized supercapacitors based on onion-like carbon. Nature nanotechnology, 5(9), pp.651-654.

[7] Korenblit, Y., Rose, M., Kockrick, E., Borchardt, L., Kvit, A., Kaskel, S. and Yushin, G., 2010. High-rate electrochemical capacitors based on ordered mesoporous silicon carbide-derived carbon. Acs Nano, 4(3), pp.1337-1344.

[8] Tsai, W.Y., Gao, P.C., Daffos, B., Taberna, P.L., Pérez, C.R., Gogotsi, Y., Favier, F. and Simon, P., 2013. Ordered mesoporous silicon carbide-derived carbon for high-power supercapacitors. Electrochemistry Communications, 34, pp.109-112.

[9] Futaba, D.N., Hata, K., Yamada, T., Hiraoka, T., Hayamizu, Y., Kakudate, Y., Tanaike, O., Hatori, H., Yumura, M. and Iijima, S., 2006. Shape-engineerable and highly densely packed single-walled carbon nanotubes and their application as super-capacitor electrodes. Nature materials, 5(12), pp.987-994.

[10] Du, C. and Pan, N., 2006. Supercapacitors using carbon nanotubes films by electrophoretic deposition. Journal of Power Sources, 160(2), pp.1487-1494.

[11] Wu, Z.S., Parvez, K., Feng, X. and Müllen, K., 2013. Graphene-based in-plane micro-supercapacitors with high power and energy densities. Nature communications, 4.

[12] Qi, D., Liu, Z., Liu, Y., Leow, W.R., Zhu, B., Yang, H., Yu, J., Wang, W., Wang, H., Yin, S. and Chen, X., 2015. Suspended wavy graphene microribbons for highly stretchable microsupercapacitors. Advanced Materials, 27(37), pp.5559-5566.

[13] Niu, Z., Zhang, L., Liu, L., Zhu, B., Dong, H. and Chen, X., 2013. All-Solid-State Flexible Ultrathin Micro-Supercapacitors Based on Graphene. Advanced Materials, 25(29), pp.4035-4042.

[14] Lin, J., Zhang, C., Yan, Z., Zhu, Y., Peng, Z., Hauge, R.H., Natelson, D. and Tour, J.M., 2012. 3-dimensional graphene carbon nanotube carpet-based microsupercapacitors with high electrochemical performance. Nano letters, 13(1), pp.72-78.

[15] Kaempgen, M., Chan, C.K., Ma, J., Cui, Y. and Gruner, G., 2009. Printable thin film supercapacitors using single-walled carbon nanotubes. Nano letters, 9(5), pp.1872-1876.

[16] Kaempgen, M., Duesberg, G.S. and Roth, S., 2005. Transparent carbon nanotube coatings. Applied Surface Science, 252(2), pp.425-429.

[17] Artukovic, E., Kaempgen, M., Hecht, D.S., Roth, S. and Grüner, G., 2005. Transparent and flexible carbon nanotube transistors. Nano Letters, 5(4), pp.757-760.

[18] Kaempgen, M., Lebert, M., Nicoloso, N. and Roth, S., 2008. Multifunctional carbon nanotube networks for fuel cells. Applied Physics Letters, 92(9), p.094103.

[19] Niu, Z., Dong, H., Zhu, B., Li, J., Hng, H.H., Zhou, W., Chen, X. and Xie, S., 2013. Highly Stretchable, Integrated Supercapacitors Based on Single-Walled Carbon Nanotube Films with Continuous Reticulate Architecture. Advanced Materials, 25(7), pp.1058-1064.

[20] Y Yu, C., Masarapu, C., Rong, J., Wei, B. and Jiang, H., 2009. Stretchable Supercapacitors Based on Buckled Single-Walled Carbon-Nanotube Macrofilms. Advanced Materials, 21(47), pp.4793-4797.

[21] Yu, C., Masarapu, C., Rong, J., Wei, B. and Jiang, H., 2009. Stretchable Supercapacitors Based on Buckled Single-Walled Carbon-Nanotube Macrofilms. Advanced Materials, 21(47), pp.4793-4797.

[22] Kim, J.H., Nam, K.W., Ma, S.B. and Kim, K.B., 2006. Fabrication and electrochemical properties of carbon nanotube film electrodes. Carbon, 44(10), pp.1963-1968.

[23] Ma, C.W., Huang, P.C. and Yang, Y.J., 2015, January. A paper-like micro-supercapacitor with patterned buckypaper electrodes using a novel vacuum filtration technique. In 2015 28th IEEE International Conference on Micro Electro Mechanical Systems (MEMS) (pp. 1067-1070). IEEE.

[24] Zhang, H., Cao, G., Yang, Y. and Gu, Z., 2008. Comparison between electrochemical properties of aligned carbon nanotube array and entangled carbon nanotube electrodes. Journal of the Electrochemical Society, 155(2), pp.K19-K22.

[25] Liu, C.G., Fang, H.T., Li, F., Liu, M. and Cheng, H.M., 2006. Single-walled carbon nanotubes modified by electrochemical treatment for application in electrochemical capacitors. Journal of Power Sources, 160(1), pp.758-761.

[26] Kim, U.J., Furtado, C.A., Liu, X., Chen, G. and Eklund, P.C., 2005. Raman and IR spectroscopy of chemically processed single-walled carbon nanotubes. Journal of the American Chemical Society, 127(44), pp.15437-15445.

[27] Čeponkus, J., Smilga, A.P., Rumskaitė, I., Puodžiūtė, I. and Šablinskas, V., 2013. Infrared absorption spectroscopy of functionalized single-walled carbon nanotubes. chemija, 24(1).

[28] Esfandiary, E., Valiani, A., Hashemibeni, B., Moradi, I. and Narimani, M., 2014. The evaluation of toxicity of carbon nanotubes on the human adipose-derived-stem cells in-vitro. Advanced biomedical research, 3(1), p.40.

[29] Shen, C., Wang, X., Zhang, W. and Kang, F., 2013. Direct prototyping of patterned nanoporous carbon: a route from materials to on-chip devices. Scientific reports, 3.

[30] In, J.B., Hsia, B., Yoo, J.H., Hyun, S., Carraro, C., Maboudian, R. and Grigoropoulos, C.P., 2015. Facile fabrication of flexible all solid-state micro-supercapacitor by direct laser writing of porous carbon in polyimide. Carbon, 83, pp.144-151.

[31] Laszczyk, K.U., Kobashi, K., Sakurai, S., Sekiguchi, A., Futaba, D.N., Yamada, T. and Hata, K., 2015. Lithographically Integrated Microsupercapacitors for Compact, High Performance, and Designable Energy Circuits. Advanced Energy Materials, 5(18).

[32] El-Kady, M.F., Strong, V., Dubin, S. and Kaner, R.B., 2012. Laser scribing of high-performance and flexible graphene-based electrochemical capacitors. Science, 335(6074), pp.1326-1330.

[33] Beidaghi, M. and Wang, C., 2012. Micro-Supercapacitors Based on Interdigital Electrodes of Reduced Graphene Oxide and Carbon Nanotube Composites with Ultrahigh Power Handling Performance. Advanced Functional Materials, 22(21), pp.4501-4510.

[34] Wang, K., Zou, W., Quan, B., Yu, A., Wu, H., Jiang, P. and Wei, Z., 2011. An All-Solid-State Flexible Micro-supercapacitor on a Chip. Advanced Energy Materials, 1(6), pp.1068-1072.

[35] Pushparaj, V.L., Shaijumon, M.M., Kumar, A., Murugesan, S., Ci, L., Vajtai, R., Linhardt, R.J., Nalamasu, O. and Ajayan, P.M., 2007. Flexible energy storage devices based on nanocomposite paper. Proceedings of the National Academy of Sciences, 104(34), pp.13574-13577.

[36] Taberna, P.L., Simon, P. and Fauvarque, J.F., 2003. Electrochemical characteristics and impedance spectroscopy studies of carbon-carbon supercapacitors. Journal of The Electrochemical Society, 150(3), pp.A292-A300.

[37] Huang, H.C., Chung, C.J., Hsieh, C.T., Kuo, P.L. and Teng, H., 2016. Laser fabrication of all-solid-state microsupercapacitors with ultrahigh energy and power based on hierarchical pore carbon. Nano Energy, 21, pp.90-105.

[38] El-Kady, M.F. and Kaner, R.B., 2013. Scalable fabrication of high-power graphene micro-supercapacitors for flexible and on-chip energy storage. Nature communications, 4, p.1475. Gao, F., Wolfer, M.T. & Nebel, C.E. Highly porous diamond foam as a thin-film micro-supercapacitor material. Carbon 80, 833–840 (2014).

[39] Lee, J.W., Xu, R., Lee, S., Jang, K.I., Yang, Y., Banks, A., Yu, K.J., Kim, J., Xu, S., Ma, S. and Jang, S.W., 2016. Soft, thin skin-mounted power management systems and their use in wireless thermography. Proceedings of the National Academy of Sciences, p.201605720.

[40] Su, Y., Liu, Z., Wang, S., Ghaffari, R., Kim, D.H., Hwang, K.C., Rogers, J.A. and Huang, Y., 2014. Mechanics of stretchable electronics on balloon catheter under extreme deformation. International Journal of Solids and Structures, 51(7), pp.1555-1561.

Chapter 7 – Highly stretchable microsupercapacitor arrays with honeycomb structures and SWCNT electrodes for integrated wearable electronic systems

The rapid development of portable and wearable electronics has greatly increased the demand for energy storage devices with similar physical properties and integration capability. This chapter introduces a honeycomb polydimethylsiloxane substrate for stretchable microsupercapacitor (MSC) arrays, which enables facile integration with other electronics. The results of this study show that such stretchable MSC arrays with single-walled carbon nanotube electrodes demonstrate excellent rate capability and power performance as well as electrochemical stability up to 150% (zero prestrain) or 275% (−50% prestrain) stretching and under excessive bending or twisting.

7.1 Introduction

The rapid growth of wearable electronic devices has increased the demand for reliable stretchable and flexible electronics. Several recent studies have been focused on the fabrication of various types of stretchable devices, such as wearable photovoltaics [1], sensitive robotic skin [2,3], epidermal electronics [4], soft surgical tools [5,6], and organic [7] or inorganic [8] LEDs. A critical need for all of these stretchable devices is the development of energy-storage systems with similar physical properties to facilitate direct integration with other electronics.

Supercapacitors are promising energy storage devices because they demonstrate higher power density, longer operation life, and better safety than batteries. To power stretchable electronics, the supercapacitors must be flexible and stretchable. The stretchability of most supercapacitors depends on the strain applied to the substrate before electrode loading [9,10], which hinders the integration with other electronic units. Miscrosupercapacitors (MSCs) with two-dimensional (2D) in-plane electrode structures allow facile integration with on-chip and wearable electronics. Because of the intrinsic features of 2D in-plane electrodes, the ionic diffusion pathways are shorter than those in conventional supercapacitors with sandwiched electrodes, which further improves the rate capability and power performance of the devices [11-13]. Furthermore, a 2D in-plane structure reduces the device thickness, which not only endows the device with greater flexibility, but also enables the integration of MSCs in the thickness direction to fully make use of the device area. This could greatly extend the output voltage range and increase the energy density of MSCs over a limited device area. More recently, the stretchability of MSC arrays was enhanced by using serpentine-like metallic interconnectors [14], introducing stiff islands in the soft elastomer substrate [15–17], or employing suspended wavy structures of graphene microribbons [18]. Although these technologies possess attractive features, none of these offer a stretching capability to large deformations (*e.g.*, >100% elongation), thus limiting the applicability to only a few wearable electronic systems.

Achieving both high stretchability and good integration capability based on current strategies is challenging. This paper presents the first systematic study showing that

honeycomb-shaped polydimethylsiloxane (PDMS) substrates can greatly increase the stretchability of devices loaded with MSC arrays. The intrinsic deformation mechanism of honeycomb structures subjected to stretching produces highly localized strains at the corners of the structure and large areas of low strain (*e.g.*, maximum (first principal) strain $\varepsilon_{max} < 0.1$ for 100% stretching), as demonstrated by finite element analysis (FEA) simulation results (Fig. 7.1). In contrast, a conventional (solid) PDMS substrate stretched by 100% exhibits a uniform strain distribution of $\varepsilon_{max} = 1.0$. Thus, if the MSC arrays and interconnects are placed in the low-strain regions of the honeycomb structure, the strain in these functional materials will be remarkably low during stretching. Moreover, the stretchable MSC arrays can be easily integrated with other electronic units, such as wireless charging systems and energy harvesters, by placing different electronic devices in the low-strain regions.
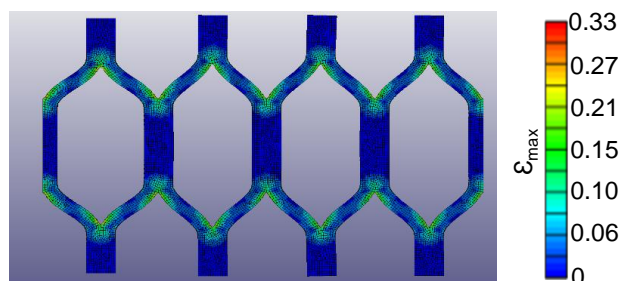
Fig. 7.1 Distribution of maximum (first principal) strain ε_{max} in a four-cell honeycomb PDMS substrate stretched by 100%.

This article includes experimental measurements from testing of the aforementioned stretchable devices, which demonstrate excellent rate capability and power performance and the capability to be cycled at a high scan rate of 100 V s^{-1} and stretched up to 150% (zero prestrain) or 275% (–50% prestrain). It is also shown that a 4×4 MSC array can be used to light a commercial light-emitting diode (LED) even when it is highly stretched. The experimental findings and FEA results illustrate the high potential of the present stretchable MSC arrays for a wide application range of wearable electronics.

7.2 Methods

7.2.1 Spray deposition of SWCNT electrodes

Purified SWCNTs (P3-SWNT, Carbon Solutions) with 1–3 at% carboxylic acid surface functional groups were used as electrode materials. The SWCNTs were dispersed in deionized (DI) water with a tip sonicator for 1–2 h to form a 0.5–1 mg/mL stable suspension. The suspension was then sprayed onto the Cr/Au layer and placed on a plate heated to 40–60°C to form ~280-nm-thick SWCNT films. The sprayed SWCNT films were used as MSC electrodes without further treatment.

7.2.2 Preparation of the gel electrolyte

The polymer electrolyte (PE) was prepared by mixing 10 mL of DI water with 10 mL of phosphoric acid (H$_3$PO$_4$) using magnetic stirring for 30 min and dissolving 10 g of polyvinyl alcohol (PVA) in 90 mL of DI water at 90°C, also assisted by magnetic stirring

for 1 h. The two solutions were then intermixed by magnetic stirring for 1 h. The PVA:H_3PO_4 ratio in the PE was fixed at 1:1 wt/vol.

7.2.3 Fabrication of stretchable MSC arrays

MSC arrays with SWCNT electrodes fabricated on a Si substrate by standard microfabrication were transferred onto a honeycomb PDMS substrate to assemble the stretchable MSC arrays. The first step of the fabrication process was to spin coat the bottom PI layer onto a Si wafer (Fig. 7.2(a)). The PI solution (ZKPI-306II, POME Sci-tech, Beijing, China) was mixed with a PI thinner (POME Sci-tech, Beijing, China) to a weight ratio of 5:1 to form a diluted PI solution, and then left overnight to allow the bubbles in the diluted PI solution to escape. The diluted PI solution was spin-coated onto a Si wafer in two steps (step 1: 800 rpm for 18 s, step 2: 6000 rpm for 60 s), soft baked in an oven at 80°C for ~3 h to evaporate the solvent, and cured in the oven at 250°C for ~2 h. The thickness of the produced PI film was ~1.3 µm. A bilayer consisting of a 5-nm-thick Cr underlayer and a 50-nm-thick Au top layer was evaporated onto the wafer and patterned using a lift-off process to form the interdigital current collectors and the interconnects between the MSCs (Fig. 7.2(b)). The lift-off process was performed in acetone using very gentle sonication. Another ~1.3-µm-thick PI layer (top PI) was spin coated, soft baked, and cured using the same process as for the bottom PI layer.

Photolithography and selective etching of the top PI layer with O_2 plasma (70 sccm, 10 Pa, 150 W, 20 min) was carried out to expose the interdigital electrode area for subsequent SWCNT deposition and formation of a honeycomb shape (Fig. 7.2(c)). The bottom and top PI layers encapsulated the Cr/Au interconnects placing them close to the neutral bending plane, thus protecting them from the stresses exerted during peeling off of the MSC array from the Si substrate. The SWCNTs were deposited onto the exposed interdigital electrode area by spray-deposition and patterned to interdigital electrodes by a lift-off process (Fig. 7.2(d)). The interdigital pattern of the SWCNT layer is the same as that of the underlying Cr/Au bilayer. The bottom PI layer was then selectively etched with O_2 plasma to match the honeycomb shape of the top PI layer (Fig. 7.2(e)).

The honeycomb PDMS substrate was fabricated by a molding process. PDMS resin and curing agent (10:1 weight ratio) were mixed for 5 min, degassed in vacuum for ~30 min, carefully poured into a poly(methyl methacrylate) (PMMA) mold to fill all the grooves in the mold, kept at room temperature on a flat surface for ~30 min to allow the PDMS solution to flow, and then cured at 60°C in the oven overnight. Subsequently, the cured PDMS was carefully peeled off from the PMMA mold to release the honeycomb PDMS substrate. To ensure a similar substrate thickness, the weight of the poured PDMS solution was kept the same in each PDMS substrate.

The fabricated devices were carefully peeled off from the Si substrate by 3M water-dissolvable tape, and transferred onto the honeycomb PDMS bottom substrate (Fig. 7.2(f)). A very thin layer of liquid PDMS solution was spread onto the PDMS substrate and partially cured at 70°C for ~15 min to bond the transferred device onto the PDMS substrate. After placing the device onto the honeycomb PDMS substrate, the whole structure was kept at room temperature for ~24 h to allow full curing of the PDMS binding layer. The

3M tape was then removed by submersing in DI water for ~8 h, the PVA-H$_3$PO$_4$ gel electrolyte was coated onto the interdigital electrodes, and the device was left at room temperature overnight for the excess water to evaporate (Fig. 7.2(g)). To encapsulate the whole MSC array, another identical honeycomb PDMS substrate was assembled together with the bottom PDMS to produce the stretchable MSC arrays (Fig. 7.2(h)).
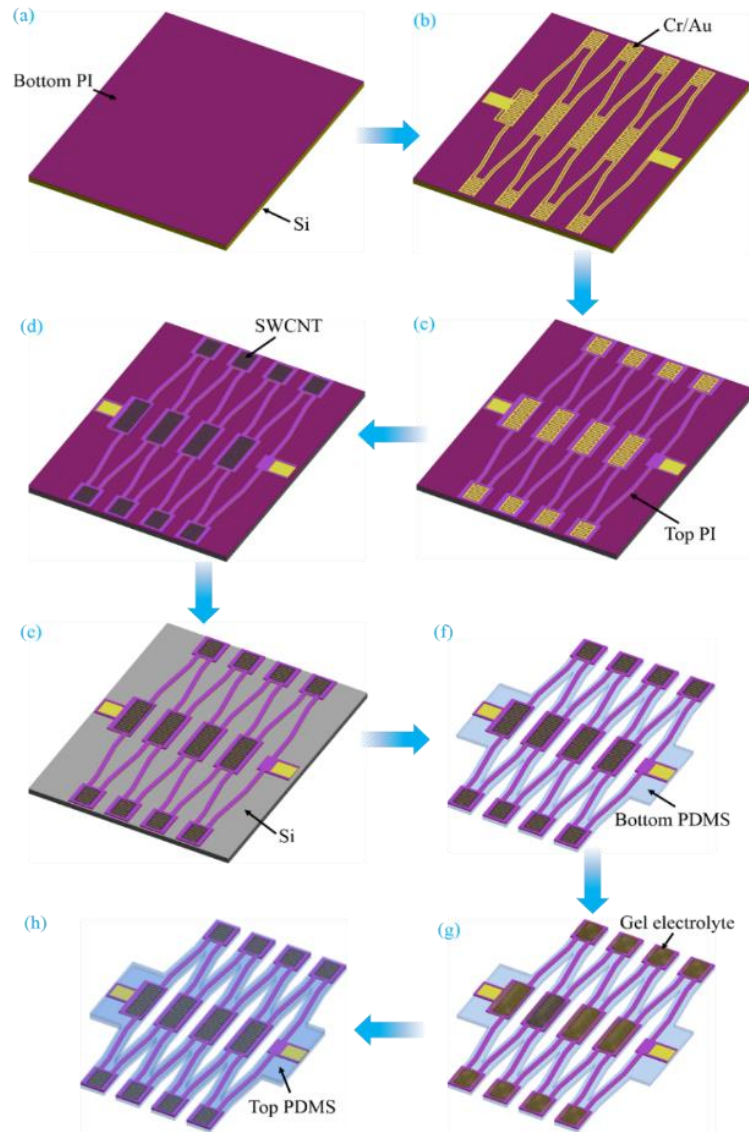
Fig. 7.2 Fabrication process of stretchable 4 × 4 MSC arrays: (a) spin coating of the bottom PI layer on a Si wafer, (b) evaporation and micropatterning of the Cr/Au bilayer, (c) spin coating and micropatterning of the top PI layer, (d) spray deposition and micropatterning of the interdigital SWCNT electrodes, (e) selective etching of the bottom PI layer, (f) transfer of the device onto a honeycomb PDMS substrate, (g) coating of the interdigital SWCNT electrodes with gel electrolyte, and (h) application of the top honeycomb PDMS superstrate to encapsulate the MSC array.

7.2.4 Characterization techniques

The microstructure of the sprayed SWCNTs was studied with an SEM (S-5500, Hitachi, Tokyo, Japan). For cross-sectional SEM imaging of the electrodes, the MSCs on the silicon substrate were sectioned perpendicular to the finger-length direction and coated with a ~1-nm-thick Au-Pd layer to improve the surface conductance. To easily distinguish the boundaries between adjacent layers in the cross-sectional SEM images, different layers were stained with various artificial colors using Adobe Photoshop.

To prepare the samples for TEM imaging, the SWCNT powder was dispersed in DI water with a tip sonicator for ~2 h to form a 0.05 mg/mL stable suspension. Then, a drop of the prepared suspension was applied on a standard Cu grid used for imaging with the TEM (JEOL JEM2011, Peabody, MA, USA).

7.2.5 Electrochemical testing

The electrochemical performance of single MSCs and 3×3 or 4×4 MSC arrays was evaluated with a two-electrode system and PVA-H_3PO_4 gel electrolyte. CV and GCD experiments were performed with a CHI 860D electrochemical workstation. In the CV tests, the scan rate was varied in the range of 0.05–100 V s^{-1} and the voltage in the range of 0–0.8 V (single MSCs), 0–2.4 V (3×3 MSC arrays), or 0–3 V (4×4 MSC arrays). In the GCD experiments, the devices were charged and discharged using a charging/discharging current of 5 nA and a voltage in the range of 0–1 V (single MSCs) or 0–3 V (4×4 MSC arrays), respectively.

The volumetric capacitance C_V was determined from the CV responses for a scan rate in the range of 0.05–100 V s^{-1} using the relation

$$C_V = \frac{1}{\mathcal{V} \, \Delta V} \int I(t) \, \mathrm{d}t \tag{1}$$

where ΔV is the potential range (0.8 and 3 V for single MSCs and 4×4 MSC arrays, respectively), $\mathcal{V}$ is the total electrode volume, which includes the volume of both the electrodes and the space between them (for 4×4 MSC arrays, the electrode volume is 16 times that of single MSCs), $I(t)$ is the current measured during CV testing, and t is the time.

Both the Au layer and the SWCNT layer contribute to the total capacitance of the MSCs. To determine the capacitance of the SWCNT layer, we subtracted the capacitance of the Au current collector from the total capacitance of the Au + SWCNT layers. CV curves of Au and Au + SWCNT for a scan rate of 10, 50, and 100 V s^{-1} are shown in Figs. 7.3(a–c), respectively. The calculated volumetric capacitance of Au + SWCNT and SWCNT versus scan rate is shown in Fig. 7.3(d). In this chapter, the capacitance of the MSCs is that contributed only by the SWCNT electrodes.
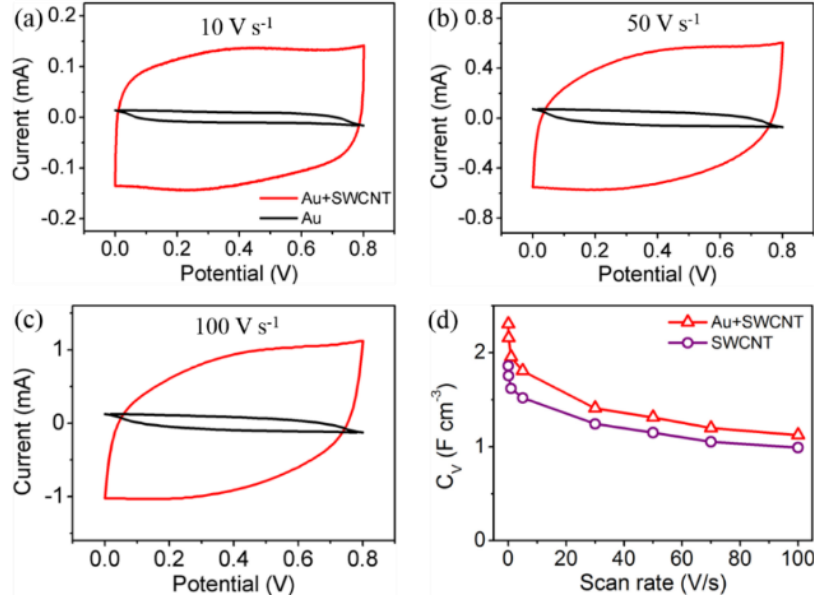
Fig. 7.3 CV curves of Au and Au + SWCNT single MSCs for a scan rate of (a) 10, (b) 50, and (c) 100 V s⁻¹ and (d) volumetric capacitance C_V versus scan rate of SWCNT and Au + SWCNT single MSCs.

The volumetric energy density E_V and power density P_V were calculated from the CV responses for a scan rate in the range of 0.05–100 V s⁻¹ using the relations

$$E_V = \frac{1}{2} \, C_V \Delta V^2 / 3{,}600 \tag{2}$$

$$P_V = \frac{1}{2} \frac{C_V \Delta V^2}{t} \tag{3}$$

where t (in seconds) is the discharge time. The energy and power density of the MSCs are those contributed by the SWCNT electrodes.

EIS tests were carried out by applying a 10 mV ac signal in the frequency range of 10^{-1}–10^6 Hz with a Solartron 1260 Impedance/Gain-Phase Analyzer (AMETEK Advanced Measurement Technology, Farnborough, Hampshire, UK). The real and imaginary parts of the impedance Z' and Z'', respectively, were recorded over the whole frequency range and plotted as Nyquist plots. The imaginary part of the capacitance C'' was estimated from the relation

$$C'' = \frac{1}{2} \frac{Z'}{\pi f |Z|^2} \tag{4}$$

where f is the frequency and $|Z| = \sqrt{Z'^2 + Z''^2}$ is the absolute value of the impedance.

To investigate the electrochemical stability of the devices, cyclic CV tests were performed in the potential range of 0–0.8 V (single MSCs) and 0–3 V (4 × 4 MSC arrays) at a scan

rate of 10 V s^{-1}. A total of 10,000 charge/discharge cycles were applied to single MSCs and 4×4 MSC arrays.

7.2.6 Mechanical testing

The mechanical tests were performed with an Instron machine. To obtain the stress-strain response of the devices, a honeycomb cell was subjected to three stretching cycles of 0–100% elongation. The flat PDMS membrane was prepared by pouring mixed PDMS resin and curing agent (10:1 weight ratio) into a Petri dish and then curing at 60°C in oven overnight. The thickness of the produced PDMS membrane is ~2 mm. For uniaxial tensile testing, the fully cured PDMS membrane was cut into 40-mm-long and 12-mm-wide strips using an ultra-sharp platinum-coated blade. The gauge length of the PDMS strips was 30 mm.

The Nike wrist band was cut into 70-mm-long and 22-mm-wide strips along the hoop direction with scissors. The thickness of a single cloth layer of Nike wrist band is ~2 mm. The gauge length of the wrist band strips for tensile tests was 60 mm. The flat PDMS strips and Nike wrist band strips were subjected to tensile loading up to 100% maximum elongation. A strain rate of 0.5 min^{-1} was used in all the tensile tests. Digital photographs of the honeycomb cell of the device, flat PDMS membrane, and cloth strip cut from a Nike wrist band subjected to uniaxial tensile tests are shown in Fig. 7.4.
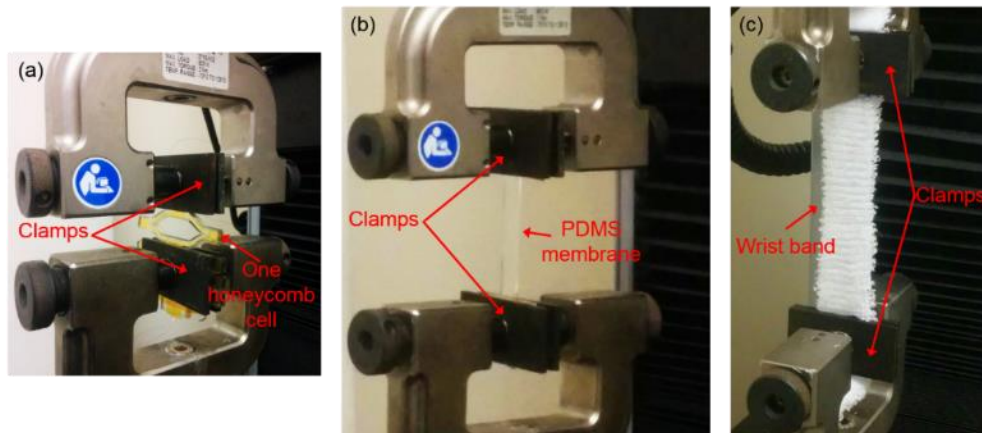
Fig. 7.4 Digital photographs showing tensile test setups of (a) a single honeycomb cell of the device, (b) a flat PDMS membrane, and (c) a cloth strip cut from a Nike wrist band.

7.2.7 FEA simulations

3D FEA simulations were performed to analyze the device deformation due to various loading conditions, including uniaxial tension/compression, bending, and twisting. The FEA model captured the elastic-plastic deformation of the metallic components and the hyperelastic behavior of the PDMS substrate. These modeling results provided insight into the capacity of the device to accommodate large deformation and insightful guidance for mechanical testing. All of the simulation results were obtained with the multi-physics FEA code ABAQUS. In each FEA model, the elastomeric PDMS substrate and the PDMS superstrate were modeled with eight-node hexahedral brick solid elements (C3D8R), while the PI (1.3 μm)/Au (50 nm)/PI (1.3 μm) layered interconnects were modeled with

quadrilateral shell elements (S4R), which were defined by composite layups. The SWCNTs and Cr layer were not modeled because of their negligible effect on the mechanical behavior of the device. Because of the good adhesion between the PI layer and the PDMS substrate, a perfect bonding among all layers was assumed in the FEA simulations. The FEA mesh was refined to ensure accurate strain mapping. The Mooney-Rivlin model was used to model the PDMS layer, with effective modulus $E_{PDMS} = 1.2$ MPa and Poisson's ratio $\nu_{PDMS} = 0.49$ obtained from the Instron measurements. The PI layer was modeled as a linear elastic material with $E_{PI} = 2.5$ GPa and $\nu_{PI} = 0.34$, whereas the Au layer was modeled as an elastic-perfectly-plastic material with $E_{Au} = 78$ GPa, $\nu_{Au} = 0.44$, and yield strength $S_Y = 234$ MPa.

7.3 Results and Discussion

The energy storage devices developed in this study consist of arrays of MSCs arranged in series and in parallel to enhance the output voltage and energy storage capability. The MSCs comprise planar interdigital electrodes with single-walled carbon nanotubes (SWCNTs) and polyvinyl alcohol-phosphoric acid (PVA-H$_3$PO$_4$) gel electrolyte. An characteristic feature of the current MSC devices is the honeycomb-like structure of the PDMS substrate (Fig. 7.5(a)), specifically designed to accommodate large deformation upon stretching, bending, and twisting without producing excessive deformation in the MSCs. The stretchability of the MSC array system is controlled by the deformation of the honeycomb PDMS structure. An exploded view of the multilayer structure of a honeycomb cell is shown in Fig. 7.5(b). The current collectors and interconnects (Fig. 7.5(b),iii) consist of a photolithographically patterned metallic bilayer of a 5-nm-thick chromium (Cr) underlayer and a 50-nm-thick gold (Au) top layer. Two ~1.3-µm-thick polyimide (PI) layers (Figs. 7.5(b),ii and iv) are used to sandwich the Cr/Au interconnects and place them close to the mechanical neutral plane. The SWCNTs with interdigital patterns (Fig. 7.5(b),v) serve as an active material for energy storage. The PVA-H$_3$PO$_4$ gel electrolyte (Fig. 7.5(b),vi) deposited onto the SWCNT electrodes provides a medium for ionic transport. All of the above layers are encapsulated by two identical PDMS honeycomb substrates (Figs. 7.5(b),i and vii), which provide long-term stability to the MSCs under ambient conditions and minimize the strain in the MSCs during stretching. A 4×4 MSC array has 16 MSCs of which four are connected in series, whereas sets of four MSCs in series are connected in parallel (Fig. 7.6). The material and fabrication details of the stretchable devices are given in Methods and illustrated in Fig. 7.7. Digital photographs of a stretchable 4×4 MSC array obtained at characteristic fabrication steps are shown in Fig. 7.8.

Although this study is mainly focused on the mechanical response and electrical performance of 4×4 MSC arrays, the capability to fabricate 3×3 MSC arrays is also demonstrated (Fig. 7.9). Digital photographs of an undeformed, compressed, and twisted 4×4 MSC array are shown in Figs. 7.5(c), (d), and (e), respectively. An optical microscope image of the interdigital SWCNT electrodes is shown in Fig. 7.5(f). The width of the electrode fingers is 500 µm, whereas the gap between the fingers is 200 µm. The top-view scanning electron microscope (SEM) image shown in Fig. 7.5(g) reveals that the spray-deposition process produced a network of randomly entangled SWCNTs. A transmission electron microscope (TEM) image of the SWCNTs is shown in the inset of Fig. 7.5(g). The size of the SWCNT bundles ranges from 10 to 30 nm, while the specific surface area of the

SWCNTs is equal to ~400 m^2 g^{-1}. Fig. 7.5(h) shows a cross-sectional SEM image of MSC electrodes fabricated on a silicon substrate. The thickness of the SWCNT layer deposited onto the Cr/Au bilayer is equal to ~280 nm.
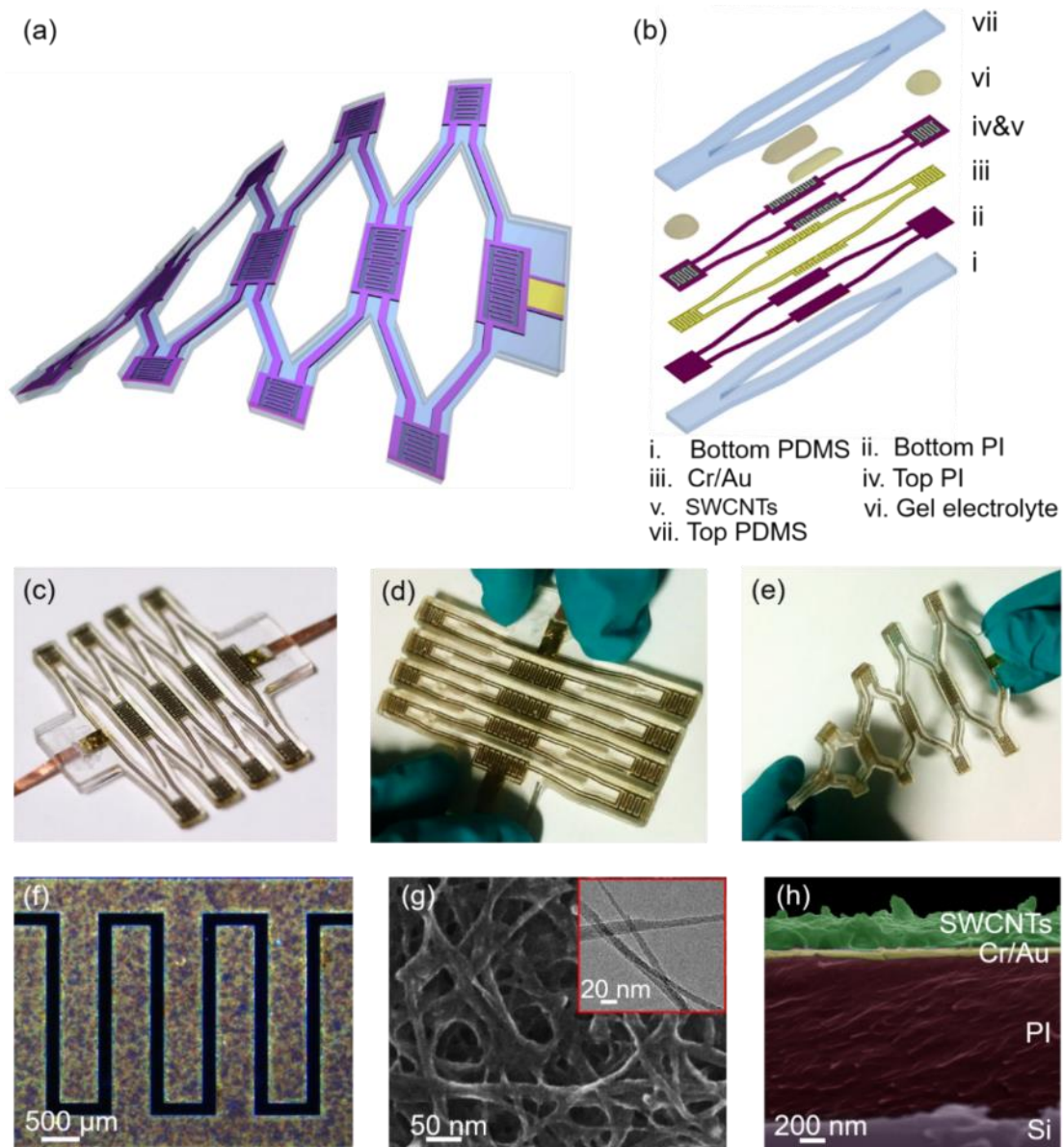
Fig. 7.5 Undeformed and deformed configurations, structural layers, and electrode microstructure of honeycomb 4 × 4 MSC arrays: (a) schematic illustration of a stretched and bended device, (b) exploded view of various structural layers of the device, digital photograph of a (c) undeformed, (d) compressed, and (e) twisted and stretched device, (f) optical microscope image of the interdigital SWCNT electrodes, (g) top-view SEM image of the SWCNT electrodes (the inset figure shows a TEM image of the SWCNTs), and (h) cross-sectional SEM image of the device on a silicon substrate (each layer is distinguished by a different color for clarity).
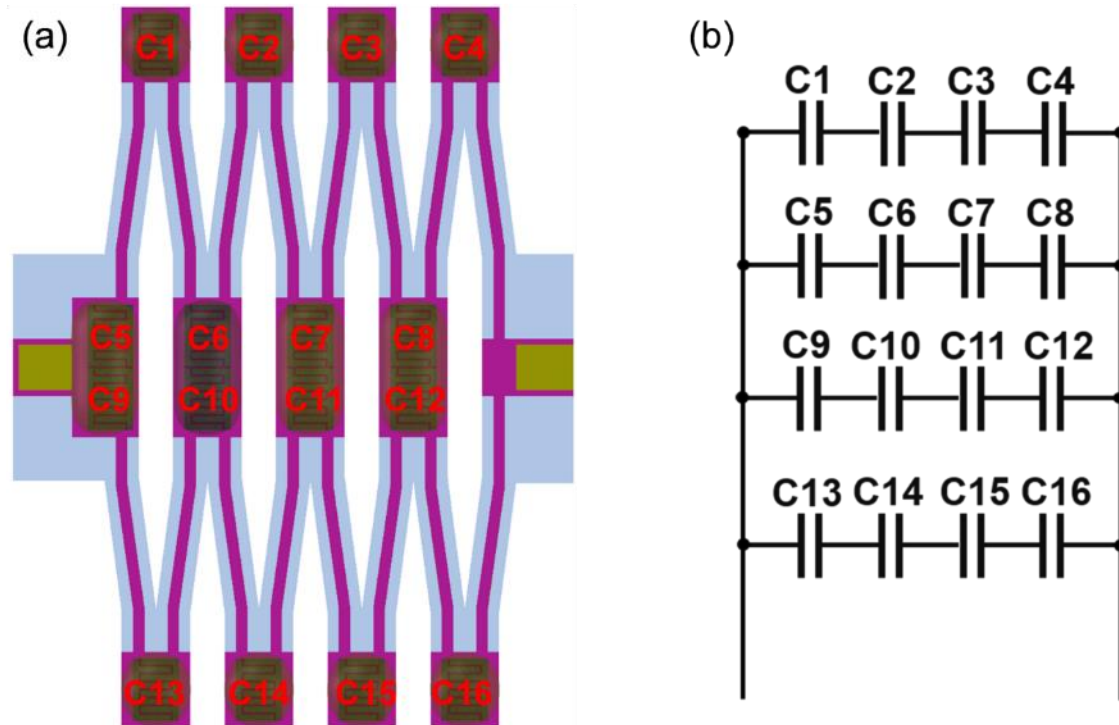
Fig. 7.6 (a) Schematic diagram showing the location of MSCs in a 4 × 4 MSC array and (b) corresponding circuit diagram.
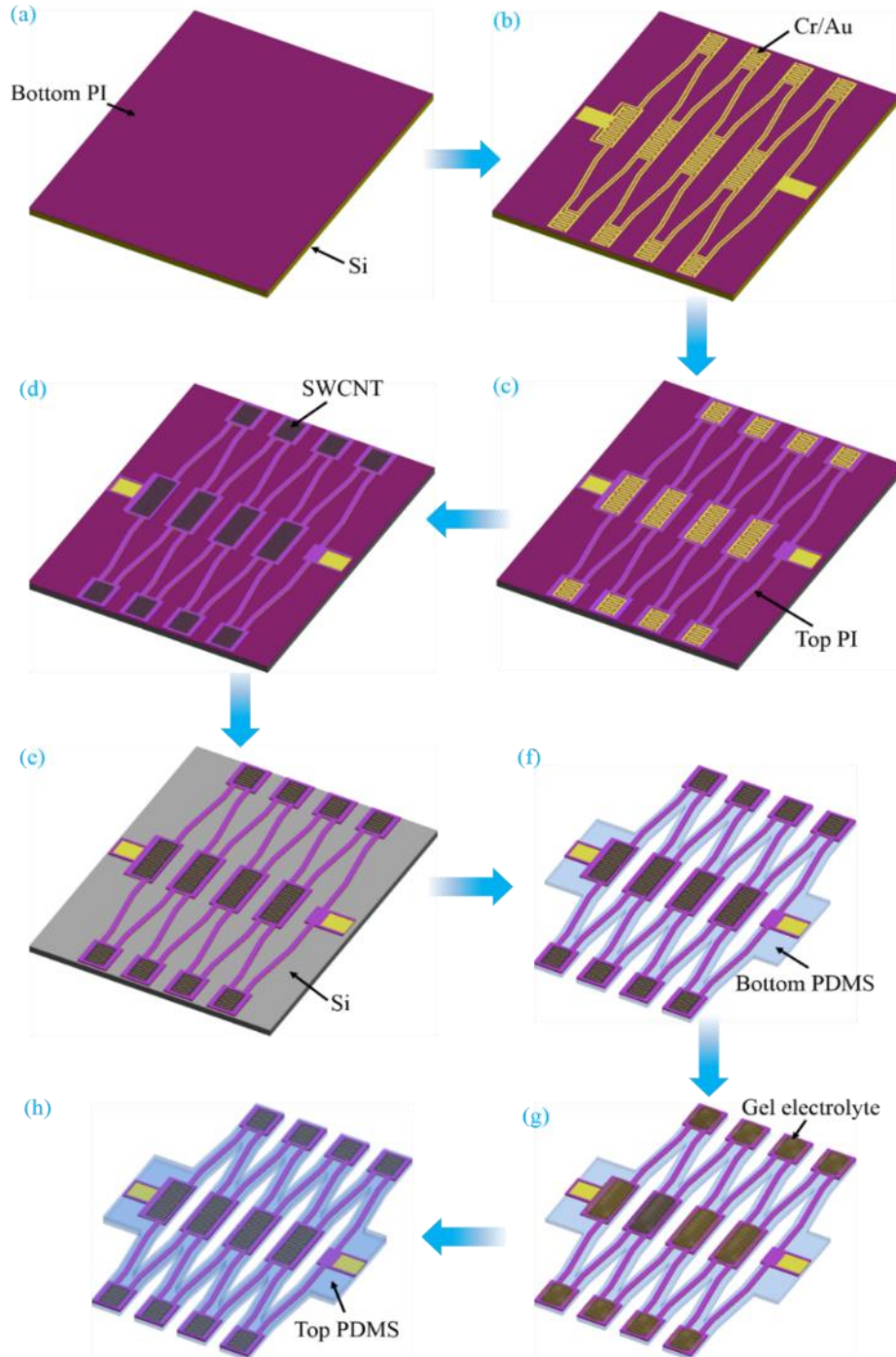
Fig. 7.7 Fabrication process of stretchable 4 × 4 MSC arrays: (a) spin coating of the bottom PI layer on a Si wafer, (b) evaporation and micropatterning of the Cr/Au bilayer, (c) spin coating and micropatterning of the top PI layer, (d) spray deposition and micropatterning of the interdigital SWCNT electrodes, (e) selective etching of the bottom PI layer, (f) transfer of the device onto a honeycomb PDMS substrate, (g) coating of the interdigital SWCNT electrodes with gel electrolyte, and (h) application of the top honeycomb PDMS superstrate to encapsulate the MSC array.
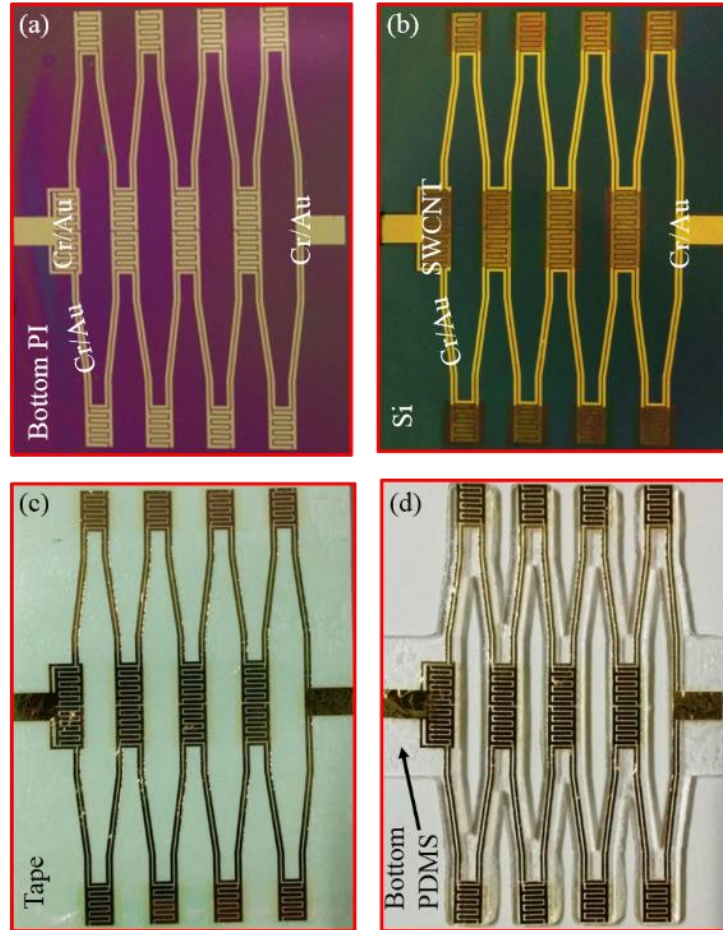
Fig. 7.8 Digital photographs of a stretchable 4 × 4 MSC array at characteristic fabrication stages: (a) patterned Cr/Au bilayer on a PI-coated Si substrate, (b) patterned interdigital SWCNT electrodes on top of the interdigital Cr/Au bilayer pattern, (c) peeled off device attached to a water dissolvable tape, and (d) device transferred onto the honeycomb bottom PDMS substrate.
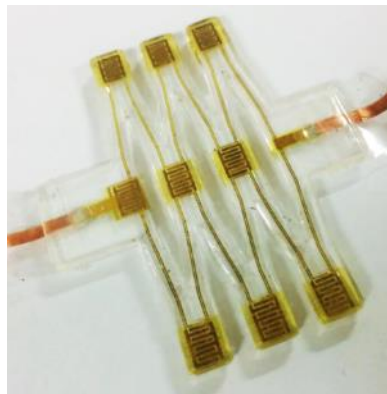
Fig. 7.9 Digital photograph of an undeformed 3 × 3 MSC array.

Figs. 7.10(a) and (b) show typical CV curves of a single MSC and a 4 × 4 MSC array, respectively, for a scan rate of 10, 50, and 100 V s–1. Both devices show nearly rectangular CV curves, even for a scan rate as high as 100 V s–1, which is indicative of the good capacitive performance and excellent rate capability of the devices. The SWCNT electrodes on the Au current collector have a much higher current compared with bare Au electrodes (Fig. 7.3). The output voltage of the 4 × 4 MSC array extends to 3 V (Fig. 7.10(b)), while that of the 3 × 3 MSC array extends to 2.4 V (Fig. 7.11). For a low scan rate of 0.05 V s^{-1}, the volumetric capacitance C_V of the single MSC with SWCNT electrodes is equal to 1.86 F cm^{-3} (areal capacitance C_A = 521 nF cm^{-2}), decreasing to 1.6 F cm^{-3} (C_A = 448 nF cm^{-2}) upon the increase of the scan rate to 1 V s^{-1} (Fig. 7.10(c)). Further increasing the scan rate to 100 V s^{-1} causes the volumetric capacitance of the single MSC to decrease to 1.0 F cm^{-3} (C_A = 280 nF cm^{-2}), representing ~54% and ~63% of the capacitance at a scan rate of 0.05 and 1.0 V s^{-1}, respectively.

The electrochemical properties of the SWCNT MSCs can be further elucidated by comparing their performance with those of other MSCs. The volumetric capacitance of the SWCNT MSCs is comparable with those of most reported electric double-layer capacitor (EDLC) MSCs (0.2–3 F cm^{-3}) [19–23]. Some other reported EDLC MSCs, such as graphene microribbon MSCs [18] and reduced graphene oxide MSCs [24], show a higher volumetric capacitance, but poorer rate capability and frequency response. Electrochemically reduced graphene oxide MSCs [25] and vertically aligned multi-walled carbon nanotube MSCs [26] show a similar high rate capability but lower volumetric capacitance compared with the SWCNT MSCs of this study. A more detailed comparison of different EDLC MSCs is given in Table 7.1. For a scan rate of 0.05 V s^{-1}, the volumetric capacitance of the 4 × 4 MSC arrays is equal to 0.15 F cm^{-3} (C_A = 42 nF cm^{-2}), decreasing to 0.08 F cm^{-3} (C_A = 22.4 nF cm^{-2}) with the increase of the scan rate to 100 V s^{-1}, representing 53% capacitance retention (Fig. 7.10(c)). (For the calculation of the volumetric capacitance see Methods.)

The galvanostatic charge/discharge (GCD) curves of the single MSC (Fig. 7.10(d)) and 4 × 4 MSC array (Fig. 7.10(e)) are fairly symmetric, approximately triangular, and do not demonstrate an obvious IR drop, *i.e.*, a sudden voltage drop at the onset of GCD discharging. This is indicative of the high coulombic efficiency, fast charge propagation across the electrodes, and low equivalent series resistance (ESR) of these devices. The excellent performance of the current devices is also illustrated by Ragone plots (Fig. 7.10(f)). The single MSC and 4 × 4 MSC array exhibit a maximum volumetric energy density of 0.17 and 0.18 mWh cm^{-3} and a maximum volumetric power density of 40 and 11 W cm^{-3}, respectively. This performance is comparable with that of previously reported high-performance EDLC MSCs [21,27–29].
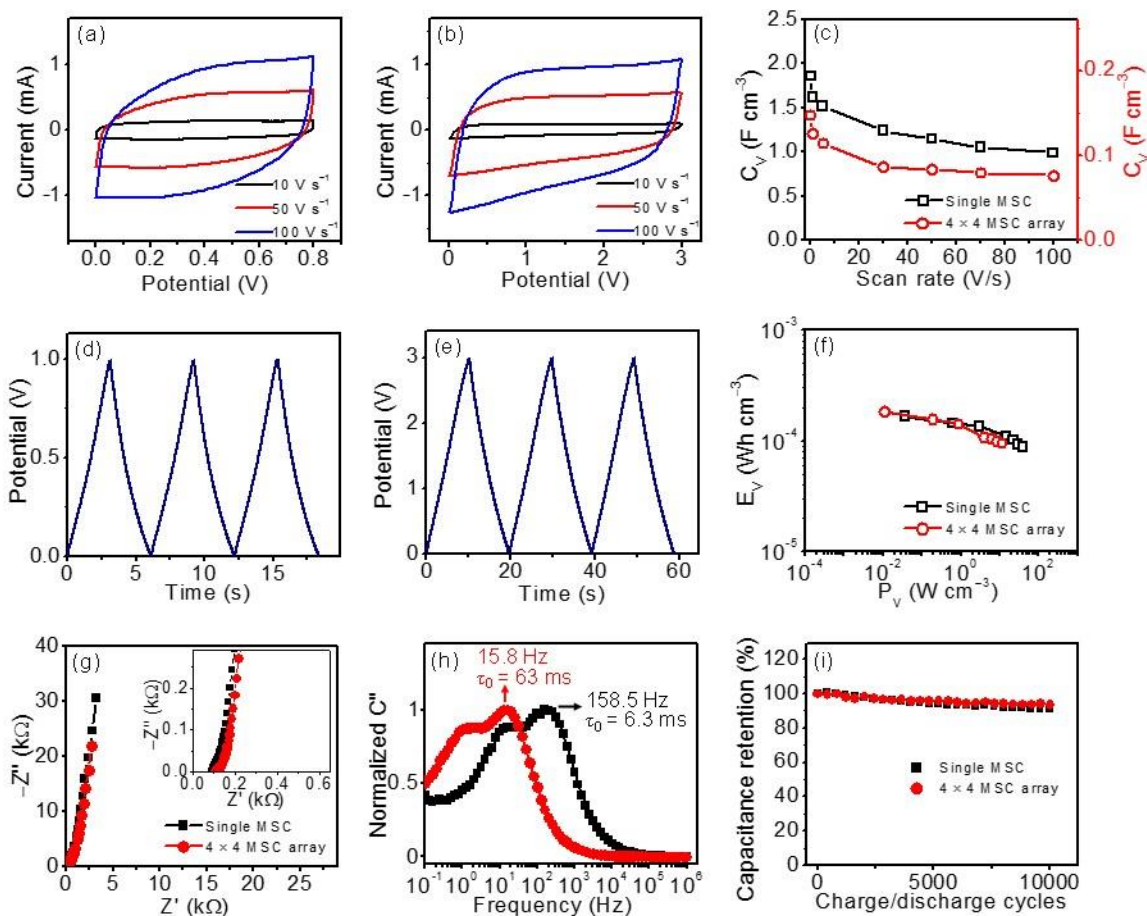
Fig. 7.10 Electrochemical performance of honeycomb single MSCs and 4 × 4 MSC arrays: (a) and (b) typical CV curves of single MSC and 4 × 4 MSC array, respectively, for a scan rate of 10, 50, and 100 V s⁻¹, (c) volumetric capacitance C_V versus scan rate, (d) and (e) potential versus time (GCD plot) for 5 nA applied current of single MSC and 4 × 4 MSC array, respectively, (f) volumetric energy density E_V versus power density P_V (Ragone plot), (g) imaginary impedance Z'' versus real impedance Z' (Nyquist plot), (h) normalized imaginary capacitance C'' versus frequency, and (i) capacitance retention versus charge/discharge cycles.

Table 7.1 Performance comparison of MSCs developed in this work and previous studies.

Electrode material	Electrode thickness (μm)	Electrolyte	Volumetric capacitance	Capacitance retention	Time constant τ_0 (ms)	Ref.
SWCNT	0.28	PVA-H_3PO_4	1 F cm^{-3} @ 100 V s^{-1}	54% @ 0.05–100 V s^{-1} 63% @ 1–100 V s^{-1} 72% @ 1–50 V s^{-1}	6.3	This work
RGO-CNT (9:1)	6	3 M KCl	3 F cm^{-3} @ 50 V s^{-1}	60% @ 1–50 V s^{-1}	4.8	[22]
Onion-like carbon	7	1 M Et$_4$NBF$_4$/ anhydrous C$_4$H$_6$O$_3$	~0.7[b] F cm^{-3} @ 100 V s^{-1}	~53% @ 1–100 V s^{-1}	26	[23]
SWCNT	~3.5	3.6 M H_2SO_4	1.04 F cm^{-3}		7	[24]
Direct laser-write porous carbon	33[a]	PVA-H_3PO_4	0.24 F cm^{-3} @ 0.01 V s^{-1}	~3%[b] @ 0.01–100 V s^{-1}		[25]
Nanoporous carbon	1–40	0.2 M K_2SO_4	2.0[c] F cm^{-3} @ 1 V s^{-1}	15% @ 0.01–1 V s^{-1}		[26]
RGO	0.025	PVA-H_3PO_4	359 F cm^{-3} @ 0.005 V s^{-1}	~42%[b] @ 0.005–1 V s^{-1}		[27]
Graphene microribbon	0.1–0.44	PVA-H_2SO_4	(13–20)[c] F cm^{-3} @ 0.5 V s^{-1}	~40%[b] @ 0.05–1 V s^{-1}		[21]
ERGO	20	25% KOH	0.24 F cm^{-3} @ 40 μA cm^{-2}	~93% @ 40–800 μA cm^{-2}	1.35	[28]
va-MWCNT	15	LiPF$_6$	~0.11[d] F cm^{-3} @ 100 V s^{-1}	~41%[d] @ 1–100 V s^{-1}	2.23	[29]

RGO = reduced graphene oxide; ERGO = electrochemically reduced graphene oxide; va-MWCNT = vertically aligned multi-walled carbon nanotubes

[a]Estimated from volumetric and areal capacitance data from the literature

[b]Estimated from specific capacitance vs scan rate data from the literature

[c]Estimated from areal capacitance and electrode thickness data from the literature
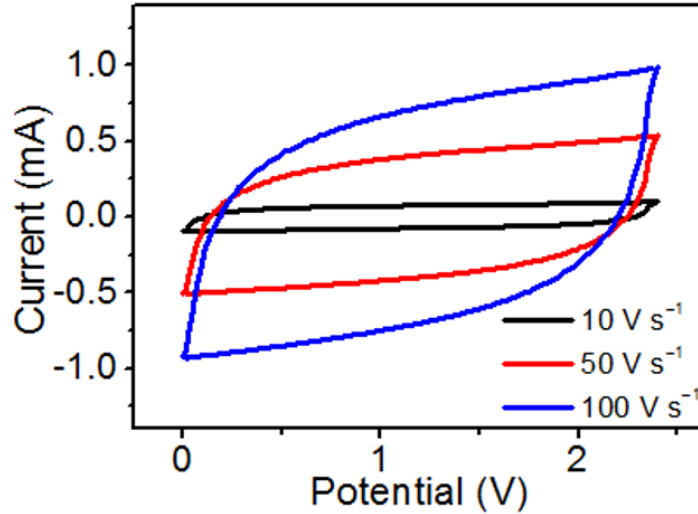
[d]Estimated from the CV curves and electrode thickness

Fig.7.11 CV curves of a 3 × 3 MSC array for a scan rate equal to 10, 50, and 100 V s^{-1}.

The frequency response of the devices was also examined by electrochemical impedance spectroscopy (EIS). A straight line with a ~90° slope was observed in the low-frequency region of the Nyquist plot (Fig. 7.10(g)) of both single MSC and 4 × 4 MSC array (see inset of Fig. 7.10(g)), which is illustrative of a nearly ideal capacitive performance. The absence of a semicircle-like response in the high-frequency region of the Nyquist plots indicates an ultrahigh ionic conductivity at the electrode/electrolyte interface [30] of the devices, which is consistent with the observed ultrahigh rate capability and high-power performance. The slightly higher ESR (estimated from the *x*-intercept in the Nyquist plots) of the 4 × 4 MSC array (106 Ω) compared with the single MSC (91 Ω) is attributed to the higher electrical resistance due to the longer Au interconnects in the 4 × 4 MSC array.

For a more informative analysis of the EIS results, the frequency dependence of the normalized imaginary part *C″* of the capacitance was examined (Fig. 7.10(h)). The fast frequency response of both single MSC and 4 × 4 MSC array is illustrated by the short relaxation time constant τ_0, which represents the minimum time for fully discharging the device with an efficiency of >50% [20,31], determined from the peak frequency f_0 of *C″* by $\tau_0 = 1/f_0$. The extremely small relaxation time constant ($\tau_0 = 6.3$ ms) of the single MSC further confirms the ultrafast charge/discharge and excellent power performance of this device. The relaxation time constant of the SWCNT MSCs ($\tau_0 = 63$ ms) is significantly lower than that of conventional EDLC MSCs ($\tau_0 \approx 10$ s) and comparable with that of aluminum electrolytic capacitors ($\tau_0 \approx 1$ ms) and high-rate MSCs ($\tau_0 = 1$–30 ms) (see Table 7.1). Nevertheless, the 4 × 4 MSC array shows a ten times higher relaxation time constant because of its intrinsically higher electrical resistance, which agrees well with the Nyquist plots (Fig. 7.10(g)). The relaxation time constant of the 4 × 4 MSC arrays can be further decreased by increasing the thickness of the Au layer. Fig. 7.10(i) provides insight into the electrochemical stability of the single MSC and 4 × 4 MSC array. Both devices maintain more than 90% of their initial capacitance even after 10,000 charge/discharge cycles. Moreover, the devices show good encapsulation capacity of gel electrolyte, as revealed by

the similar CV responses obtained soon after fabrication (day 0) and 5 days later (see Fig. 7.12).
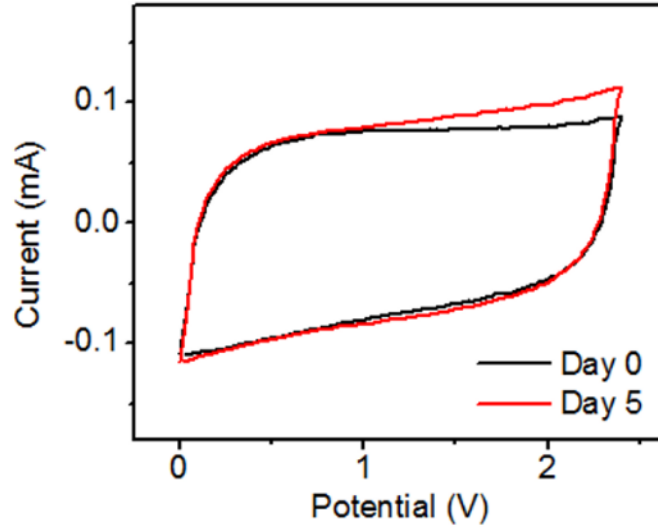

Fig. 7.12 CV curves of a 3 × 3 MSC array obtained soon after fabrication (day 0) and 5 days later.

The strain distribution in the stretchable MSC arrays during stretching was calculated with the multi-physics FEA code ABAQUS. Details about the three-dimensional (3D) FEA are given in Methods. A remarkably good agreement was found between the deformed configurations obtained from the FEA for the entire compression/elongation range examined in this study (*i.e.*, from –50% compression to 150% elongation) and optical images of the deformed devices (Fig. 7.13). The regions where the MSCs are located, referred to as the islands of the device (Fig. 7.14), hardly deform and the deformation of the whole structure is accommodated by the shrinkage (enlargement) of the voids when the device is subjected to compression (stretching). For a compression of –50%, ε_{max} in the Au layer is equal to 0.018, whereas for an elongation of 50%, 100%, and 150%, ε_{max} is equal to 0.023, 0.049, and 0.082, respectively (Fig. 7.13, right column).

The deformation of the honeycomb structure during stretching comprises two stages. For the 4 × 4 MSC array with a four-cell honeycomb structure, the first stage of deformation includes the increase of the distance between the islands and the bending of the beams (see Fig. 7.14) connecting the islands. This deformation stage represents stretching up to 100%–120%. As the stretching increases to ~150%, the beams are also gradually stretched and the strain begins to rapidly increase. This is defined as the practical stretching limit of the device. If the compression is regarded as a prestrain in the device and the reference (initial) state of the stretching process, a zero nominal strain can be assigned to –50% prestrain. Thus, –50% prestrain increases the stretching limit of the whole system to 275% (see the red color data in the left column of Fig. 7.13). In the subsequent analysis and discussion, stretching refers to the elongation applied to an undeformed device, *i.e.*, zero prestrain.
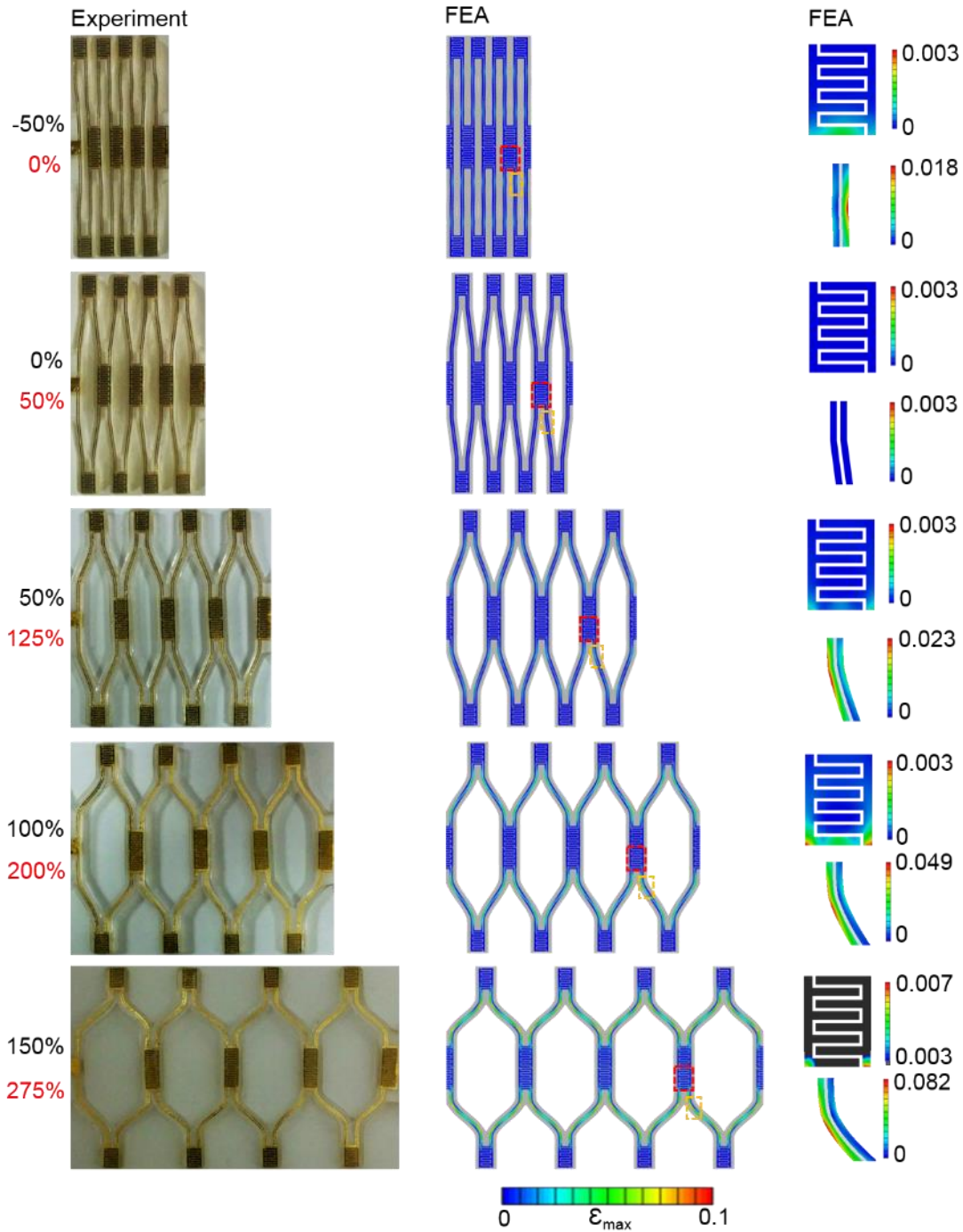
Fig. 7.13 Mechanical performance of honeycomb 4 × 4 MSC arrays: Optical images of device configuration at different deformation stages (left column) and corresponding FEA results of maximum (first principal) strain ε_{max} (middle and right columns). The right column shows the distribution of ε_{max} in capacitor and interconnect regions, respectively indicated by red and yellow dashed-line rectangular frames in the middle column.
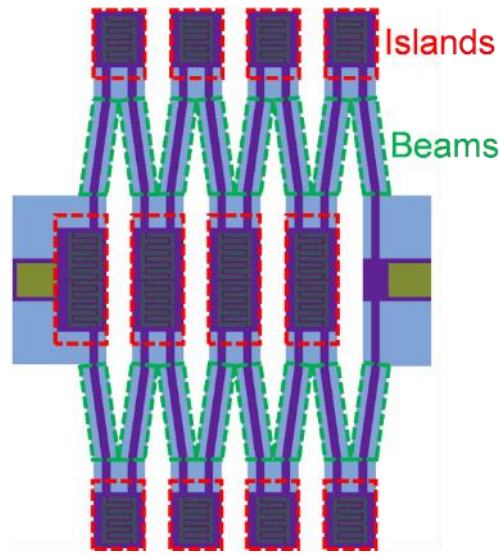
114

Fig. 7.14 Schematic illustration of regions referred to as the islands and beams of a 4 × 4 MSC array.

During stretching up to 150%, high strains develop at the corners of the PDMS substrate, whereas the strains in the islands and central beam regions are significantly smaller (Fig. 7.15(a)), confirming the very small strains in the MSCs and interconnects due to the honeycomb structure of the device. For 150% stretching, ε_{max} in the PDMS substrate is equal to 0.37 (Fig. 7.15(a)), whereas ε_{max} in the bottom PI, Au, and top PI layers is equal to 0.082 and is highly localized (Figs. 7.15(b–d)). Crack initiation at the sharp corners of the PDMS substrate occurred when the 4 × 4 MSC array was stretched to an elongation of 150%, while fracture commenced when the device was stretched to ~180%. The device stretchability can be further improved by rounding off the corners of the PDMS substrate. The islands where the MSCs are located experience almost rigid-body motion during the whole stretching process and the central regions of the beams where the interconnects are located have relatively lower strains than the corner regions of the beams. The deformation of the 3 × 3 MSC array with a three-cell honeycomb structure is similar to that of the 4 × 4 MSC array. FEA and experimental results of the 3 × 3 MSC array (Fig. 7.16) show that this device can be stretched up to ~100% (zero prestrain) or 200% (–50% prestrain). For 100% stretching, ε_{max} in the bottom PDMS, top PI, Au, and bottom PI layers of the 3 × 3 MSC array is 0.2, 0.024, 0.024, and 0.024, respectively (Fig. 7.17). Crack initiation in the 3 × 3 MSC array was also observed to occur at the sharp corners of the PDMS substrate when the device was stretched beyond 100% and fracture when the elongation was increased to ~120%.

Fig. 7.15 Distribution of maximum (first principal) strain ε_{max} in the (a) bottom PDMS, (b) bottom PI, (c) Au, and (d) top PI layers of a 4 × 4 MSC array stretched by 150%.

A comparison of the CV responses for fixed scan rate (10 V s^{-1}) provided further insight into the effect of stretching on the device capacitance. Practically identical CV curves were observed for 4 × 4 MSC arrays compressed by –50% and stretched up to 150% (Fig. 7.18(a)) and for 3 × 3 MSC arrays compressed by –50% and stretched up to100% (Fig. 7.19). Three consecutive stretching cycles were simulated to examine the stress-strain response of various structural materials of the 4 × 4 MSC arrays. The stress-strain curves of the PI layer, Au interconnect, and Au capacitor obtained from FEA simulations of cyclic stretching up to 100% (see Fig. 7.20) show that after three stretching cycles of maximum elongation equal to 100%, ε_{max} in the PI layer and the Au capacitor is about 0.049 and 0.003, respectively, whereas ε_{max} in the Au interconnects after the first stretching cycle is equal to 0.049.

Fig. 7.16 Optical images of a 3 × 3 MSC array at different deformation stages (left column) and corresponding FEA results of maximum (first principal) strain ε_{max} in the Au layer (right column).
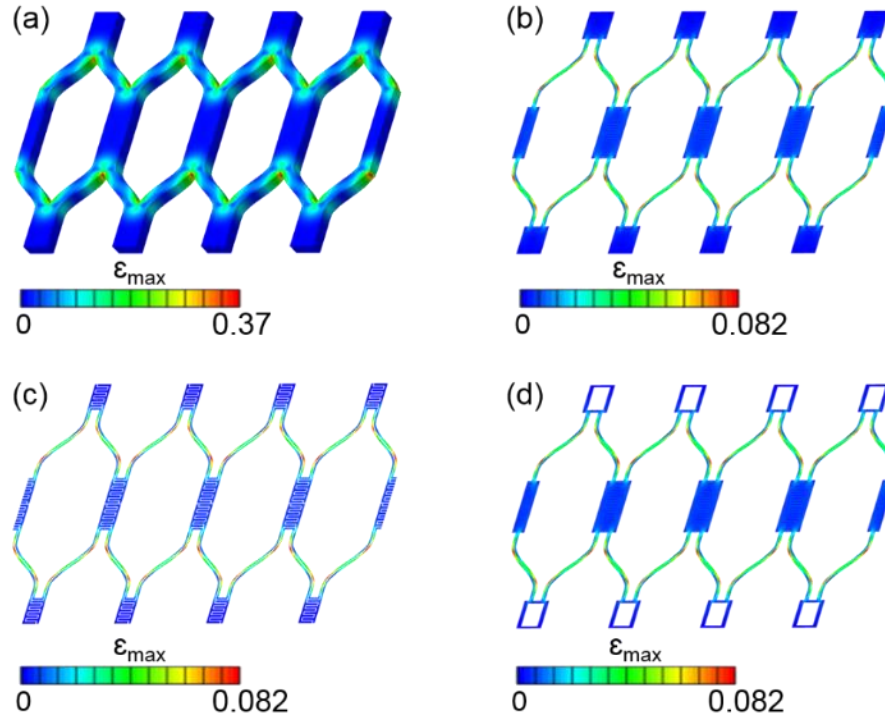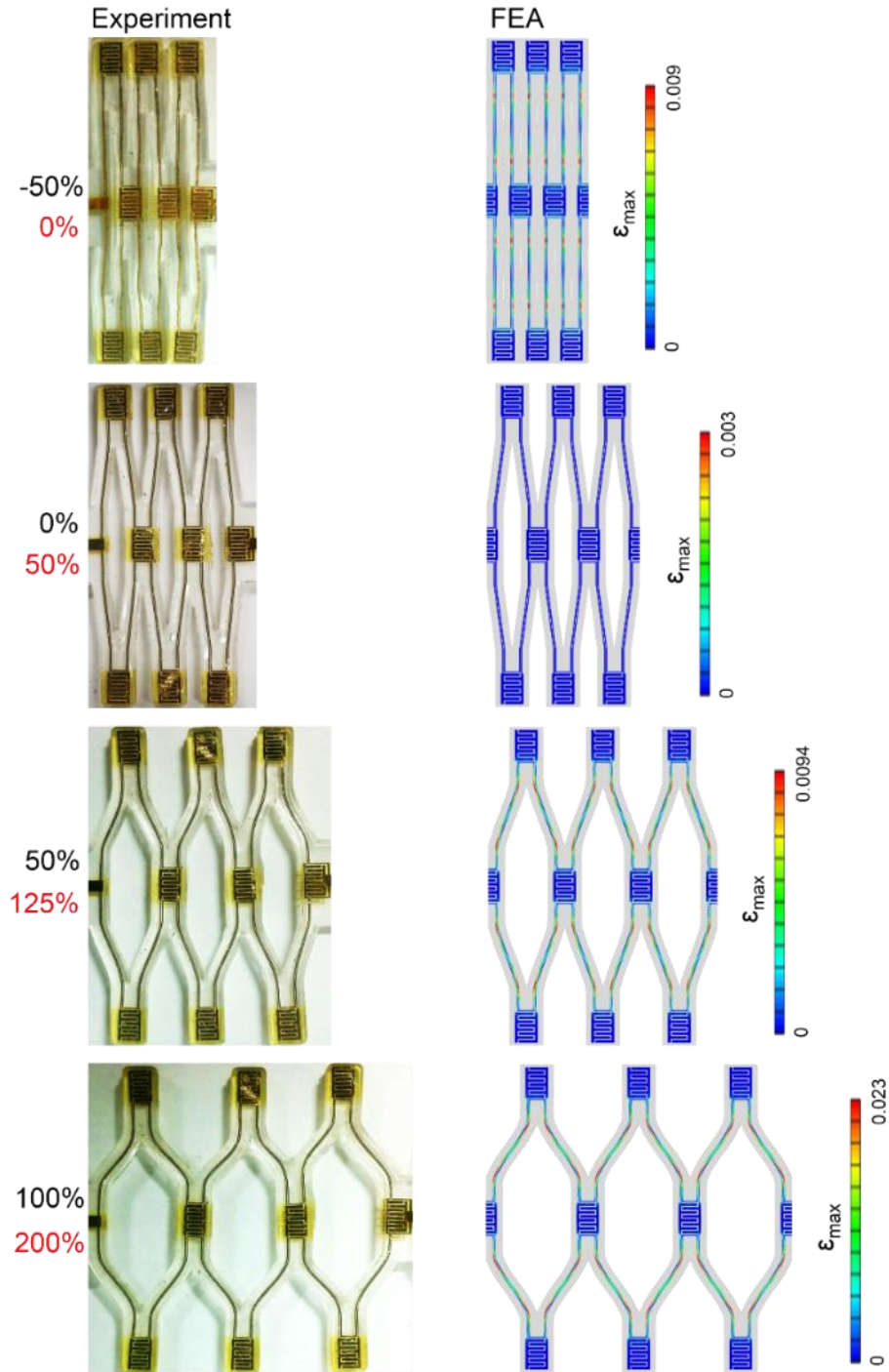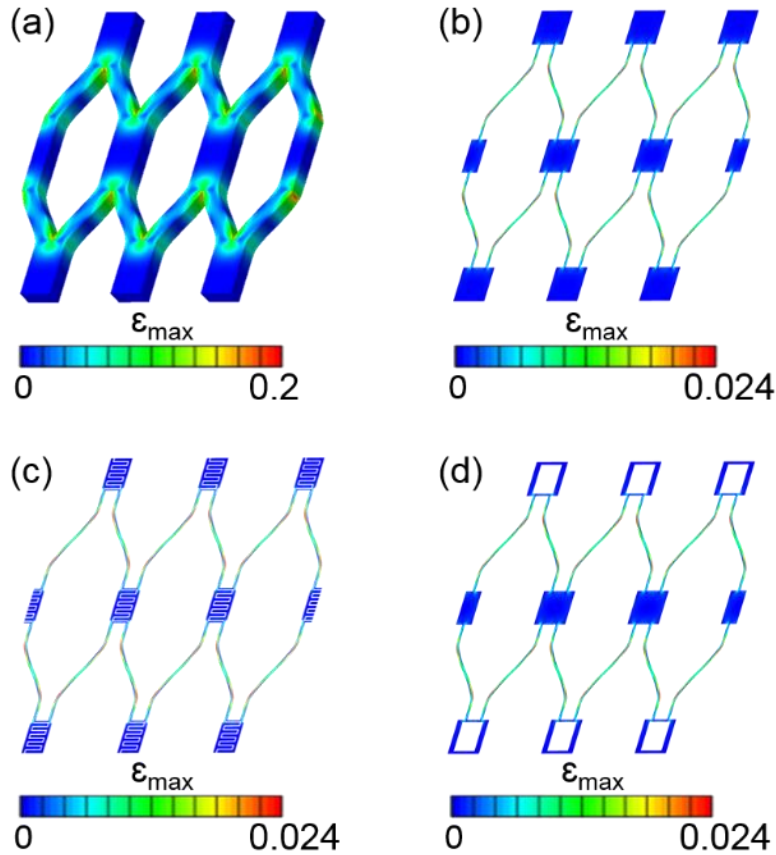
Fig. 7.17 Distribution of maximum (first principal) strain ε_{max} in the (a) bottom PDMS, (b) bottom PI, (c) Au, and (d) top PI layers of a 3 × 3 MSC array stretched by 100%.

As discussed above, the islands in the honeycomb structure exhibit nearly rigid-body motion and very low strain during stretching; thus, these regions are dedicated to functional materials and electronic devices (*e.g.*, MSCs) which should be protected from large strain. The honeycomb structure enables facile integration of various electronic devices on a substrate. For example, the MSC array can be integrated with an energy harvester and a power management circuit on a honeycomb substrate to form a self-powered system, in which the energy collected by the energy harvester passes through a power management circuit and is stored in the MSC array for powering other electronic units, such as sensors, actuators, and miniaturized displays. The integration of a power management chip with a stretchable 3 × 3 MSC array was also demonstrated in this study (Fig. 7.21). Further work will be carried out to integrate an energy harvester in the same system and demonstrate its functionality.
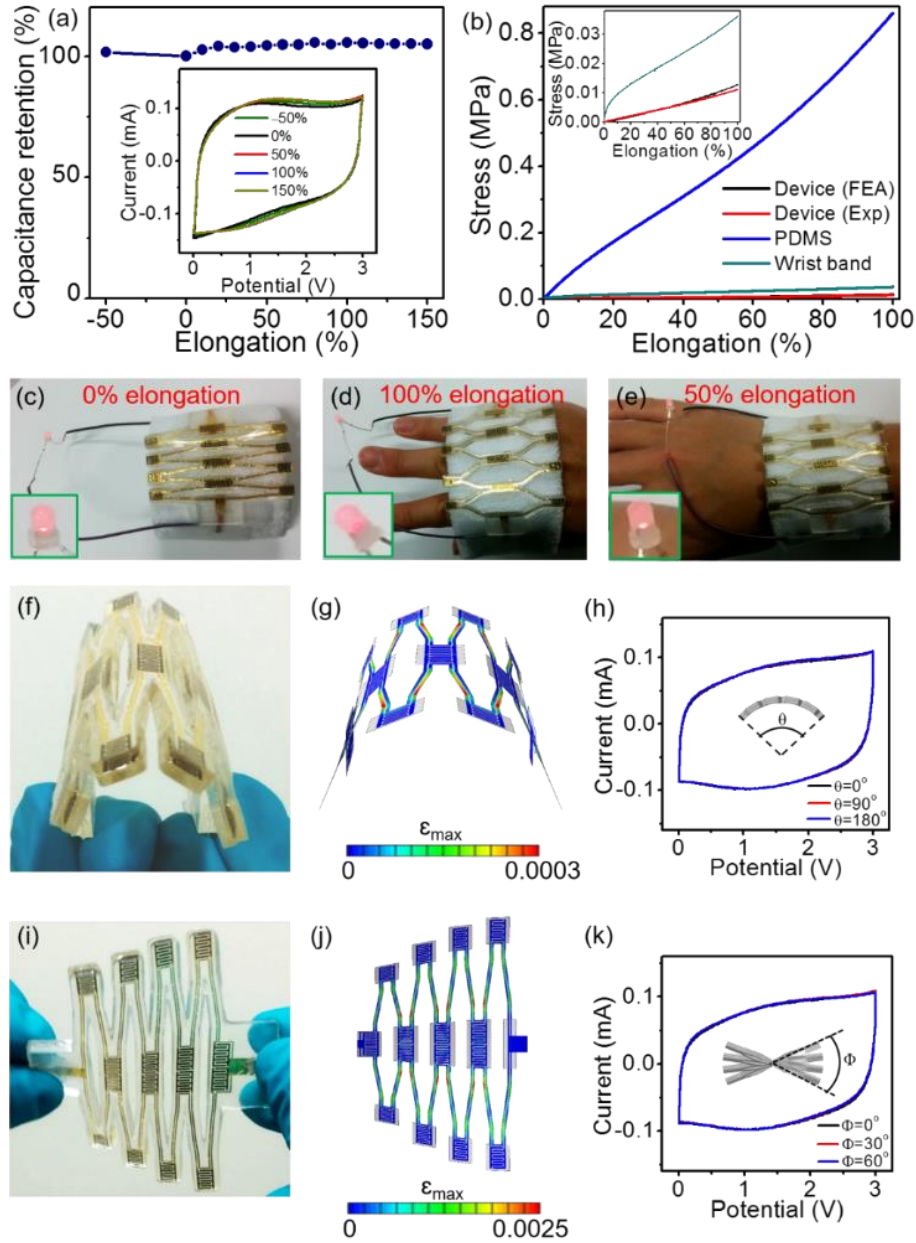
Fig. 7.18 Electrical and mechanical performance of honeycomb 4 × 4 MSC arrays: (a) capacitance retention versus elongation (the inset figure shows CV curves for –50% compression and 0–150% elongation), (b) experimental stress-strain curves of honeycomb MSC, solid PDMS membrane, and Nike wrist band (the FEA stress-strain curve of the honeycomb MSC is also included for analysis validation), (c)–(e) a commercial LED (turn-on voltage = 2 V, operation current ≈ 20 mA) lit by a honeycomb MSC device bonded to a Nike wrist band at different elongations, (f) digital photograph of a honeycomb MSC bended by 180º and (g) corresponding maximum (first principal) strain ε_{max} distribution in the Au layer, (i) digital photograph of a honeycomb MSC twisted by 60º and (j) corresponding ε_{max} distribution in the Au layer, and overlapping CV curves for different (h) bending and (k) twisting angles.

Fig. 7.19 Capacitance retention versus elongation of a 3 × 3 MSC array (the inset figure shows CV curves for –50% compression and 0–100% elongation).

An application example of stretchable electronics is the smart wrist band system. The objective here is to self-power these wearable electronics by storing in the MSC arrays the energy harvested from sport activities. For this purpose, a stretchable device must possess adequate stretchability, excellent mechanical stability, and sufficient compliance (softness) to prevent discomfort to the u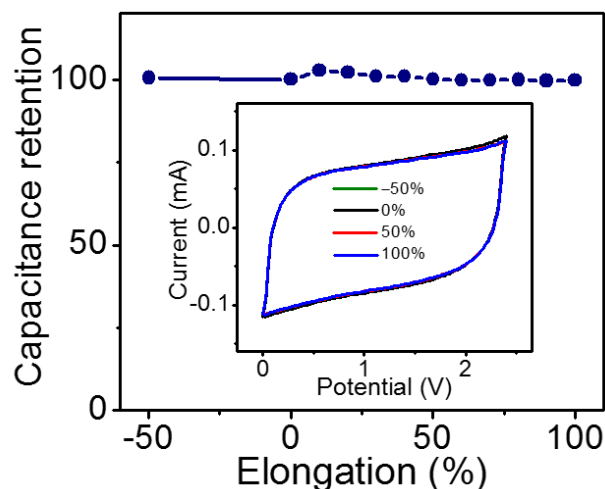ser. As observed in the trial tests of this study, the in-use maximum elongation of a wrist band is ~100%, which is smaller than the stretchability limit of the devices presented here. To verify that the honeycomb devices are softer and more compliant compared with wrist bands and flat PDMS membranes, tensile tests were performed in the 0–100% stretching range (Fig. 7.4). A Nike wrist band and a solid PDMS membrane were used as controls in these tests. In both tensile experiments and FEA simulations, a honeycomb cell of a 4 × 4 MSC array was subjected to three stretching cycles of 100% maximum elongation. The stress-strain curves of the honeycomb device obtained from these experiments and FEA simulations are nearly identical (Fig. 7.18(b)). The elastic modulus of the device extracted from the tensile tests and simulations is equal to 11 and 12.6 kPa, respectively, showing a good agreement between experiments and FEA. Moreover, the slopes of the stress-strain curves of the honeycomb device are much smaller than those of the PDMS membrane and the Nike wrist band (see inset of Fig. 7.18(b)), a proof of the greater compliance of the present devices. The elastic modulus of the Nike wrist band (~30 kPa) is about three times higher than that of the honeycomb device. The PDMS membrane exhibits a two-stage stress-strain response. In the 0–65% elongation range, the elastic modulus of the PDMS membrane is equal to 1.07 MPa, increasing to 1.26 MPa with the increase of the elongation above 65%. Both of these elastic modulus values are two orders of magnitude higher than the elastic modulus of the honeycomb devices. The stiffening of the PDMS membrane encountered for elongations >65% is due to the unraveling and stretching of the polymer chains. Therefore, the present honeycomb devices demonstrate high potential for wrist band systems.
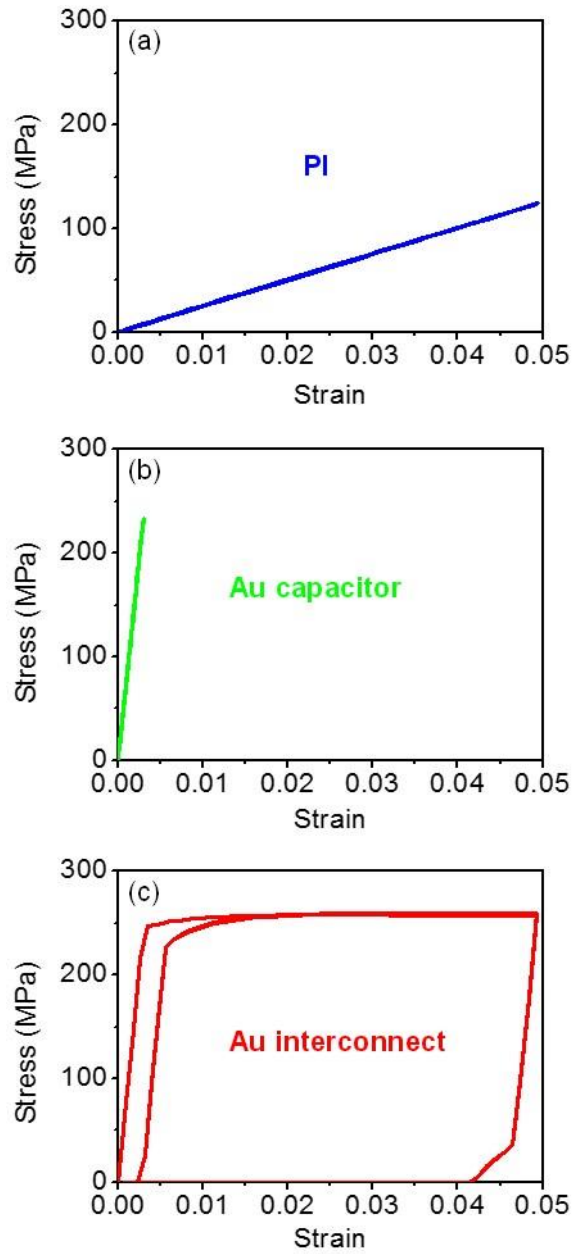
Fig. 7.20 FEA simulations of a three-cycle stress-strain response of (a) PI layer, (b) Au capacitor, and (c) Au interconnect of a 4 × 4 MSC array for stretching up to 100%.
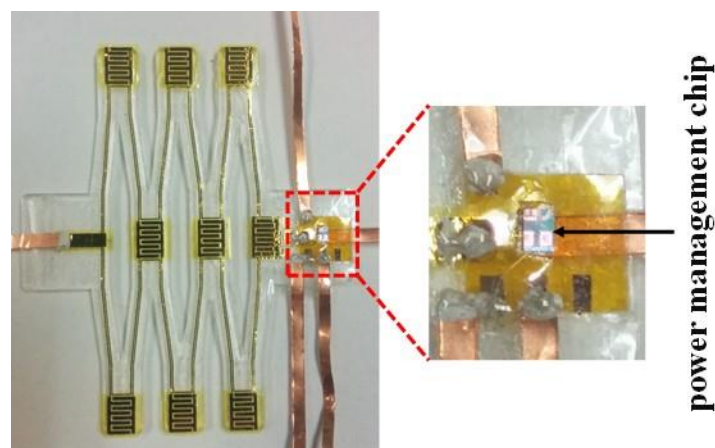
Fig. 7.21 A 3 × 3 MSC array integrated with a power management chip on a honeycomb substrate.

Fig. 7.18(c) shows a commercial LED (turn-on voltage = 2 V, operation current ≈ 20 mA) lit by a 4 × 4 MSC array attached to a honeycomb PDMS substrate, which is bonded to a Nike wrist band. The process of putting on the wrist band with the stretchable device induces stretching of the whole system by 100% (Fig. 7.18(d)), whereas ~50% stretching and slight bending occur during wearing the wrist band (Fig. 7.18(e)). However, neither of the two deformation states produces any noticeable dimming of the LED (Figs. 7.18(d) and 4(e)). Because of the limited energy stored in the very thin SWCNT electrodes, the operation time of the LED lid by the 4 × 4 MSC array was less than 1 s. The energy capacity of the MSC arrays can be increased by depositing a thicker SWCNT film or by modifying the SWCNT electrodes with faradaic capacitance materials, such as a metal oxide or a conductive polymer.

Figs. 7.18(f) and (i) show digital photographs of a 4 × 4 MSC array on a honeycomb PDMS substrate subjected to 180° bending and 60° twisting, respectively. The corresponding deformed configurations obtained from FEA (Fig. 7.22(a) (bending) and Fig. 7.22(b) (twisting)) are in good agreement with experimental results (Fig. 7.18(f) (bending) and Fig. 7.18(i) (twisting)). For 180° bending, $\varepsilon_{\max}$ in the Au layer is equal to 0.0003 (Fig. 7.18(g)), *i.e.*, an order of magnitude smaller than the yield strain of Au (0.003). For all bending angles in the 0°–180° range, $\varepsilon_{\max}$ in the Au layer is significantly below the yield strain (Fig. 7.23(a)). The extremely small strain in the Au layer is intrinsic of the honeycomb structure of the device. Because the Au layer is sandwiched by two identical PI layers and another two identical PDMS substrates, it is located very close to the neutral plane of bending of the whole structure. Twisting introduces larger strains in the device compared with bending. For 60° twisting, $\varepsilon_{\max}$ in the Au layer is equal to 0.0025 (Fig. 7.18(j)). The Au layer exhibits purely elastic deformation in the 0°–60° twisting angle range (Fig. 7.23(b)). Compared with stretching, both bending and twisting generate relatively smaller strains in the Au layer. These results suggest that both 0°–180° bending and 0°–60° twisting are not expected to degrade the electrochemical performance of the honeycomb MSC array. This is confirmed by the CV curves of bended and twisted devices. As shown in Figs. 7.18(h) and 7.18(k), the response of the deformed devices is identical to that of the

undeformed device, confirming the excellent mechanical stability of the stretchable honeycomb devices.

The materials and schemes reported in this work provide guidance for the design of energy storage devices suitable for powering stretchable electronic devices, such as optoelectronics, displays, sensors, and actuators. The nearly rigid-body motion of the islands in the honeycomb structure offers much higher stretchability than previous reports and facile integration of various electronics on the same substrate. The deployment of ultrathin EDLC electrode materials endows the MSCs great flexibility, excellent electrochemical performance, and potential of extending device integration in the thickness direction. Further improvements can be made by optimizing the honeycomb structure to achieve even higher stretchability and surface coverage of effective devices and increase the energy density of honeycomb MSC devices by surface modification of the SWCNTs. The present study provides stimulus for further investigations toward the integration of energy storage devices, power management circuits, and energy harvesters on honeycomb-like highly stretchable substrates, which can enhance the design of self-powered wearable electronics systems.
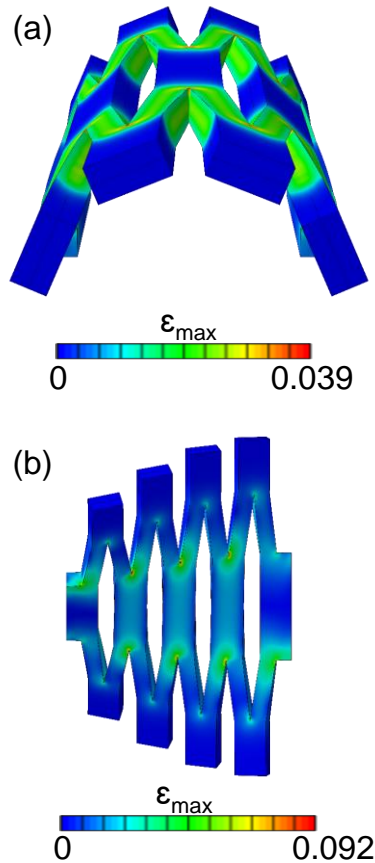

Fig. 7.22 Distribution of maximum (first principal) strain ε_{max} in the PDMS layer of a 4 × 4 MSC array (a) bended by 180º and (b) twisted by 60º.
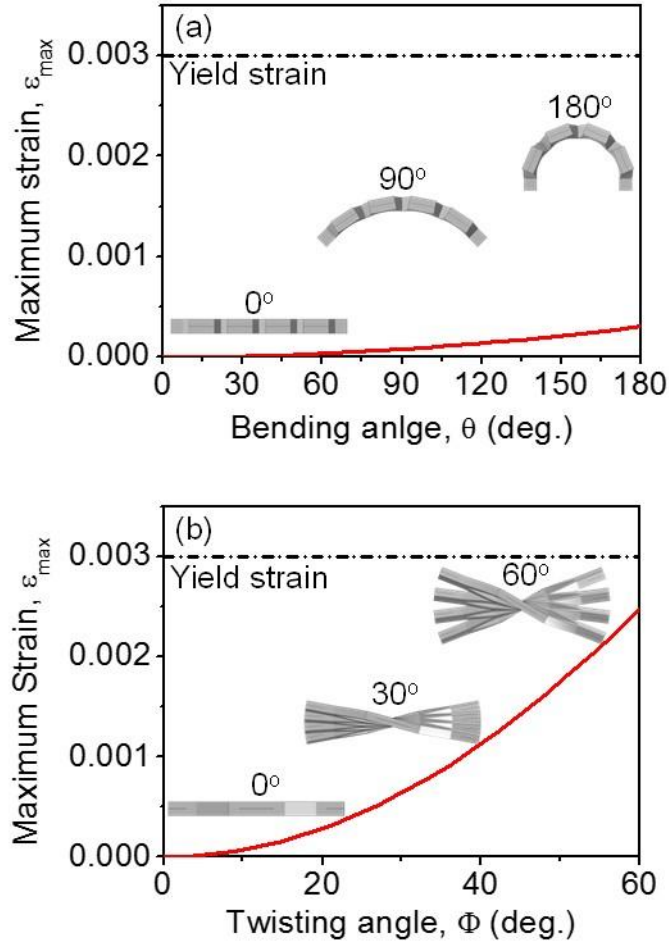
Fig. 7.23 Maximum (first principal) strain ε_{max} in the Au layer of a 4 × 4 MSC array as a function of (a) bending and (b) twisting angle. The inset figures in (a) show side-view schematics of the deformed device for 0º, 90º, and 180º bending angle, whereas the inset figures in (b) show schematics of the deformed device for 0º, 30º, and 60º twisting angle.

7.4 Conclusions

Highly stretchable MSC arrays with SWCNT electrodes and PVA-H_3PO_4 gel electrolyte were fabricated on honeycomb PDMS substrates. A characteristic feature of the design is that the stretchability of the MSC array system is controlled by the deformation of the honeycomb PDMS structure. The devices demonstrate good capacitive performance and excellent rate capability. The FEA simulations revealed remarkably low strains in the MSCs and interconnects even for excessive stretching, bending, and twisting. The device capacitance remained stable even up to 150% stretching, 180º bending, and 60º twisting, a proof of the excellent mechanical stability of the stretchable MSCs. The findings of this work demonstrate the high potential of the present stretchable MSC arrays for a wide application range of wearable electronics, such as wrist and head band systems and wearable computing systems.

7.5 References

[1] Yoon, J., Baca, A.J., Park, S.I., Elvikis, P., Geddes, J.B., Li, L., Kim, R.H., Xiao, J., Wang, S., Kim, T.H. and Motala, M.J., 2008. Ultrathin silicon solar microcells for semitransparent, mechanically flexible and microconcentrator module designs. Nature materials, 7(11), pp.907-915.

[2] Mannsfeld, S.C., Tee, B.C., Stoltenberg, R.M., Chen, C.V.H., Barman, S., Muir, B.V., Sokolov, A.N., Reese, C. and Bao, Z., 2010. Highly sensitive flexible pressure sensors with microstructured rubber dielectric layers.Nature materials, 9(10), pp.859-864.

[3] Takei, K., Takahashi, T., Ho, J.C., Ko, H., Gillies, A.G., Leu, P.W., Fearing, R.S. and Javey, A., 2010. Nanowire active-matrix circuitry for low-voltage macroscale artificial skin. Nature materials, 9(10), pp.821-826.

[4] Kim, D.H., Lu, N., Ma, R., Kim, Y.S., Kim, R.H., Wang, S., Wu, J., Won, S.M., Tao, H., Islam, A. and Yu, K.J., 2011. Epidermal electronics. Science,333(6044), pp.838-843.

[5] Kim, D.H., Lu, N., Ghaffari, R., Kim, Y.S., Lee, S.P., Xu, L., Wu, J., Kim, R.H., Song, J., Liu, Z. and Viventi, J., 2011. Materials for multifunctional balloon catheters with capabilities in cardiac electrophysiological mapping and ablation therapy. Nature materials, 10(4), pp.316-323.

[6] Xu, L., Gutbrod, S.R., Ma, Y., Petrossians, A., Liu, Y., Webb, R.C., Fan, J.A., Yang, Z., Xu, R., Whalen, J.J. and Weiland, J.D., 2015. Materials and fractal designs for 3D multifunctional integumentary membranes with capabilities in cardiac electrotherapy. Advanced Materials, 27(10), pp.1731-1737.

[7] Sekitani, T., Nakajima, H., Maeda, H., Fukushima, T., Aida, T., Hata, K. and Someya, T., 2009. Stretchable active-matrix organic light-emitting diode display using printable elastic conductors. Nature materials, 8(6), pp.494-499.

[8] Hu, X., Krull, P., de Graff, B., Dowling, K., Rogers, J.A. and Arora, W.J., 2011. Stretchable Inorganic-Semiconductor Electronic Systems. Advanced materials, 23(26), pp.2933-2936.

[9] Chen, T., Xue, Y., Roy, A.K. and Dai, L., 2013. Transparent and stretchable high-performance supercapacitors based on wrinkled graphene electrodes.ACS nano, 8(1), pp.1039-1046.

[10] Niu, Z., Dong, H., Zhu, B., Li, J., Hng, H.H., Zhou, W., Chen, X. and Xie, S., 2013. Highly Stretchable, Integrated Supercapacitors Based on Single-Walled Carbon Nanotube Films with Continuous Reticulate Architecture.Advanced Materials, 25(7), pp.1058-1064.

[11] Shen, C., Wang, X., Zhang, W. and Kang, F., 2011. A high-performance three-dimensional micro supercapacitor based on self-supporting composite materials. Journal of Power Sources, 196(23), pp.10465-10471.

[12] Li, S., Wang, X., Xing, H. and Shen, C., 2013. Micro supercapacitors based on a 3D structure with symmetric graphene or activated carbon electrodes.Journal of Micromechanics and Microengineering, 23(11), p.114013.

[13] Pu, J., Wang, X., Zhang, T., Li, S., Liu, J. and Komvopoulos, K., 2015. High-energy-density, all-solid-state microsupercapacitors with three-dimensional interdigital electrodes of carbon/polymer electrolyte composite.Nanotechnology, 27(4), p.045701.

[14] Kim, D., Shin, G., Kang, Y.J., Kim, W. and Ha, J.S., 2013. Fabrication of a stretchable solid-state micro-supercapacitor array. ACS nano, 7(9), pp.7975-7982.

[15] Hong, S.Y., Yoon, J., Jin, S.W., Lim, Y., Lee, S.J., Zi, G. and Ha, J.S., 2014. High-density, stretchable, all-solid-state microsupercapacitor arrays.ACS nano, 8(9), pp.8844-8855.

[16] Lee, G., Kim, D., Kim, D., Oh, S., Yun, J., Kim, J., Lee, S.S. and Ha, J.S., 2015. Fabrication of a stretchable and patchable array of high performance micro-supercapacitors using a non-aqueous solvent based gel electrolyte.Energy & Environmental Science, 8(6), pp.1764-1774.

[17] Lim, Y., Yoon, J., Yun, J., Kim, D., Hong, S.Y., Lee, S.J., Zi, G. and Ha, J.S., 2014. Biaxially stretchable, integrated array of high performance microsupercapacitors. ACS nano, 8(11), pp.11639-11650.

[18] Qi, D., Liu, Z., Liu, Y., Leow, W.R., Zhu, B., Yang, H., Yu, J., Wang, W., Wang, H., Yin, S. and Chen, X., 2015. Suspended wavy graphene microribbons for highly stretchable microsupercapacitors. Advanced Materials, 27(37), pp.5559-5566.

[19] Beidaghi, M. and Wang, C., 2012. Micro-Supercapacitors Based on Interdigital Electrodes of Reduced Graphene Oxide and Carbon Nanotube Composites with Ultrahigh Power Handling Performance. Advanced Functional Materials, 22(21), pp.4501-4510.

[20] Pech, D., Brunet, M., Durou, H., Huang, P., Mochalin, V., Gogotsi, Y., Taberna, P.L. and Simon, P., 2010. Ultrahigh-power micrometre-sized supercapacitors based on onion-like carbon. Nature nanotechnology, 5(9), pp.651-654.

[21] Laszczyk, K.U., Kobashi, K., Sakurai, S., Sekiguchi, A., Futaba, D.N., Yamada, T. and Hata, K., 2015. Lithographically Integrated Microsupercapacitors for Compact, High Performance, and Designable Energy Circuits. Advanced Energy Materials, 5(18).

[22] In, J.B., Hsia, B., Yoo, J.H., Hyun, S., Carraro, C., Maboudian, R. and Grigoropoulos, C.P., 2015. Facile fabrication of flexible all solid-state micro-supercapacitor by direct laser writing of porous carbon in polyimide. Carbon,83, pp.144-151.

[23] Shen, C., Wang, X., Zhang, W. and Kang, F., 2013. Direct prototyping of patterned nanoporous carbon: a route from materials to on-chip devices.Scientific reports, 3.

[24] Niu, Z., Zhang, L., Liu, L., Zhu, B., Dong, H. and Chen, X., 2013. All-Solid-State Flexible Ultrathin Micro-Supercapacitors Based on Graphene.Advanced Materials, 25(29), pp.4035-4042.

[25] Sheng, K., Sun, Y., Li, C., Yuan, W. and Shi, G., 2012. Ultrahigh-rate supercapacitors based on eletrochemically reduced graphene oxide for ac line-filtering. Scientific reports, 2, p.247.

[26] Ghosh, A., Le, V.T., Bae, J.J. and Lee, Y.H., 2013. TLM-PSD model for optimization of energy and power density of vertically aligned carbon nanotube supercapacitor. Scientific reports, 3.

[27] Wang, S., Hsia, B., Carraro, C. and Maboudian, R., 2014. High-performance all solid-state micro-supercapacitor based on patterned photoresist-derived porous carbon electrodes and an ionogel electrolyte. Journal of Materials Chemistry A, 2(21), pp.7997-8002.

[28] Gao, W., Singh, N., Song, L., Liu, Z., Reddy, A.L.M., Ci, L., Vajtai, R., Zhang, Q., Wei, B. and Ajayan, P.M., 2011. Direct laser writing of micro-supercapacitors on hydrated graphite oxide films. Nature Nanotechnology,6(8), pp.496-500.

[29] El-Kady, M.F., Strong, V., Dubin, S. and Kaner, R.B., 2012. Laser scribing of high-performance and flexible graphene-based electrochemical capacitors.Science, 335(6074), pp.1326-1330.

[30] Pushparaj, V.L., Shaijumon, M.M., Kumar, A., Murugesan, S., Ci, L., Vajtai, R., Linhardt, R.J., Nalamasu, O. and Ajayan, P.M., 2007. Flexible energy storage devices based on nanocomposite paper. Proceedings of the National Academy of Sciences, 104(34), pp.13574-13577.

[31] Taberna, P.L., Simon, P. and Fauvarque, J.F., 2003. Electrochemical characteristics and impedance spectroscopy studies of carbon-carbon supercapacitors. Journal of The Electrochemical Society, 150(3), pp.A292-A300.

Chapter 8 – Summary

This dissertation focuses on two main topics – electrospun PLLA microfibers for tissue engineering applications and micro/nanostructured carbon materials, including activated carbon/polymer electrolyte (AC/PE) composite, graphene/polymer electrolyte (Gr/PE) composite and SWCNTs, for energy storage applications. The main findings and key conclusions of the work included in this dissertation are summarized below.

(1) Electrospun bilayer PLLA membranes, consisting of a layer with aligned fibers (AFL) and a layer with randomly oriented fibers (RFL), were found to be more porous than single-layer membranes with randomly oriented fibers. The bilayer membranes exhibited higher porosity and superior mechanical properties compared with single-layer membranes having randomly oriented fibers. These features are particularly beneficial for cell infiltration and mechanical stability of scaffolds used in tissue engineering. The bilayer membranes also demonstrated strain hardening, characterized by fiber alignment in the stress direction and localized necking. Contrary to traditional fracture resulting in the abrupt decrease of stress capacity, the bilayer membranes showed a long tail of gradually decreasing stress comprising multiple instantaneous stress relaxation (microfracture) events, especially at high strain rates, which contributed to their high toughness. The high membrane porosity and good mechanical properties of the bilayer membranes, in conjunction with the good biocompatibility and biodegradability of PLLA scaffolds, are illustrative of the potential of these membranes for tissue engineering applications.

(2) *In vivo* implantation experiments with electrospun bilayer PLLA membranes were carried out with a rat model to illustrate their biological performance. The histology and immunohistochemistry studies showed that the bilayer membranes enhanced cell infiltration, distribution, and proliferation, collagen formation, and vascularization compared with conventional single-layer membranes consisting of randomly oriented fibers. The obtained results indicated that limitations associated with the inadequate porosity and mechanical strength of scaffolds fabricated by conventional electrospinning can be overcome with the present bilayer scaffolds, thereby enabling further advances in the application of electrospun fibrous scaffolds in tissue engineering.

(3) AC/PE and Gr/PE composite electrode materials were developed for all-solid-state 3D MSCs. The MSCs with PE in the electrode materials demonstrated significantly better electrochemical performance (i.e., higher capacitance and better rate capability) than conventional MSCs with PVDF as binder in the electrode materials, attributed to the increase of the surface area of active materials that was accessible by electrolyte ions and shorter ion diffusion path. The AC/PE MSCs showed higher areal capacitance, but poorer rate capability than Gr/PE MSCs. Electrolyte ion diffusion between the graphene nanosheets in the Gr/PE electrodes triggered an electro-activation process, which increased the specific capacitance by ~70% after 10,000 charge/discharge cycles. The AC/PE MSCs also showed good cyclic performance, exhibiting 80% capacitance retention after 10,000 charge/discharge cycles. The findings of these studies demonstrate the high potential of 3D

all-solid-state MSCs with PE incorporated in the electrode material for a wide range of power microsystem applications.

(4) SWCNTs spray-deposited on free-standing ultrathin PI substrates were used as electrode materials for ultrathin flexible MSCs. The MSCs were fabricated by combining conventional lithography and mechanical peel-off techniques. The SWCNT MSCs demonstrated unprecedented power density of 1125 W cm^{-3}, attributed to the high conductivity and easily accessible surface area of SWCNT network deposited by the spray-deposition method, and the small gap between the interdigital fingers of the in-plane electrodes. The microdevices also demonstrated excellent electrochemical stability, showing ~96% capacity retention after 100,000 charge/discharge cycles. This is important when compared with microbatteries whose relatively short lifetime may be a major limitation in most applications. Furthermore, the SWCNT MSCs showed exceptional flexibility, as demonstrated by bending, folding, and rolling, which paves the way for potential applications of MSCs as flexible energy storage devices in portable, stretchable, and/or wearable electronic devices.

(5) Highly stretchable MSC arrays with SWCNT electrodes were fabricated on honeycomb PDMS substrates. The MSC arrays demonstrated good capacitive performance and excellent rate capability. FEA simulation results revealed remarkably low strains in the MSCs and interconnects even after excessive stretching, bending, and twisting. SWCNT MSCs subject to 150% stretching, 180° bending, and 60° twisting did not show any significant degradation in electrochemical performance. The findings of this study demonstrate the high potential of the developed stretchable MSC arrays for a wide application range of wearable electronics, such as wrist and head band systems and wearable computing systems.